Dielectron Mass Spectra in $\sqrt{s_{NN}} = 200$ GeV Cu+Cu Collisions at PHENIX

A Dissertation Presented

by

Sarah Catherine Campbell

to

The Graduate School

in Partial Fulfillment of the Requirements

for the Degree of

Doctor of Philosophy

in

Physics

Stony Brook University

August 2011

UMI Number: 3475490

Dissertation Publishing

UMI 3475490

Stony Brook University

The Graduate School

Sarah Catherine Campbell

We, the dissertation committee for the above candidate for the Doctor of Philosophy degree, hereby recommend acceptance of this dissertation.

Thomas K. Hemmick – Dissertation Advisor
Professor, Department of Physics and Astronomy

John Hobbs – Chairperson of Defense
Professor, Department of Physics and Astronomy

Derek Teaney
Professor, Department of Physics and Astronomy

Martin Purschke
Physicist, Brookhaven National Laboratory

This dissertation is accepted by the Graduate School.

Lawrence Martin
Dean of the Graduate School

Abstract of the Dissertation

Dielectron Mass Spectra in $\sqrt{s_{NN}} = 200$ GeV Cu+Cu Collisions at PHENIX

by

Sarah Catherine Campbell

Doctor of Philosophy

in

Physics

Stony Brook University

2011

The dielectron mass spectrum consists of light vector meson decays, correlated heavy quark contributions and decays from other hadronic and photonic sources. Thermal radiation and modifications to the light vector mesons may provide additional signals at low masses above known hadronic sources. The PHENIX $\sqrt{s_{\mathrm{NN}}} = 200$ GeV Au+Au and Cu+Cu analyses have measured a centrality dependent excess in the the low mass region between 0.15 GeV/c^2 and 0.75 GeV/c^2. Between the ϕ and the J/ψ, in the intermediate mass range, the correlated heavy quark decays are the primary dielectron source; direct photons may augment this region as well.

The Cu+Cu system is sensitive to the onset of the dielectron excess. By studying the Cu+Cu mass spectra and yields as a function of pair p_T and collision centrality we obtain further understanding of its behavior. Comparisons to the PHENIX Au+Au and p+p measurements an extrapolations from theory are presented.

iii

I take to your reckless and composite chords - I add to them, and cheerfully pass them forward.

<div align="right">– Walt Whitman</div>

Contents

List of Figures

List of Tables

Acknowledgements

Thank you to my husband, my friends and my family. I could not have done this without your support.

Chapter 1

Introduction

The high temperatures and densities created in a relativistic heavy ion collision break down the protons and neutrons within the nucleus restoring chiral symmetry and creating a deconfined plasma of the underlying particles, quarks and gluons. As the plasma cools and expands it forms particles that stream out of the collision and are measured in the PHENIX detector. Through these particles we glean information about the plasma and its production. By studying this extreme condition of nuclear matter we gain insight into the underlying physics and symmetries in nuclear materials.

The dielectron spectrum is particularly illustrative of these medium effects. It contains all processes that produce electron-positron pairs. Electrons can provide direct information about all stages of a heavy ion collision. This is because they do not participate in strong interactions. Once emitted electrons are unaffected by later stage effects such as hadronization. Signals within the dielectron spectrum can contain direct information about the early collision. However, these early collision pairs are hidden among all of the other dielectron production mechanisms. By studying the entire mass spectrum out to 4 GeV/c^2, we look beyond specific resonances and see deviations from the expected hadronic behavior.

The dielectron mass spectrum contains an excess over expected yields in Cu+Cu collisions with a collision energy per nucleon pair of 200 GeV. The spectrum was measured by the PHENIX experiment using data taken in 2005 at the Relativistic Heavy Ion Collider at Brookhaven National Laboratory. Within the dielectron mass spectrum, the expected signals are enhanced with additional production processes and modified by the interaction with the deconfined material created in the collision, a new phase of matter called a quark gluon plasma.

This document details the measurement and meaning of the dielectron excess in Cu+Cu collisions as determined by the PHENIX experiment. The remainder of this chapter provides introductory information on nuclear interactions, the history and evolution of relativistic heavy ion collisions, and the characteristics of the dielectron spectrum with a focus on in medium modifications.

(a) Quark annihilation

(b) Quark annihilation with gluon bremstralung

(c) Gluon-Compton scattering
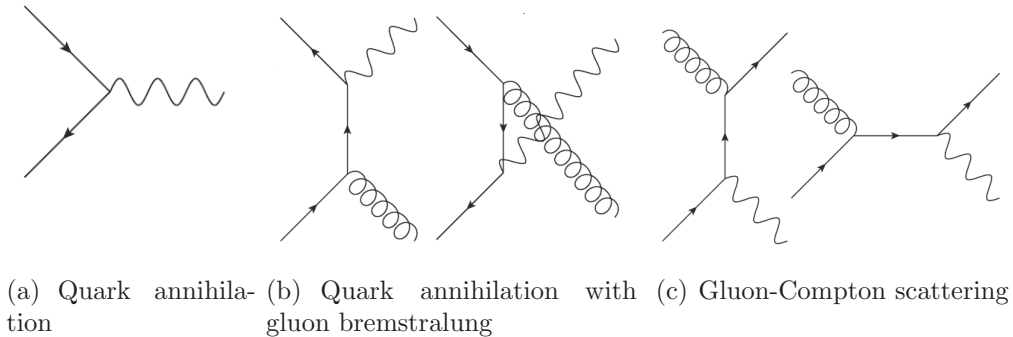
Figure 1.1: Feynman diagrams for quark annihilation, quark annihilation with gluon bremstralung and gluon-Compton scattering. In each diagram time runs to the right, quarks are denoted by lines with arrows, anti-quarks have backward facing arrows, gluons are spiral lines and photons are sinusoidal lines. Virtual photons created in these processes are detected as dielectron pairs.[1]

1.1 Theory of nuclear matter

The theoretical understanding of high energy nuclear phenomena is based on the standard model and field interactions. A short introduction to strong interactions and quantum chromo-dynamics is given focusing on the fundamental concepts of nuclear interactions. The extreme cases at high temperature or density of quark-gluon plasma and chiral symmetry restoration are also presented.

1.1.1 Strong interactions

The standard model characterizes the four physical forces (strong, electromagnetic, weak, gravitational) as field interactions between elementary particles with mediating bosons. This text focuses on the strong force where quarks interact via mediating gluons. There are six quarks, the three light quarks (up, down, strange) and the three heavy quarks (charm, bottom, top).

Feynman diagrams provide a graphical understanding of the interactions between quarks and gluons. A few diagrams for processes that produce dielectron pairs from virtual photons are in Figure 1.1. In each, the horizontal direction is time and different line types correspond to different particle types as listed in the caption. In the strong interaction the system's energy, momentum, charge, color charge, spin and parity are conserved. Certain particle numbers such as lepton number, baryon number and strange quark number are also conserved.

Table 1.1: Quark charges and masses

Quark	charge	intrinsic mass	m_{eff} in mesons	m_{eff} in baryons
up	2/3	0.0075 GeV/c^2	0.310 GeV/c^2	0.363 GeV/c^2
down	-1/3	0.0042	0.310	0.363
strange	2/3	0.150	0.483	0.538
charm	-1/3	1.1	1.5 [4]	1.5
top	2/3		>23	>23
bottom	-1/3	4.2	4.7	4.7

Each quark has fractional electromagnetic charge ($\pm 1/3$ or $\pm 2/3$), an intrinsic spin of $\pm 1/2$ and carries a color charge (red, green, blue). Anti-quarks carry anti-color charges. There are eight gluon types, each carries a color and anti-color charge. A quark interacting with a gluon is altered, its color charge changes. Gluons can interact with other gluons. These gluon loops complicate calculations and provide some of the higher order effects that make in understanding strong interactions so difficult.

Individual quarks are confined into colorless bound states. Quarks and anti-quarks combine in twos or threes creating colorless composite particles where the color charges either cancel (a red anti-red pair) or combine (red-green-blue). Three quarks bind together to produce a baryon; a quark anti-quark pair produces a meson.

Light quark meson masses

Equation 1.1 gives simple calculation of the light quark meson masses,

$$m = m_{q1} + m_{q2} + A\frac{S_1 \cdot S_2}{m_{q1}m_{q2}} \tag{1.1}$$

where m is the meson mass, m_{q1} and m_{q2} are the effective quark masses, S_1 and S_2 are the quark spin states and A is a coefficient related to $|\psi(0)|^2$. The quark spin coupling term, $S_1 \cdot S_2$, is reminiscent of the hyperfine splitting seen in the hydrogen atom. This term has two states, either the quark's spins are aligned as in the vector meson case or the quark spins are not aligned as is the pseudo-scalar meson case. For example, the ρ meson is a light vector meson made up of a superposition of u and d quarks, $(u\bar{u} - d\bar{d})/\sqrt{2}$. Equation 1.1 uses the fit value for A of 0.16 GeV/c^2 and the effective quark masses, m_{eff}, for mesons are used as listed in Table 1.1. The mass of the ρ meson is calculated as 0.78 GeV/c^2 and measured as 0.77 GeV/c^2 [2] an agreement within one percent. [3]

This explanation of the light meson masses is over-simplified. The effective quark masses, m_{eff}, of the light quarks (up, down and strange) are much larger than the intrinsic quark masses listed in Table 1.1. For the light quarks the effective quark masses are primarily from the dynamical properties of the quantum-chromodynamics, in particular the relationship of

3
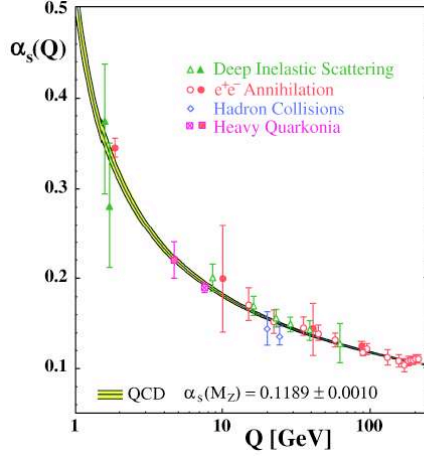
Figure 1.2: The coupling constant, α_S, dependance on the momentum transfer, Q. Various experimental results are shown. The lines correspond to a pQCD calculation. [6]

the quarks to the chiral and gluon condensates.

1.1.2 Quantum-chromodynamics

Quantum-chromodynamics (QCD) is the theoretical framework for quark-gluon interactions. The QCD lagrangian is

$$\mathcal{L} = \bar{q}_k \left(i\gamma^\mu \delta_\mu - m_k \right) q_k - g \left(\bar{q}_k \gamma^\mu T_a q_k \right) G_\mu^a - \frac{1}{4} G_{\mu\nu}^a G_a^{\mu\nu} \tag{1.2}$$

where q_k and $\bar{q}_k$ are the kth quark color fields, γ^μ are the Dirac matrices, m_k is the kth quark's mass parameter, G_μ^a are the gluon gauge fields, and $G_{\mu\nu}^a$ is the gluon field strength tensors. The QCD lagrangian follows the symmetry of the super unitary group of dimension three, SU(3). The T_a terms are the 3×3 generating matrices for the color SU(3) group. The coupling strength between the gluons and quarks, g, is related to the strong coupling constant α_S, $g = \sqrt{4\pi\alpha_S}$. [5]

QCD's theoretical framework is analogous to the framework in quantum-electrodynamics (QED), the theory for electromagnetic interactions. The strength of QCD and QED interactions is determined by their coupling constants, α_s and α respectively. In QED, α is relatively stable with values of approximately 1/137. In QCD, α_S varies with the distance between the interacting partons or the interaction's momentum transfer, Q^2, as detailed in

Equations 1.3.

$$\alpha_S\left(Q^2\right) = \frac{12\pi}{(11 * N_c - 2 * N_f)\, log\left(Q^2/\Lambda^2\right)}\left(1 + higher\ log\ terms\right) \tag{1.3}$$

where Λ is related to the scale constant and N_c and N_f are the number of color charges and light quark flavors respectively. At large distances, i.e. $Q^2 \approx \Lambda^2$, α_S increases and the interactions become stronger. Confinement is a result of this behavior. Should a quark attempt to leave a bound state, quark loops begin to form and polarize the vacuum enhancing the system's color charge until a $q\bar{q}$ pair is pulled out of the vacuum creating bound states. At small distances, i.e. $Q^2 >> \Lambda^2$, α_S is weakened allowing quarks and gluons to move freely. This is called asymptotic freedom and is a result of the distributed gluon cloud reducing the effective color charge for interactions within the cloud. Figure 1.2 shows experimental confirmation of this asymptotic behavior. The scale constant, Λ, is set by fixing the α_S value at the mass of the Z^0 boson, $\alpha_S\left(m_{Z^0}\right) = 0.118 \pm 0.002$, giving a Λ of 217^{+25}_{-23} MeV [7].

QCD calculations at small α_S are feasible using perturbative QCD because higher order effects, requiring higher powers of α_S, are small. These calculations are relegated to the close neighborhood of the parton or large momentum transfers, Q^2. The long range behavior describing the probability of parton hadronization is parameterized from electron-positron collider measurements. These probabilities called fragmentation functions and are independent of the original collision process. In a heavy ion collision we must also consider the motion of the parton within each nucleon. Parton distribution functions provide a partons' momentum distribution; they are measured in deep inelastic scattering experiments. The patching together of parameterized and calculated information is called factorization. In this method theorists have calculated cross sections for various interactions including, jets and dileptons from hard processes and Drell-Yan. Unfortunately many of the low mass dielectron signals are in the non-perturbative regime where α_S is large and factorization is known to fail. [8]

At low Q^2, QCD calculations are extremely difficult due to the higher order terms that must be considered. Lattice QCD calculations provide an alternative method to quantify the QCD interactions in this regime. It is a computationally intensive process. The action of the QCD lagrangian is calculated in small regions of four dimensional time-space, called plaquettes. By restricting the calculations to small plaquettes many of the large scale complications of QCD are avoided. A lattice of plaquettes is calculated and integrated. This process is repeated with random variations in the quark and gluon fields until the stable state is found. Physical quantities are obtained once the plaquette size is extrapolated to zero. [7] [9]
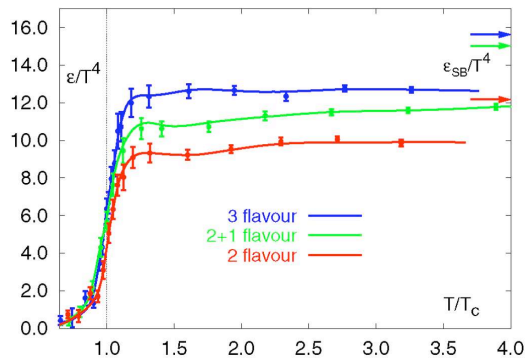
Figure 1.3: The energy density in units of T^4 is plotted a function of the temperature scaled by the critical temperature for a variety of quark numbers or flavors. The arrows on the right mark the Stefan-Boltzman limit for an ideal gas of quarks and gluons. [10]

1.1.3 Quark-gluon plasma

A consequence of asymptotic freedom is that at very short distances, or very large Q^2, confinement breaks down and quarks and gluons move freely. A system at high temperature or density achieves the small distances or large Q^2 to create deconfined matter. This idea was first raised in 1975 by Collins and Perry for low-temperature high-density neutron stars [11]. In the same year Cabibbo and Parisi described the deconfined material as a new phase of matter [12]. In 1978 Shuryak extended the theory to high temperatures and named the new phase of matter a quark-gluon plasma (QGP) [13]. The required energy density, ϵ, and critical temperature, T_C, to achieve the phase transition can be approximated using dimensional arguments resulting in values of $\epsilon \approx 1$ GeV/fm^3 and $T_C \approx 175$ MeV. This places the phase transition region in the nonperturbative regime of QCD. [10]

Lattice QCD calculations are necessary to further our theoretical understanding of the QCD phase transition accessible at RHIC. Figure 1.3 shows lattice QCD results for phase transitions assuming different numbers of quark flavors. The energy density in units of temperature to the fourth is plotted a function of scaled temperature. A steep transition in energy density occurs at the critical temperature, $T = T_C$. The plateau ϵ/T^4 values are below the Stefan-Boltzman limit that assumes an ideal gas of quarks and gluons. The phase transition is not first order and is most likely a smooth crossover. First order phase transitions are discontinuous between the two phases and include a period where the temperature is constant and the latent heat increases results in a slushy mixed phase where both states coexist in equilibrium. Smooth crossover transitions are extended continuous transitions without a mixed phase. Both first order and crossover transitions restore broken symmetries.

The phase diagram for the QGP transition is shown in Figure 1.4. This is plotted as a function of the system's temperature, T, and baryo-chemical potential, μ_B. The baryo-

6
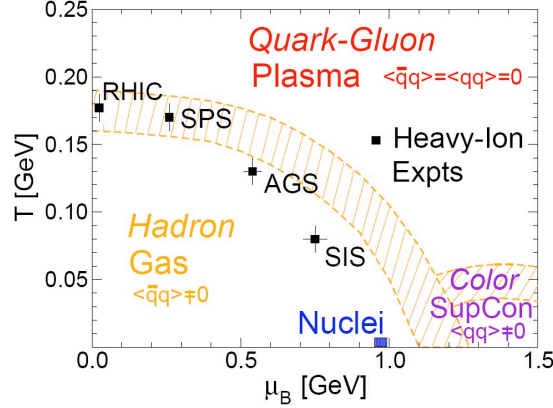
Figure 1.4: The QGP phase diagram plotted as a function of the baryo-chemical potential, μ_B and the temperature, T. The QGP phase transition is shown as the hatched arc region. At below this arc a hadron gas phase and normal nuclear matter is present, above it a QGP is formed. At high μ_B and low T, a color superconductor is expected. Points show the areas of phase space that are accessible at heavy ion colliders. [14]

chemical potential is analogous to the chemical potentials seen in thermodynamics. It is the amount of energy increased in the system when a baryon is added assuming the system's volume and entropy are constant [15]. The baryo-chemical potential is related to the system's net baryon density, the number of baryons minus the number of anti-baryons. Higher values of μ_B can be reached experimentally by reducing beam energies. RHIC beam energies are large enough so that the μ_B and net baryon density are low. This is a result of transparency, a phenomena where the non-interacting partons in the colliding nuclei pass through the collision region and continue in the beam direction away from any created material.

A critical point is expected but its location is unknown. Scans of the collisions energy in the range $\sqrt{s_{NN}} = 9 - 200$ GeV extend RHIC measurements to higher μ_B hoping to find the critical point. Above the critical point, a first order phase transition is expected. Below the critical point, in the region of the $\sqrt{s_{NN}} = 200$ GeV RHIC collisions, the transition is a smooth crossover. The lack of a mixed phase in the RHIC QGP transition complicates the understanding of ρ mesons modified by the QGP. However it is possible that the hadron formation could occur at differing stages of the transition for the various bound states. This could allow for early ρ formation within residual QGP material.

1.1.4 Chiral symmetry

In the QGP phase transition confinement is lifted and chiral symmetry is restored. In a chiral symmetric system, quark masses reduce to zero and left- and right-handed chiral

$\bar{q}$q-excitations of the QCD vacuum

Energy (MeV)

f_1 *(1420)*

a_1 *(1260)* f_1 *(1285)*

ϕ *(1020)*

f_0 *(400-1200)* ρ *(770)* ω *(782)*

P-S, V-A *splitting*
in the physical vacuum

π *(140)*
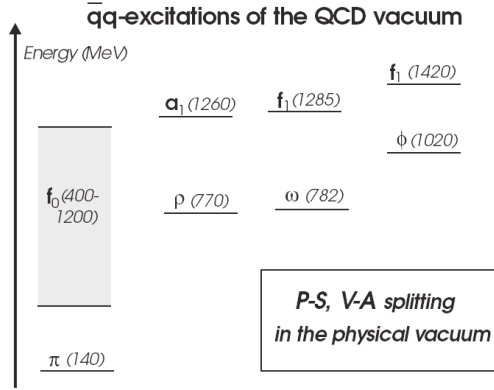
Figure 1.5: The light meson chiral pairs with the mass splitting between the pseudoscalar and scalar mesons, (π, f_0), and the axial vector and vector mesons, (ρ, a_1), (ω, f_1) and (ϕ, f_1). The masses of each particle are listed in parenthesis and the vertical scale displays the energy separation. [14]

states no longer mix. A brief discussion of chirality and chiral symmetry is presented below.

QCD states have either left or right chirality or handedness based on how they permute under rotations in flavor space, $e^{i\phi\cdot(\lambda_F/2)}$ where ϕ is the rotation angle and λ_F is the generator of the transformation. The vector and axial vector currents are presented in Equation 1.4

$$j^{\mu}_{Va} = \bar{q}\gamma^{\mu}\frac{\lambda^a_F}{2}q \ \ and \ \ j^{\mu}_{Aa} = \bar{q}\gamma^{\mu}\gamma_5\frac{\lambda^a_F}{2}q \tag{1.4}$$

where q and $\bar{q}$ are the quark states, γ^{μ} and γ_5 are related to the Dirac matrices and λ_F is related to the flavor transformation. Chiral symmetry follows the $SU_L(3) \times SU_R(3)$ symmetry relation. The left and right chiral states do not mix and opposite parity states are degenerate.

When quarks are massive, chiral symmetry is explicitly broken. The vector current can only be conserved when the quark flavors have the same mass, the axial vector current requires quark masses of zero. Even with massless quarks the axial vector current is not conserved. Light quark mesons obtain their masses primarily from their QCD interactions such as the quark condensate and not from the intrinsic quark masses. These QCD interactions generate the effective quark meson masses listed in Table 1.1. However, light quark mesons do not show a mass degeneracy between with their chiral partner mesons. The masses of the ρ and a_1 mesons differ, $m_\rho = 0.770$ GeV and $m_{a_1} = 1.230$ GeV [2]. The meson couplets are shown in Figure 1.5. When massless quarks do not reconcile the gauge transformation, the symmetry is spontaneously broken.

The order of the chiral symmetry is related to $\langle q\bar{q} \rangle$, the quark condensate. When chiral symmetry is restored, the quark condensate is zero, $\langle q\bar{q} \rangle = 0$. In the spontaneously broken

chiral state, there is a non-zero quark condensate, $\langle q\bar{q} \rangle \neq 0$. Another consequence of spontaneous chiral symmetry breaking is that the ground state solution $q = |0\rangle$ is not invariant. This means that the potential is non-zero in the ground state. Since QCD has parity conservation, ie the potential has reflection symmetry, there are multiple invariant solutions and potential minima. Choosing between the solution states breaks the chiral symmetry and produces eight massless Goldstone bosons.

(a) V(σ, π) (b) V(σ, $\pi = 0$)
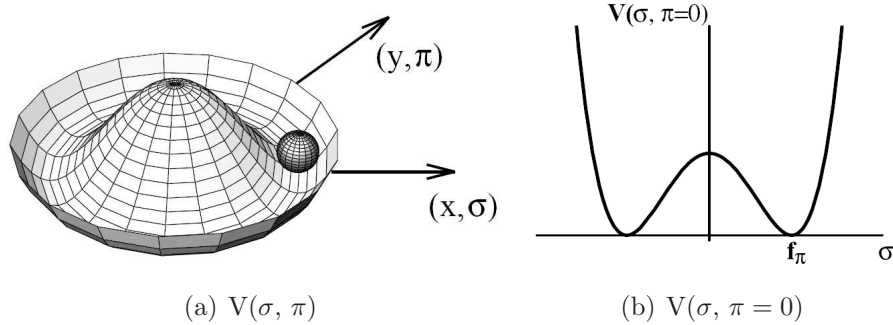
Figure 1.6: The mexican hat potential in three dimensions and shown as a slice at $\pi = 0$. [16]

Figure 1.6 shows a mexican hat potential modeling the effective QCD behavior at zero temperature. Here f_π is related to the order of the chiral symmetry, and π and σ fields describe the set of axial vector transformations. In this example the π field is rotational. Rotational movements along the bottom of the potential well are energetically identical, these are called π-excitations and correspond to the massless Goldstone bosons. The σ field is radial, movement on this axis requires additional energy. The additional energy creates a mass difference between a meson and it's chiral partner. Theoretical calculation of this additional energy find the a_1 mass follows $m_{a_1} = \sqrt{2}m_\rho$ [17], which is in agreement with the measured values [2]. When chiral symmetry is restored these chiral partner states become degenerate and the π excitations will become massive. [14] [15] [16] [18] [19] [20]

1.2 Relativistic heavy-ion collisions

In a relativistic heavy ion collision, the colliding particles undergo a cacophony of nuclear interactions. The goal here is not to study one type of interaction for its own sake but to use these signals to understand the many-bodied behavior of the nuclear material. D. Allan Bromley put this nicely when he wrote:

> [I]n contrast to particle physics, where ever more energy is delivered to ever-decreasing volumes, in high-energy heavy ion work we are delivering ever-increasing

energies to much larger volumes - volumes large enough to contain a large number of nucleons and thus at least in principal large enough to display entirely new collective phenomena. [21]

A relativistic heavy ion collision creates the high temperatures and density needed to restores chiral symmetry and create a quark gluon plasma. The QGP phase transition is exactly the sort of collective phenomena Bromley is referring to. This section continues with a brief overview of previous heavy ion experiments and the definitions a few relevant terms. A description of the evolution of a heavy ion collision and key measurements identifying QGP formation at RHIC are presented.

1.2.1 Experimental history

Relativistic heavy ion interactions were first measured in cosmic ray balloon flights in the 1940s [22]. By the late 1950's scientists were able to create relativistic heavy ions in the laboratory by re-purposing proton synchrotrons to accelerate heavy ion beams. In 1971 at Lawrence Berkeley National Laboratory, a beam from the SuperHilac was injected into the Bevatron creating the Bevalac. The Bevalac was able to look beyond the interactions between nuclei and generate collisions between individual nucleons [21].

At this time promising theoretical work predicted the QGP phase transition. This generated interest in relativistic heavy ion collisions as they provide a mechanism to obtain the high energy densities necessary for QGP. Unfortunately the 1-2 GeV per nucleon nitrogen beams available at the Bevalac were not up to the task. [23]

Accelerator advances in the 1980's led to higher energy beams of heavier nuclei directed at fixed target experiments. The Alternating Gradient Synchrotron (AGS) at Brookhaven National Laboratory (BNL) provided oxygen and silicon beams at collision energies per nucleon pair, $\sqrt{s_{NN}} \approx 5$ GeV, and the Super Proton Synchrotron (SPS) at European Organization for Nuclear Research (CERN) accelerated oxygen, sulfur, lead and indium beams to collision energies per nucleon pair of around 20 GeV. At AGS energies nuclear stopping created a baryon rich collision region. Higher energies at SPS allow the nonparticipating spectator nucleons to pass through the interaction region lowering the net baryon density. Measurements of strangeness enhancement relative to elementary interactions confirm that thermal equilibrium is reached at AGS and SPS. J/Ψ suppression, a signal of QGP formation [24], was measured at SPS but a misunderstanding of cold nuclear effects complicated the interpretation delaying the discovery of the QGP at SPS.

In 2000 the Relativisitic Heavy-Ion Collider (RHIC) program started at BNL. RHIC collides gold and copper at $\sqrt{s_{NN}} = 200$ GeV using the AGS as an injector. The RHIC experiments were the first to identify QGP formation and study the characteristics of the plasma. The heavy ion program at the Large Hadron Collider (LHC) at CERN, started in 2010 with $\sqrt{s_{NN}} = 2.76$ TeV lead collisions. Measurements from the LHC experiments have already begun to produce interesting new results in a higher energy regime.

1.2.2 Definitions of terms

- Leptons are a class of point-like particle consisting of neutrinos, electrons, muons and taus. Muons and taus are heavier versions of electrons. All of these particles are without color charge and interact primarily electromagnetically or weakly.

- The collision energy per nucleon pair, $\sqrt{s_{NN}}$, relates the beam energies and the number of accelerated nucleons. For p+p collisions at $\sqrt{s_{NN}} = 200$ GeV, there are two colliding proton beams at 100 GeV. For Au+Au and Cu+Cu collisions at the same $\sqrt{s_{NN}}$ the beams are at 19.7 and 6.3 TeV respectively.

- A particle's transverse momentum, p_T, is the momentum perpendicular to the beam direction, $p_T = |p|sin(\theta)$ where p is the particle's momentum and θ is the direction of the particle relative to the beam axis. The longitudinal momentum, p_L is the momentum parallel to the beam direction. Transverse kinetic energy, KE_T, is calculated much like standard kinetic energy but with the transverse momentum instead of the momentum. Transverse mass, m_T is calculated from the mass and transverse momentum in much the same way energy is calculated, $\sqrt{m^2 + p_T^2}$. Within this dissertation the p_T often refers to the p_T of the dielectron pair.

- Rapidity, y, is a kinematic variable related to the relativistic velocity in the beam direction. It is defined in Equation 1.5.

$$y = \frac{1}{2}ln\left(\frac{E + p_L}{E - p_L}\right) \tag{1.5}$$

Rapidity is invariant under Lorentz transformations making it preferable for theoretical calculations. Unfortunately, it is hard to determine experimentally. An approximate value of the rapidity, the pseudorapidity, η, is measurable using the angle of particle emission relative to the beam axis, θ, $\eta = -ln[tan(\theta/2)]$. In a relativistic environment where $p >> m$, the pseudorapidity and rapidity are essentially equal.

- Centrality characterizes the amount of overlap in a heavy ion collision. Collisions where the nuclei completely overlap are called central while more glancing collisions are called peripheral. Centrality is determined by measuring the amount of non-interaction nucleons downstream from the collision. In Figure 1.7 the spectator nucleon distribution measured in the PHENIX Beam-beam counter is divided into centrality classes according to population percentages. The 0-10% centrality group is made up of central collisions while 80-90% has peripheral collisions. For minimum bias data the trigger is set so the number of events within centrality groups of the same percentage width are approximately the same.

- Characterizations of the collision centralities are calculated using a geometric model, called the Glauber model. It uses the shapes of the nuclei to estimate the number of
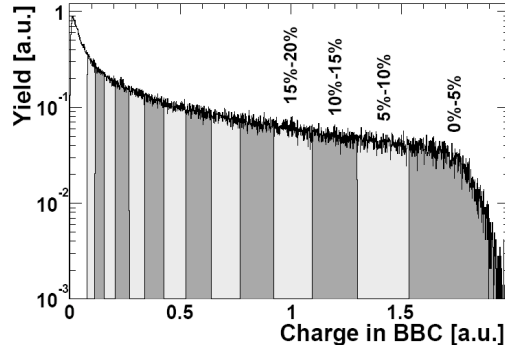
Figure 1.7: The distribution of the spectator nucleon population measured in the PHENIX Beam-beam counter (BB or BBC). The distribution is divided into percentage based centrality groups. [25]

nucleons participating in the collision, N_{Part}, and the number of independent nucleon-nucleon collisions, N_{Coll}. A constant nucleon-nucleon cross-section of 42 mb is assumed [26]. Medium and collective effects are not included. Because N_{Coll} is not measureable, a Glauber Monte Carlo is used to find the mean N_{Part} and N_{Coll} for a given centrality group in a collision system.

These two numbers provide a mechanism to compare the collision environment in Cu+Cu to that in Au+Au. Central Cu+Cu collisions of 0-10% centrality have $N_{Part} = 98.2 \pm 2.4$ and $N_{Coll} = 192.7 \pm 20.7$. This is similar to 35-40% Au+Au collisions where $N_{Part} = 102.7 \pm 4.3$ and $N_{Coll} = 188.6 \pm 20.6$. The variation in the centrality bin width between collisions with the same N_{Part} and N_{Coll} shows that the Cu+Cu system can study the onset of QGP formation with increased resolution in centrality.

1.2.3   Collision evolution

Relativistic heavy ion collisions evolve through a variety of stages. Dielectron are emitted in each stage. The accelerated nuclei are Lorentz contracted into flat pancakes. As they approach the collision the nuclei quickly decelerate emitting coherent bremsstrahlung radiation [28]. The initial collision consists of hard scattering interactions between the partons in the nuclei. These interactions have large momenutm transfers and scale as a function of the number of collisions, N_{Coll}. Dielectrons produced from Drell-Yan processes and jets formed from fragmenting partons are created in these hard interactions.

In the collision, the two ions pass through each other creating a hot dense matter at central rapidities [27], Figure 1.8. The nuclei's non-interacting components continue in the beam direction. The generated matter at midrapidity is a result of the high temperatures and energy densities created during the collision allowing a phase transition from the normal
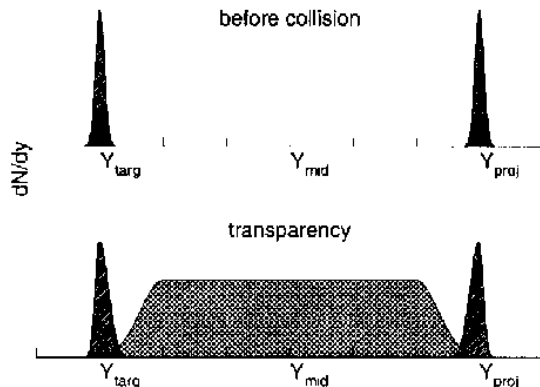
Figure 1.8: Diagram of the nuclear matter distribution in rapidity, y, according to the Bjorken picture. The upper plot shows the approach of two relativistically flattened nuclei. After the collision, in the lower plot, the non-interacting partons move away from the collision. The mid-rapidity region is populated by material created in the collision. [27]

nuclear regime and into a region where confinement is broken and a plasma of quarks and gluons is created. In this plasma, quarks become massless and chiral symmetry is restored. Dielectrons are produced as a result of processes in the Quark Gluon Plasma (QGP).

As the matter cools, quarks become confined creating a resonance gas of interacting hadrons. Hadronic collisional broadening and pion-pion annihilation provide additional the dielectron yields. The hadronization stage ends when inelastic collisions cease and the final particle mesons and baryons are formed. At this point the relative hadron compositions are set. Chemical-hydrodynamic models extract the temperature of this so-called chemical freeze out using various hadronic ratios [29].

The remaining matter quickly thermalizes and expands. Elastic collisions are no longer possible as the hadron's mean free path is larger than the remaining fireball. The momentum distributions of particles are set. The expansion creates an excess of high p_T particles beyond what is expected from a simple thermal distribution; this is called radial flow. The almond shape of the matter, a result of the geometric overlap between the two nuclei, leads to a momentum asymmetry as particles stream out traveling with different path lengths in the medium. This phenomenon is called elliptic flow, v_2. These flows are well described by ideal hydrodynamic models that characterize the matter as a nearly perfect fluid. Each of these stages are depicted in Figure 1.9.

1.2.4   QGP signals at RHIC

Heavy ion collisions at RHIC have obtained the high energy densities necessary to produce a quark gluon plasma (QGP). The signatures of QGP formation in Au+Au collisions have
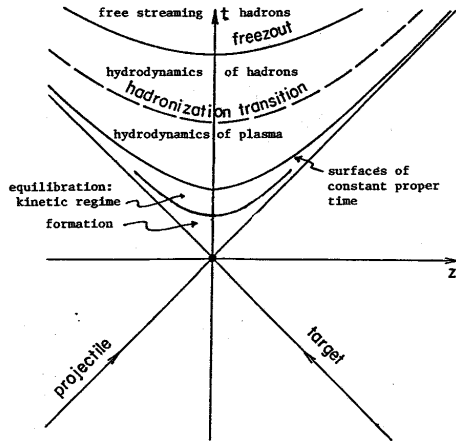
Figure 1.9: Diagram of the space-time evolution of a heavy ion collision plotted on the relativistic light cone. [7]

been detailed at length in the RHIC experiments' white papers [10] [30] [31] [32]. The QGP is known to produce large energy loss and partonic elliptic flow for both light [33] [34] [35] and heavy quarks [36] [37]. This energy loss is studied with the nuclear modification factor, R_{AA}, defined in Equation 1.6.

$$R_{AA} = \frac{dN_{AA}}{\langle N_{Coll} \rangle dN_{pp}} \tag{1.6}$$

where dN_{ii} is the differential yield in either the p+p or Au+Au collision system and $\langle N_{Coll} \rangle$ is the mean number of collisions in the centrality bin. R_{AA} values of one mean that the heavy ion collisions are like $\langle N_{Coll} \rangle$ independent p+p collisions. R_{AA} values below one means that particle production is suppressed below what is expected from $\langle N_{Coll} \rangle$ independent p+p collisions.

Figure 1.10(a) shows the R_{AA} for pions and direct photons as a function of the number of participating nucleons in the collision, N_{Part}. The plot shows that neutral pions are suppressed below N_{Coll} scaled p+p collisions while direct photons are unaffected. The azimuthal asymmetry, v_2, for light quarks follows quark scaling as shown in Figure 1.10(b). Figure 1.10(c) presents the R_{AA} and v_2 for non-photonic single electrons. Non-photonic electrons are the result of open charm decay providing a measure of the heavy quark behavior. High p_T non-photonic electrons exhibit the same suppression and flow effects as the light quark mesons. This characterizes the QGP as having very early thermalization and a strong interaction even for the heavy charm quarks. The direct photon p_T spectrum for central Au+Au collisions, Figure 1.10(d), is compared to theoretical calculations of thermal photon emission. These thermal models find initial QGP temperatures between 300 and 600 MeV

14
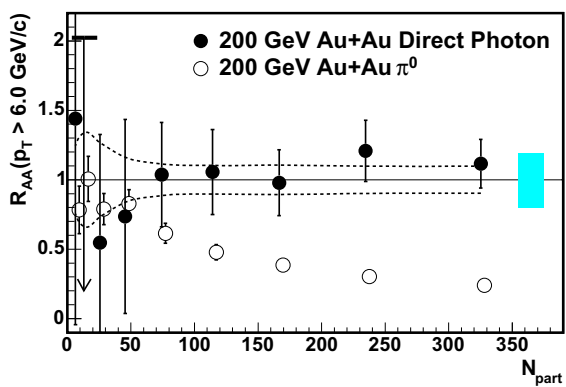
(a) R_{AA} of π^0 and γ_{Direct} [34]
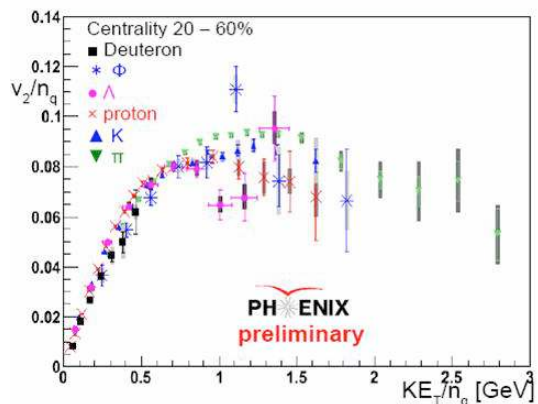
(b) partonic v_2 scaling [38]
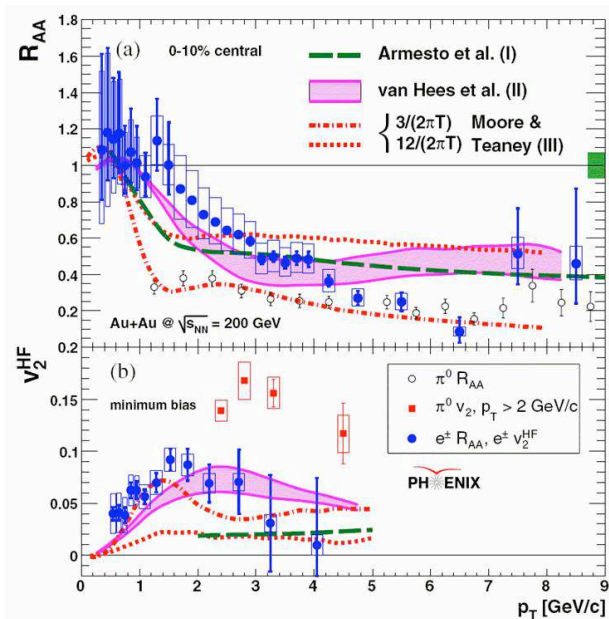
(c) R_{AA} and v_2 of non-photonic electrons [39]
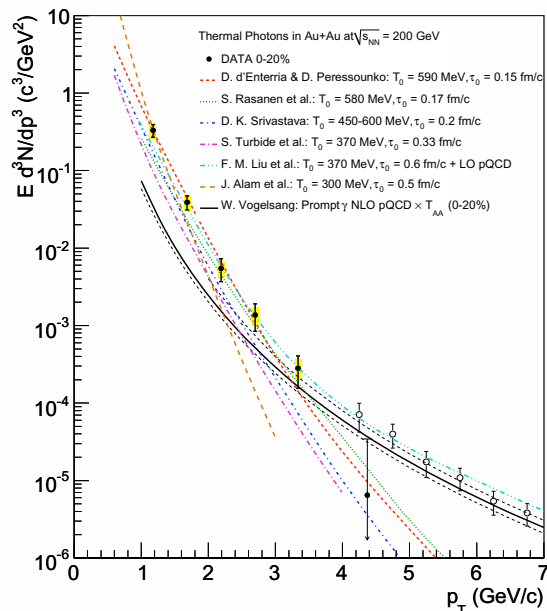
(d) γ_{Direct} p_T spectra [40]

Figure 1.10: PHENIX results highlighting QGP behavior.
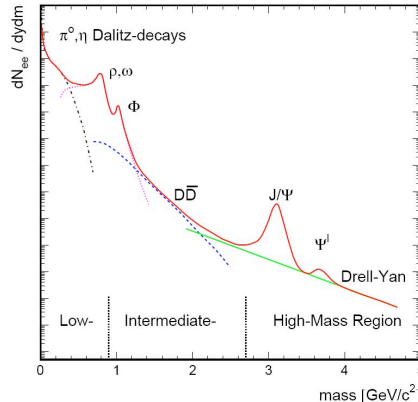
Figure 1.11: The dielectron mass spectrum contains various signals including dalitz decays from pseudoscalar mesons (π^0, η), resonances from vector mesons (ρ, ω, ϕ, J/ψ and ψ') and the correlated open charm ($D\bar{D}$) and Drell Yan components. The different mass regions are clearly marked with the low mass region below the ϕ, the intermediate mass region between the ϕ and the J/ψ and the high mass region above the J/ψ. [20]

[40], well above the expected transition temperature of 175 MeV.

Measurements in the Cu+Cu collisions system have shown the same QGP signatures [38] [41] confirming that QGP is created at Cu+Cu energy densities. Cu+Cu collisions provide an system with a similar geometry as Au+Au collision but with fewer participating partons, resulting in a lower energy density. This allows us to study the nature of the QGP onset and separate geometric and energy density effects.

1.3 Dielectron mass spectrum

The dielectron mass spectrum contains signals continuously emitted throughout the collision. As colorless particles, electrons primarily interact electromagnetically and have limited final state interactions. This makes dielectrons an ideal probe of the QGP. They can measure quantities from early stages of the collision. Direct photon measurements have similar early stage access but are hindered by lower signal to backgrounds rates particularly at low momenta. Dielectron spectral measurements provide the potential to measure the temperatures and the time-spans of various collision stages by decomposing the emission yields of various sources with theoretical understanding of the emission rates.

The dielectron spectrum contains a variety of signals, many are shown in Figure 1.11. The free streaming vector mesons (ρ, ω, ϕ, J/ψ and ψ') decay into dielectrons forming resonance peaks. The pseudoscalar mesons (π^0, η and η') Dalitz decay creating exponentially falling line shapes. Pre-collision coherent bremstralung radiation from decelerating nuclei has a

16

negligible contribution and is not included [28]. Hard processes such as Drell Yan and prompt photons primarily from $q\bar{q}$ annihilation provide additional early collision signals. Drell Yan pairs are seen in Figure 1.11 at masses above the J/ψ. Prompt photons are not included in Figure 1.11 but they are expected at high and intermediate masses. Thermal radiation emitted in the fireball produces virtual photons that decay into dielectrons; these have been identified at low masses and high p_T [42]. Dielectron emission may even occur before the QGP equilibrates [43].

Pair production of heavy quarks results in another dielectron signal. The correlated heavy quarks hadronize into open charm or bottom meson pairs. When both of the mesons decay semi-leptonically the resulting electron-positron pair maintains the correlation from the pair production of the heavy quarks. This is true for both charm and bottom quark production, $c\bar{c} \rightarrow D\bar{D} \rightarrow e + e-$ and $b\bar{b} \rightarrow B\bar{B} \rightarrow e + e-$. The open charm component peaks at masses of 0.5 GeV/c^2, but it is the dominant signal in the region above the ϕ. The open bottom component is expected to overwhelm open charm at masses above the J/ψ. The heavy quark behavior in the QGP is its own interesting field of study. Suppression at high p_T [39] and changes in the angular distributions [44] [45] have been measured. There is the potential of centrality dependant changes in the intermediate mass region due to these modifications of the heavy quarks. Statistical limitations have hindered the understanding of this region.

Additional modifications to the dielectron spectrum as a result of the QGP include the suppression of mesons formation due to energy loss and enhanced thermal and prompt photon emission leading to dileptons. A variety of theoretical work considers the modifications of light vector mesons in the collision medium. In particular, the short-lived ρ meson, $\tau \approx 1.3$ fm/c, provides a probe to study the effects of the residual medium on it's mass. These light vector meson mass modifications will be presented in more detail later in this section followed by a review of recent continuum dilepton mass spectrum measurements in heavy ion systems. One caveat related to the various dilepton signals is that the signal strength of any one process in the spectrum depends on its relative production rate and emission timespan.

1.3.1 Light vector meson modification theories

Dilepton spectrum modifications have been proposed through a variety of mechanisms. Here we discuss three of them, a broadening of the ρ mass from medium hadron-hadron interactions, a dropping of the ρ mass due to medium temperature effects, and a combination of broadening and/or dropping masses assuming parton hadron string dynamics (PHSD). One relevant difference between the theories is what is the nature of the medium leading to the modification, in the broadened ρ theory it is the hadron gas, in the dropping mass it is a medium undergoing chiral symmetry restoration and in the PHSD it is a pre-hadronized medium with massive quasi-particles. First the broadened mass theory will be presented, then the dropping mass mechanism and finally PHSD.
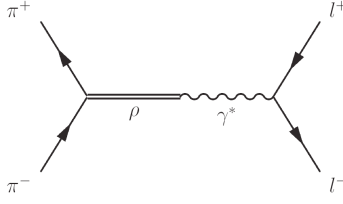
Figure 1.12: Diagram of pion annihilation forming an intermediate ρ meson. The ρ becomes a virtual photon and decays into an electron-positron pair. [20]

Broadened ρ masses

Medium broadened ρ mesons result from pion annihilation and other many-body interactions in the expanding hadronic fireball. A Feynman diagram for pion annihilation with the intermediate ρ meson is in Figure 1.12, the ρ becomes a virtual photon before decaying into dielectrons. The hadron gas phase exists for approximately 10 fm/c allowing for multiple generations of ρ mesons to be created, decay and regenerate throughout the phase's duration. When a ρ decays into dielectrons, the electrons pass through the hadronic gas with minimal interaction since the electron's mean free path is larger than the size of the fireball.

The broadened ρ contribution is calculated with an effective lagrangian and either the vector dominance model or a chiral reduction formulism. In the chiral reduction formulism, in medium electromagnetic correlators are constructed based on the vacuum correlators with QCD sum rules, nuclear photo-absorption and lattice QCD constraints. These correlators while not vector dominant maintain a ρ and a_1 dominance.

In the hadronic many-body approach the ρ meson propagator is defined as Equation 1.7,

$$D_\rho^{L,T}\left(q_0, q; \mu_B, T\right) = \frac{1}{M^2 - m_\rho^2 - \Sigma_{\rho\pi\pi} - \Sigma_{\rho M}^{L,T} - \Sigma_{\rho B}^{L,T}} \tag{1.7}$$

where m_ρ is the mass of the ρ, M is the dielectron pair mass, the L and T superscripts refer to the longitudinal and transverse modes and $\Sigma_{\rho i}$ are the in medium self-energies related to the various interactions, ie with the pionic cloud ($\pi\pi$), mesons (M) or baryons (B). In the vacuum, baryon and meson self energies are zero and $\Sigma_{\rho\pi\pi}^{L,T}$ provides the width of the pion resonance. In medium, $\Sigma_{\rho M}^{L,T}$ and $\Sigma_{\rho B}^{L,T}$ are non zero and $\Sigma_{\rho\pi\pi}^{L,T}$ includes additional contributions such as pion Bose enhancement.

In a heavy ion collision, the temperatures are high enough that the width as a result of this broadening grows to the size of the mass itself, a 'melted' resonance. The broadened ρ contribution is often considered with additional hard and thermal QCD processes. The hadron gas contributions must be folded into the full space time integrated spectrum so proper characterization of the temperature, lifetime and expansion rate of the hadronic

phase must be known. The broadened ρ has explained the excesses measured at CERES and NA60 and the enhancement at masses above 0.6 GeV/c^2 in the PHENIX minimum bias Au+Au spectrum. The PHENIX Au+Au excess at masses below 0.6 GeV/c^2 is not understood.

Brown-Rho scaling

In 1991 Gerry Brown and Mannque Rho predicted that the masses of the light vector mesons decrease as the temperature and/or density of the medium increases [46]. The masses drop proportionally as a result of the restoration of chiral symmetry according to Equation 1.8,

$$\frac{m_N^*}{m_N} \approx \frac{m_V^*}{m_V} \approx \frac{f_\pi^*}{f_\pi} \tag{1.8}$$

where the asterisks refers to a property in medium, m_N is the mass of the nucleon, m_V is the mass of the ρ or ω vector mesons and f_π is the pion decay constant, which is related the order of the chiral phase transition. This scaling relation is a obtained by starting with an effective chiral lagrangian in free space and maintaining the symmetries constraints of QCD as the scale changes to account for the hot/dense medium. An alternative derivation of the scaling property can be produced using hidden local symmetry theory with a vector manifestation [47]. Theories based on in medium QCD sum rules resulted in similar mass reductions in medium [48].

Brown-Rho scaling has been shown to be linked to effects in a variety of measurements including the anomalously long lifetime of C^{14} [49] and mass shifted omega mesons produced in the nucleus via photo-production [50]. In a heavy ion experiment, the scaling behavior manifests itself as a superposition of mass shifted ρ mesons each emitted at different temperatures as the medium cools. Initial calculations of Brown-Rho scaling successfully described the CERES data [51] [52]. But when ρ mesons produced by pion annihilation in the hadron gas stage are considered, Brown-Rho scaling was not needed to describe the NA60 data. More recent theories have questioned whether the dielectron channel is capable of providing a direct measure of Brown-Rho scaling in heavy ion collisions.

Parton hadron string dynamics

Parton hadron string dynamics (PHSD) is a parton transport model that describes the full evolution of the system including hard scattering, string formation, QGP formation, hadronization and interactions among hadrons. It takes an effective theory approach. Hadronic yields are calculated using a statistical hadronization model. Inelastic baryon-baryon and meson-baryon collisions are included. The pre-hadronized system is modeled on interacting massive quasi-particles with broad spectral functions and off-shell non-perturbative versions of pQCD processes such as:

- quark annihilation, $q\,\bar{q} \to l^+\,l^-$

- quark annihilation with gluon bremstralung, $q \, \bar{q} \to g \, l^+ \, l^-$
- gluon-Compton scattering, $q \, g \to q \, l^+ \, l^-$
- virtual gluon decay, $g^* \to q \, \bar{q} \, l^+ \, l^-$
- virtual quark decay, $q^* \to q \, g \, l^+ \, l^-$

Some of the Feynman diagrams for these interactions were presented earlier in Figure 1.1. One of the nice aspects of this model is that it considers not only a dropping mass scenario and a broadened mass scenario but also a scenario where the mass drops and broadens. It has successfully reproduced the low mass excess for both the CERES and NA60 data and describes the PHENIX excess above 0.6 GeV/c^2 but not the excess at lower masses. In the comparison to PHENIX data, the hadron decay channels are tuned to match the p+p spectrum and the hadronic contributions are extended to the Au+Au spectrum. [53] [1]

1.3.2 Dielectron continuum measurements

The DLS experiment at the Bevatron found an enhancement in the dilepton spectrum [54]. The dilepton excess called "the DLS puzzle" was later confirmed by the HADES experiment at the SIS at GSI [55]. Modified spectral shapes of light vector mesons were measured at lower energies using photo-production by the TAPS experiment at MAMI [50], although modifications were not seen in the CLAS experiment at Jefferson National Laboratory [56]. Recent high energy heavy ion dilepton continuum measurements, from the CERES and NA60 experiments at the SPS in CERN and the PHENIX and STAR experiments at RHIC are presented in more detail below.

CERES

The Cherenkov Ring Electron Spectrometer (CERES) experiment [57] [58] located at CERN used a fixed target bombarded with a beam from the SPS. Data was collected between 1992 and 2000. The dielectron continuum mass spectra is measured at midrapidity focusing on the low mass region in a variety of collision systems and energies.

Figure 1.13 displays two proton+nucleus collision systems, p+Be and p+Au at 450 AGeV, and two nucleus+nucleus collision systems, S+Au at 200 AGeV and Pb+Au at 158 AGeV. The spectra in both of the proton+nucleus systems are in good agreement with the hadronic cocktail of expected yields. The nucleus+nucleus spectra show excesses above the hadronic cocktail for masses above 0.2 GeV/c^2. In each case the excess is quantified in the mass region 0.2 to 1.5 GeV/c^2 with an enhancement factors, $F = \int spectrum / \int cocktail$; the factors are 5 ± 0.7 [stat] ± 2 [sys] in S+Au and 2.31 ± 0.19 [stat] ± 0.55 [sys] ± 0.69 [decays] in Pb+Au.

In Figure 1.13(b) the Pb+Au CERES data is compared to the unmodified cocktail (thin solid) and theoretical calculations assuming ρ production through pion annilhation where the ρ's mass distribution is unmodified, i.e. the vacuum spectral function (solid), modified with a reduced mass (dash-dot) or modified with a broadened mass (solid). The data are
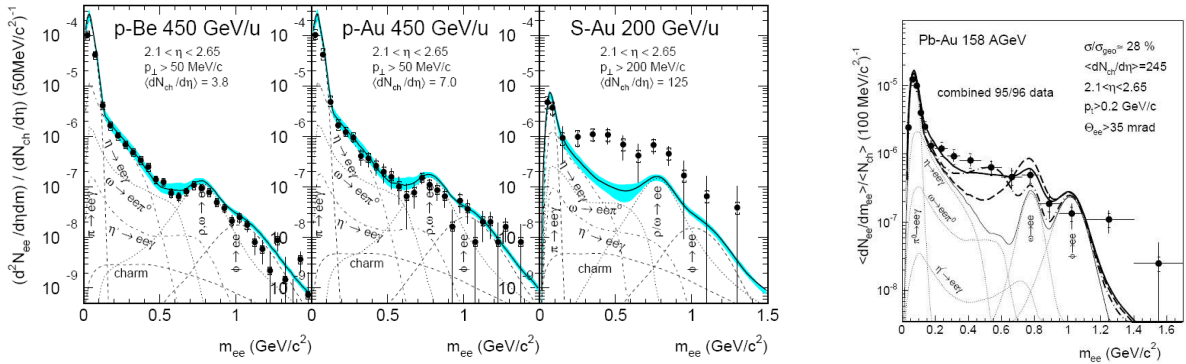
Figure 1.13: CERES dimuon spectra for p+Be and p+Au at 450 GeV/A, S+Au at 200 GeV/A, Pb+Au at 158 GeV/A. The Pb+Au spectrum is compared with the standard cocktail of hadronic sources (light solid line) and theoretical calculations including a vacuum ρ spectral function (dashed line), dropping ρ mass (dash-dot line) and a broadened ρ (solid). [59]

well described by both the dropping and broadened ρ. The vacuum ρ spectral function is not sufficient. PHSD calculations (not shown) also describe the data using both the broadened mass and the combined broadened and shifted mass curves [53]. It is apparent that ρ's are modified but the exact nature of the modification, either broadening and/or dropping mass, is unclear.

Further study of the excess in the Pb+Au 158 AGeV spectra provide insight into the ρ modification. It increases at a faster than linear rate with the charged particle density, consistent with production in two-body collision processes such as pion-pion annihilation. The mass spectra partitioned for pair transverse momenta above and below 0.5 GeV/c, show the enhancement is primarily at low p_T and a smaller enhancement exists for pairs with transverse momentum above 0.5 GeV/c. Each of the modification theories are able to reproduce the p_T behavior via different mechanisms [59]. At reduced beam energies of 40 AGeV, the Pb+Au dielectron spectrum has a larger excess than at 158 AGeV with an enhancement factor of 5.9 ± 1.5 [stat] ± 1.2 [sys] 1.8 [decays]. The system's total baryon density, the sum of the baryon and antibaryon number, is maximal at 40 AGeV. The increase in F suggests that total baryon density is a significant contributing factor. [60]

NA60/NA50

The NA60 experiment was also located at CERN. A beam from the SPS hit a fixed target upstream of the detector. NA60 was an upgrade of the NA50 experiment [61] with the addition of a silicon-vertex telescope [62]. The dimuon spectrum are measured in a variety of proton+nucleus and nucleus+nucleus collision systems. Dimuon pairs have the
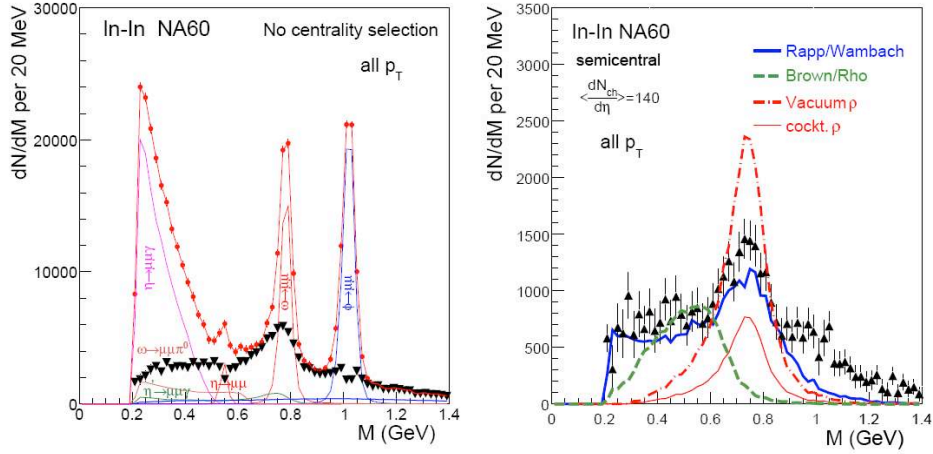
Figure 1.14: NA60 In+In 158 AGeV dielectron spectrum with (left) and without (right) the subtraction of the η, η', ω, and ϕ cocktail contributions. The remaining excess after the cocktail subtraction is compared to the unmodified vacuum ρ cocktail contribution and two theoretical contributions, the Brown-Rho dropping mass scenario and the broadened mass Rapp-Wambach theory. Both calculations were provided by Rapp. [63]

benefit of excluding the π dalitz source increasing the signal to background relative to a similar dielectron measurement. Relevant NA60 and NA50 results are briefly discussed.

NA50 p+nucleus collisions used Al, Cu, Ag and W targets. The resulting mass spectra are well described by hadronic, Drell Yan and correlated heavy quark contributions. NA50 nucleus+nucleus collisions of S+U at 200 AGeV and Pb+Pb at 158 AGeV found an excess at intermediate masses, inconsistent with Drell Yan [64]. The addition of the silicon-vertex telescope improved mass resolution and provided the ability to identify off-vertex decays from open charm at NA60. The 158 AGeV In+In measurement confirmed the NA50 intermediate mass excess and found that it was not due to off-vertex charm decays but thermal photons [65]. NA60's improved resolution and high statistics led to a very precisely measured spectrum. The ρ meson's spectral function was isolated by subtracting the cocktail components of the other hadronic signals and compared to both a dropping mass scenario (Brown-Rho) and a broadened mass shape (Rapp-Wambach). Figure 1.14 shows the spectrum with and without the cocktail subtraction and with the theoretical lines calculated by Rapp [63]. The broadened ρ line describes the data better than the dropping mass line particularly at masses above the ρ resonance. The PHSD lines broadened mass scenario (not shown) best describes the excess; the PHSD theoretical broadened ρ line is highly similar to the broadened curve calculated by Rapp seen in Figure 1.14 [53].
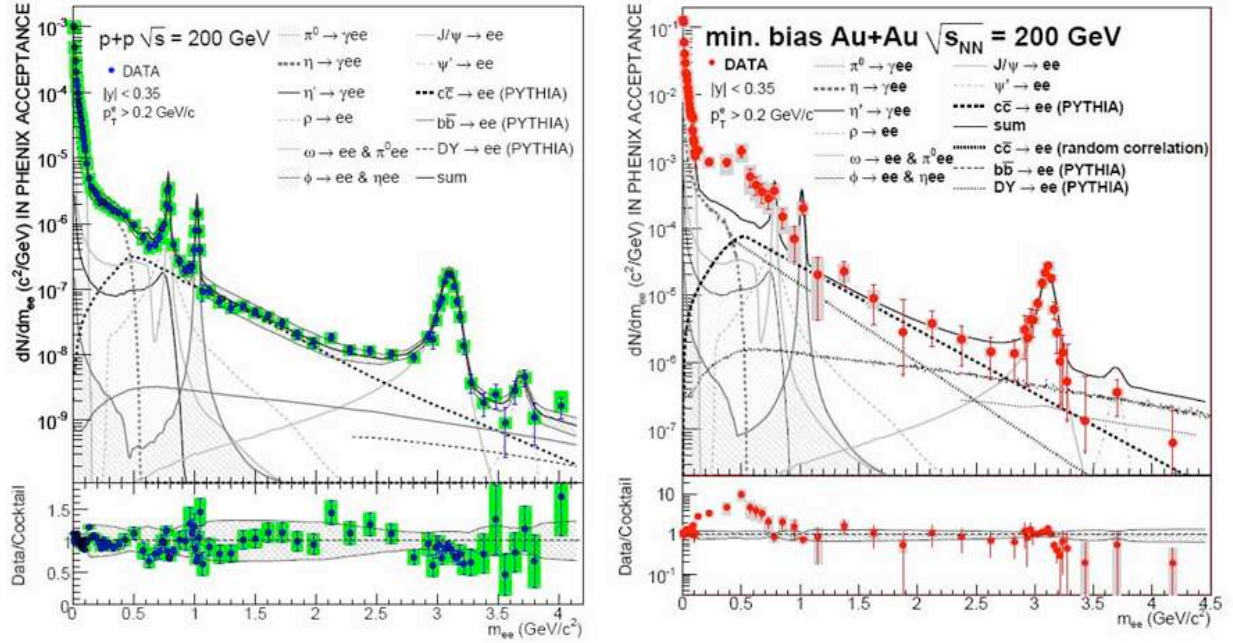
(a) p+p and Min. Bias Au+Au dielectron spectra
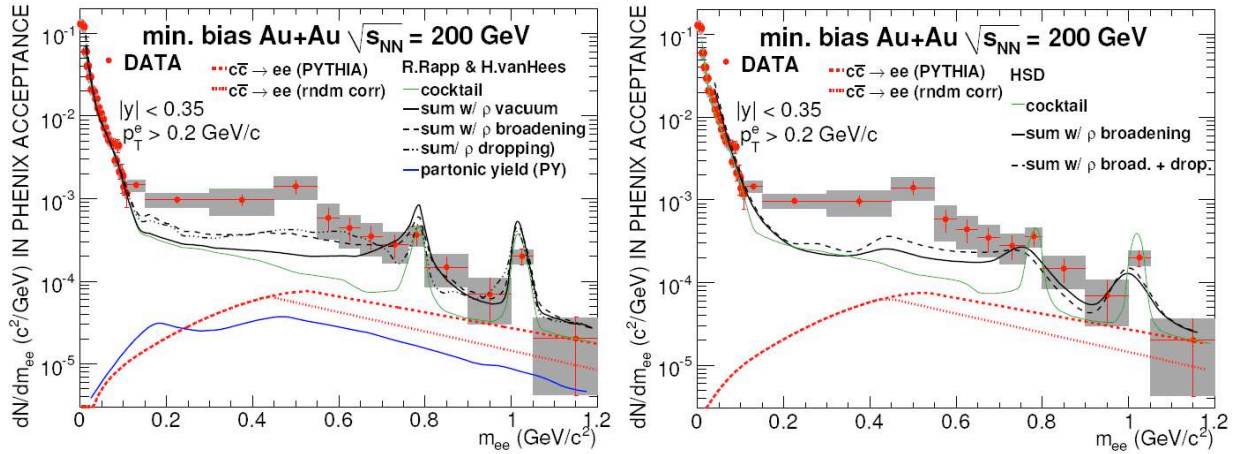
(b) Min. Bias Au+Au spectrum compared to theoretical curves

Figure 1.15: PHENIX dielectron spectra for p+p and Au+Au collisions at $\sqrt{s_{NN}} = 200$ GeV are shown on the upper plots. These spectra are restricted to pairs within the PHENIX acceptance. On the lower plots the low mass region of the minimum bias Au+Au data is compared with theoretical calculations by Rapp (left) and PHSD calculations by Cassing and Bratkovskaya (right). [40]

PHENIX

PHENIX first measured the dielectron continuum at midrapidities in the Au+Au system at $\sqrt{s_{NN}} = 200$ GeV using data taken in 2004 [40]. This $\sqrt{s_{NN}} = 200$ GeV p+p measurement soon followed using data from 2005 [66]. The p+p spectrum agrees well with cocktail of known hadronic sources. The Au+Au minimum bias measurement shows no excess in the intermediate mass region but the centrality dependent spectra are less clear in this region. The Au+Au minimum bias, 0-10% and 10-20% spectra shows a large excess at low masses. The low mass excess increases at a rate faster that N_{Part} with centrality. The excess yield is dominated by the low p_T contribution. At high p_T the excess is attributed to a virtual photon contribution; this seen in both the p+p and Au+Au spectra [42]. Theory comparisons to the minimum bias Au+Au low mass measurement are unable to describe the full extent of the excess, particularly at masses below 0.6 GeV/c^2 and p_T below 0.5 GeV/c. In Figure 1.15(b), curves from both PHSD [53] and broadened ρ [67] provide the best agreement [40]. Further theoretical work on the lowest mass and p_T component and the centrality dependence of the excess is necessary. [40]

STAR

(a) p+p

(b) Au+Au
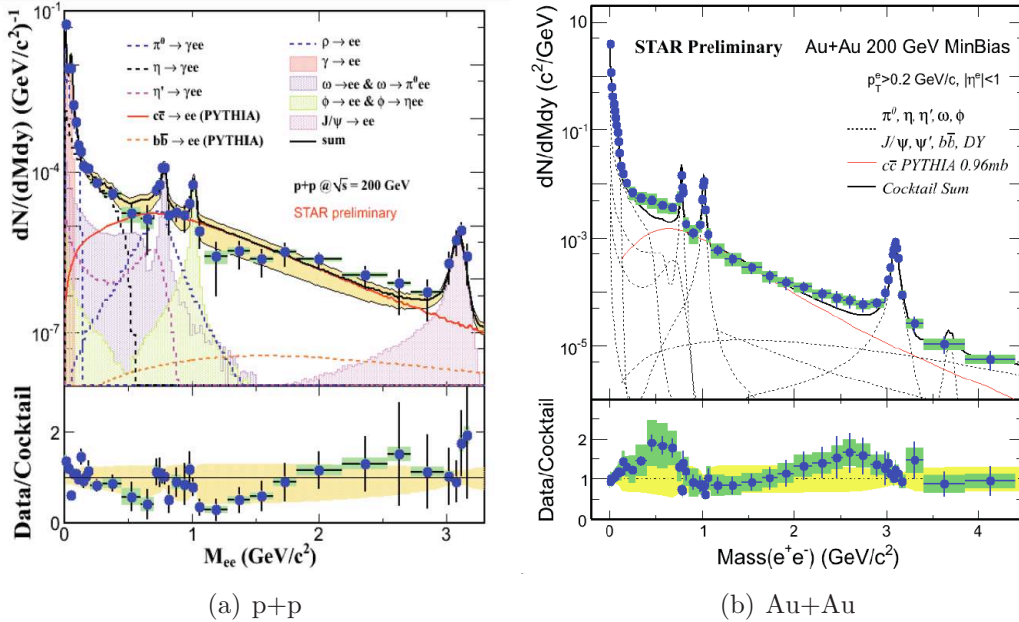
Figure 1.16: STAR dielectron spectra for $\sqrt{s_{NN}} = 200$ GeV p+p and minimum bias Au+Au. Both spectra are compared with the cocktail of known hadronic sources. The spectra are into the full 2π acceptance. [68]

In May 2011, STAR presented preliminary $\sqrt{s_{NN}} = 200$ GeV Au+Au and p+p dielectron spectra with data taken at RHIC. The Au+Au minimum bias and most central, 0-10%, spectra show excesses above the expected hadronic sources. Excess factors in the mass region 0.15 to 0.75 GeV/c^2 are $1.4 \pm 0.06 \pm 0.38$ and $1.54 \pm 0.09 \pm 0.45$ for the minimum bias and 0-10% spectra respectively. Because these spectra are so recent theoretical comparisons are not yet available. [68]

This is not the first time the STAR experiment has measured the ρ meson. In 2004, STAR published a ρ meson measurement in the pion channel, $\rho \to \pi\,\pi$, for $\sqrt{s_{NN}} = 200$ GeV p+p and peripheral (40% - 80%) Au+Au [69]. At low p_T, $p_T < 2$ GeV/c, the Au+Au ρ meson's mass peak shifts downward relative to the p+p peak position by approximately 0.3 GeV/c^2. A weaker mass shift of is seen in the high multiplicity p+p collisions suggesting a multiplicity dependance. These small mass shifts may be the result of Bose-Einstein correlations and rescattered pions from the $\pi\,\pi \to \rho \to \pi\,\pi$ interaction in medium. Theoretical study by the proponents of both the dropping and broadened ρ scenarios agree that the small decrease of the ρ mass in the pion channel is most likely the effect of dynamical interactions in the hadron gas phase [70] [71]. Since pions are measured in the final state they are influenced by the hadronic gas phase to a higher degree.

1.4 Purpose of thesis

The dielectron spectrum in Cu+Cu collisions provides increased accuracy to study the onset of the enhancement at low masses seen in PHENIX Au+Au measurements. Additionally the Cu+Cu system compared with the Au+Au could allow the separation of collision multiplicity and flow effects. This enhancement is due in part to modification of the ρ meson, with various theories for different types of modification. Additional sources of dielectron pairs stem from thermal and prompt photons from virtual photon emission from the fireball and hard $q\bar{q}$ annihilation processes. There is also a heavy quark contribution that may be modified by QGP energy loss such as the known suppression of high p_T non-photonic single electrons produced by open heavy meson semi-leptonic decays [39] and the known variation of opening angles between leptons from heavy quarks [44].

The dissertation is organized as follows. Chapter 2 describes the RHIC accelerator complex and the PHENIX experiment. Chapter 3 focuses on how detector hits are processed into tracks, the data quality and identification cuts are also discussed. Chapters 4 and 5 detail the various backgrounds occurring in the dielectron spectrum and how backgrounds are removed. Chapter 6 presents the efficiency corrections that repair the subtracted spectra adjusting for detector dead areas and poor detector response. Chapter 7 studies the systematic errors inherent in the analysis focusing particularly on the background subtraction and the efficiency correction. In Chapter 8, the hadronic cocktail of known sources is produced and compared to the Cu+Cu spectra. Chapter 9 relates the Cu+Cu results to previous dielectron measurements and theoretical calculations. Finally, the conclusions and some ideas

for future measurements are presented.

Chapter 2

Experimental Apparatus

2.1 Relativistic Heavy-Ion Collider

The Relativistic Heavy-Ion Collider (RHIC) is located at Brookhaven National Lab in Upton, NY. Heavy ions, or polarized protons, are accelerated to relativistic speeds using a series of accelerators. Figure 2.1 shows the location of each component of the accelerator complex. Particles start at the Tandem Van de Graaff accelerator (1), pass through to the Booster (3), enter the Alternating Gradient Synchrotron (5) and are injected into the RHIC ring (6). Once in the 2.4 mile RHIC ring, they are split into two counter circulating beams of particle bunches (each 25 cm long for Au+Au collisions) that orbit and cross at six interaction points [72]. Experiments detect the collision ejecta at the interaction points along the ring. Currently two experiments, STAR and PHENIX, take data at RHIC at the 6 o'clock and 8 o'clock positions respectively. In the past two additional experiments, PHOBOS and BRAHMS, also performed RHIC measurements.

2.2 PHENIX

The PHENIX detector measures photons, leptons, and hadrons, both the identified (i.e. π, K, p) and at high transverse momenta. This is done using a variety of subsystems. The subsystems are divided among the central arm detectors, muon detectors and global detectors. Figure 2.2 provides beam- and side- views of the detector; the central arm detectors are represented in the beam-view and the global and muon detectors are shown in the side-view. The interaction region is surrounded by the central magnet with an axial field parallel to the beam. The central arm detectors measure photons, electrons and hadrons and are located at mid-rapidity and have only partial azimuthal coverage. The muon arms detect muons using a pair of forward spectrometers and tracking detectors with full azimuthal coverage. The global detectors are located along the beamline and measure the interaction's start time, vertex and multiplicity. The global and central arm detectors are the primary detectors used
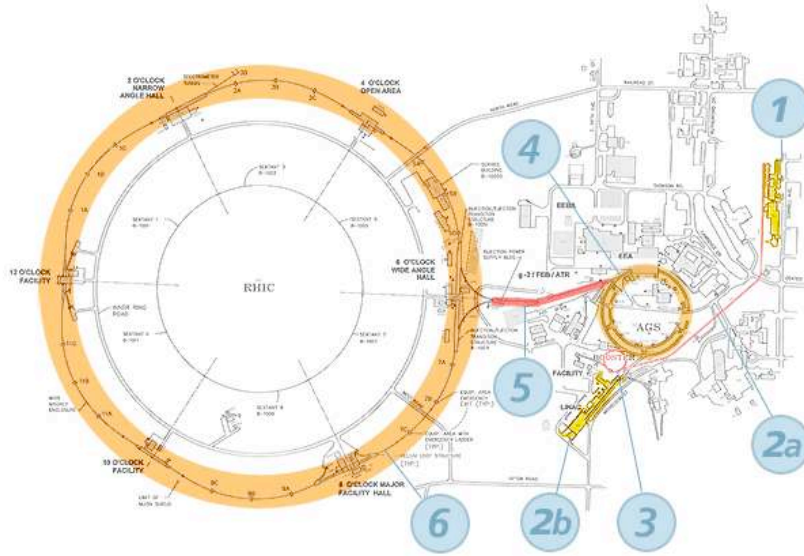
Figure 2.1: Diagram of the Relativistic Heavy-Ion Collider complex. Particles start at the Tandem Van de Graaff accelerator (1), pass through to the Booster (3), enter the Alternating Gradient Synchrotron (5) and are injected into the RHIC ring (6). [72]
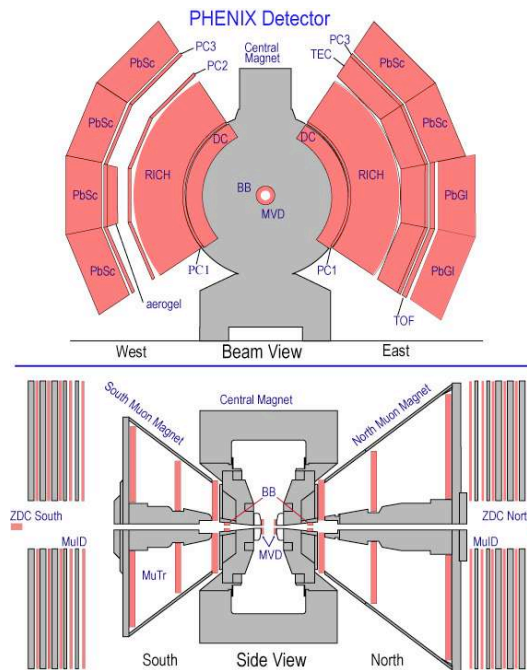
Figure 2.2: Beam- and side-views of the PHENIX detector in 2004 and 2005. [73]
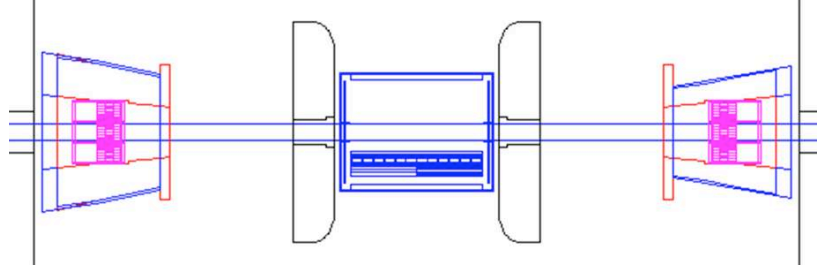
Figure 2.3: Schematic drawing of the beam-beam counter shown in magenta.

in this analysis and are presented in more detail below [74].

2.3 Global Detectors

The relevant global detectors for this analysis are the beam-beam counters (BB) and zero degree calorimeters (ZDC). Both of these detectors measure beam fragments to determine the event's start time, z-vertex and centrality. The detectors are located along the beamline, each with a module north and south of the interaction region. The BB is closer to the collision region while the ZDC is located past the muon arms as seen in the side-view of the detector in Figure 2.2.

2.3.1 Beam-beam Counter

The beam-beam counters (BB) are located around the beampipe outside of the poles of the central magnet 144 cm from the center of the interaction region. They consist of two counters, one north and one south of the collision point, each with full azimuthal coverage and a pseudo-rapidity range of $\pm|3.0 - 3.9|$. The counters have an outer diameter of 30 cm and an inner diameter of 10 cm with a 1 cm clearance between the detector and the beampipe. Each counter consists of an array of 64 Cerenkov counters with 3 cm quartz radiators and a photo-multiplier tube readout. Due to it's location near the beampipe and central magnet the detector functions within in a high radiation environment. It is used in heavy ion and p+p collisions and is responsive in both high and low multiplicity environments.

The BB measure the timing and energy deposition of forward charged particles. It determines the collision time and position along the beam axis and produces a trigger on minimum bias events. The collision time is obtained by measuring the arrival time of prompt charged particles. It provides a start time for the hadron identification in the Time-Of-Flight detector; the resulting start time resolution of 96 ps, which allows us to separate pions and kaons up to a momentum of 2.4 GeV/c. The beam axis or z-vertex position is determined by comparing the average hit times of particles in the north and south counters. A z-vertex
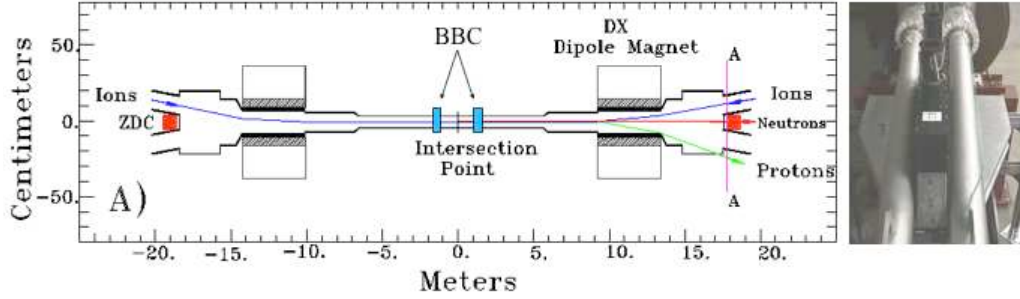
Figure 2.4: Zero degree calorimeter.

position of less than 30 cm and multiple hits on both sides of the BB are required for an event to be classified as minimum bias. The collision centrality is determined using the BB multiplicity measurement. Centrality is classified into percentage centrality classes with $0 - 10\%$ being the most central portion and $60 - 94\%$ being the most peripheral portion. In Cu+Cu measurements only the BB measurements are used; Au+Au collisions have used the BB in conjunction with the ZDC to determine centrality. [75]

2.3.2   Zero Degree Calorimeters

The zero degree calorimeters (ZDC) measure neutrons in 4 mrad cones around the beampipe, 18 m north and south of the collision point beyond the muon arms. They are 10 cm wide and 13.6 cm high hadronic calorimeters with 5 mm tungsten alloy absorber plates. While the hadronic showers are not fully contained, the energy resolution at 100 GeV is between 19% and 17.6% depending on whether three or four modules are used. The single neutron energy resolution is 25%.

The measured neutrons come from beam fragments and evaporative emission from the colliding nuclei. Charged particles are deflected by the nearby magnets as shown in Figure 2.4. As in the BB case, a ZDC coincidence in the north and south is used for minimum bias selection. In the event that the BB is unable to reconstruct the z-vertex, the timing difference between the north and south ZDC modules can also be used to determine the z-vertex position; this was not necessary in the Cu+Cu measurements. The total neutral energy measured by the ZDC allows us to monitor the luminosity and determine event multiplicities. [76] [77]

2.4   Central Arm Detectors

The two central arms of PHENIX are located at mid rapidity, $|\eta| < 0.35$, on the east and west sides of the interaction region beyond the range of the magnetic field. They are
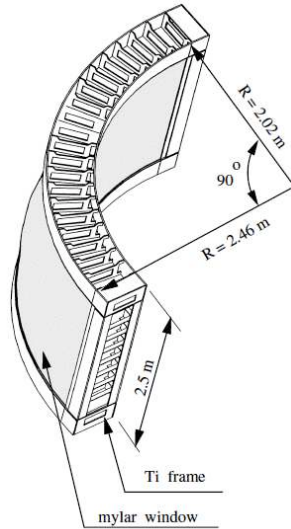
Figure 2.5: The drift chamber frame. [79]

cylindrical arcs around the beam axis with a partial azimuthal coverage of about 90° for each arm.

The detectors in the central arms are layered as shown in the beam-view of Figure 2.2. The drift chamber (DC) is the inner most layer, followed by the first pad chamber (PC1), the ring imaging cherenkov detector (RICH), the second pad chamber (in the west arm only), the time expansion chamber (in the east arm only), a third pad chamber and the electro-magnetic calorimeter (EMC). Aerogel and time-of-flight detectors, which are useful for particle identification [78], are located between the second and third pad chambers in the west arm and between the third pad chamber and the electro-magnetic calorimeter in the east arm respectively. This analysis uses the DC and PC1 for tracking and momentum determination and the RICH and EMC for electron identification; these detectors will be discussed in further detail below.

2.4.1 Drift Chambers

The drift chambers are located 2 m along the beam axis with inner and outer radii from the beam axis of 2.02 and 2.46 m respectively. Titanium frames with mylar windows at the front and back enclose the chamber volume, Figure 2.5. The volume is filled with approximately 3200 anode wires stretched, primarily in the z direction, across the interior and a gas mixture of 50% argon, 50% ethane and < 1% ethanol. Charged particles pass through the detector ionizing the gas. The free electrons drift onto the anode wires and register as detector hits. To ensure hit recognition at high multiplicities (up to 500 tracks in

4.5 degr.

V2 − planes

U2 − planes

X2 − planes

Termination wires

Back wire

V1 − planes

Gate wires

U1 − planes

Potential wire

sense (anode) wire

X1 − planes

anode plane

cathode plane

Sector, side view

Wire orientations, top view

~ 1800 mm

U   X   V
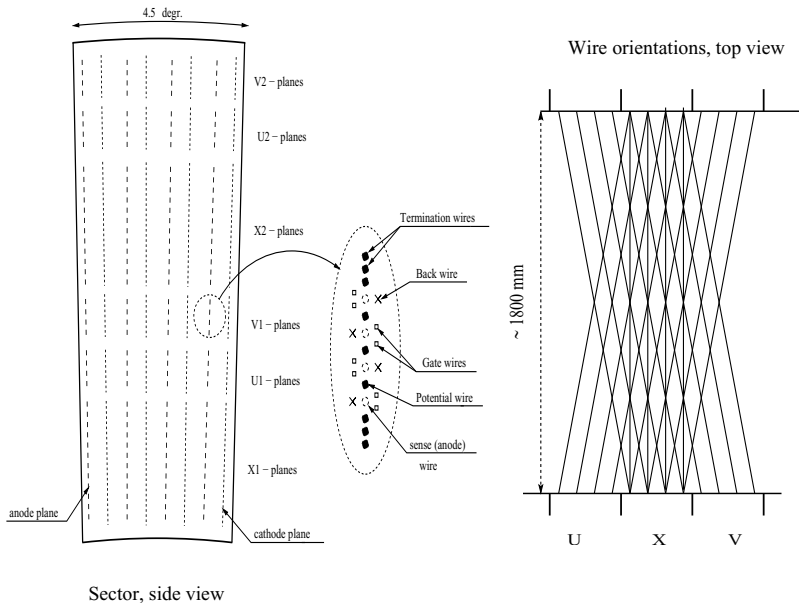
Figure 2.6: A drift chamber keystone with X, U, and V wires modules. The wire orientation and location in a drift chamber sector are shown. The wire configuration that makes up a cell is also presented including the anode wire, two gate wires, a back wire and the potential wires. [79]

a $\sqrt{s_{NN}} = 200$ GeV Au+Au event), the wires are divided within each arm into north and south regions using a non-conductive kapton separator. This segmentation also allows for a 100 μm carbon fiber support beam that lightens the wire tension load on the titanium frame to 4.5 tons and introduces only a small amount of additional material into each chamber.

The two DC arms consist of twenty keystones each with an angular bite of 4.5^o in ϕ. Figure 2.6 presents top- and side-views of a DC keystone. A keystone has two layers of wire modules (X1 and X2) that follow the beam axis and four layers of stereo wire modules (U1, V1, U2 and V2). Stereo wires are tilted azimuthally at angles of 6° relative to the X wire modules. Stereo wires beginning in one keystone end in the neighboring keystone. The top-view diagram in Figure 2.6 shows this. The X modules allow for track measurements in the r-ϕ plane. Stereo modules allow for additional pattern recognition and z position determination, ideally to match the position measurement in the PC1. The modules are stacked radially. The inner wire module layer is an X module (X1), followed by two stereo wire modules (U1, V1) which are tilted in opposite directions in ϕ; this is then repeated in the same order for a second layer of each module type (X2, U2, V2). The positions and relative geometry of pieces within the DC are calibrated at the beginning of the yearly data taking using zero-field data. For the 2005 data set I performed this calibration.
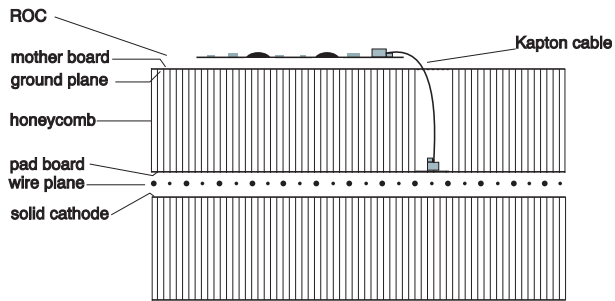
Figure 2.7: Diagram of a pad chamber board. [79]

The wire modules contain eight alternating anode and cathode wire planes in the r-z plane and each located at different ϕ positions. Each plane consists of twelve wires in an X module and 4 wires in a U or V module. Between the anode and cathode there is a 2 to 2.5 cm drift distance in the ϕ direction. The cathode wires produce a constant electric field causing the ionized electrons to drift with a constant velocity toward the anode wires. Anode wires are surrounded by additional wires that facilitate the drift measurement, Figure ??. These wires are potential wires, gate wires and back wires.

Potential wires are located above and below each anode wire; they produce a strong electric field and define active regions for each wire. Two gate wires are located to one side in front of the anode wire. They focus the drifting electrons toward the anode wire and separate the regimes of neighboring anode wires; as a result a single wire samples only 3 mm of the ionization trail. Back wires are held at a low potential and block the flow of electrons from the non-gate wire side reducing the signal rate by a factor of two. There remains a 2 mm left-right ambiguity between the back wire and the anode wire. The probability of the anode registering a hit from the back wire side is less than 5%. The gate and back wire configuration alternates for neighboring anode wires. A cell consists of a collection of one anode wire, two gate wires, a back wire and the potential wires.

The DC measurement is a series of timing pulses at each cell; the mean timing pulse width is approximately 35 ns. The time difference between the DC measurement and the event start time from the BB is used to calculate the hit position using the drift velocity. The drift velocities are determined using drift chamber online calibrations, a system which I maintained and oversaw for Run 5. Typical drift velocity values are 5 cm/μs. The resulting single wire efficiency is $95 - 96\%$ and the single wire resolution is 165 μm. [79]

2.4.2   Pad Chambers

The pad chambers provide three dimensional spatial point measurements using a multi-wire proportional chamber. They are the only non-projective detectors in the central arms. There are three pad chambers in PHENIX. The first pad chamber (PC1) is located in both
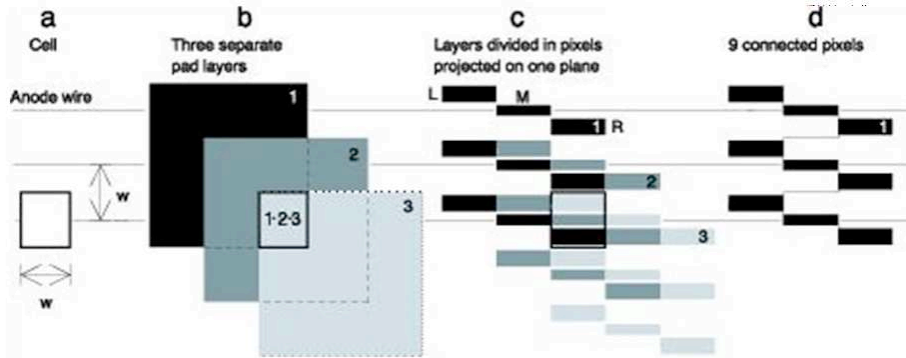
Figure 2.8: A pad chamber pad configuration with nine pixel cells.

arms between the DC and the RICH. The second pad chamber (PC2) is in the west arm behind the RICH. The third pad chamber (PC3) is in front of the EMC in both arms. PC1 provides the z position confirmation in the tracking algorithm. It contributes to the momentum measurement via the p_Z component and the track vector direction. PC2 and PC3 provide hadron rejection in the EMC allowing us to remove secondary particles from decays after or outside the aperture of the DC and PC1. While important, hadron rejection and secondary interactions are not issues in this analysis and the dead areas in these detectors would further complicate our understanding of the detector's aperture. The remainder of this section focuses on PC1.

PC1 consists of anode wires inside a gas volume bounded by cathode planes. This sounds similar to the DC but it is quite different. Instead of many planes of anode wires strung through a large volume, there is only one plane of anode wires within each detector and the cathode planes are panels that define the gas volume. A charged particle travels through the gas volume creating an avalanche on the anode wire. As a result of the avalanche, image charges are formed on a segmented pixel array on the top cathode; the effected pixel locations provide the position measurement and pattern recognition. The detector's position resolution is determined by the pixel size.

PC1 has eight independent 0.5 m^2 volumes in each arm located at eight ϕ positions. Each volume is made up of two cathode panels stacked on top of each other with anode wires strung in the layer between the panels and oriented in the z direction, as seen in Figure 2.7. The anode wires are separated by 8 mm to achieve a position resolution of $\pm$ 4 mm. The cathode panels are placed on FR4-honeycomb-FR4 sandwich boards. The top cathode is segmented into a pixel array while the lower cathode is solid copper. Readout electronics lie on top of the sandwich board and are connected to the pixel (or pad) board via a microconnector and kapton cable. The resulting detector is very light with little material inside the fiducial volume and a radiation thickness of 1.2% including the electronics.
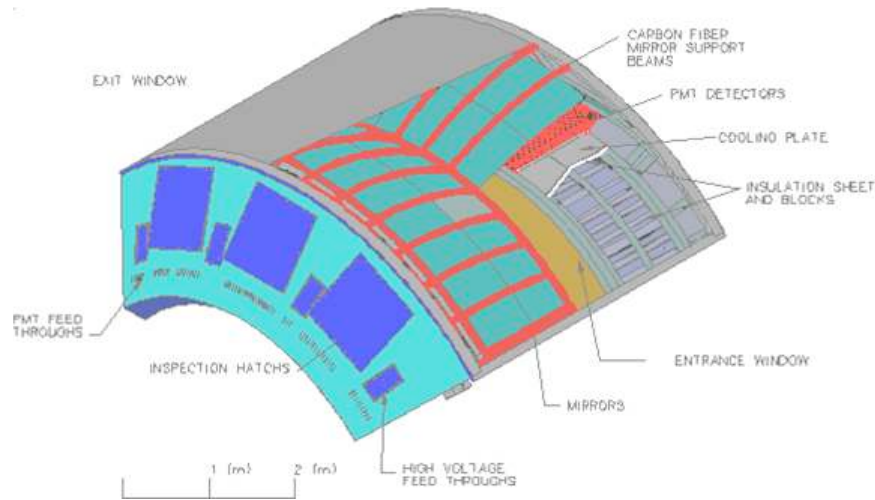
Figure 2.9: Diagram of the ring imaging Cherenkov detector. [80]

The PC1's position resolution are determined by the pixel size. A response area of 8.4 x 8.4 mm^2 is desired. Reading out such a large number of individual pixels is not possible due to the required readout channel cost and the likelihood of false hits using the discriminator readout method. A novel pad design was created to deal with these issues, Figure 2.8. A pad consists of nine pixels, three parallel sets of three diagonal cells each, Image d in Figure 2.8. Cells within a pad are read out together. A hit requires three distinct but interwoven pad responses, which reduces electronic noise and the likelihood of a false hit. The triple hit requirement reduces the number of channels read out by a factor of three. It also provides enough information to identify the individual neighboring pixels within the three pads that are the hit source, Image c in Figure 2.8. This is possible because with our interleaved pixel geometry and pad definitions three nearby pads only have one set of neighboring cells. The desired response area of 8.4×8.4 mm^2 is divided between the three pixels, defining two side pixels of 2.7×8.2 mm^2 and one center pixel of 1.5×8.2 mm^2. The resulting pad geometry has a z direction resolution of ± 1.7 mm. [79]

2.4.3 Ring Imaging Cherenkov Detector

The ring imaging Cherenkov detector (RICH) is a threshold gas Cherenkov detector. Electrons pass through the gas emitting a cone of Cherenkov photons. The photons are focused into a ring by spherical mirrors and reflected onto a photo-multiplier tube (PMT) array. The ring position characterizes the direction of the electron track; parallel tracks that fire the RICH illuminate the same ring. An average of twelve photons per ring are created for $\beta = 1$ particle with a path-length of 1.2 m. The projected cherenkov rings form ellipses with typical diameters of 8 cm or 11.8 cm on the PMT array.
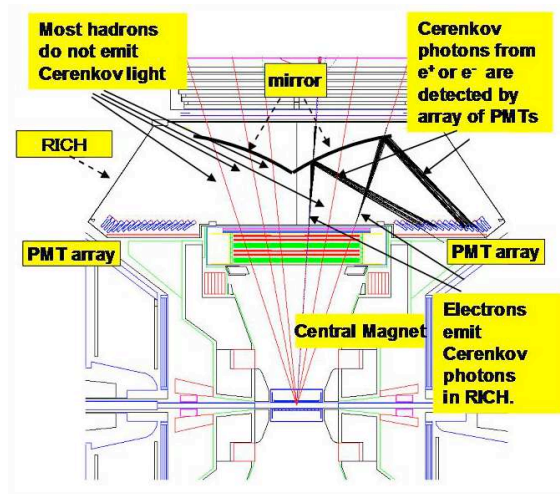
Figure 2.10: Internal view of the ring imaging Cherenkov detector showing the spherical mirrors nd focal plane. [81]

The RICH is located at radii between 2.575 and 4.1 m from the beamline and have a θ angular bite ranging from 70° to 110°. There is one 40 m^3 aluminum walled gas volume in each arm with available radiation lengths varying from 87 to 150 cm depending on incident angle. Material within the detector volume is minimized to prevent photon conversions and multiple scattering. The radiator length from the entrance window to the mirror surface ranges from 0.9 to 1.5 at 90° and deviations of 20° from normal. The vessel is filled with CO_2 radiating gas at a pressure of 0.5 inches of water above the ambient pressure. CO_2 gas optimizes the electron pion discrimination by reducing background rates, has a high pion threshold, and provides stability in the number of photoelectrons generated from one electron. It has an electron threshold of 18 MeV/c with a much higher pion threshold of 4.65 GeV/c.

Each RICH vessel contains two PMT arrays and two mirror arrays. The PMT arrays are placed outside of the gas volume near the mirror's focal plane. They are tucked behind the central magnet protecting them from particles produced by the collision, and encased in ferroperm shielding to block stray magnetic fields up to 100 G. A PMT array consists of 16×80 tubes divided into modules of 32 tubes each. There are 5120 PMTs total.

Each PMT has a UV transparent glass window, a 25 m diameter bi-alkaline photocathode and a 50.8 mm diameter Winston cone that serves as a light collector. They have gains greater than 10^7 and a quantum efficiency of 20% at 300 nm. The mirror arrays consist of 48 carbon fiber epoxy mirror panels in two 2 x 12 groupings that form intersecting spherical surfaces with a total reflecting area of 20 m^2. [80] [81]
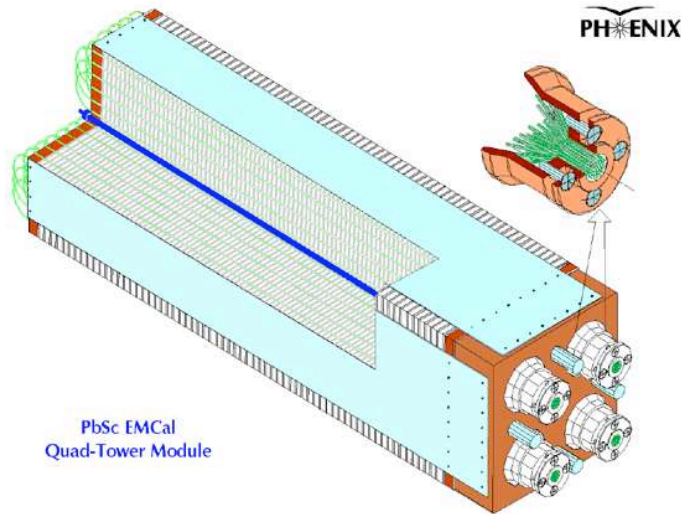
Figure 2.11: A PbSc EMC calorimeter tower module. [82]

2.4.4 Electro-magnetic Calorimeter

The electro-magnetic calorimeter (EMC) measures the energies and spatial positions of photons and electrons. The calorimeter consists of six lead scintillator (PbSc) sampling calorimeters and two lead glass cherenkov detectors (PbGl). Four of the PbSc sectors are located in the west arm and the other two are in the top two sectors of the east arm. The PbGl sectors are located at the two lower sectors of the east arm behind the Time-of-Flight detector. The PbSc sectors provide a better linearity, timing and hadronic response. The PbGl sectors have better granularity and energy resolution. [82]

PbSc

The PbSc is a shashlik-type sampling calorimeter meaning that the intensity of the measured shower light corresponds to the deposited energy. Photons and electrons enter the calorimeter and hit the lead absorber layer creating a shower at the front of the towers; typical showers have a radiation length of 18 χ_o. Hadrons may also shower in the calorimeter but they will travel farther down the tower before radiating and may punch through the back of the tower without depositing all of their energy. A separate re-calibration is required to identify the hadrons in the calorimeter using the time of flight response. I performed the hadronic time of flight re-calibration for the PbSc in the 2004 Au+Au data set.

A single tower in the PbSc consists of sixty six alternating cells of lead and plastic scintillator edge plated with aluminum. Wavelength shifting fibers are threaded through the layers and connect to a 30 mm photomultiplier tube at the back of the tower. Four towers are grouped into a module, optically isolated and read out together, Figure 2.11. Thirty six
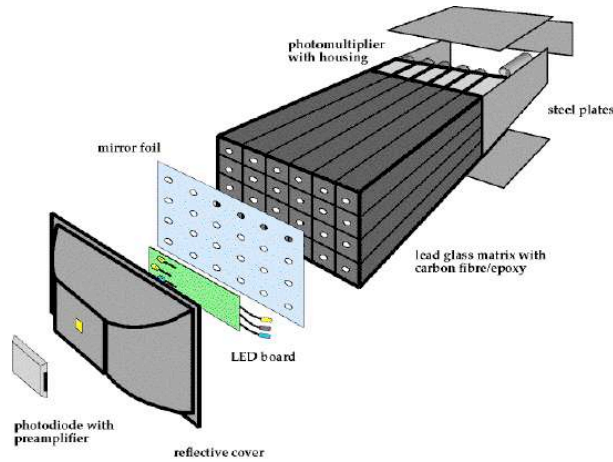
Figure 2.12: PbGl electro-magnetic supermodule. [82]

modules are grouped together in a steel frame to form supermodules; Eighteen supermodules make up a sector.

The PbSc tower gains are calibrated using a pulsed ultra-violet YAG laser distributed across different modules using optical splitters and fibers grated to simulate a 1GeV shower across each module. The final energy resolution for photons and electrons after noise corrections of the PbSc detector is $8.1\%\sqrt{E\left(GeV\right)}\oplus2.1\%$ with the 8.1% stochastic error from the sampling and the 2.1% intrinsic error due to non-uniformities in the detector such as boundary effects, tower hot spots, variations in shower depth and attenuation angle.

PbGl

The PbGl is a Cherenkov calorimeter. Cherenkov radiation is emitted as photons and electrons pass through the leaded glass. Hadrons with momenta above their respective Cherenkov thresholds (pions $\approx$ 106 MeV/c, protons $\approx$ 715 MeV/c) may generate light in the PbGl. But typically, hadron measurements in these sectors rely on the high-precision TOF detector located directly in front of the PbGl.

The PbGl has 9216 towers. Towers are 40 mm x 40 mm x 400 mm in volumes of leaded glass. They are wrapped in aluminized mylar and read out with photomultiplier tubes. Each sector has 192 supermodules laid out 16×12. Supermodules consist of twenty four towers, glued together in a self-supporting array of six towers by four towers. Six supermodules, in a two by three array, share a readout motherboard for data acquisition.

Chapter 3

From hits to electron tracks

The detector hits detailed in the previous chapter are decoded into particle track information and individual electron tracks are identified for the analysis. This is done in a process called production. The produced data is recalibrated, correcting any minor initial calibration errors. The data must then pass a series of cuts designed to maintain data quality at the run level, the event level and the track level. The surviving good tracks pass a series of electron identification cuts. This chapter details production, recalibration, quality requirements and electron identification.

3.1 Production

Production is the computational process by which particle tracks are formed out of the individual hits in each detector. The raw data files with the hit information are processed by computer codes into data files that contain event and track information. Year to year the production code changes with the introduction of new detectors and methods of calibration. The pro.73 production library is used in this analysis. The production of the 2005 Cu+Cu 200 GeV data set was lead by Carla Vale at Brookhaven National Laboratory and took six to seven months; this includes the additional time used to aggregate the file segments into larger run based file outputs.

The production algorithm works in high multiplicity environments such as central Au+Au collisions and has a low rate of producing false or "ghost" tracks. All tracks start at the primary vertex and are mapped in the r-ϕ direction displayed in Figure 3.1. Individual tracks are assumed to follow a straight trajectory once they reach the central arm detectors since they are outside of the range of the central magnet's field.

A Hough transform algorithm is used to discern between potential track trajectories. This consists of making all possible tracks using the hits in the X1 and X2 layers of the DC within a reasonable region. Each potential track is characterized by two orthogonal parameters, the azimuthal angle of the track at the DC, ϕ_{DC}, and the angular deviation of
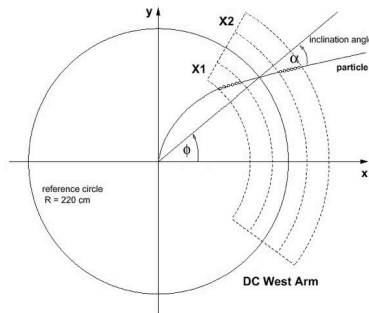
Figure 3.1: Diagram of the α and ϕ_{DC} tracking variables.

the track slope from ϕ_{DC}, α; shown in Figure 3.1. These parameters are used, as opposed to the standard y=mx+b formalization, because they are bounded by 2π. A two-dimensional Hough array stores these parameters for all possible tracks. Local density maxima, determined by a minimum threshold requirement, in the Hough array space provide most-likely track candidates. Later steps improve the characterization of the tracks and perform background track removal. The track finding efficiency is better than 99%. The double track resolution is better than 2 mm, this is due to the 35ns mean timing pulse width in the DC [83].

Additional association between the tracks and other detectors reduces background and ghost tracks. In most cases this is done at the analysis stage by cutting on the separation between the track projection and the hit location in the respective detector. The RICH is an exception to this method. The pattern recognition for the Cherenkov rings in the RICH uses the track candidate as a seed in the search to find Cherenkov rings.

3.2   The EWG data set

Production output consist of various root files for the different data sets. The root files contain data nodes in ROOT's TTree format. This analysis uses the EWG Minimum Bias data set which consists of electron candidate tracks that satisfy the minimum bias trigger. EWG files contain a central arm node, a global node, the sync object and various additional nodes. The central arm node consists of the central arm track information the production of which we have discussed above. The global node contains event specific information such as the event centrality and z-vertex position. The sync object ensures that when multiple files are opened in the PHENIX input-output framework that they will access the same events at the same time. The global node and central arm node are the data nodes primarily used in this analysis.

The EWG data set is a subset of the CNT data set, charged particle tracks in the central

40

Table 3.1: EWG data set cuts

EWG Cut
n0 > 1 ‖ sn0 > 1
$0.3 < ecore/\text{p} < 2$ c
$0.15 < p_T < 25$ GeV/c
$emcsdphi\_e < 4$ && $emcsdz\_e < 4$
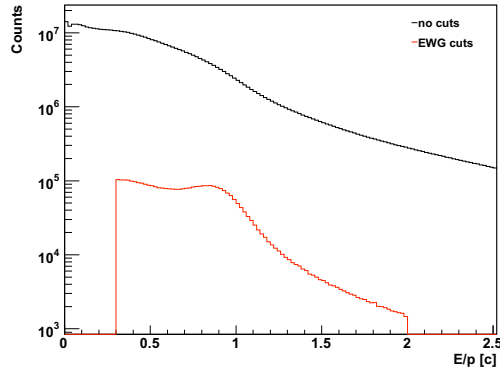
Figure 3.2: The Energy over momentum, E/p, using a subset of the CNT dataset with the EWG cuts detailed in Table 3.1 applied.

arms. EWG files have a reduced content in the central arm node. They only contain events where the vertex is within ±50 cm of the detector's center. The number of tracks are also reduced by requiring rudimentary electron identification cuts listed in Table 3.1; the track variables mentioned here are described in detail in the next section. Figure 3.2 shows the reduction in tracks due to these cuts. This means the EWG file set has a much smaller foot print in the PHENIX computing universe than the CNT file set. As a result Run 5 EWG files are all available on disk for any user to access at any time. In contrast only a portion of the Run 5 CNT data set is available on disk; the full Run 5 CNT data set is in dCache and accessible via the AnalysisTrain. The AnalysisTrain is a code submission architecture that aims to efficiently access the files in dCache in an organized fashion for multiple analyses. The AnalysisTrain was created by Thomas Hemmick, Nate Emerson, Wolf Holzmann and I and is currently maintained and run by Chris Pinkenburg and Nathan Grau.

Table 3.2: Quality values with the bit patterns and their meanings

Quality	Bit pattern	Meaning according to the bit pattern
61, 62, or 63	1 1 1 1 x x	(X1, X2, or X1 & X2) unique PC1 and UV hits
49, 50, or 51	1 1 0 0 x x	(X1, X2, or X1 & X2) unique PC1, no UV hits
29, 30, or 31	0 1 1 1 x x	(X1, X2, or X1 & X2) unique UV hit, a PC1 hit
21, 22, or 23	0 1 0 1 x x	(X1, X2, or X1 & X2) UV and PC1 hits
17, 18, or 19	0 1 0 0 x x	(X1, X2, or X1 & X2) PC1 hit, no UV hits

3.3   Central track variables

As mentioned in the earlier section production results in file outputs containing the event and track information. Only the relevant variables for this analysis are discussed. For clarity, we've separated these variables into two groups: tracking variables and electron variables. Tracking variables are based on primarily DC and PC1 information and detail the track geometry, momentum and matching between DC and PC1. The electron variables provide electron identification using information from the RICH and EMC. Hit quality (ring or shower characteristics), hit geometry and matching of detector hit to track are the relevant fields.

3.3.1   Tracking variables

The tracking variables consist of quality, the momentum, p, and geometric values. The geometric variables are the polar angle, θ, the azimuthal angle at the DC, ϕ_{DC}, the azimuthal angle at the vertex, ϕ_0, and angular deviation of the track slope from ϕ_{DC}, α. Figure 3.1 displays the relationship between ϕ_{DC} and α. The PC1 z-coordinate, *zed*, the East/West location of the track, *arm*, and the north/south half of the hit in the drift chamber, *dcside*, are additional geometric variables. The *nx1hit* and *nx2hit* variables are the number of hits in the X1 and X2 sections of the DC respectively.

The *quality* variable, refers to the track quality or matching between the PC1 and DC in the tracking algorithm. PC1 matching is important because while the U and V layers of the DC provide some z-position information, the z-position is primarily determined by a PC1 hit. The *quality* variable allows the analyzer to differentiate between tracks with different levels of coincidence and uniqueness in the PC1, U/V and X layers of the DC. The *quality* values are determined by a bit pattern; the values, bit pattern and meanings are detailed in Table 3.2.

3.3.2 Electron variables

Electron variables using the RICH detector are *center_z*, *center_phi*, *npe0*, *n0*, *chi2*, *disp*, and *sn0*. The *center_z* and *center_phi* variables are the ring's z and ϕ coordinates. The *npe0* and *n0* variables are the number of photoelectrons and number of fired phototubes within an annulus with an inner radius 3.8 cm and outer radius 8.4 cm. The *chi2* variable is a χ^2-like value with units of cm^2 that characterizes the ring shape; a cut on *chi2/npe0* mimics a reduced χ^2. The *disp* variable characterizes the displacement between the track projection in the RICH and the ring center. The *sn0* variable takes into account the probability of a random association between a track and a Cherenkov ring. It is a "swapped" variable meaning that the *n0* is calculated in the same way as described earlier but with false correlations. False correlations are constructed by keeping the tracks in the same location but flipping the RICH geometry across the North/South line. The *sn0* is looking for the number of phototubes fired in a ring on the track's mirrored side of the RICH.

Electron variables using the EMC are the core shower energy, *ecore*, the probability that the shower was electro-magnetic, *prob*, and track separation variables for electrons, *emcsdphi_e* and *emcsdz_e*. The track separation variables are sigmalized, meaning that they are not distances or angular differences but are the sigma away from zero assuming a gaussian spread.

3.4 Recalibration

After data production, some variables have sub-optimal distributions. Additional calibrations are calculated based on this output. Ideally the production code would be corrected and the data would be re-produced with the new calibrations in effect. However, it is not cost effective or timely to rerun the production to implement these calibrations when they can be corrected using the existing information in the output. A MasterRecalibrator framework was created to apply calibrations to the data nodes at run time. Different calibrations are registered to the MasterRecalibrator and then they are available to all users. This was managed by Anne Sickles and created with the help of Chris Pinkenburg.

Two relevant recalibrations were applied in this analysis, one for the electron track separation variables in the EMC and a second for the beam shift calibration. The electron track separation variables in the EMC, *emcsdphi_e* and *emcsdz_e*, are calibrated to provide the correct sigma variation as opposed to the distance or angular separations. This was done using gaussian fits of the distributions by Susumu Oda. The beam shift calibration compensates for variations in the vertex position by shifting the location of the detectors in the tracking space such that the distance between the vertex and the detector position is correct. I calculated and implemented the beam shift calibration for the 2005 dataset.
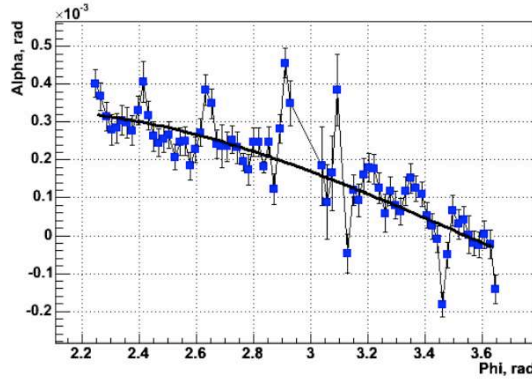
Figure 3.3: The α versus ϕ_{DC} distributions for the east arm of the DC for the zero field run 152825. The blue points are the data and the black line represents the fit using Equation 3.1.

3.4.1 Beam shift calibration

The beam shift calibration is done using zero field runs taken in 2005. This is a secondary alignment calibration adjusting for changes in location of the detectors due to moving the arms during the access or shifts in the beam location. These secondary shifts are typically at or below a millimeter. A full DC alignment was performed at the beginning of the 2005 run by myself and my advisor, Thomas Hemmick. The full alignment consists of determining the tilts of individual wire boards and the locations of the X1 and X2 layers within the DC as well as the location of the whole DC. This is a more involved process but it is similar to the beam shift calibration described below.

Zero field runs allow us to determine the vertex position. All tracks are straight and their α values should be zero. Plotting α versus ϕ_{DC} shows any deviation. Deviations follow the functional form

$$\alpha = \frac{dx}{R} * sin\phi_{DC} + \frac{dy}{R} * cos\phi_{DC} \qquad (3.1)$$

where R is 220 cm. The vertex offsets, dx and dy, are found by fitting the α versus ϕ_{DC} curves with Equation 3.1 as seen in Figure 3.3. This is done separately for each arm; in 2005 the two arms gave consistent offsets.

The vertex offsets are applied in the recalibrator adjusting the α value by Equation 3.1. The transverse momentum, p_T, is then scaled by the absolute value of the ratio of the old α over the new α; the momentum is scaled as well. Similarly the track's charge and ϕ_0, the azimuthal angle at the vertex, are adjusted to be consistent with the new α value.

Once the vertex offset is settled the momentum scale is set using the J/ψ mass as a standard candle. This entails making a J/ψ mass spectra using electron-positron pairs where the pair mass is dominated by the lepton momenta. The J/ψ peak is fit. The momentum

Table 3.3: Good track requirements

Cut on Good Tracks
quality $= 63, 51$, or 31
$\theta \geq 0$
$20 \geq p_T \geq 0.2$ GeV/c

scale is set to adjust the mass scale so that the J/ψ peak occurs at the correct location, 3.096 GeV. For the 2005 dataset, the momentum scale adjustment is 2%.

3.5 Quality requirements

The quality requirements maintain acceptance and detector stability between runs, between events and between tracks.

At the run level, quality assurance is performed on the data to determine which run numbers are associated with poor running conditions. These run-time problems are typically associated with dead areas in the aperture or other variations in the detector response due to voltage and temperature fluctuations. This is based off of an initial run list available from the production website [84]. The run list is cross referenced with the electronic logbook to remove any additional runs flagged as bad. Bad runs consist of converter runs, zero field runs, runs with drastic reductions of acceptance due to detector holes and runs where the necessary detectors are operating sub-optimally as determined by the online monitoring. The remaining run list is cross referenced with the output from the PHENIX quality assurance website [85] looking at the electrons per event in the different detector arms.

At the event level the primary cut is the z-vertex cut. Only events that occur with a z-vertex position within ± 25 cm of the detector origin are used. Outside of this z-vertex range events have an acceptance that is not as well understood due to edge effects. Additionally larger portions of these events are missed because they are more likely to be outside the detector aperture. The only other requirement is that the magnetic field is on, this is confirmed using the inner and outer coil currents.

High quality tracks consists of a track reconstruction component and an acceptance component. Ensuring tracks are well reconstructed is done by using cuts on the *quality* variable and requiring other sanity checks. These cuts are listed in Table 3.3. The *quality* variable was detailed in an earlier section with the meanings listed in Table 3.2. We require a *quality* of 63, 51 or 31; this insists on both the X1 and X2 layers in the DC and a PC1 hit that is unique or a PC1 hit with a unique UV hit. The θ cut ensures that any track in the central arms has a θ in between 60° and 120°. The transverse momentum is restricted to within the detector's measurable range. An additional cut, not listed in Table 3.3, requires that the track not cross from the north side of the detector to the south side and vice versa.
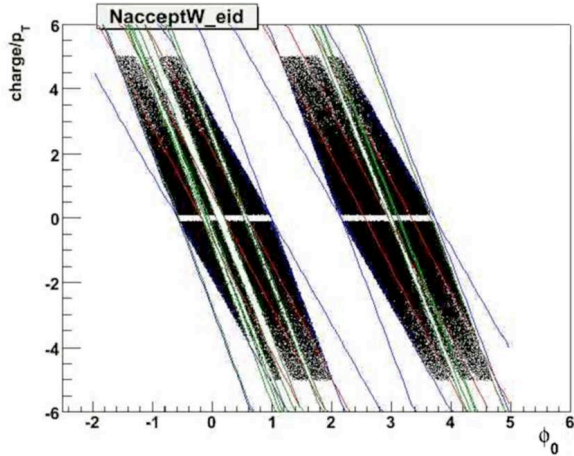
Figure 3.4: A map of the detector acceptance, ϕ_0 vs. charge/p_T, overlaid with ideal aperture lines in blue, EMC sector lines in red and the fiducial cut lines in green. The acceptance lines are listed in Table 3.4

The acceptance component consists of providing a mask of acceptance lines restricting tracks to the standard detector acceptance. This prevents any over correction of these acceptance holes, one of this measurements larger source of systematic errors. The requirements of the mask are shown in Figure 3.4 and are listed in Table 3.4.

3.6 Electron identification cuts

Electrons are identified using the EMC and RICH detectors. Electron tracks fire a Cherenkov ring in the RICH and shower in the EMC. The electron identification cuts shown in Table 3.5 ensure that the tracks are well matched to both the RICH ring and EMC shower and that the ring and shower are well characterized. The RICH ring requirements ensure that a ring fired, $n0 \geq 1$, that the ring has a typical ring shape, $chi2/npe0 < 15$, and that the ring aligns with the track, $disp < 10$. The EMC shower requirements guarantees that there is a shower, $ecore \geq 0.15$, it is an electro-magnetic shower, $prob > 0$, due to an electron, $ecore/\mathrm{p} \geq 0.5$, that is located near the track, 5 sigma matching cut.

The energy over momentum, E/p or $ecore/\mathrm{p}$, quantity best displays the ability of these cuts to remove non-electron tracks. Electrons are characterized by energy over momentum values close to one since the electron mass is minimal. Figure 3.5 displays the electron identification cuts from Table 3.5 successively applied on the EWG data set in the following order: the RICH $disp$ cut, the RICH ring shape cut, the RICH $n0$ cut, the EMC track matching cut, the electromagnetic shower probability, the EMC shower energy cut, the p_T cut and finally the energy over momentum cut.

46

Table 3.4: Acceptance mask defining the ideal aperture and dead areas

Cut	Value
Ideal East arm aperture	$\phi - 0.309 * \frac{charge}{p_T} > 2.16$
	$\phi - 0.309 * \frac{charge}{p_T} < 3.731$
	$\phi - 0.206 * \frac{charge}{p_T} > 2.16$
	$\phi - 0.206 * \frac{charge}{p_T} < 3.731$
	$\phi - 0.275 * \frac{charge}{p_T} > 2.16$
	$\phi - 0.275 * \frac{charge}{p_T} < 3.731$
Ideal West arm aperture	$\phi - 0.309 * \frac{charge}{p_T} > 0.982$
	$\phi - 0.309 * \frac{charge}{p_T} < -0.589$
	$\phi - 0.206 * \frac{charge}{p_T} > -0.589$
	$\phi - 0.206 * \frac{charge}{p_T} < 0.982$
	$\phi - 0.275 * \frac{charge}{p_T} > -0.589$
	$\phi - 0.275 * \frac{charge}{p_T} < 0.982$
EMC sector boarders	$\phi - 0.275 * \frac{charge}{p_T} = 2.5528$
	$\phi - 0.275 * \frac{charge}{p_T} = 2.9455$
	$\phi - 0.275 * \frac{charge}{p_T} = 3.3383$
	$\phi - 0.275 * \frac{charge}{p_T} = -0.1963$
	$\phi - 0.275 * \frac{charge}{p_T} = 0.1965$
	$\phi - 0.275 * \frac{charge}{p_T} = 0.58925$
Dead areas	$0.193 > \phi - 0.219 * \frac{charge}{p_T} > -0.0614$
	$-0.0614 > \phi - 0.219 * \frac{charge}{p_T} > -0.1272$
	$0.5877 > \phi - 0.219 * \frac{charge}{p_T} > 0.522$
	$3.022 > \phi - 0.219 * \frac{charge}{p_T} > 2.956$
	$3.1316 > \phi - 0.219 * \frac{charge}{p_T} > 3.1096$
	$-0.107 > \phi - 0.206 * \frac{charge}{p_T} > -0.181$
	$3.731 > \phi - 0.206 * \frac{charge}{p_T} > 3.6692$
	$-0.5664 > \phi - 0.206 * \frac{charge}{p_T} > -0.589$

Table 3.5: Electron identification cuts

Cut
$n0 \geq 1$
$chi2/npe0 < 15$
$ecore/\mathrm{p} > 0.5$ c
$ecore > 0.15$ GeV
$prob > 0$
$disp < 10.0$
5 sigma emc track matching cut
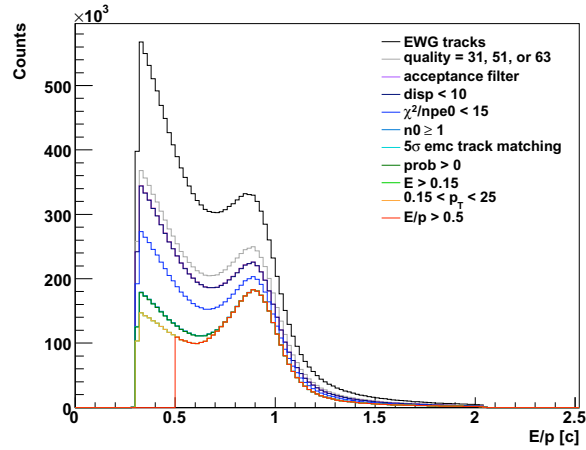
Figure 3.5: Histogram of the Energy over momentum, E/p, using the EWG dataset. Various electron identification cuts are applied in succession and detailed in the legend.

The electron cuts detailed here are fairly loose compared to what is typically used in single electron analyses. The loose electron identification cuts are not a problem since this is a pair analysis and the correlation between an electron-positron pair is the measured signal not individual electrons. Electron tracks are quite rare; typically we see one electron per twenty events in minimum bias collisions. A mis-identified electron track is unlikely to have another electron to pair with it. In the rare event where that does happen, the pair is unlikely to be truely correlated and a combinatorial pair is generated. The following section will discuss the removing combinatorial pairs and other background pairs in more detail.

Chapter 4

Making pairs, identifying backgrounds

Identified electron and positron tracks within an event are paired. The mass and p_T are calculated for each pair according to Equations 4.1.

$$m = c^{-2}\sqrt{(E_+ + E_-)^2 - (\boldsymbol{p_+} \cdot \boldsymbol{p_-})^2 c^2}$$
$$p_T = \sqrt{(p_{+x} + p_{-x})^2 + (p_{+y} + p_{-y})^2}$$
$$E_+ = \sqrt{\boldsymbol{p_+}^2 c^2 + m_e^2 c^4}$$
$$E_- = \sqrt{\boldsymbol{p_-}^2 c^2 + m_e^2 c^4} \tag{4.1}$$

All possible pairs within an event are made. This is done because it is difficult to determine which electrons and positrons share the same source. The resulting spectrum, Figure 4.1, contains the signal pairs in addition to a large number of background pairs. The background sources are:

- combinatorial pairs
- detector overlap effects
- conversion pairs
- correlated pairs due to jets
- correlated pairs with a common ancestor

The largest background is the combinatorial background. These are non-physical pairs from unrelated electrons and positrons in the same event. Non-physical background pairs are also due to detector overlap effects. These pairs result from the finite segmentation in the RICH detector and the difficulty separating adjacent rings on the RICH PMT array. The remaining background sources contain physical correlations that we are not interested in measuring. Conversion pairs result when a photon converts in the detector material or gas. Correlated jet pairs occur when both the electron and positron are from separate decays
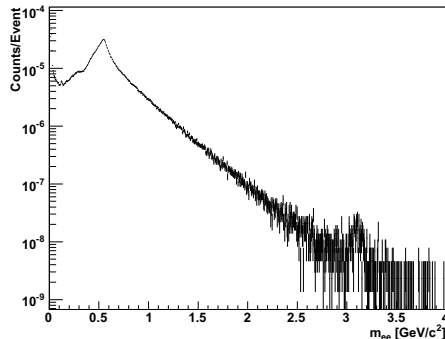
Figure 4.1: The mass distribution of all electron-positron pairs.

produced within the same jet pair. Pairs correlated by a common ancestor are produced in decay chains where multiple electron-positron pairs are created, a combinatorial pair within the chain is correlated by their common ancestor.

We are able to remove the backgrounds using two strategies, pair cuts and statistical background removal. Conversion pairs and detector overlap are identified and discarded by applying pairs cuts. The remainder of the backgrounds, combinatorial pairs and both types of correlated pairs, are removed statistically. This is done by first generating the background shapes, normalizing the shapes to the background levels and then subtracting each background component. The statistical background removal method is explained in more detail in Chapter 5.

To aide normalizing and removing the backgrounds statistically, like-sign pairs are generated. The like-sign pair spectra contain only background pairs, there are no like-sign signal pairs. We mention the like-sign pairs here to include like-sign background pairs in the discussion of the various backgrounds. All of these background sources produce like-sign background pairs except for the conversion pairs. Figure 4.2 presents the electron-electron and positron-positron mass spectra. The like-sign mass spectra are drastically different from the unlike-sign pair mass spectrum in Figure 4.1. This is the result of the lack of physical signal and the different detector acceptances as a result of the magnetic field. Similarly, the background sources generate different unlike- and like-sign distributions.

This chapter presents the various backgrounds in detail for both unlike- and like-sign pairs. Pair cuts, when applicable, are described. The generation of the various backgrounds needed for the statistical removal method are also discussed.

4.1 Backgrounds removed by pair cuts

Pair cuts consist of identifying and removing the background pair. The individual electrons and positrons that make up the pairs are still available for other pairings. We use
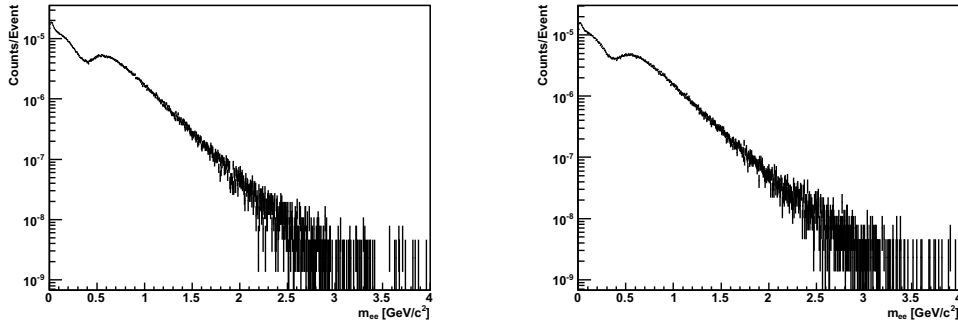
Figure 4.2: The mass distributions of all measured electron-electron and positron-positron pairs.

pair cuts to reject backgrounds from detector overlap effects and photon conversions. These background pairs are classified in part by their track geometry.

4.1.1   Detector overlap

The RICH detector is the source of overlap background pairs. Overlap in the RICH occurs when parallel tracks enter the detector. Spherical mirrors focus light emitted from either track onto the same location in the PMT array, Figure 4.3 contains a diagram of the focusing. This results in false electron identification for tracks that are coincidentally parallel to a true electron track. This creates a variation in the hadron rejection that is correlated the p_T of the electrons within the event, since the slope of a track is roughly $1/p_T$. The variation in hadron rejection changes event-by-event because the sampled electron p_T differ. When these hadrons pair with other electron identified tracks they generate the standard combinatorial background pairs. When they pair with their parallel electron they do so above the combinatorial rate creating a peaked structure.

Both like- and unlike-sign background pairs are created by detector overlap. The leptons in like-sign pairs are bent equally by the magnetic field resulting in pairs with a small opening angle and therefore a small mass. The leptons in unlike-sign pairs are bent in opposite directions by the magnetic field; this results is a larger opening angle and masses near 0.6 GeV/c^2. Figure 4.4 shows the unlike- and like-sign mass distributions with overlap pairs and with the pairs removed using the pair cut.

We remove these pairs by requiring that the ring centers are separated by more than twice the nominal ring size. This is calculated using each track's ring location according to Equations 4.2. A requirement of a distance greater than or equal to ten is applied which

52
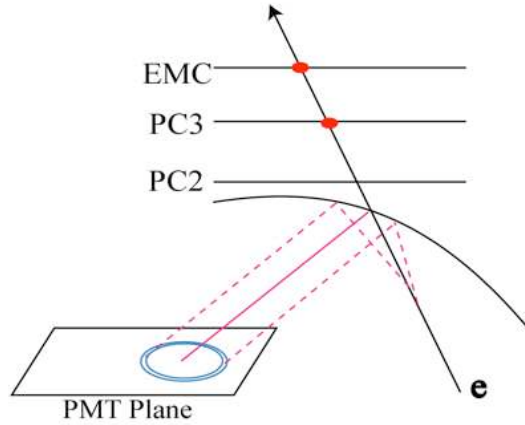
Figure 4.3: Diagram of the ring imaging Cherenkov detector focusing of the Cherenkov light into a ring on the PMT array.
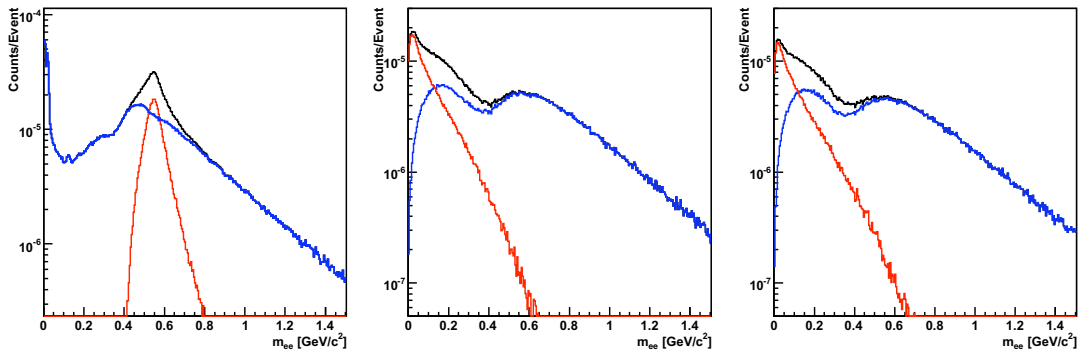
Figure 4.4: The mass distributions for electron-positron, electron-electron and positron-positron pairs with and without the overlap pair cut. The removed pairs are shown in red.
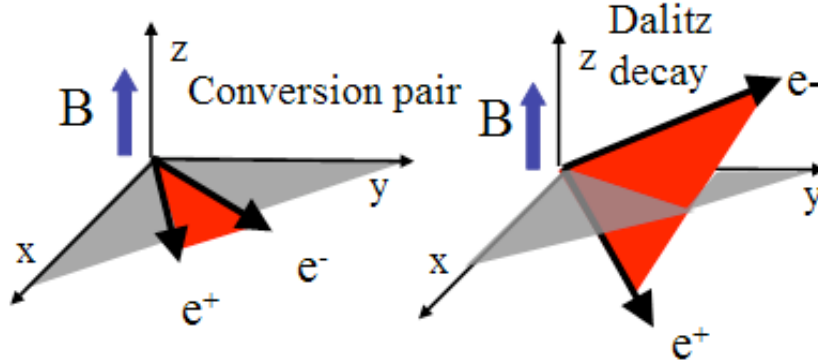
Figure 4.5: Diagram of the opening angle orientation of conversion pairs. It is compared to the random orientation of the opening angle for pairs from a Dalitz decay.

prevents any overlap in the PMT array and requires fully distinct rings.

$$\delta center = \sqrt{\left(\frac{center_{\phi 1} - center_{\phi 2}}{0.01}\right)^2 + \left(\frac{center_{z1} - center_{z2}}{3.6}\right)^2} \qquad (4.2)$$

4.1.2 Conversion pairs

High energy photons interact with the nuclei in the detector material and convert into electron-positron pairs. The detector is designed to minimize conversions by using materials with large radiation lengths, $1/\chi_0$. As a result pair production occurs primarily in the beampipe with some additional conversions in the air and the detector support structure. As mentioned earlier, photon conversion produces only electron-positron pairs; no like-sign background pairs are generated.

When the photon converts the electron-positron pair are originally co-moving. Once they enter the magnetic field region they separate as a result of their opposite charges creating a small opening angle. The conversion pair's opening angle is in the plane perpendicular to the magnetic field as shown in Figure 4.5. The two leptons travel through the detector and are reconstructed as separate tracks. The momentum of off-vertex decay products, such as the electron and positron, are mis-reconstructed since the tracking algorithm automatically connects tracks back to the collision vertex. This results in a pair mass that is roughly proportional to the distance between the conversion point and the collision vertex. Beam pipe conversions peak at a pair mass of 0.02 GeV/c^2. Air conversions extend to masses of 0.4 Ge/c^2 with peaks due to the PHENIX support structure structure at masses of 0.07 and 0.12 GeV/c^2.
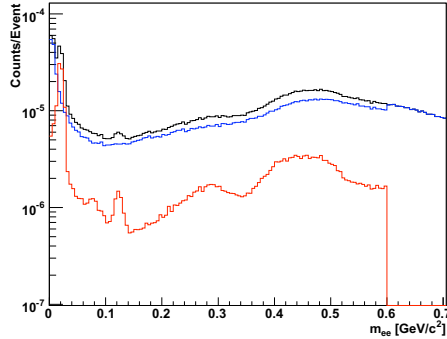
Figure 4.6: The mass distribution of electron-positron pairs with and without the conversion cut applied in blue and black respectively. The removed pairs are shown in red.

The pair's orientation relative to the magnetic field, ϕ_V, and mass serve as indicators of a pair's photon conversion origins. This helps us distinguish conversion pairs from signal pairs with small opening angles, such as pion Dalitz decay pairs. We remove electron-positron pairs with opening angles within 0.06 rad of the plane perpendicular to the magnetic field and masses below 0.6 GeV/c^2 where conversions are prevalent. A stronger ϕ_V cut, removing ϕ_V less than 0.25 rad, is applied at masses below 0.05 GeV/c^2 where beampipe conversions are strongest. Figure 4.6 shows the mass spectrum with and without the conversion cut applied in blue and black respectively. The removed pairs are shown in red. The detector overlap cut described earlier is applied. In Figure 4.6 the beampipe conversions are clear at mass 0.02 GeV/c^2. Peaks due to the support structure are seen at masses of 0.07 and 0.12 GeV/c^2. Air conversions produce a peak at a mass of 0.28 GeV/c^2. The peak at 0.45 GeV/c^2 is due to the combinatorial background pairs that coincidentally fail the conversion cut.

4.2   Combinatorial background pairs

Some backgrounds can not be identified making background removal with pair cuts impossible. This is the case for combinatorial pairs and correlated pairs due to jets and common ancestry. Instead we remove these backgrounds statistically. Combinatorial background pairs are presented. Both types of correlated pairs are discussed in the next section.

Combinatorial background pairs are due to uncorrelated electrons and positrons in the same event. For example an event with four electrons from two uncorrelated pion Dalitz decays result in two signal pairs, from the Dalitz pairs, and two combinatorial unlike-sign pairs, from pairs across the two separate decays, and two combinatorial like-sign pairs, one of each sign. In general, as the number of electrons, N_- and positrons, N_+, within an event increase the number of combinatorial pairs increases roughly as that number squared;
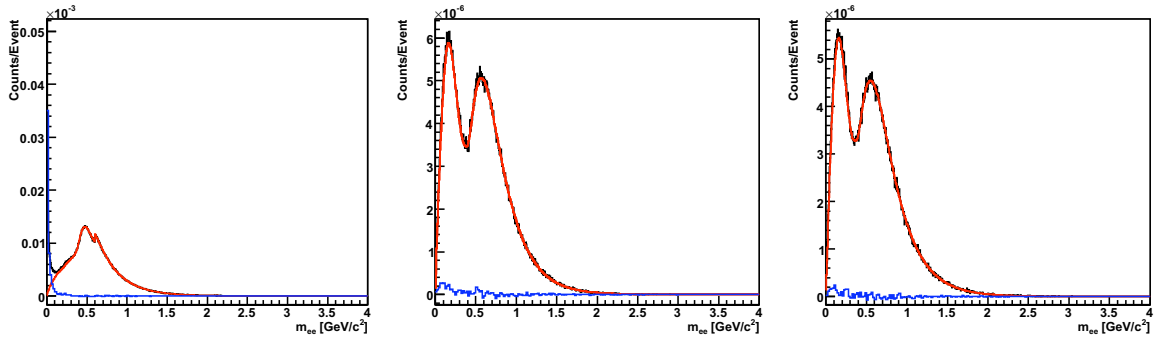
Figure 4.7: The mass spectra for electron-positron, electron-electron and positron-positron pairs. Combinatorial background spectra, roughly normalized, are shown in red and the blue histogram is the subtraction.

$N_- * N_+$ unlike-sign pairs are created and $N_- (N_- - 1)$ or $N_+ (N_+ - 1)$ for the electron-electron and positron-positron pairings respectively. The combinatorial background is the largest background and is typically orders of magnitude larger than the desired signal.

The combinatorial background shape is generated, normalized and subtracted from the signal measurement. Figure 4.7 shows the unlike- and like-sign mass spectra with the pair cuts applied overlaid with the roughly normalized combinatorial background shape achieved via event mixing. The blue histogram is the spectrum with the combinatorial removed. The majority of the measured pairs are due to the combinatorial background. This background has a substantially different shape in the unlike- and like-sign spectra because of the different pair acceptance as a result of the charges moving the in magnetic field. A small excess background remains in the like-sign spectra at low mass. These pairs are the remaining correlated backgrounds due to jets and common ancestors described in the next section.

The combinatorial background shape is generated by creating non-physical pairs from similar events guaranteeing pairs without any physics signals. This is called event mixing. We ensure that the similar events are used for creating these background pairs by classifying each event in groups by their centrality and z-vertex values. This is necessary because the combinatorial shape changes with the multiplicity, p_T distribution and acceptance variations across the group classification. Event mixing in is described in more detail in Chapter 5. Figure 4.8 show the generated combinatorial backgrounds for the dielectron mass spectra using fifty groups divided according to ten centrality and five z-vertex classifications. In Figure 4.8 the drastic increase in the size of the combinatorial background in more central collisions is apparent. This is because the combinatorial background grows with the multiplicity squared and central collisions have higher multiplicities. The combinatorial background shapes are also vary with centrality. Event mixing and the generation of the combinatorial background will be discussed in more detail in Chapter 5.

(a) Unlike-sign pairs   (b) Like-sign pairs
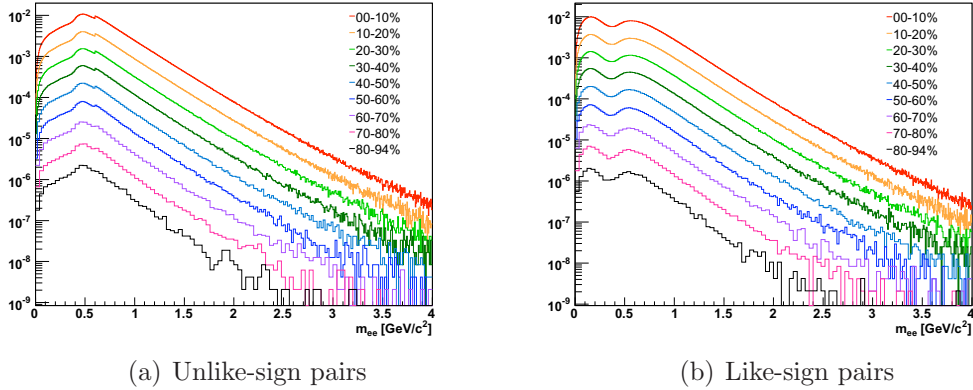
Figure 4.8: The like- and unlike-sign combinatorial shapes generated for centralities separated in 10% groupings, with 80-90% and 90-94% summed together. Here the sum of both the electron-electron and positron-positron pairs are combined for the like-sign pairs.

4.3 Correlated pairs

There are two types of correlated background pairs, those from an underlying jet correlation and those from hadronic decays that share a common ancestor. These backgrounds are similar to the combinatorial background in that they are the result of pairing many leptons in the event. However these pairings maintain the correlation from their production dynamics and are not simple random pairings of the electron-positron sample. This means that their shape can not be reproduced using event mixing. Instead various simulations are used to generate the correlated background shapes taking into account the restrictions due to the intrinsic production dynamics.

These simulations are subtracted from the data after being normalized by their background rates. The simulations are weighted according to the efficiency of the electron identification cuts and the detector dead areas found in the data are applied. The dead areas in the detector acceptance detailed in Chapter 3. The electron identification efficiency is presented in Chapter 6.

4.3.1 Jet correlated background pairs

Background pairs due to jet correlations typically result from two pions within a jet that Dalitz decay creating two electron-positron signal pairs as seen in Figure 4.9. As in the example in the combinatorial pairs subsection, two additional non-signal electron-positron pairs and electron-electron and positron-positron pairs are created. These background pairs maintain information from the jet correlation of the pions effecting the pair distributions, particularly the pair variables mass, p_T and $\Delta\phi$.
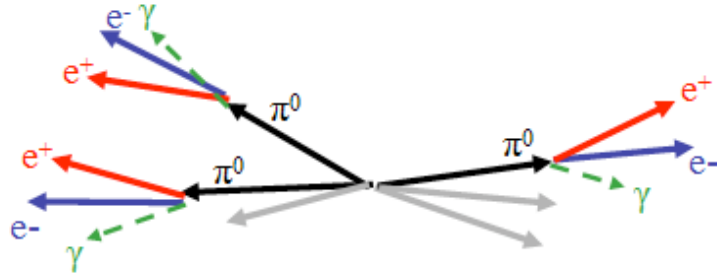
Figure 4.9: Diagram of the jet geometry leading to jet correlated backgrounds.
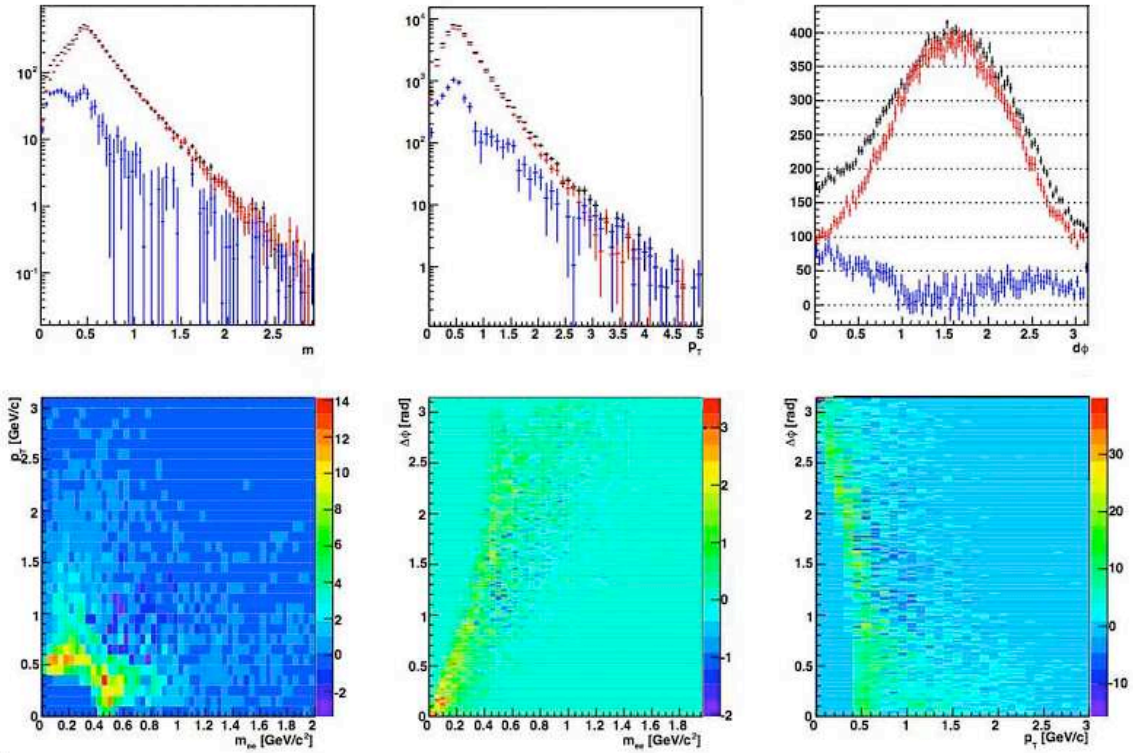
Figure 4.10: The top row shows the unlike-sign correlated jet pair mass, p_T, and $\Delta\phi$ spectrum for all pairs (black), background event pairs (red) and background event subtracted pairs (blue). The second row shows the subtracted spectrum in two-dimensional projections of mass vs. p_T, mass vs. $\Delta\phi$, and p_T vs. $d\phi$.
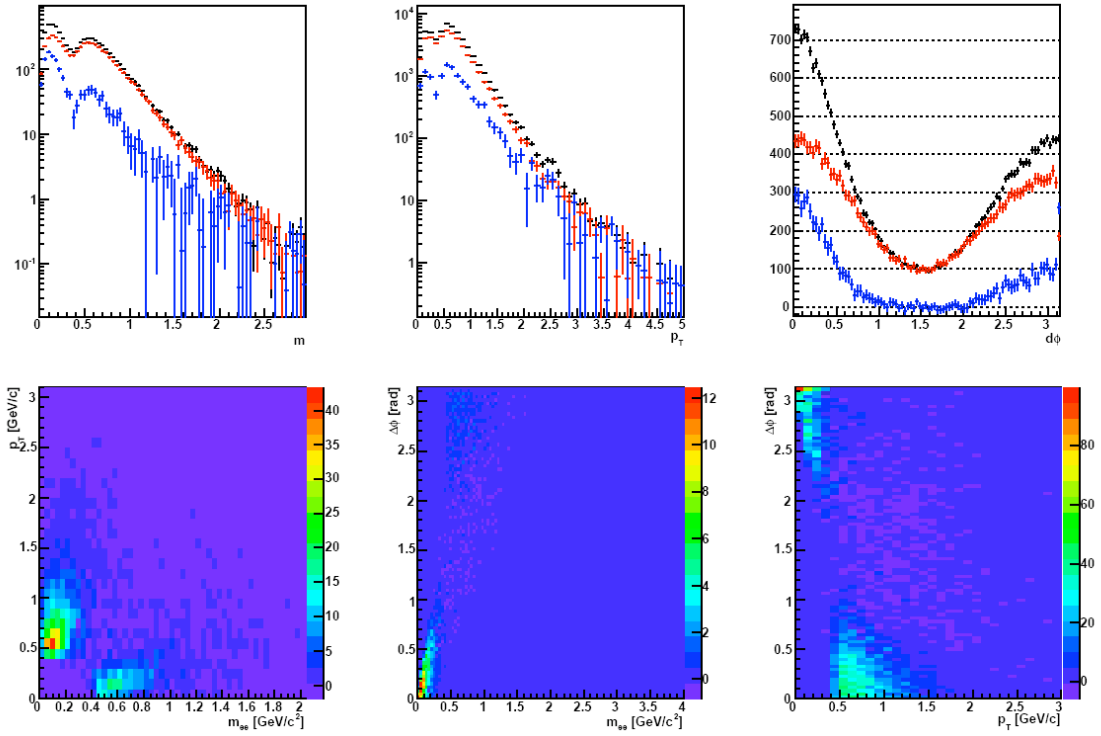
Figure 4.11: The top row shows the like-sign correlated jet pair mass, p_T, and $\Delta\phi$ spectrum for all pairs (black), background event pairs (red) and background event subtracted pairs (blue). The second row shows the subtracted spectrum in different two-dimensional projections of mass vs. p_T, mass vs. $\Delta\phi$, and p_T vs. $\Delta\phi$.
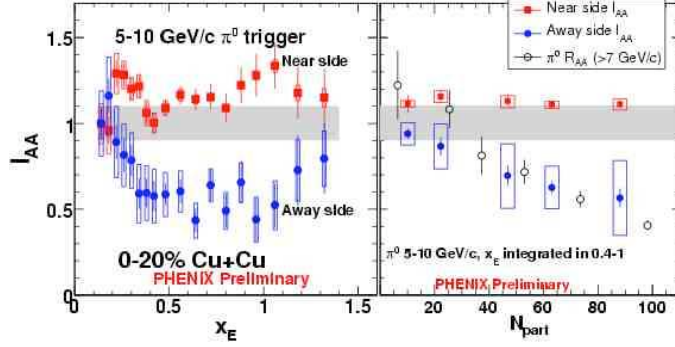
Figure 4.12: The measured I_{AA} in Cu+Cu collisions vs. N_{Coll}. [86]

The jet background is simulated by Torsten Dahms using Pythia, a p+p event and jet generator. In the simulation the pions created by the jet were modified to preferentially undergo Dalitz decay to maximize the relevant pairs produced in the simulation. Both like- and unlike-sign background lepton pairs are made. The Pythia simulation spectrum contains an underlying p+p event that is removed. This is done by randomly generating events flat in ϕ and θ with the Pythia p_T distribution, area normalizing these background events' spectrum to the simulation in the region $\Delta\phi$ 70° to 110° and subtracting the event from the simulation. This subtraction is shown in Figure 4.10 and Figure 4.11 for unlike- and like-sign pairs respectively.

The subtracted spectrum is the correlated jet background assuming an unmodified p+p jet. It depicts the standard jet $\Delta\phi$ distribution with near- and away-side peaks in both the like- and unlike-sign $\Delta\phi$ spectrum. This bimodal near- and away-side jet structure are also seen in the mass and p_T spectrum where the near-side jet component peaks at a low masses and high p_T, the away-side jet component peaks at masses near 0.7 GeV/c^2 and p_T below 0.5 GeV/c. The higher p_T in the near-side jet is a result of the low m_T acceptance hole due to the minimum p_T cut on single electrons.

Cu+Cu jets differ from p+p jets; they undergo jet suppression [41]. The away-side jets are altered in the more central collisions. Figure 4.12 shows the I_{AA}, the ratio of the away-side yield in Cu+Cu over the away-side yield in p+p, versus N_{Coll}, the number of collisions, in Cu+Cu collisions. We expect this suppression to alter the away-side jet shape in mass and p_T. To model this we reduce the away-side jet component as a function of centrality according to the measured Cu+Cu I_{AA}. Figure 4.13 shows the effect of the reduction in the away-side jet on the correlated jet mass spectrum.
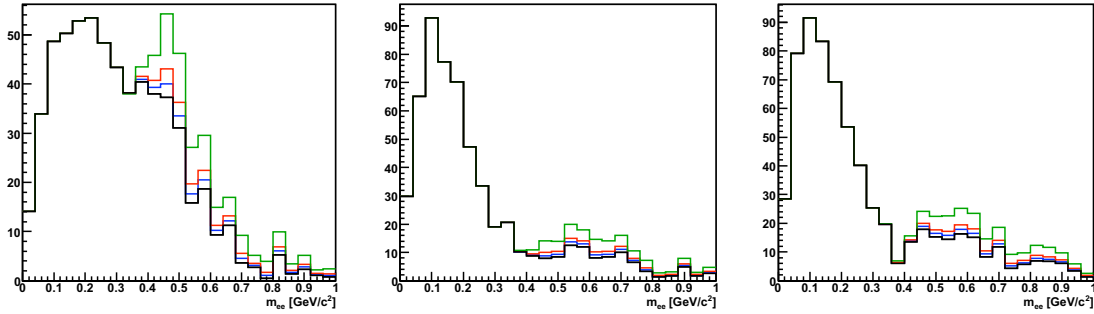
Figure 4.13: The jet background adjusted by I_{AA} for each of the centrality bins (0-10% green, 10-20% red, 20-40% blue, 40-94% black) for electron-positron pairs, electron-electron pairs and positron-positron pairs.

4.3.2 Correlated pairs with a common ancestor

Pairs correlated by a common ancestor are produced in decay chains where multiple electron-positron pairs are produced, a combinatorial pair within the chain is correlated by the common ancestor. First lets discuss as an example, a hadronic Dalitz decay with a photon conversion. In this case the following pairs result:

- the electron-positron pair from the Dalitz decay
- the electron-positron pair from the photon conversion
- the electron-electron pair, one from the Dalitz decay and one from the photon conversion
- the positron-positron pair, one from the Dalitz decay and one from the photon conversion
- two electron-positron pairs, in each one is from the Dalitz decay and one is from the photon conversion

The electron-positron pair from the Dalitz decay is a physical signal pair that is included in the dielectron measurement with the many other hadronic Dalitz pairs. The electron-positron pair from the photon conversion is removed by the conversion pair cuts detailed earlier in this chapter. The remaining pairs are an example of background pairs correlated by a common ancestor, the original hadron.

Correlated pairs with a common ancestor are primarily emitted from π^0 and η mesons. Background pairs resulting from other hadronic decay chains are unlikely. Lower production rates and low branching ratios conspire against additional sources. These mesons produce correlated background pairs from Dalitz decay with a photon conversion, as described in the earlier example, double Dalitz decays. The η also decays into three π^0 each of which may dalitz or double Dalitz decay.

In the double Dalitz decay case it is legitimate to classify all four of the unlike sign pairs as physics signal, even the pairs could be considered hadronic signal. However we will compare our dielectron spectrum to a cocktail of known hadronic decays. This cocktail is generated using Exodus, a hadronic decay simulator. Exodus is described in more detail in Chapter 8. One important characteristic of Exodus is that it does not create the combinatorial pairing of decays with more than two electrons. We label the like-sign pairs and two of the unlike-sign pairs from double Dalitz decay as background to be consistent with EXODUS. Within this construct, a pion double Dalitz decay have similar background production rates and decay kinematics and as a Dalitz decay with a photon conversion.

To simulate the η and π^0 decays, I create a modified Exodus, exodusDD, that properly deals with the combinatorial pairings in these decays. The following decay channels are simulated.

$$\pi^0 \to e^+e^-e^+e^-$$
$$\eta \to e^+e^-e^+e^-$$

$$
\begin{array}{llll}
\eta \to \pi^0\pi^0\pi^0 \to e^+e^-e^+e^- & e^+e^-e^+e^- & e^+e^-e^+e^- \\
\qquad\qquad\quad \to \gamma\gamma & e^+e^-e^+e^- & e^+e^-e^+e^- \\
\qquad\qquad\quad \to \gamma\gamma & \gamma\gamma & e^+e^-e^+e^- \\
\qquad\qquad\quad \to \gamma e^+e^- & \gamma e^+e^- & \gamma e^+e^- \\
\qquad\qquad\quad \to \gamma\gamma & \gamma e^+e^- & \gamma e^+e^- \\
\qquad\qquad\quad \to \gamma\gamma & \gamma e^+e^- & e^+e^-e^+e^- \\
\qquad\qquad\quad \to \gamma e^+e^- & \gamma e^+e^- & e^+e^-e^+e^- \\
\qquad\qquad\quad \to \gamma e^+e^- & e^+e^-e^+e^- & e^+e^-e^+e^-
\end{array}
$$

The decay kinematics are identical to those used in Exodus. Each electron or positron is weighted by their momentum dependent efficiency and required to pass through the realistic PHENIX aperture. The simulation gives us an initial estimate of the correlated background due to a common ancestor. Pairs are classified as unlike-sign signal, unlike-sign background and the two like-sign backgrounds. Unlike-sign signal is shaped like the standard π^0 and η Dalitz curves and extends no further than the η mass, 0.547 GeV/c^2. The unlike- and like-sign background pairs have humped shapes with kinematic limits at their common ancestor's mass, 0.135 GeV/c^2 for the π^0 and 0.547 GeV/c^2 for the η. Background pairs from the η to three π^0 decays have kinematic limits at 2/3 the η mass. These shapes are presented in Figure 4.14.

Adjusting for the conversion contribution

External conversions, such as the Dalitz decay with a photon conversion, are not directly simulated and must be included. These decay chains have similar kinematics to the double Dalitz decays that are simulated. We calculate the background yields of the external conversions and the simulated decays and scale the simulated double Dalitz backgrounds accordingly. Only the background yields are altered. The signal pairs are unadjusted; photon

conversion pairs in the signal are removed via a pair cut. The scale factor is calculated by comparing the different yields with and without conversions in the decay chain. The yield for a decay is calculated according to Equation 4.3.

$$Yield = \frac{dN}{dy} * \frac{meson}{\pi} * d_P * P\left(meson \rightarrow N_P\right) \tag{4.3}$$

where $\frac{dN}{dy}$ is the multiplicity, d_P is the pair degeneracy, and $P\left(meson \rightarrow N_P\right)$ is the decay probability of the meson into N_P lepton pairs.

The ratio of the expected yield with conversions over the yield without conversions is the scaling factor. The $\frac{dN}{dy}$ and meson-to-pion ratios cancel and the ratio consists of the pair degeneracy and the decay probability. The probabilities for the η and π^0 photonic, Dalitz and double Dalitz decays are calculated according to Equation 4.4.

$$P\left(meson \rightarrow 0\right) = BR_{\gamma\gamma}\left(1 - c\right)^2$$
$$P\left(meson \rightarrow 1\right) = 2 * BR_{\gamma\gamma}\left(1 - c\right)c + BR_{\gamma e^+ e^-}\left(1 - c\right)$$
$$P\left(meson \rightarrow 2\right) = BR_{\gamma\gamma}c^2 + BR_{\gamma e^+ e^-}c + BR_{e^+ e^- e^+ e^-} \tag{4.4}$$

where BR are the branching ratios for the various decays and c is the conversion probability, 0.2429% in PHENIX. Table 4.1 presents the degeneracies and probabilities for the η and π^0 decays with and without photon conversions. The background pair degeneracies follow Equation 4.5.

$$d_P = N_P * \left(N_P - 1\right) \tag{4.5}$$

The sum is weighted with d_P. The ratios are the summed values with photon conversions, $c \neq 0$, over the values without photon conversions, $c = 0$. The double Dalitz background pairs are scaled by 2.1178 and 1.0025 for the π and η respectively. These scalings account for the additional background yield due to Dalitz decays with a photon conversion.

Table 4.1: π and η Dalitz and Double Dalitz decays

		$P\left(c \neq 0\right)$		$P\left(c = 0\right)$			
N_P	d_P	π Value	η Value	π Value	η Value	π Ratio	η Ratio
0	0	0.9832	0.3911	0.988	0.3931		
1	0	0.0167	0.0087	0.012	0.0068		
2	2	6.64e-5	0.0079	3.14e-5	0.0079		
sum		1.33e-4	0.01582	6.28e-5	0.01578	2.1178	1.0025

The $\eta \rightarrow 3\pi^0$ scalings have many decay channels that produce background pairs. The addition of conversion pairs further complicates this background. Using the pion decay probabilities listed in Table 4.1 simplifies the calculation. All combinations of pion decay

Table 4.2: $\eta \to 3\pi^0$ decays

N_P	d_P	Probability	$P(c \neq 0)$	$P(c = 0)$	Ratio
0	0	$P(\pi^0 \to 0)^3$	0.9504	0.9644	
1	0	$3P(\pi^0 \to 0)^2 P(\pi^0 \to 1)$	0.0486	0.0351	
2	2	$3P(\pi^0 \to 0) P(\pi^0 \to 1)^2$	8.28e-4	4.26e-4	
2	0	$3P(\pi^0 \to 0)^2 P(\pi^0 \to 2)$	1.92e-4	9.20e-5	
3	6	$P(\pi^0 \to 1)^3$	4.7e-6	1.73e-6	
3	4	$6P(\pi^0 \to 0) P(\pi^0 \to 1) P(\pi^0 \to 2)$	6.56e-6	2.23e-6	
4	10	$3P(\pi^0 \to 1)^2 P(\pi^0 \to 2)$	5.59e-8	1.36e-8	
4	8	$3P(\pi^0 \to 0) P(\pi^0 \to 2)^2$	1.30e-8	2.92e-9	
5	16	$3P(\pi^0 \to 1) P(\pi^0 \to 2)^2$	2.22e-10	3.55e-11	
6	20	$P(\pi^0 \to 2)^3$	2.92e-13	3.10e-14	
		sum weighted by d_P	5.57e-4	2.84e-4	1.9612

channels are considered and shown in Table 4.2.

The background pair degeneracies in the $\eta \to 3\pi^0$ case are more complicated as well. Equation 4.5 no longer holds. We do not want to double count background pairs due to pion double Dalitz which have already been considered in the double Dalitz factors presented earlier in this section. As a result Equation 4.5 has an $-2*n$ correction term where n is the number of the $\pi^0 \to 2$ decays. Again a pair degeneracy weighted sum is calculated and the ratio of the sum with conversions and without conversions is the adjustment factor. The $\eta \to 3\pi^0$ background pairs are scaled by 1.9612 to account for the additional background yield from photon conversions in the decay chain.

Each of the individual decay background components are scaled by their appropriate factors and then summed. Figure 4.14 shows the mass distributions of the correlated backgrounds with a common ancestor for unlike-sign signal pairs, unlike-sign background pairs and the positive and negative like-sign pairs.
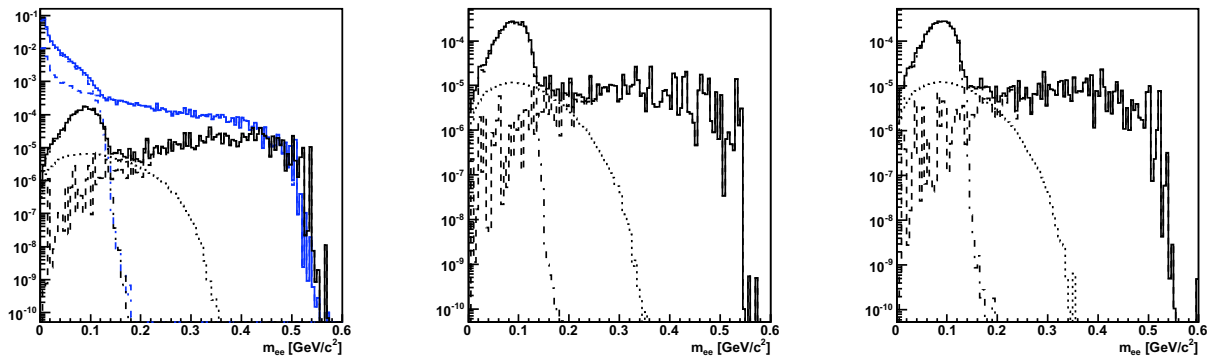
Figure 4.14: The simulated common ancestor pair mass distributions for electron-positron pairs (signal in blue and background in black), electron-electron pairs and the positron-positron pairs. The sum is the solid line, the pion are dot-dashed lines, the eta are dotted lines and the eta to three pions are dashed lines.

65

Chapter 5

Statistical background removal

Statistical background removal consists of generating the background shape, determining the background rates and subtracting the background spectrum. The combinatorial background and the correlated backgrounds due to jet pairs and a common ancestor are removed with this method. The jet and common ancestor correlated backgrounds are simulated with Pythia and a modified Exodus. The combinatorial background is created using the event mixing technique.

When generating the background shapes we produce background pairs above their expected rates. This is done so that the shape of the background is well understood. However the generated background must be scaled or normalized to the correct background level. The like-sign spectra help determine and confirm the background levels; it is instrumental in calculating the background normalizations. The event mixing technique and the generator code used are presented in more detail below. This is followed by a discussion of the background normalization and subtraction.

5.1   Event mixing

Event mixing consists of taking electrons (positrons) from one event and making pairs with an positrons (electrons) from a separate event. The constructed pairs contain no physical correlation. Only random combinatorial background pairs are made.

Event mixing is done using a rolling buffer method. The electrons (positrons) in the current event are mated with the positrons (electrons) in previous events with a similar centrality and z-vertex classification. Figure 5.1 presents a diagram of the mixing for unlike-sign pairs. First pairs are made between the electrons and positrons in the current event. Then the electrons (positrons) within the current event are paired up with positrons (electrons) from previous events. Because the mixing occurs with many previous events in the buffer, far more combinatorial pairs are generated across events than in the current event. As a result the combinatorial background distribution is understood to a high statistical accuracy.
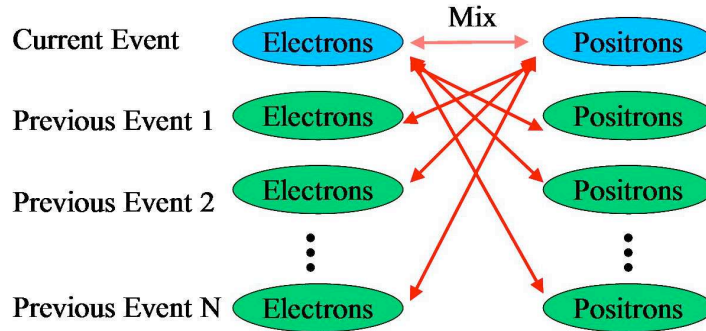
Figure 5.1: Diagram of the rolling event buffer method for electron-positron mixing with a buffer depth of N. The current event is shown in blue and the collection of electrons and positrons from previous events are shown in green. The pairing of electrons and positrons in the current event is shown as the pink arrow whereas the generation of pairs across events is shown as the red arrows.

However, the combinatorial background rate must be determined to normalize the combinatorial background distribution to the correct amount, this is discussed in detail later in the chapter. The number of events that are mixed with the current event is called the depth of the mixing, Figure 5.1 displays mixing with a depth of N. This analysis uses a depth of one hundred events. Using such a large depth and a large number of pools has the advantage of creating a well defined background shape with a reduced shape error. Like-sign pairs are created in an analogous procedure to the unlike-sign pairs using the same previous event subset. In this process it is important to treat the mixed event pairs identically to the same event pairs, any discrepancy could lead to deviations in the combinatorial shapes between the mixed and same events.

The combinatorial background shape within a event depends upon the event's multiplicity, detector acceptance, and momentum distribution. For this reason events are mixed among events that are similar in centrality, z-vertex range, and reaction plane orientation. This is required since the combinatorial shapes differ among these groupings, or pools, often as a result of the variations in acceptance, particle production rates and p_T distributions. In Chapter 4 the effects of increased multiplicity in more central collisions on the combinatorial background were presented. Shape combinatorial background variations also occur as a result of centrality and z-vertex pooling. Figure 5.2 shows the variation of combinatorial shapes over the centrality groups in like- and unlike-sign pairs. Both the like- and unlike-sign backgrounds have been scaled to match the 0-10% centrality group below 0.15 GeV/c^2 in mass to make the shape comparison easier. The more peripheral centralities have a lower combinatorial yield and drop more steeply at high mass in both the like- and unlike-sign combinatorial backgrounds. All events in this analysis are classified as belonging in one

(a) Unlike-sign spectra   (b) Like-sign spectra
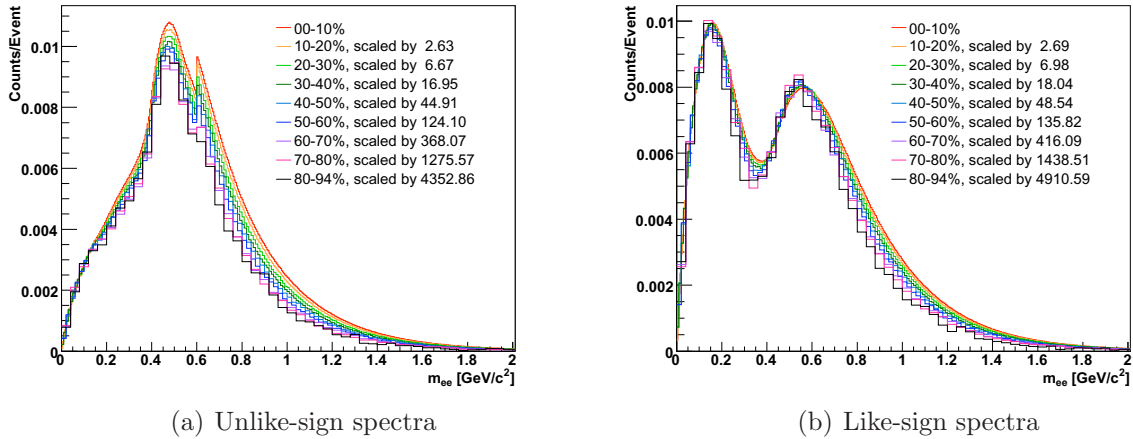
Figure 5.2: The combinatorial shapes for like-sign and unlike-sign pairs generated for the combined z-vertex bins and centralities separated in 10% groupings, with 80-90% and 90-94% are summed together. The sum of both the electron-electron and positron-positron pairs are shown. All of the centralities have been scaled to agree with the 0-10% combinatorial background at masses below 0.15 GeV/c^2. This shows the shape variation in the combinatorial background as a function of centrality.

of fifty event pools, ten centrality groupings and five z-vertex ranges. Detector acceptance variations are controlled by mixing events with the same run number.

5.1.1 CabanaBoy

The system of event mixing described above is common in pair analyses. Typically each analyzer generates their own code for event mixing. Thomas Hemmick, Jason Kamin and I created a generalized mixed event background generator called CabanaBoy. CabanaBoy is able to maintain generality by utilizing object oriented coding and inheritance structures in C++. All analysis specific aspects of the code are isolated into two user defined input classes that follow predefined inheritance structures, called Cutter and Histo classes. Methods and member objects of the classes are then called within the CabanaBoy structure when it is necessary to apply the user specific information.

The Cutter object inherits from a base class that requires the class define methods for the event cut, identify the two particles used in the mixing and any pair cuts. The Histo object inherits from a base class where deques of pointers to functions and histogram objects are defined. Inside the user's specific Histo object the histograms are booked and functions are defined that characterize the histogram axes. From start to finish, CabanaBoy creates output histograms, registers them to the input/output manager and initializes the mixing structure for each pool grouping. The event cut, defined in the user's Cutter object, is applied and
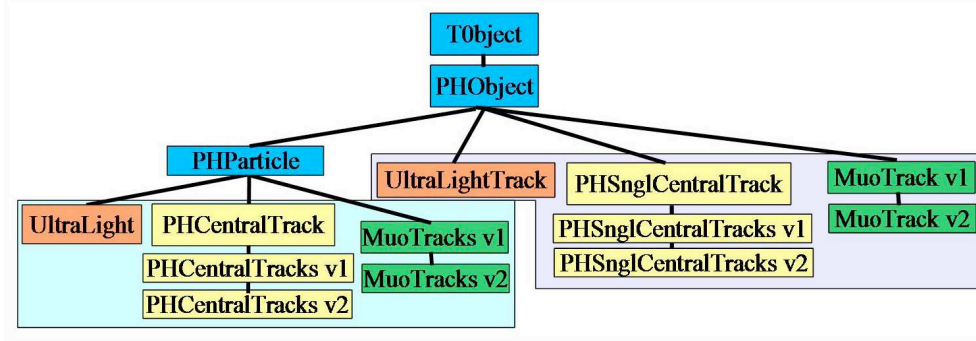
Figure 5.3: Diagram of the PHENIX data class inheritance tree.

events are classified among the pools. Within each event, the tracks are identified as the two desired particle types and placed into smaller container classes reducing the memory overhead. Same event pairings are made between the container classes. Mixed event pairs are made between the current event's container classes and the stored classes from previous events in the rolling buffer. The current event's container classes are then stored in the rolling buffer and the process is repeated with the next event.

Making the same event pairs consist of matching all of the first particle type, Type1, with all of the second particle type, Type2. For each pair we apply pair cuts from the user's Cutter object and calculate the pair output using the functions defined in the user's Histo object and fill the appropriate histograms. We also create the pairings of Type1 with Type1 and Type2 with Type2, apply the pair cuts and store this information in two separate histograms with the same axes.

Mixed event pairs are generated between the Type1 (Type2) particles from the current event and Type2 (Type1) particles from the N previous events, creating $\sum_{i=0}^{N} N1_{current\,event} * N2_i + N1_i * N2_{current\,event}$ pairs before applying the same pair cut. The mixed event pair output is calculated using the same user's functions as the same event pairs and mixed event histograms are filled. Similarly Type1-Type1 and Type2-Type2 mixed event pairs are made, the pair cut is applied and two more histograms are filled.

For each histogram the user defines six histograms with the same binning and axes are made per event pool. One set of three histograms (Type1-Type2, Type1-Type1, and Type2-Type2) for the same event pairings and a second set of three histograms for the mixed event pairings. This is done separately in each event pool. In my analysis one histogram defined in the Cutter results in filling three hundred output histograms, six in each of the fifty event pools.

To maintain generality one more technical aspect had to be overcome in the CabanaBoy code. The various data sets store the track information in different class objects. CabanaBoy needs a general track class for all potential particle types. Luckily we were able to exploit

the polymorphism and covariance that results from the inheritance structure in the PHENIX track classes. The PHENIX class structure is shown in Figure 5.3, not all classes are shown. PHObjects serve as a base class to the SingleTrack objects, holding information relating to one track, and the PHParticle object. The PHParticle class and it's daughter Track classes are a container classes holding collections of their respective SingleTrack objects. PHParticle objects are defined by their ability to create clones and to add to their collections. This satisfies a necessary requirement in the CabanaBoy code allowing the construction of the Type1 and Type2 particle collections; these collections are PHParticle class objects. All daughter track classes are cast via a static cast into PHParticle objects in the top level CabanaBoy code. They are mixed as PHParticle objects and when user specific cuts or calculations are applied they are cast back into their original class where they retain access to the methods of their original class. These casts occur in the user supplied Cutter or Histo codes. The ability of the class to access it's original methods after being cast as a base class is called covariance. This is a key component of C++ which allows the success of the general mixing engine. As a side comment, we use static casts in order to ensure that the PHParticle objects are cast back into their original class type, if they are miscast into a different type a static cast will fail while a dynamic cast will not.

5.1.2 UltraLights

While the majority of the PHENIX container classes inherit from PHParticle there are exceptions to the class hierarchy. We implement a new container class object called UltraLights that do inherit from PHParticle as a work around for this limitation of our data classes. UltraLight objects are filled during runtime with UltraLightTrack objects and saved in the root node tree to be accessed later, presumably by CabanaBoy. The additions to the node tree exist only during runtime and are not saved to disk. UltraLightTracks inherit from the PHObject base class and behave similarly to the SingleTrack objects detailed earlier. They have a methods to access the p_x, p_y, p_z and E single track information. The UltraLight structure allows a user to define their own daughter classes of the UltraLights and UltraLightTracks for container and single track classes respectively. User-defined daughter classes allow the user to store additional double and integer track information in the single track and container class formats. The addition of the UltraLight objects allow analyzers more flexibility in how they implement their analyses in CabanaBoy.

UltraLights were originally imagined to correct for the exclusion of the photon data set from CabanaBoy because the photon container class does not inherit from PHParticle. However, users have implemented UltraLights for as varied uses as storage for triggered particle types that maintain access to the trigger information and pre-coupling photons into neutral pions for an $\omega \to \pi^0 \pi^+$ analysis.

5.2 Normalization

The event mixing code detailed above generates the combinatorial background at levels above and beyond the measured combinatorial background. The over-production of combinatorial background is done purposefully to ensure that the combinatorial shape is well defined. The generated combinatorial background must be scaled to the level seen in the same event pairs.

The like-sign spectrum serves as a testing ground to establish the background normalizations. It determines the background rates because it consists entirely of background pairs and has no physical signal pairs. The backgrounds are fully removed when the subtracted like-sign spectrum has zero yield. Once this is accomplished the same normalizations are applied to the unlike-sign spectrum. This is possible because the backgrounds are generated at the same rates for the like- and unlike-sign spectra.

Initially we hoped to normalize the combinatorial background by calculating the combinatorial background rate according to pair production rates in the like- and unlike-sign pairs. This calculation results in a combinatorial background yield of $2\sqrt{<N_{--}> \times <N_{++}>}$ where $<N_{--}>$ and $<N_{++}>$ are the mean number of electron-electron and positron-positron pairs respectively. However, this calculation assumes no additional background sources in the like-sign spectra beyond the combinatorial pairs and those removed by the pair cuts, i.e. no correlated backgrounds.

The existence of the correlated backgrounds complicates the background normalizations. The combinatorial background and the two types of correlated background, those from jet sources and those from common ancestor decays, are present in the like-sign yields. The measured like-sign pairs must be parsed into each of the component background sources. The common ancestor correlated background is set using the measured pion signal. Separating the correlated jet background from the combinatorial background is more difficult. First we will discuss the normalization of the common ancestor correlated background. This is followed by a section on the iterative normalization procedure developed to normalize both the jet and combinatorial backgrounds.

5.2.1 Correlated pairs with a common ancestor

The normalization of the common ancestor background is set using the measured pion signal. The background simulation described in Chapter 4 calculates the unlike-sign signal pairs below the η mass in addition to the unlike-sign and like-sign background pairs. The unlike-sign signal pairs are dominated by pion Dalitz decay pairs. These pairs serve as a candle to match the scale of our simulated output with the measured unlike-sign signal in the pion region. The backgrounds in this region are low providing a clean calculation of the scale factor. Once the scaling for the unlike-sign signal is known it can be applied to the unlike- and like- sign backgrounds.
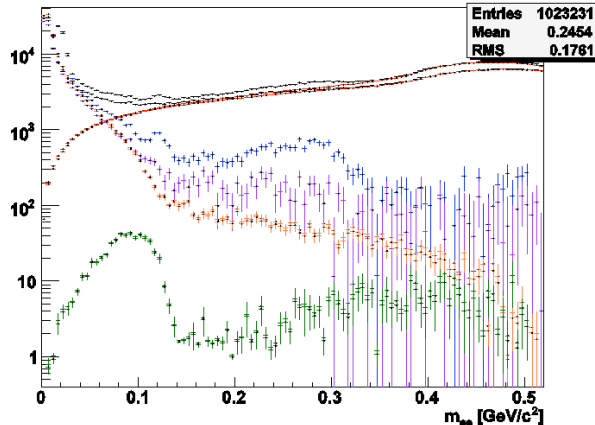
Figure 5.4: The low mass unlike-sign measured signal (black), a roughly normalized combinatorial background (red), and signal minus combinatorial spectra with and without the conversion pair cut (blue, purple) are shown with the unlike-sign multi-lepton pair decay signal (orange) and the unlike-sign multi-lepton pair decay background component (green).

Figure 5.4 shows the unlike-sign measured mass spectra with a roughly normalized combinatorial background and the subtracted spectra with and without the conversion pair cut. The simulated unlike-sign signal and correlated background components are shown at their normalized levels. The subtracted spectra with the conversion pair cut is aligned with the simulated unlike-sign signal. The correlated common ancestor background is consistently an order of magnitude lower than the subtracted spectrum.

5.2.2 Iterative normalization procedure

Once the correlated backgrounds due to a common ancestor are removed we focus on normalizing the remaining two backgrounds, the combinatorial pairs and the jet correlated pairs. While these two backgrounds have very different shapes, their normalizations are inversely correlated. An over-estimate of the correlated jet background may be compensated by an underestimate of the combinatorial background and vice versa. Initially, a χ^2 fit to determine the combinatorial and jet normalizations was attempted. Unfortunately, the data are unable to resolve stable fits with a χ^2 analysis. An iterative procedure determines normalizations that with the background shapes well describe the like-sign spectra.

An initial normalization for the combinatorial background is calculated by taking like-sign integral yields in a region where the simulated like-sign jet background is minimal and the combinatorial background dominates, masses above 0.6 GeV/c^2. An initial jet background normalization is calculated using the measured like-sign yield over the entire like-sign spectrum after subtracting the initially normalized combinatorial background. By

construction, this provides a solution with a zero net yield in the like-sign spectrum.

While the net yield is zero there may be a non-flat like-sign shape. There is often a better solution to describe the like-sign spectra with the combinatorial and jet correlated backgrounds. To determine this we recalculate the combinatorial background normalization. This is done in the same region where it was initially calculated only now we remove the correlated jet background using the previously calculated jet normalization. The jet normalization is recalculated using the new combinatorial background normalization. This procedure is iterated. The general formula for the calculations of the normalizations in the ith iteration is presented in Equation 7.2.

$$N_i^{CB} = \int_R \frac{BG_{LS}^{CB}}{FG_{LS} - N^{DD}BG_{LS}^{DD} - N_{i-1}^{Jet}BG_{LS}^{Jet}}$$
$$N_i^{Jet} = \int \frac{BG_{LS}^{Jet}}{FG_{LS} - N^{DD}BG_{LS}^{DD} - N_i^{CB}BG_{LS}^{CB}} \tag{5.1}$$

where $\int_R$ is the integral over the region above 0.6 GeV/c^2 in mass, N_i^{CB} is the ith combinatorial normalization, the other integrals are over the entire mass and p_T space, BG_{LS}^{CB} is the like-sign combinatorial background, FG_{LS} is the measured like-sign spectrum, N^{DD} is the common ancestor correlated background normalization, BG_{LS}^{DD} is the common ancestor correlated background, N_i^{Jet} is the ith correlated jet background normalization and BG_{LS}^{Jet} is the correlated jet background. Over a thousand iterations are calculated to ensure that the procedure stabilizes. The normalization typically settles within fifty iterations. This procedure considers the effect of the correlated jet background in the like-sign spectra in determining the combinatorial background normalization. Figures 5.5 and 5.5(b) show the combinatorial and jet background normalization parameters as a function of the iteration step for different centralities.

5.3 Subtraction

Once the background normalizations are determined the backgrounds are scaled accordingly and subtracted from the measured pairs, creating the subtracted spectra as described to Equation 5.2.

$$Sub_{LS} = FG_{LS} - N_{CB} * BG_{LS}^{CB} - N_{DD} * BG_{LS}^{DD} - N_{Jet} * BG_{LS}^{Jet}$$
$$Sub_{ULS} = FG_{ULS} - N_{CB} * BG_{ULS}^{CB} - N_{DD}BG_{ULS}^{DD} - N_{Jet} * BG_{LS}^{Jet} \tag{5.2}$$

The like-sign subtracted spectra contains no signal and is flat at zero, confirming that all the backgrounds are at the correct levels. The unlike-sign subtracted spectra contain only signal. These spectra are uncorrected for any of the cut efficiencies or detector deadarea effects. These identification and reconstruction efficiencies will be addressed in Chapter 6.
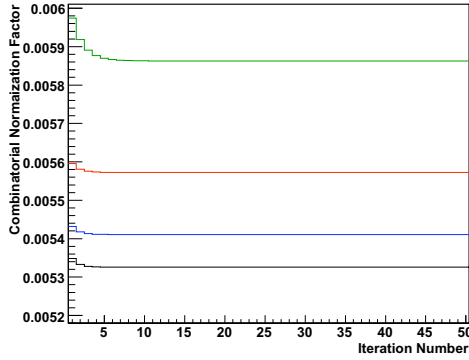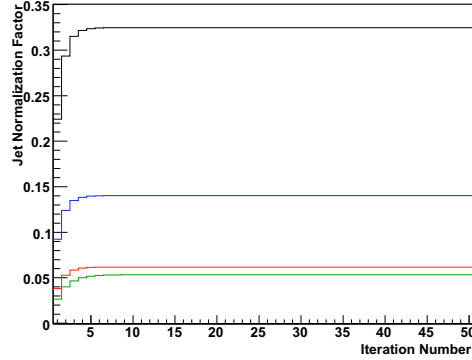
(a) Combinatorial Normalizations   (b) Jet Normalizations

Figure 5.5: The normalization parameters for the combinatorial and jet backgrounds versus the iteration step. The centralities 0-10% (black), 10-20% (blue), 20-40% (red), and 40-94% (green) are shown in different colors.

First we present like-sign background subtracted spectra then the unlike-sign subtracted spectra. Various cross checks on the subtractions are also performed.

5.3.1 Like-sign subtracted spectra

Before the like-sign spectra is background subtracted it is useful to compare the measured like-sign pair spectra to the total background determined by the iterative normalization procedure. Figure 5.6 presents this comparison for each centrality bin. Underneath the primary plot are ratios, R, of the measured like-sign pairs over the total background for each of the centrality groups. The comparison between the measured like-sign pairs and the total background is very good. The ratios are flat as a function of mass and have less than a 5% variation in all of the centralities until the statistics in the measured like-sign pairs leads to large fluctuations. These statistical accuracy decreases at higher masses and in the more peripheral centrality bins. The like-sign spectra has been rebinned into a variable binning in the main plot and before the ratio is calculated in order to reduce the effects due to statistical fluctuations. To confirm that the like-sign spectra is well described by all of the backgrounds we fit the ratio of the measured spectra over the sum of the backgrounds with a horizontal line over the entire mass range and in the region of masses above one GeV/c^2. The fit results are consistent with one in both regions; they are presented in Table 5.1.

Figure 5.7 shows the like-sign subtracted spectra in four centrality bins. In each centrality there is zero signal after the backgrounds have been subtracted. While there are fluctuations in the fully subtracted spectra (blue) the points are consistent with zero. As expected the combinatorial background (red) is the largest background component with the backgrounds
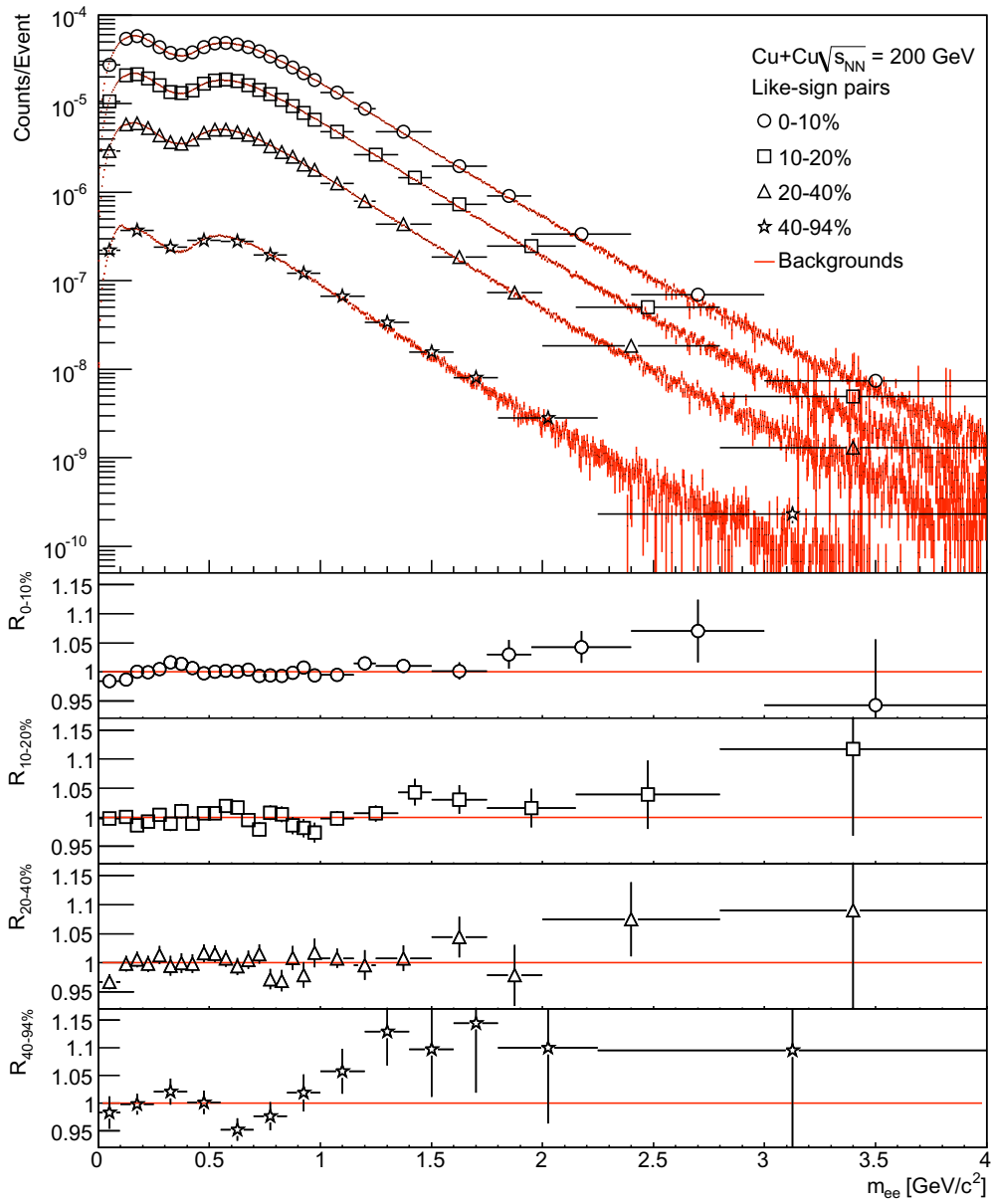
Figure 5.6: Like-sign pairs before background subtraction are shown in black for the various centrality groups. Their respective combined backgrounds are shown in red. The ratio, R, of the like-sign pairs over the background are shown underneath for each of the centralities.

Table 5.1: Flat line fit of the measured like-sign pairs over the total background.

Centrality	Fit parameter for $0 < m < 4$ GeV/c^2	For $1 < m < 4$ GeV/c^2
$0 - 10\%$	0.9998 ± 0.0016	1.0042 ± 0.0047
$10 - 20\%$	0.9995 ± 0.0025	1.0050 ± 0.0072
$20 - 40\%$	0.9992 ± 0.0035	1.0052 ± 0.0100
$40 - 94\%$	0.9951 ± 0.0085	1.0162 ± 0.0172
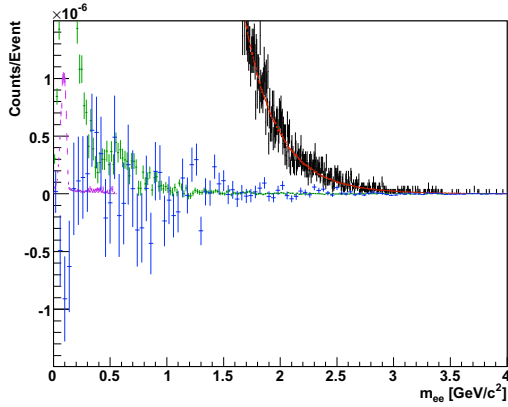
(a) 0-10%
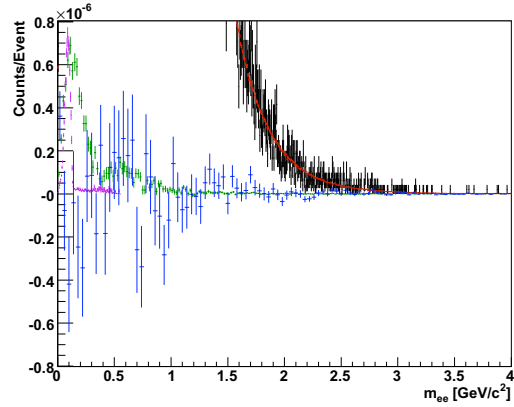
(b) 10-20%
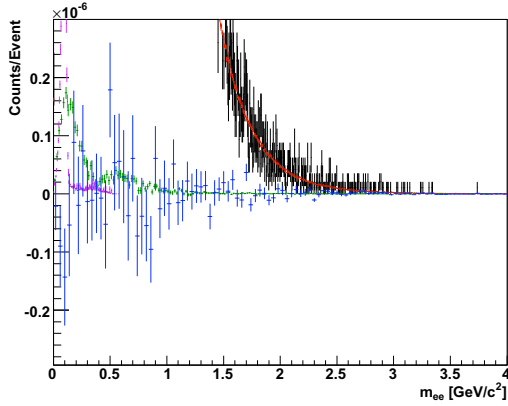
(c) 20-40%
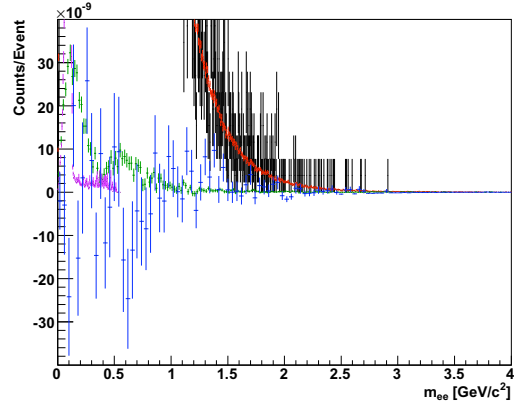
(d) 40-94%

Figure 5.7: The like-sign mass distributions showing the subtraction and backgrounds in each centrality grouping. All pairs are in black, the combinatorial background is in red, the double dalitz component is in purple, the jet background is in green and the fully subtracted data is in blue. Here some of the points have been rebinned to view the plot more easily.

from common ancestor decays and jets (purple and green respectively) contributing primarily at masses below 0.6 GeV/c^2.

(a) 0-10%

(b) 10-20%

(c) 20-40%

(d) 40-94%
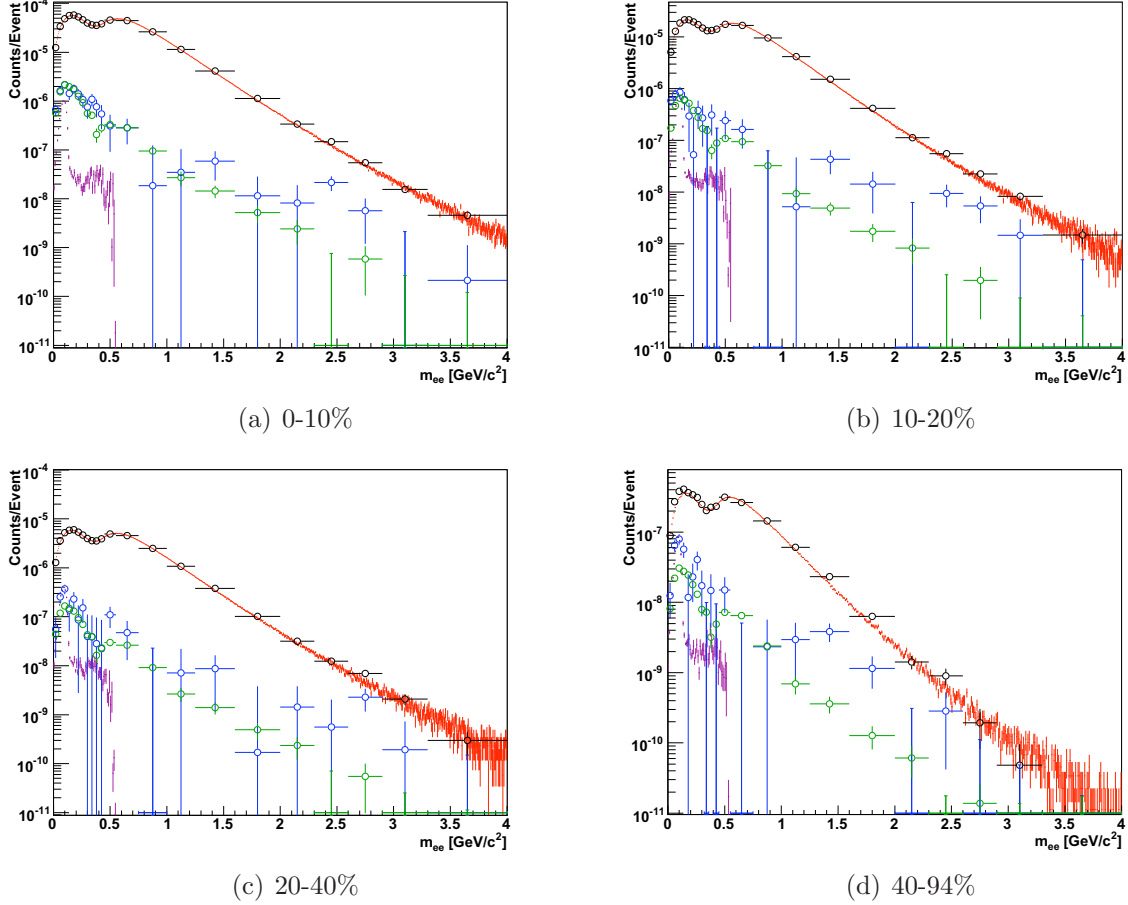
Figure 5.8: The like-sign mass distributions showing the subtraction and backgrounds in each centrality bin. All pairs are black, the combinatorial background is red, the double dalitz component is purple, the jet background is green and the subtracted data, with only the combinatorial subtracted, is blue.

Figure 5.8 shows the contributions from the correlated backgrounds. These plots are the same results with a log scale on the y-axis and variable rebinning at the x-axis. Here the subtraction (blue) is the measured spectra with only the combinatorial background removed; this shows the nice match between the spectra with the combinatorial background removed and the correlated backgrounds. An additional cross-check of the like-sign spectra's description by the backgrounds consists of comparing the mass spectra in various pair p_T slices. This is shown in Figure 5.9 for each centrality in p_T slices 0-5, 0-1, 1-2 and 2-5 GeV/c.

It is apparent that the like sign mass pairs are well described by the total background in each of the p_T groupings for all of the centralities.

(a) 0-10%

(b) 10-20%

(c) 20-40%

(d) 40-94%
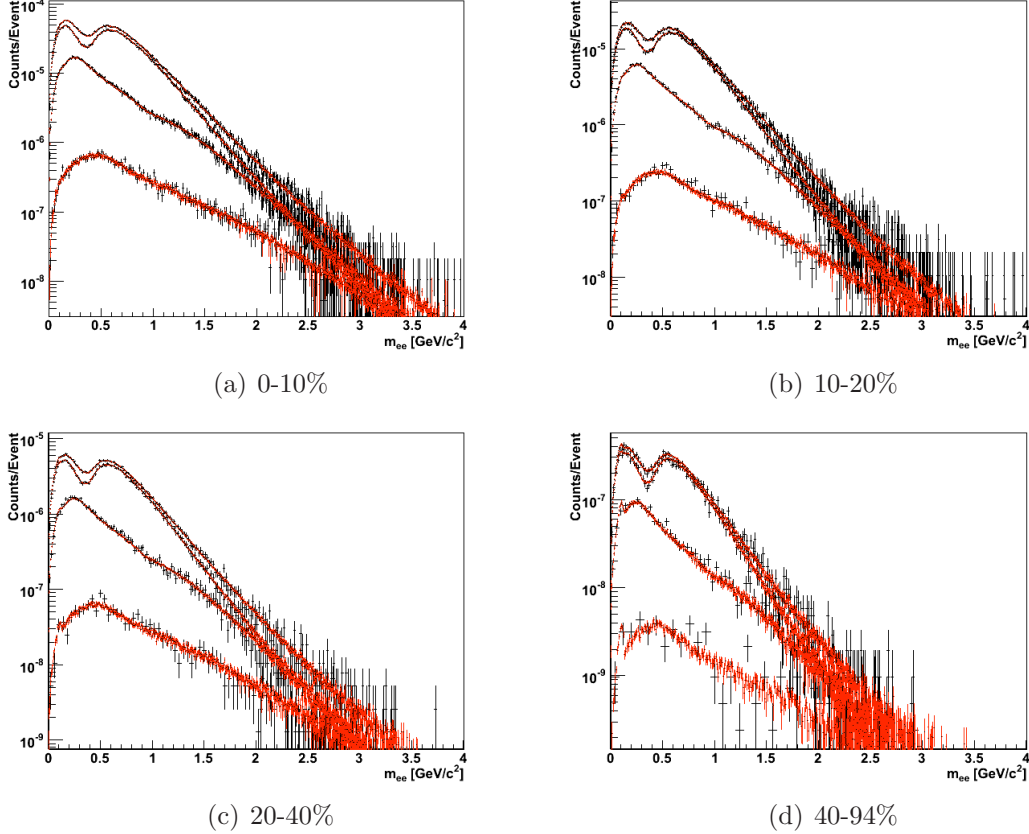
Figure 5.9: The like-sign mass distributions in p_T slices showing the good description of the like sign by the background in each centrality grouping. All pairs are in black, the total background is in red. The top plot is the entire pair p_T range, from 0-5 GeV/c, the next three plots are over the pair p_T ranges 0-1, 1-2, and 2-5 GeV/c.

5.3.2 Unlike-sign subtracted spectra

The unlike-sign spectra are compared to the determined total background. Figure 5.10 shows the spectra for each centrality class. The ratio, R, of the unlike-sign pairs over the total background are presented. The R values provide a shorthand for the signal-to-background ratio for each spectrum. At the lowest masses where there is little background there is a large signal due to pion Dalitz decay. So much so that it requires a log scale. Signal pairs from J/ψ decay create a peak near masses of 3 GeV/c^2. Figure 5.11 provides a more detailed
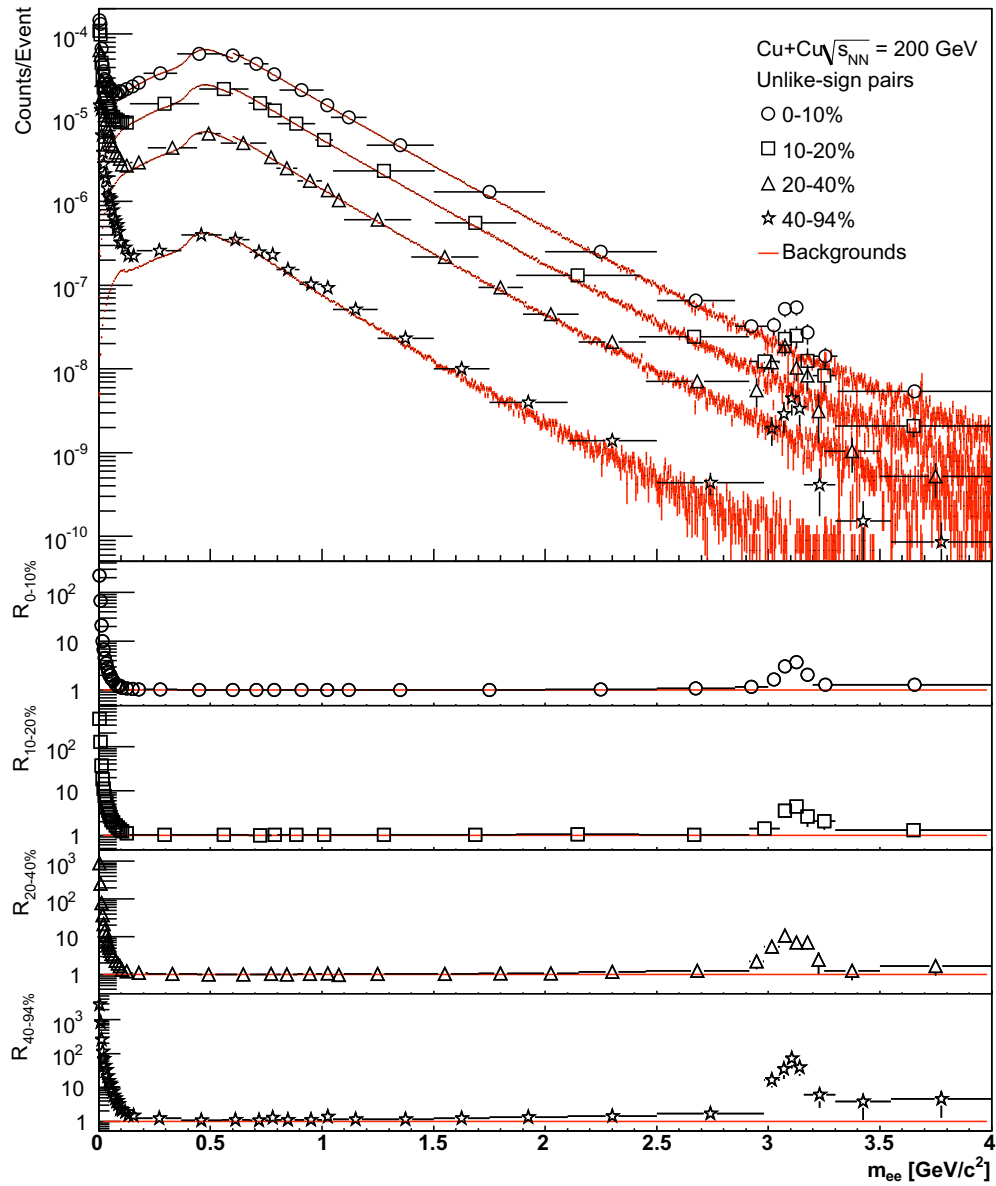
Figure 5.10: Unlike-sign pairs before background subtraction are shown in black for the various centrality groups. The combined backgrounds are shown in red. The ratio, R, of the unlike-sign pairs over the background are shown underneath for each of the centralities.
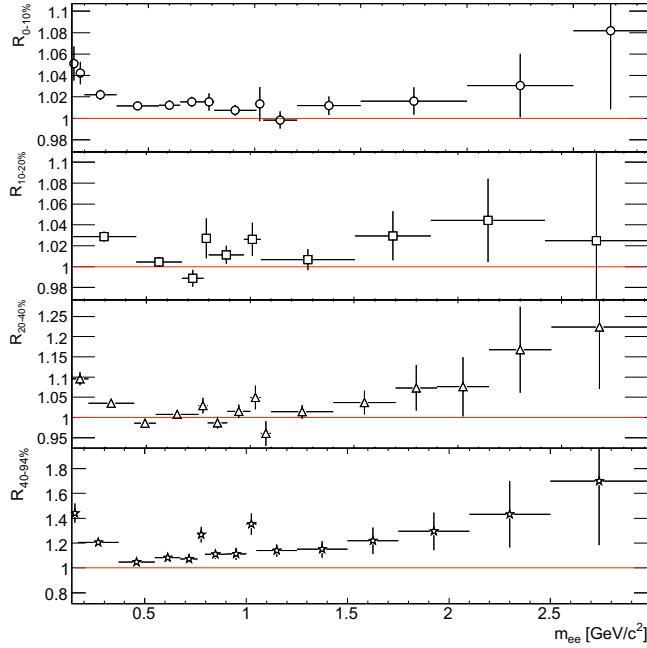
Figure 5.11: Ratio of unlike-sign pairs over total background.

look at the same values on a linear scale zoomed in the mass region between the π and the J/ψ mesons. It is clear that as the mass increases and the backgrounds decrease the signal-to-background rises. The spectrum from more peripheral collisions has a higher signal-to background than more central collisions. This is the result of a decrease in the correlated background production and combinatorial background production rates. The combinatorial background production rates are lower because of the decreased multiplicity in peripheral events.

When the like sign pairs are well described by the backgrounds, the backgrounds are subtracted from the unlike sign pairs. Figure 5.12 shows the unlike-sign spectra in the four centrality bins with the combinatorial background component subtracted (blue). This is the analogous plot to Figure 5.8. The correlated backgrounds (black and purple) are below the subtracted spectra in all cases allowing for the physics signal. Once the correlated backgrounds are subtracted we have the fully subtracted spectra, shown in Figure 5.13. The fully subtracted spectra appears very similar to the subtraction with only the combinatorial background removed. This is because the correlated backgrounds are small compared to the physics signal. As with the like sign spectra we can look at the unlike sign pairs and the total background in different p_T slices, Figure 5.14, showing the total background below all

80

(a) 0-10%

(b) 10-20%

(c) 20-40%

(d) 40-94%
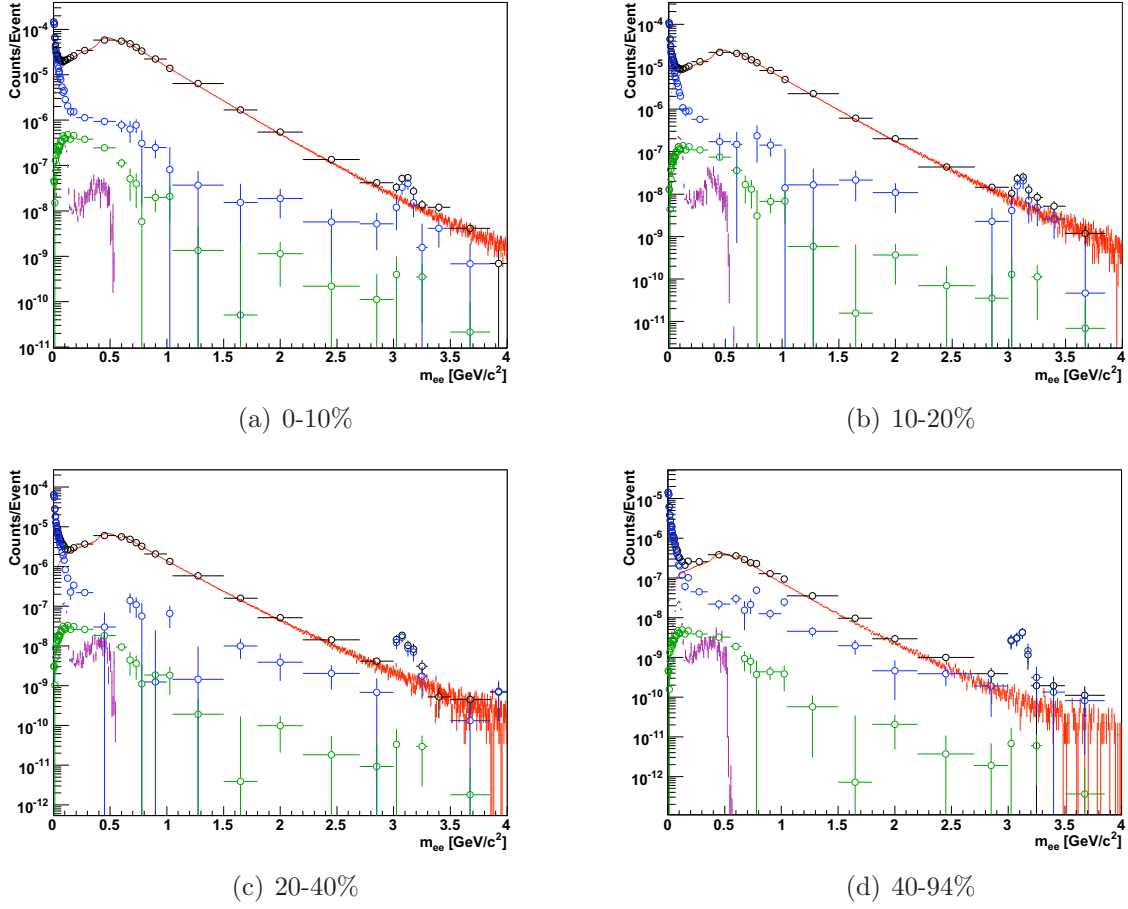
Figure 5.12: The unlike-sign distributions showing the subtraction and backgrounds in each centrality grouping. All pairs are in black, the combinatorial background is in red, the double dalitz component is in black, the jet background is in green and the subtracted data, with only the combinatorial subtracted, is in blue.

of the measured pairs in all p_T groups and for all centralities.

(a) 0-10%

(b) 10-20%

(c) 20-40%

(d) 40-94%
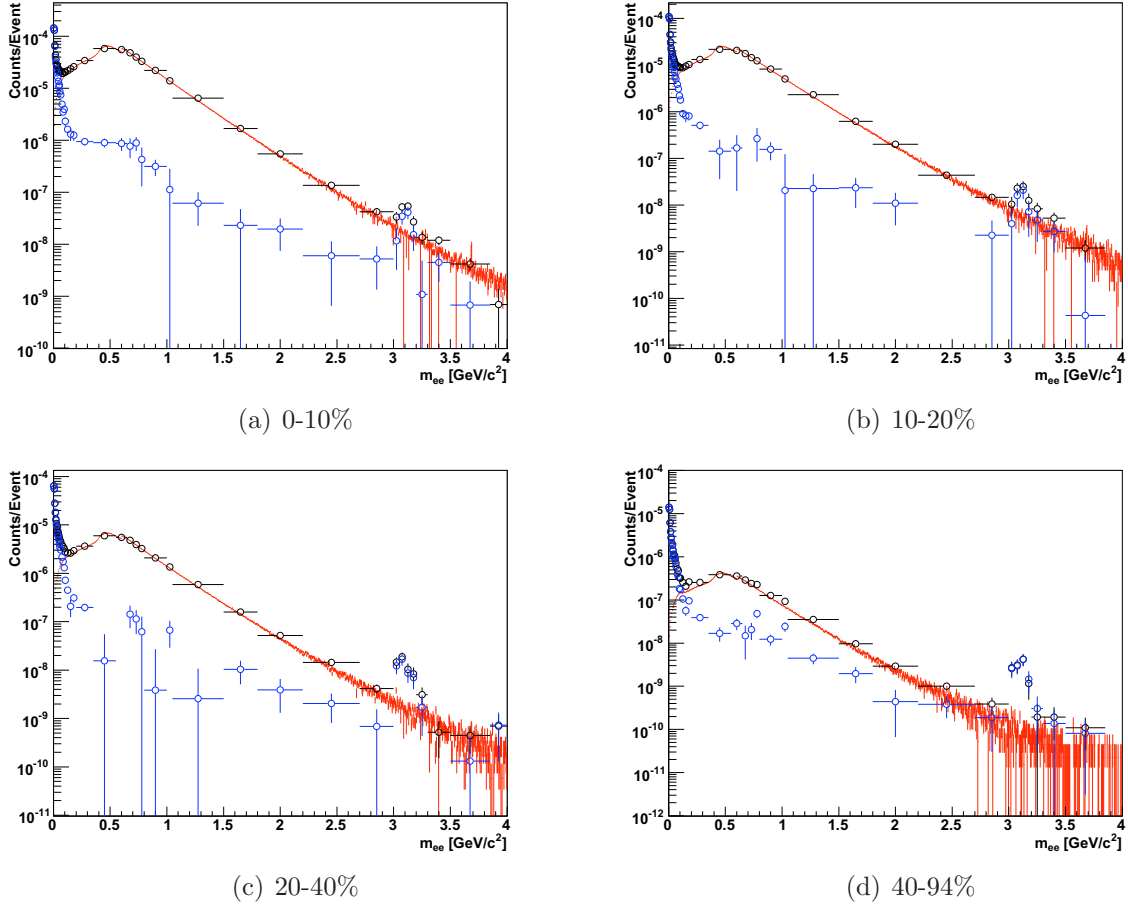
Figure 5.13: The unlike-sign mass distributions showing the unlike sign pairs (black), the total background (red) and the full subtraction (blue) in each centrality grouping.

Minimum Bias

After the subtracted spectra are determined in each of the centrality groups, a spectrum containing all measured centralities, also known as a minimum bias spectrum, is obtained. The minimum bias spectrum is simply the average of subtracted spectra weighted by the size of the centrality groupings. It is preferable to calculate this average after all of the subtractions are made, because variations in background shapes are well understood in the various centrality groupings. Figure 5.15 shows the minimum bias spectrum of dielectron pairs with the spectra in each of the centrality groups. As expected the minimum bias

(a) 0-10%

(b) 10-20%

(c) 20-40%

(d) 40-94%
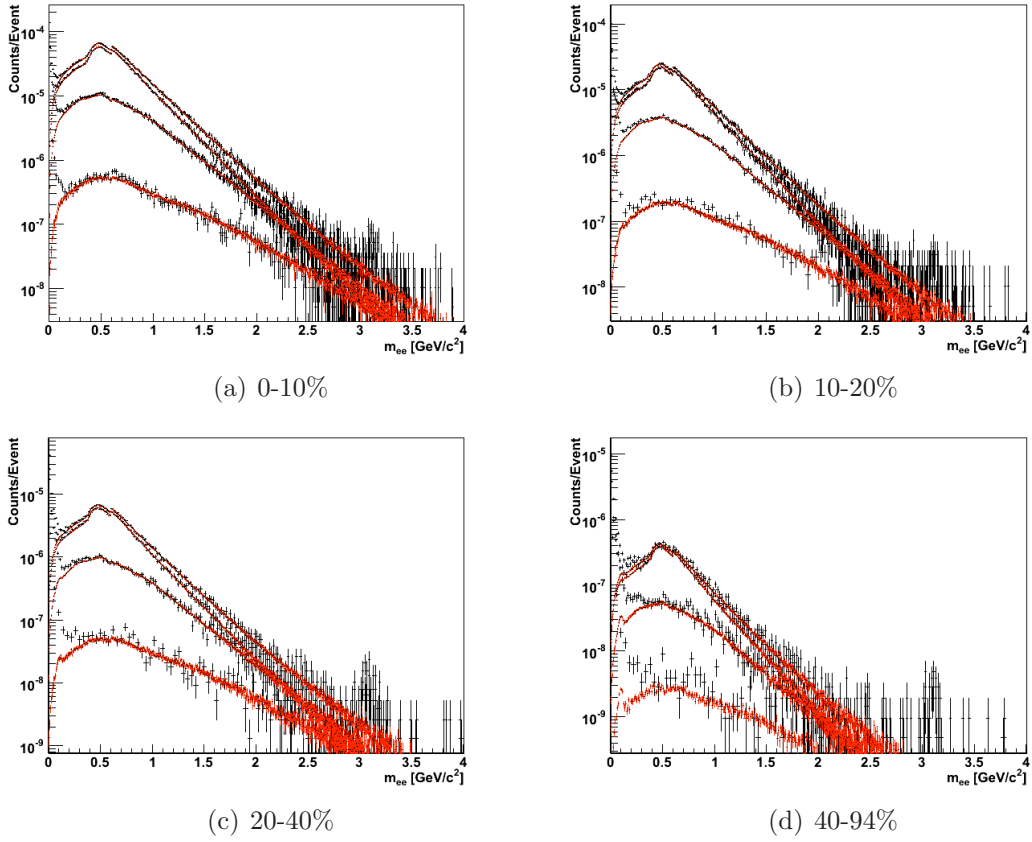
Figure 5.14: The unlike-sign mass distributions showing the unlike sign pairs (black) and the total background (red) in each centrality grouping. The top plot is the entire pair p_T range, from 0 -5 GeV, the next three plots are over the pair p_T ranges 0-1GeV, 1-2GeV, and 2-5GeV

(a) All unlike-sign pairs

(b) Subtracted unlike-sign pairs
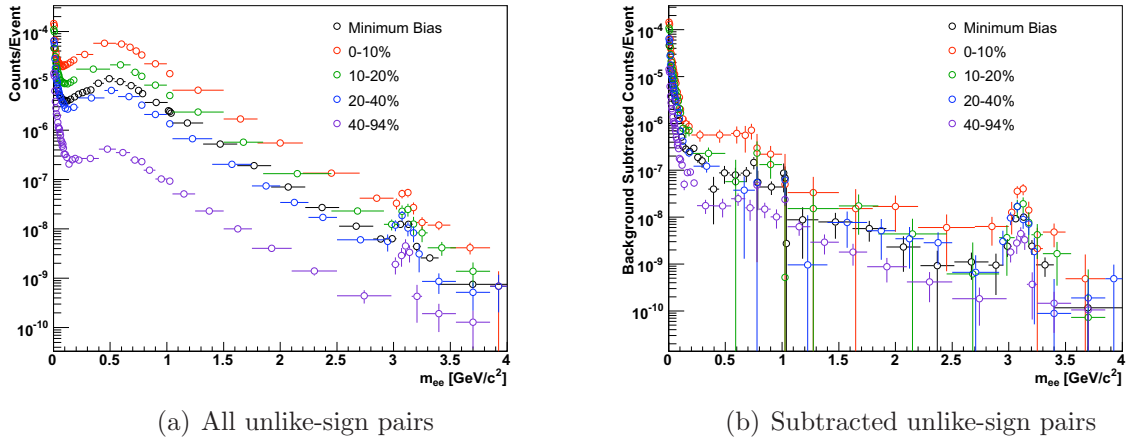
Figure 5.15: The minimum bias unlike-sign mass distributions displayed with the various centrality groupings. Both the background subtracted and unsubtracted spectra are shown.

spectra are located between the 10-20% and 20-40% distributions for both the unsubtracted and subtracted pairs. The minimum bias subtraction is presented in Figure 5.16 where all of the background components are calculated using the weighted average method.

(a) Combinatorial subtraction   (b) Full subtraction
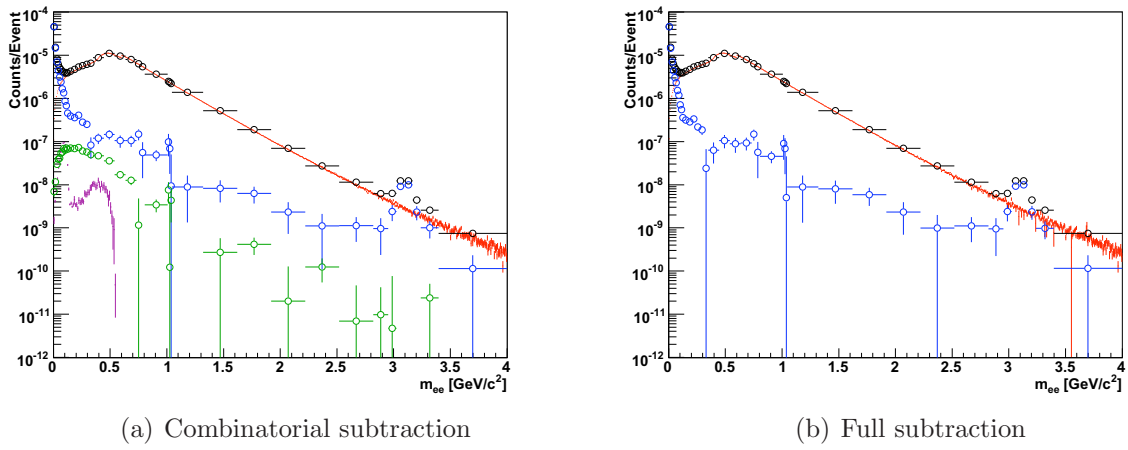
Figure 5.16: The minimum bias unlike-sign mass spectrum with each of the background components. Both images show all of the measured pairs (black) and the combinatorial background (red). On the left only the combinatorial background is subtracted (blue) and the common ancestor (purple) and jet backgrounds (green) are shown. On the right the common ancestor and jet backgrounds are also removed creating the full subtraction spectrum (blue).

Chapter 6

Efficiency corrections

After subtracting the backgrounds, the resulting spectra are corrected for the loss of true electron pairs due to electron identification cuts, pair cuts and lost tracks during reconstruction. The electron identification efficiency adjusts the spectra to include signal pairs from electron tracks that did not satisfy our electron cuts. The pair cut efficiency adjusts the spectra to include the signal pairs that are removed by pair cuts. The reconstruction efficiency corrects for any electrons lost in holes within the ideal PHENIX aperture and other issues preventing track reconstruction.

These corrections allow comparisons between different PHENIX results with different cuts and aperture holes are possible as well as a comparison between the data and the hadronic cocktail of expected dielectron pairs within the ideal PHENIX aperture. It transforms plots of Counts/Event into the invariant mass spectra corrected into the PHENIX acceptance, or dN/dm into the PHENIX acceptance. Equation 6.1 provides a mathematical definition of dN/dm,

$$\frac{dN}{dm} = \frac{Counts}{Event} \frac{1}{\delta m_{ee}} \epsilon \tag{6.1}$$

where Counts/Event is the number of measured pairs after background subtraction divided by the number of events, δm_{ee} is the x-axis bin width in GeV/c^2 and ϵ is the efficiency correction. The efficiency correction is found using a 2005 Cu+Cu PISA Monte Carlo simulation and applied as a function of the pair's mass and p_T.

6.1   Generating electron-positron pairs

Pairs are simulated with a flat distribution in mass, p_T, azimuth and rapidity. They are contained within a larger ϕ and charge/p_T range than the ideal PHENIX aperture, Figure 6.1

Two simulations are used. For both, the rapidities, y, are between positive and negative 0.5 units of rapidity. The first simulation is larger with 20 million events in a mass range
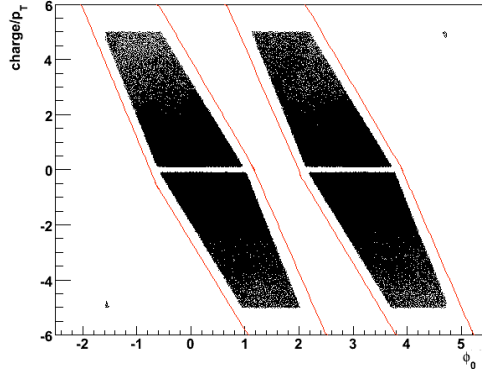
Figure 6.1: Acceptance, ϕ_0 vs. charge/p_T, of the simulated ideal PHENIX aperture overlaid with aperture lines for the generated input in red.

of 0-5 GeV/c^2 and a pair p_T range of 0-8 GeV/c. The second simulation is smaller with 10 million events and in a smaller area, a mass range of 0-2 GeV/c^2 and a pair p_T range of 0-2 GeV/c. The smaller simulation is necessary to increase the statistics in the sensitive region at low masses and low transverse momenta. For each of the simulations the pair mass versus p_T distributions without any cuts beyond the ideal PHENIX aperture is made. This is the generated spectra.

Copies of the simulations are processed to reproduce the effects electrons undergo in the detector, in track reconstruction, in electron identification and pairs cuts. The data-like mass versus p_T spectra is created. The ratio of the surviving pairs over the generated pairs provides the efficiency. In this way the efficiencies for the electron identification, pair cuts and reconstruction are combined into one correction. This correction is applied differentially in the pair's mass and p_T.

6.2 Simulating the detector

The generated pairs are processed through PISA. PISA uses GEANT3 to simulate the particles' interaction with the detector material producing simulated track hit information. A deadmap of the detector dead areas is inserted into the simulated aperture. Reference run 151649 is used to generate the deadmap. Tracks are reconstructed using a code library similar to the data's production library. The simulated track variables are adjusted to reproduce the data's distributions; this includes calibrating the track parameters and applying p_T and mass weights.

Since the simulation is used find the combined efficiency for electron pairs it is important that the simulation faithfully reproduces the data. This is ensured by calibrating the simulation variable distributions to match the data, applying a realistic p_T and mass weights to

87

the simulation and reproducing acceptance effects due to dead areas and detector aperture. First the simulation calibration is discussed followed by the p_T and mass weights and finally a cross-check of the acceptance effects.

6.2.1 Simulation calibration

The following simulated variables are adjusted so that their distributions reproduce the measured distributions:

- $emcsdphi\_e$
- $emcsdz\_e$
- $ecore$/p

Each of these variables have a momentum dependant calibration and are discussed in more detail below.

EMC matching variables

The EMC electron matching variables, $emcsdphi\_e$ and $emcsdz\_e$, are presented together here because the same method is used even though they are calibrated separately. The $emcsdphi\_e$ is calibrated separately for both charges in each of the eight EMC sectors. The $emcsdz\_e$ is calibrated in each sector; there is no discernable difference in the $emcsdz\_e$ distributions of opposite charges. The calibration consists of fitting the variable distributions in momentum slices with gaussian curves. The centers and sigmas of the gaussian fits are plotted as a function of the momentum slice center and fit with Equation 6.2

$$c\left(p\right) = a_0 \left(a_3 - e^{-1*a_1*(p-a_2)}\right)$$
$$\sigma\left(p\right) = b_0 \left(b_2 - e^{-1*b_1*p}\right) \tag{6.2}$$

where $c\left(p\right)$ is the function describing the gaussian centers, $\sigma\left(p\right)$ is the function describing the gaussian widths, p is the slice's momentum center and a_i and b_i are the various fit parameters. These functions were chosen because they reproduce the simulated distributions well and converge at high momentums. The calculated fit parameters are presented in Table 6.1 and Table 6.2. Figures 6.2, 6.3 and 6.4 show the variable distributions with the fits.

As explained in the Chapter 3, the $emcsdphi\_e$ and $emcsdz\_e$ are sigmalized variables. This means that they have gaussian distributions with centers of zero and widths of one. In the data these distributions are required by the recalibration process described in Chapter 3. The simulated data is altered in a similar method to recalibration. Using the fit results from the simulated distributions we alter the simulated variables track by track, subtracting the distribution centers and dividing by the distribution widths from each, presented in Equation

Table 6.1: Fit parameters for *emcsdphi_e* simulated distributions

Arm	Sector	Charge	a_0	a_1	a_2	a_3	b_0	b_1	b_2
0	0	-1	0.085	1.75	1.004	0.970	1.158	5.0	0.869
0	0	1	-0.043	1.75	0.907	-0.947	1.216	5.0	0.835
0	1	-1	0.102	0.55	1.699	0.761	0.891	5.0	1.138
0	1	1	-0.077	1.75	0.701	-0.983	1.081	5.0	0.963
0	2	-1	0.008	1.75	1.951	0.194	1.058	5.0	0.969
0	2	1	-0.096	0.80	1.353	0.313	1.293	5.0	0.795
0	3	-1	0.834	1.75	-0.743	-0.025	1.072	5.0	0.957
0	3	1	-0.043	1.75	1.262	0.785	0.943	5.0	1.067
1	0	-1	0.052	1.75	1.358	0.677	-1.851	5.0	-0.530
1	0	1	-0.025	1.60	1.550	0.027	0.259	5.0	3.815
1	1	-1	0.177	1.75	0.061	-0.805	0.466	5.0	2.525
1	1	1	-0.123	1.75	0.584	1.160	2.676	5.0	0.455
1	2	-1	0.042	1.52	1.542	-1.192	1.271	5.0	0.804
1	2	1	-0.100	0.53	1.534	0.756	0.618	5.0	1.670
1	3	-1	0.023	1.75	1.166	-2.124	0.380	2.4	2.634
1	3	1	-0.078	1.75	0.369	0.867	0.659	5.0	1.563

Table 6.2: Fit parameters for *emcsdz_e* simulated distributions

Arm	Sector	a_0	a_1	a_2	a_3	b_0	b_1	b_2
0	0	0.172	0.48	3.148	0.002	1.615	1.1	1.577
0	1	13.555	0.65	-8.240	0.0001	1.378	1.0	1.824
0	2	0.008	0.45	2.766	-1.143	1.685	1.2	1.483
0	3	22.523	-0.0004	-85.133	1.038	1.497	1.0	1.687
1	0	28.197	8.94	-0.192	-0.001	1.256	0.9	1.978
1	1	27.466	3.00	-1.148	-0.0004	1.428	1.1	1.739
1	2	6.577	1.75	-2.124	-0.008	1.611	1.1	1.557
1	3	3.491	1.25	-2.805	-0.013	1.386	1.0	1.803

(a) Arm 0 Sector 0   (b) Arm 0 Sector 1

(c) Arm 0 Sector 2   (d) Arm 0 Sector 3

(e) Arm 1 Sector 0   (f) Arm 1 Sector 1

(g) Arm 1 Sector 2   (h) Arm 1 Sector 3

Figure 6.2: The simulated electron *emcsdphi_e* vs. momentum distributions. The red points are the centers. The black lines are the functions of the fit of the center values as a function of momentum and two lines representing the two sigma cuts above and below.

90

(a) Arm 0 Sector 0

(b) Arm 0 Sector 1

(c) Arm 0 Sector 2

(d) Arm 0 Sector 3

(e) Arm 1 Sector 0

(f) Arm 1 Sector 1
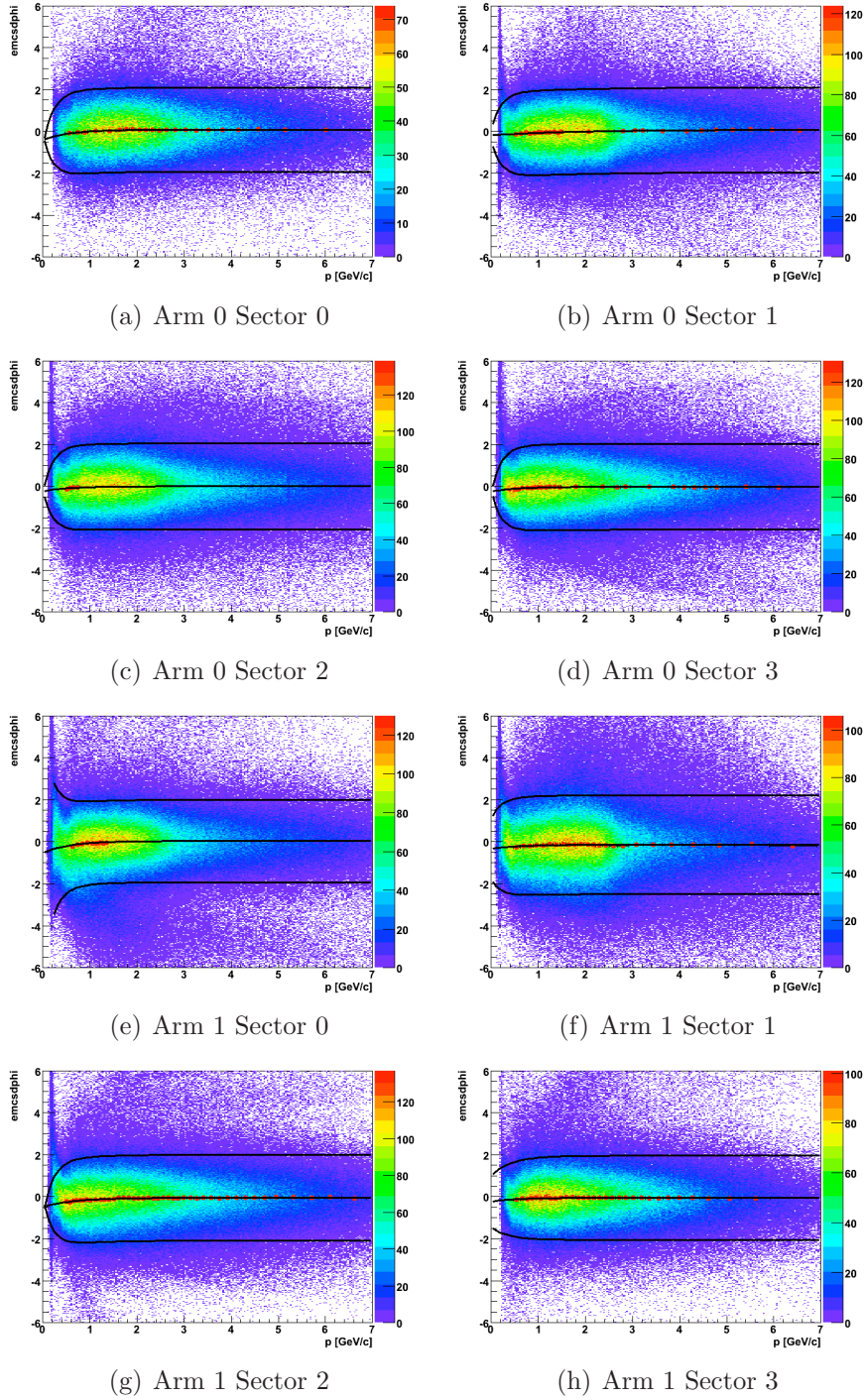
(g) Arm 1 Sector 2

(h) Arm 1 Sector 3

Figure 6.3: The simulated positron *emcsdphi_e* vs. momentum distributions. The red points are the centers. The black lines are the functions of the fit of the center values as a function of momentum and two lines representing a two sigma cut above and below.

(a) Arm 0 Sector 0   (b) Arm 0 Sector 1

(c) Arm 0 Sector 2   (d) Arm 0 Sector 3

(e) Arm 1 Sector 0   (f) Arm 1 Sector 1

(g) Arm 1 Sector 2   (h) Arm 1 Sector 3

Figure 6.4: The simulated *emcsdz_e* vs. momentum distributions for electron and positrons. The red points are the centers. The black lines are the functions of the fit of the center values as a function of momentum and two lines representing a two sigma cut above and below.
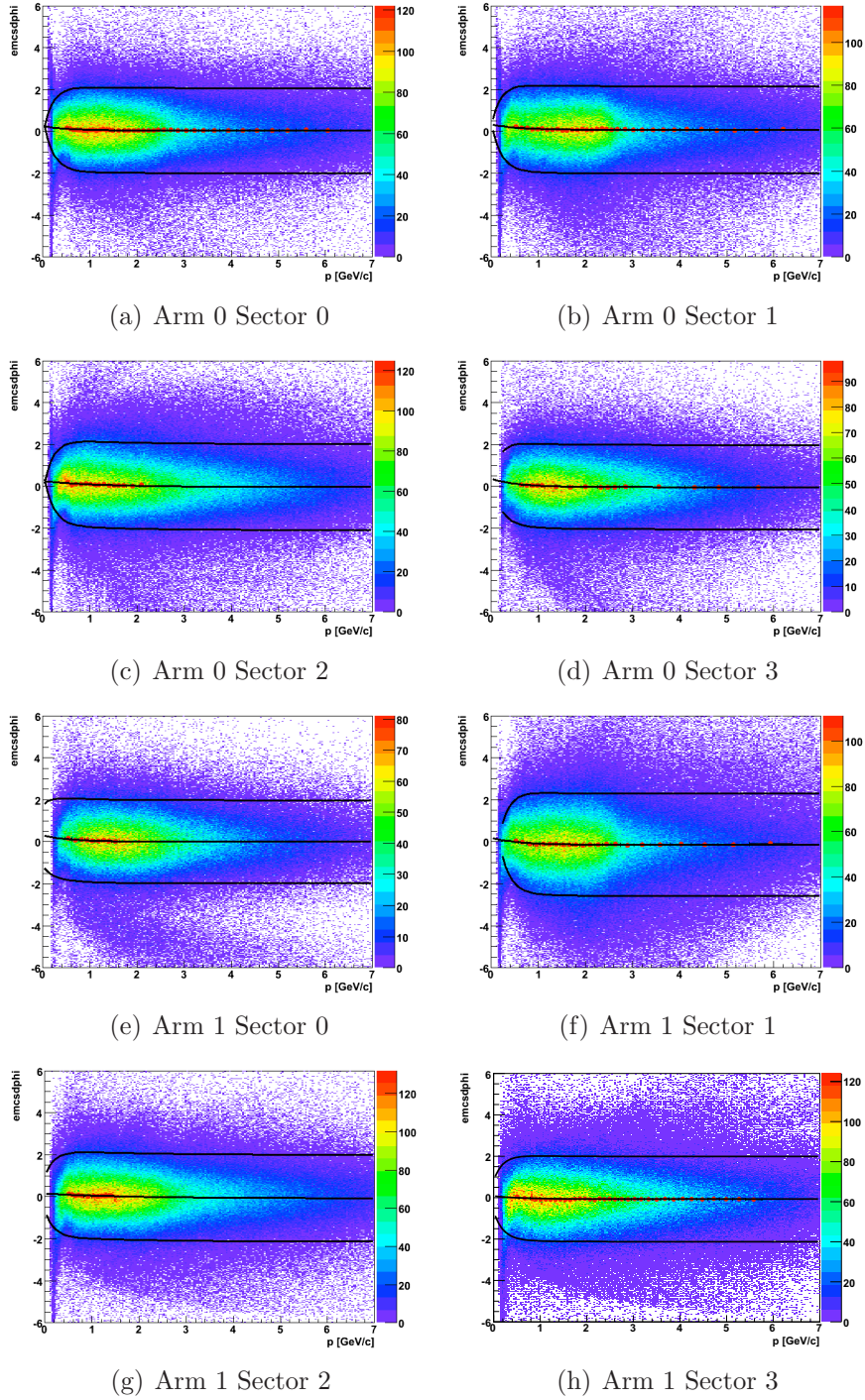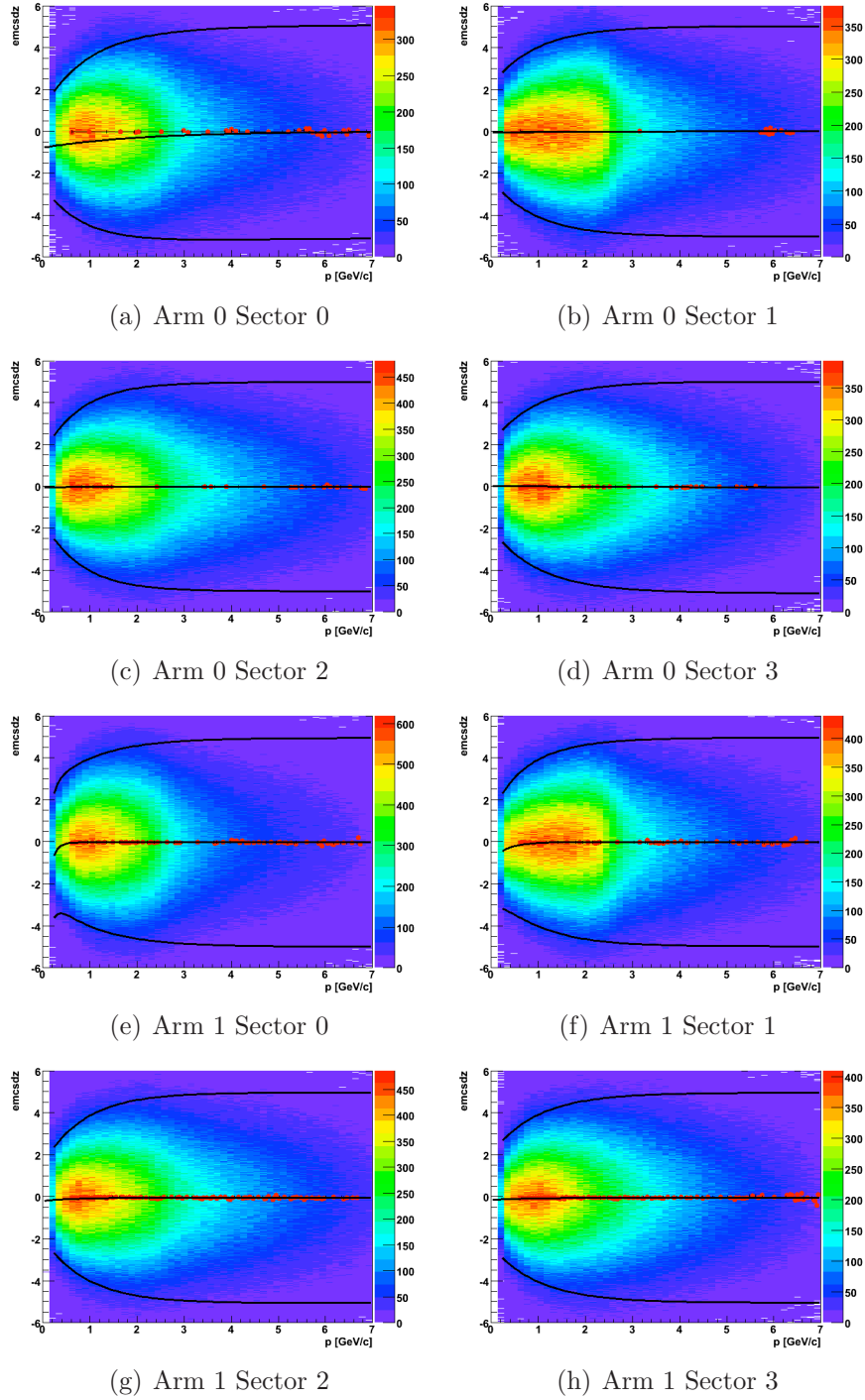
92

$$emcsdphi\_e' = \frac{(emcsdphi\_e - c_{sdphi}(p))}{\sigma_{sdphi}(p)}$$

$$emcsdz\_e' = \frac{(emcsdz\_e - c_{sdz}(p))}{\sigma_{sdz}(p)} \tag{6.3}$$

where *emcsdphi_e'* and *emcsdz_e'* are the corrected simulation variables, *emcsdphi_e* and *emcsdz_e* are the uncorrected simulation variables. The $c_{sd*}(p)$ and $\sigma_{sd*}(p)$ are the centers and sigmas calculated from Equation 6.2 using the simulated track momentum as the input. This creates the desired data-like distributions of the simulation for the EMC matching variables. This is a minor adjustment for *emcsdphi_e*. The *emcsdz_e* distributions were made narrower by approximately a factor of two.

Energy over momentum

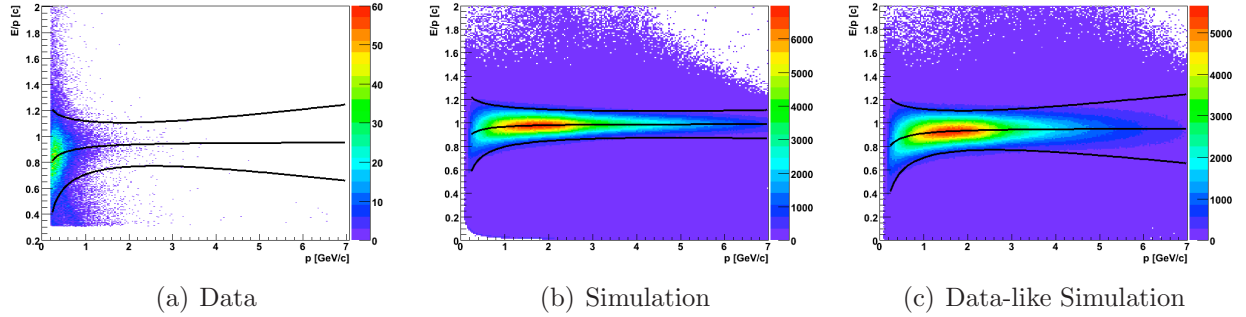(a) Data   (b) Simulation   (c) Data-like Simulation

Figure 6.5: The energy over momentum distributions plotted as a function of momentum for electron and positrons in data, simulation and the adjusted data-like simulation. The black lines are functions of the peak center values and plus and minus two sigma using the respective fit results. The lines in the data and data-like simulation plots are identical.

Adjusting the energy over momentum, *ecore*/p, distributions is more complicated. This variable's distribution in the data is not as simply described. Instead we calculate the parameters necessary to calibrate the *ecore*/p for both the data and simulation, creating *ecore*/p distributions where the electron identification peak centers at zero and has a width of one. This is done by a series of gaussian fits in p_T slices. The extracted offsets and widths are plotted and fit as a function of p_T and fit according to Equations 6.4

$$c(p) = a_0 \left(1 - e^{-1*a_1*p^{a_2}}\right)$$

$$\sigma(p) = \sqrt{\left(b_0 + b_1/\sqrt{E}\right)^2 + b_2^2 p^2} \tag{6.4}$$

where $c(p)$ is the function describing the peak centers, $\sigma(p)$ is the function describing the peak widths, p is the slice's momentum center and a_x and b_x are the various fit parameters. The parameters characterizing the peak widths are the detector resolutions, $b_0 + b_1/\sqrt{E}$ characterizes the EMC resolution and $b_2 p$ describes the DC resolution. Table 6.3 presents the calculated parameters for data and simulation. The data determined EMC and DC resolutions are in agreement with the known detector response. In contrast the simulation's DC resolution, while a good fit, is below the DC detector's resolution. These functions fit the data and the simulation well as seen in Figure 6.5. Once this information in known, the

Table 6.3: Fit parameters for $ecore$/p distributions

Source	a_0	a_1	a_2	b_0	b_1	b_2
Simulation	0.9913	3.8115	0.3046	0.0188	0.0665	0.006
Data	0.9535	3.1354	0.3442	0.0111	0.0903	0.020

simulation is altered to produce the data's distribution by first transforming it to the sigmalized value and then applying the inverse of the data's calibration. This is done according to Equation 6.5,

$$eop' = \left(\frac{eop - c_{sim}(p)}{\sigma_{sim}(p)} \right) * \sigma_{data}(p) + c_{data}(p) \tag{6.5}$$

where eop is a short hand for the simulation's $ecore$/p and eop' is the simulation's corrected data-like $ecore$/p. The $c_i(p)$ and $\sigma_i(p)$ are functions that calculate the offsets and widths for the fits to the data and simulation respectively according to the functional form Equation 6.4. The resulting energy over momenutum versus momentum distribution is shown in Figure 6.5.

6.2.2 Mass and p_T weights

The simulated pairs are thrown with flat mass and p_T distributions, this ensures our ability to populate the entire of the mass and p_T phase space. However the dielectron spectra fall very steeply in mass and p_T. The simulation is weighted as a function of the mass and p_T to account for the effect of the steeply falling distributions. The known hadronic mass and p_T spectra from the simulated cocktail discussed in Chapter 9 are used to obtain the mass and p_T weights. The hadronic cocktail does not have the PHENIX acceptance applied and narrowly peaked resonances (ω, ϕ, J/ψ, ψ') are removed to ensure that the detector resolution effects are not included. The weights are obtained by fitting the cocktail's pair p_T spectra with a modified Hagedorn distribution, Equation 6.6, in mass slices.

$$w(p_T) = A * p_T \left(e^{-1\left(ap_T + bp_T^2\right)} + p_T/p_0 \right)^{-n} \tag{6.6}$$
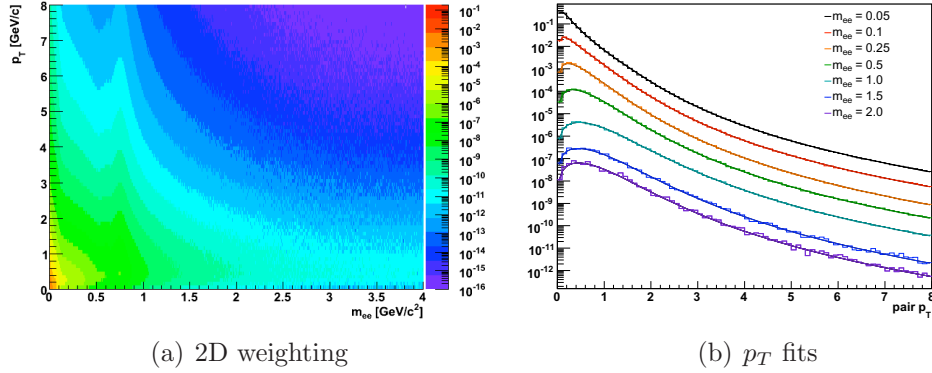
(a) 2D weighting   (b) p_T fits

Figure 6.6: The generated hadronic components in mass vs. p_T used to determine the weighting. The p_T distributions and fits for select masses.

where, $w(p_T)$ is the weight and the five parameters (A, a, b, p_0, n) characterize the p_T function in each mass slice. In this way we create a family of curves, $w_m(p_T)$, all with the same functional form but with different sets of parameters (A, a, b, p_T, n) depending on the mass. The mass determines which function, $w_m(p_T)$, is applied and the p_T is the value used to evaluate the function. By fitting mass slices ten times smaller than the mass bin widths in the measured data we account for the data's steeply falling spectra over the data's mass bins. Figure 6.6 shows the hadronic spectrum used to determine the weights and histograms of the simulated p_T distributions in mass slices with their fits.

6.2.3 Checking the acceptance

As a cross-check on our simulation we compare the simulated acceptance with the reference run's acceptance. The weighted simulation's acceptance is compared to the measured aperture. Figures 6.7 and 6.8 show comparisons between the weighted simulation and data acceptances. Figure 6.7 presents the acceptance phase space in ϕ_0 versus the charge over p_T of the leptons. Figure 6.8 shows the acceptance distribution in the ϕ measured at the DC, ϕ_{DC}. Both show a good agreement between the measured data and the simulation. The ϕ_{DC} distribution is more dependent on the simulation's weighting.

6.3 Applying the correction to the data

6.3.1 The efficiency correction

The simulated data is plotted as a function of the pair's mass versus p_T with and without the dead areas and various cuts applied for both the large and small simulations. The large

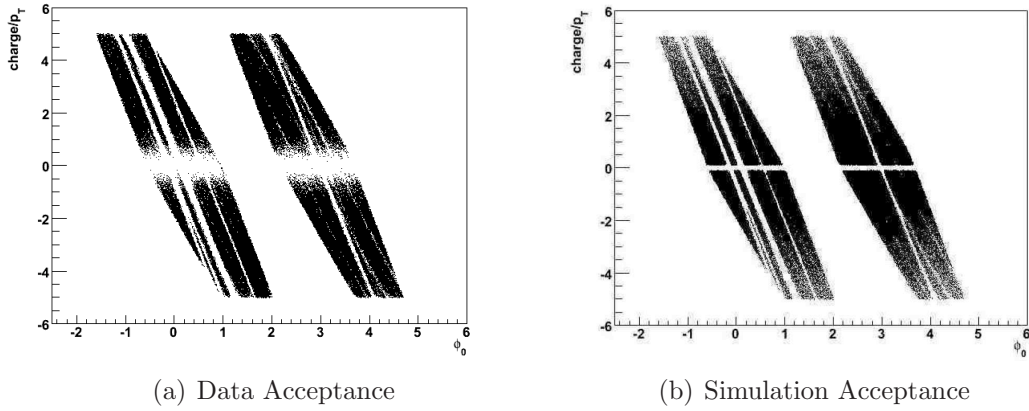(a) Data Acceptance   (b) Simulation Acceptance

Figure 6.7: The ϕ_0 vs. charge/p_T of leptons in the reference run, 151649, and the simulation after applying the fiducial cuts and ideal PHENIX aperture.
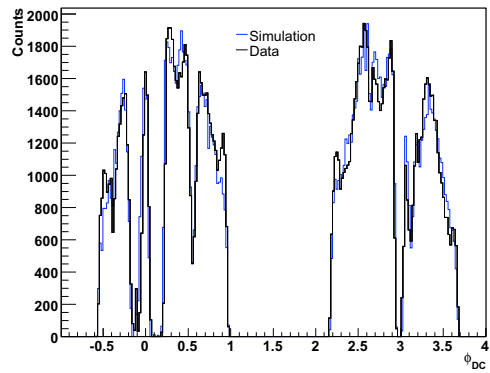

Figure 6.8: The drift chamber ϕ distributions for the data (blue) and the weighted simulation (black).

96

and small simulations are combined with and without the cuts applied. Figure 6.9 shows the combined simulations with and without the weighting applied and with and without the cuts applied.
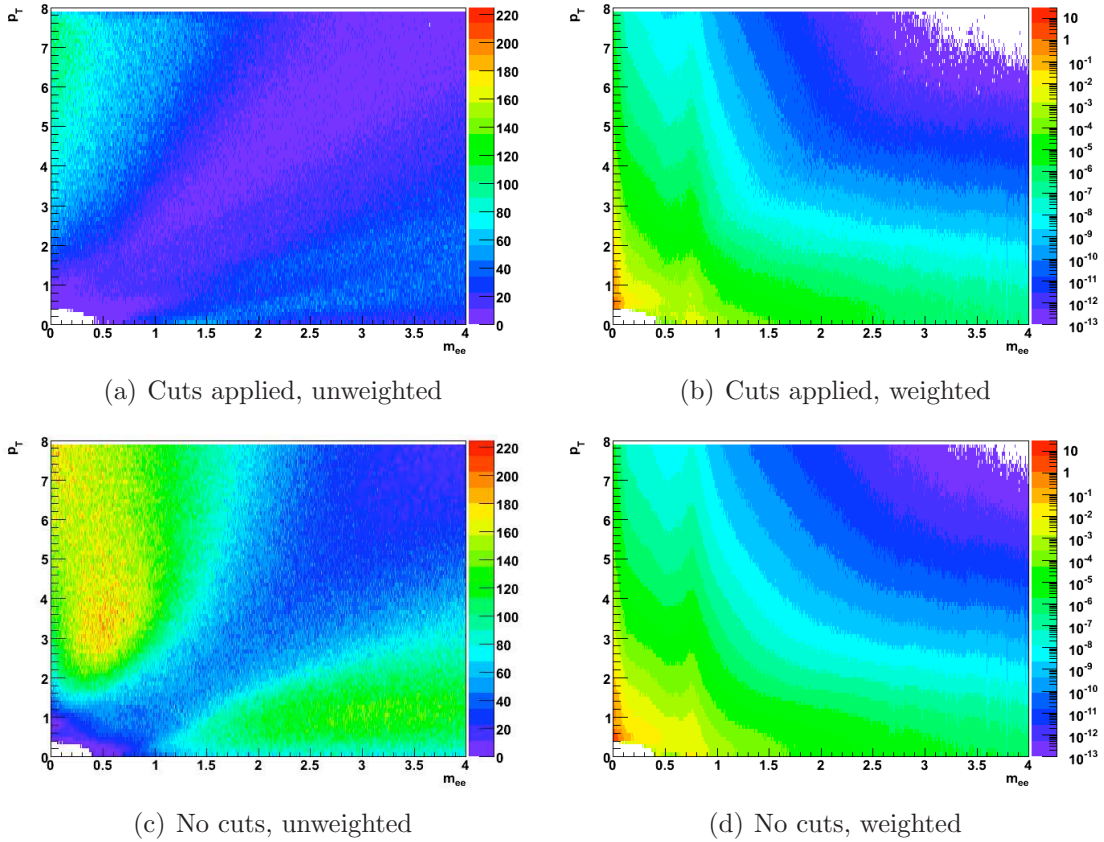

(a) Cuts applied, unweighted

(b) Cuts applied, weighted

(c) No cuts, unweighted

(d) No cuts, weighted

Figure 6.9: The simulated mass vs. p_T with and without the weighting applied. The simulation with and without the acceptance and aperture cuts is shown.

The efficiency is determined by taking the ratio of the combined simulations with the cuts applied over those without cuts. The inverse of the efficiency is applied to the spectra to correct for the reduced yield as a result of the efficiency. Figure 6.10 shows efficiency as a function of mass and p_T with some rebinning as it extends to higher mass and p_T values. Because it is often difficult to conceptualize the two dimensional correction Figure 6.11 shows the effect of the efficiency correction in the mass and p_T axes. The combined efficiency correction and that for the conversion pair cut, the electron identification and reconstruction efficiency are presented.

The same efficiency correction is applied to the subtracted spectra in each of the centrality bins. Figure 6.12 shows the subtracted spectra with and without the efficiency correction
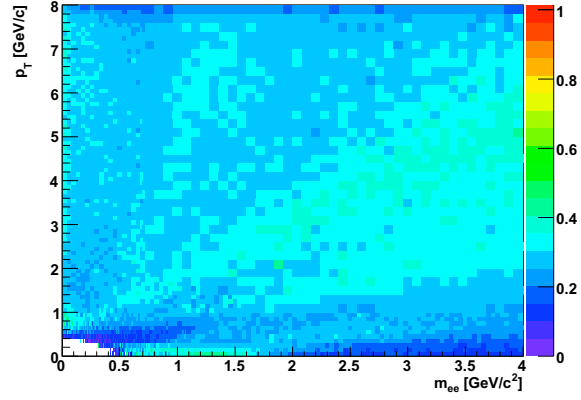
Figure 6.10: The efficiency as a function of mass and p_T.

(a) mass

(b) p_T
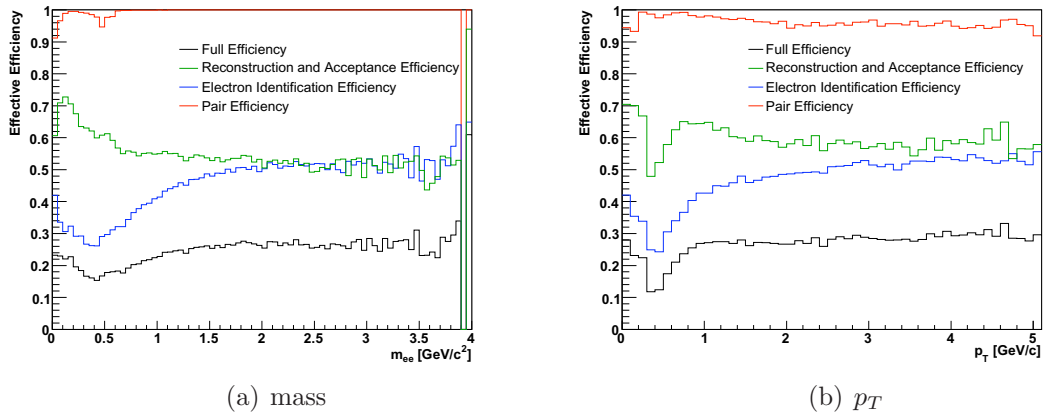
Figure 6.11: The ratio of the uncorrected mass spectra over the corrected mass spectra as a function of mass and p_T. The effective efficiency for the various corrections are applied and the total is also shown. This provides an effective understanding of the efficiency correction in each dimension.

applied for each of the centrality groupings. The comparison of the corrected and uncorrected spectra displays the effect of the two dimensional efficiency correction has on the mass spectra.

Figure 6.12: The mass spectra in each centrality grouping and in the minimum bias with (circles) and without (squares) the efficiencies applied.

Chapter 7

Systematic Errors

To understand the meaning of the efficiency-corrected background subtracted spectra we need to know the systematic errors inherent in this analysis. Systematic errors 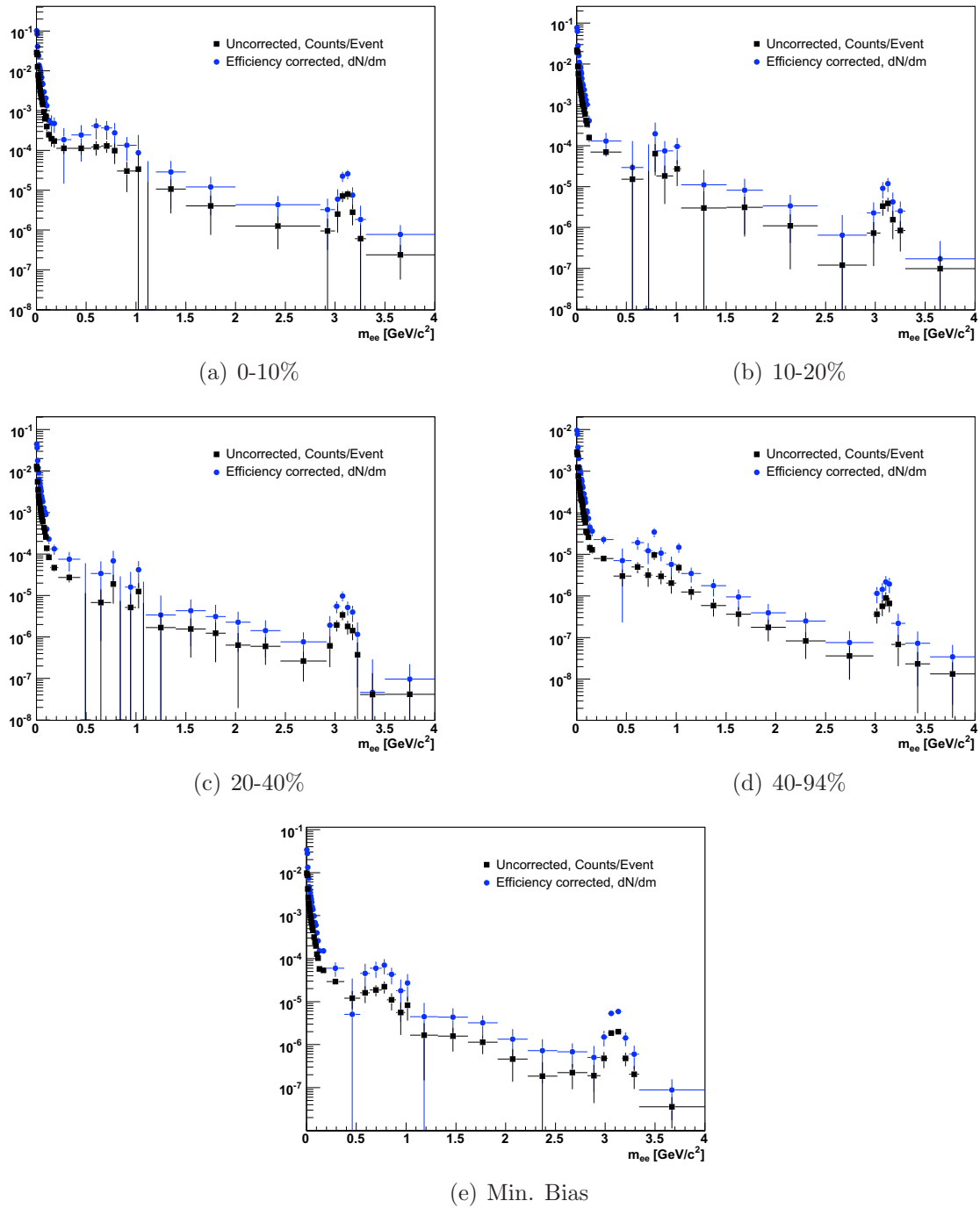result from the efficiency correction and background subtraction including both the background normalizations and shapes. First the efficiency correction systematic errors are presented. The systematic errors for the background subtraction for each of the background sources, combinatorial, jet and common ancestor are then discussed. Each of these systematic errors are combined to produce the systematic error for the mass spectra. The effect of the component background variation on the iterative normalization procedure is also studied.

7.1   Efficiency correction systematic errors

The systematic errors from the efficiency correction are based on the simulation's measurement of the acceptance and the single electron efficiency. The systematic error in determining the pair cut efficiencies are presented. These are combined with additional systematic errors that take into account occupancy effects, the charm acceptance and centrality determination. First the systematic error from the simulation's acceptance is discussed. The systematic error from the single electron identification efficiency is then presented. Finally each of these systematics are combined into the efficiency correction's total systematic error for electron pairs.

7.1.1   Error from the simulation's acceptance

The systematic error on the simulation's acceptance is determined by comparing the ϕ_{DC} distribution in the simulation to the same distribution in the data. Run 151649 is used as a reference run for the data comparison and the simulation is p_T weighted. Figure 6.8 shows the comparison of the two ϕ_{DC} distributions where the simulation is scaled to match the data using the entire ϕ_{DC} area. The systematic error is calculated by comparing the ratio of

Table 7.1: Systematic error of simulated acceptance

Normalization region	Error
$\phi_{DC} \in$ [-0.52, -0.22]	1.79%
$\phi_{DC} \in$ [0.22, 0.52]	2.84%
$\phi_{DC} \in$ [0.56, 0.86]	2.69%
$\phi_{DC} \in$ [2.41, 2.62]	1.45%
$\phi_{DC} \in$ [3.24, 3.54]	1.91%
Simulation Acceptance Error	2.84%

Table 7.2: Systematic error of simulated single electron identification cuts.

Cut	error
quality cut	3.26%
EWG cut	6.95%
p_T cut	0.00004%
disp cut	0.001%
Chisq cut	3.96%
EMC matching cut	0.07%
ecore	0.04%
n0 cut	0.14%
E/p cut	0.28%
quadrature sum	8.64%

yields in five different regions of the ϕ_{DC} distribution. These are presented in Table 7.1. The systematic error of the simulation's acceptance is the largest variation; an error of 2.84%.

7.1.2 Error from the electron identification

The systematic error on the simulation's electron identification efficiency is calculated by determining the loss of each electron identification cut and assuming that half of the loss is the error for each cut. Each of these errors are summed in quadrature resulting in the systematic error on the single electron identification efficiency. The systematic errors for each cut and the combined electron identification efficiency systematic error are presented in Table 7.2. The systematic error from the single electron efficiency, 8.64%, is doubled giving the systematic error in the electron efficiency of the pair, 17.29%.

Table 7.3: The systematic error of the simulated pair

Source	Region	Error
Pair e^- ID cuts	All	17.29%
Occupancy	All	3%
Acceptance	All	2.84%
Charm acceptance	m > 0.5	5%
Centrality	All	10%
Conversion pair cut	m < 0.6	6%
Overlap pair cut	0.4 < m < 0.6	5%
Total	m < 0.4	21.26%
Total	0.4 < m < 0.5	21.84%
Total	0.5 < m < 0.6	22.41%
Total	m > 0.6	21.00%

7.1.3 Error of the simulated pair

The systematic errors from the simulated pairs consist of twice the single electron error summed in quadrature with the acceptance error, the pair cut errors and additional errors due the centrality selection and occupancy effects. These errors and their sums in various mass ranges are listed in Table 7.3. The systematic error on the pair cuts are estimated as 5% and 6% for the conversion and detector overlap pair cuts respectively. These systematic errors take into account the ability of the simulation to determine their efficiency correctly and the likelihood that backgrounds are not fully removed by the cuts. The occupancy or embedding systematic error, 3%, considers the effect that high particle density has on the reconstruction algorithm and therefore the electron efficiency. It is calculated by doubling the single electron embedding efficiency which is determined by placing one simulated electron track in a real heavy ion event. The charm acceptance systematic error, 5%, considers the different kinematics in a heavy quark correlated pair and the resulting variation in their acceptance compared to the hadron decay pairs considered by the simulation. An additional 10% systematic error represents the accuracy of the centrality determination. These additional systematic error values are based on earlier determinations in the p+p and Au+Au dielectron analyses [40].

7.2 Subtraction systematic errors

The systematic errors for the background subtraction consider the errors in the generated background shapes and normalizations. Since there are three background types, the errors in the normalizations and shapes are considered for each. First the common ancestor background shape and normalization systematic errors are introduced. Then the system-

atic errors for the jet and combinatorial background normalizations are presented. This is followed by a discussion of the systematic errors due to shape variations in the jet and combinatorial backgrounds. Finally the effects of the background shape variations on the iterative normalization procedure are studied.

7.2.1 Common ancestor background errors

The common ancestor systematic error consists of the normalization error and the shape error. First the normalization error is presented followed by the shape error. These errors are then summed in quadrature and applied to the common ancestor background component and propagated to the subtracted spectra.

Common ancestor background normalization error

The normalization systematic errors are calculated by propagating the statistical errors of the yields in the normalization calculations. Each of the background normalizations are integrated yields in regions of the like-sign data's phase space relative to the generated backgrounds.

The common ancestor background is normalized using a portion of the measured pion yield. The size of the common ancestor background is known relative to the generated pion Dalitz yield; this was discussed in Chapter 4. The normalization is calculated using the ratio of the generated pion dalitz pairs to the measured unlike-sign pion dalitz spectrum in the mass region 0 - 0.05 GeV/c^2 where pion dalitz decays dominate. The same normalization is applied to the common ancestor background. The unsubtracted unlike-sign spectra are used in these normalizations; this is justifiable because all of the backgrounds are minimal compared to the overwhelming pion Dalitz signal in the low mass region.

Table 7.4: Relative errors for the common ancestor normalization

Centrality	$\Delta \int FG_{ULS}$	$\Delta \int BG_{ULS}^{DD}$	ΔN^{DD}
0-10%	0.6154%	0.7706%	0.9862%
10-20%	0.7360%	0.7706%	1.0656%
20-40%	0.6883%	0.7721%	0.6927%
40-94%	0.5785%	0.7626%	0.9572%

The relative normalization systematic error is calculated by propagating the statistical errors of the yields in the normalization region for both the generated and measured pion Dalitz pairs. Equation 7.1 details the calculation of the normalization systematic error in

104

terms of the relative statistical errors of the data and simulated spectra.

$$\Delta N^{DD} = \sqrt{\left(\Delta \int FG_{ULS}\right)^2 + \left(\Delta \int BG_{ULS}^{DD}\right)^2} \qquad (7.1)$$

where ΔN^{DD} is the relative systematic error on the normalization, $\Delta \int FG_{ULS}$ is the relative statistical error of the unsubtracted unlike-sign spectrum integrated in the normalization region and $\Delta \int BG_{ULS}^{DD}$ is the relative statistical error of the generated pion dalitz pair yield in the normalization region. Table 7.4 shows the data's relative statistical error, the generated pion's relative statistical error and the normalization's relative systematic error for each centrality group. The resulting systematic errors on the common ancestor normalizations are around one percent of the normalization in each centrality group.

Common ancestor background shape error

Each background is generated using a different method. The validity of each generation method and the resulting background shapes serve as estimates for the systematic error of these shapes. The common ancestor backgrounds are generated using a modified Exodus, a phenomenological event generator. Exodus is discussed in more detail in Chapter 8. Here a quick overview of the modified Exodus framework and adjustments used to create the common ancestor backgrounds and the expected systematic error on the generated shape is given.

The modified Exodus framework simulates the common ancestor backgrounds by generating π's and η's within their known yield, p_T and rapidity distributions, decaying them into electrons and positrons using the decay channels presented in Chapter 4, filtering the decay products through the ideal PHENIX acceptance and applying the detector resolution. The single particles are efficiency weighted and filtered through detector dead areas. The background yield is adjusted to include additional yields from conversion pairs as described in Chapter 5 and pair cut efficiencies are applied. This results in the simulated common ancestor backgrounds used in this analysis.

The dominant source of systematic error stems from providing the event generator with the known π and η yield and distributions. The accuracy of the simulated common ancestor background is limited by the underlying assumptions and the uncertainty in the input π and η yields and p_T spectra. An overall relative systematic error on the common ancestor background of 20% is applied in each centrality to the common ancestor background component. This 20% value is based on the systematic errors from the measured PHENIX π and η spectra. These systematic errors are summed in quadrature and the resulting relative errors is presented in Table 7.5.

Table 7.5: Systematic errors for the common ancestor background

Centrality	Systematic error
0-10%	20.0243%
10-20%	20.0284%
20-40%	20.0120%
40-94%	20.0229%

7.2.2 Combinatorial and jet normalization error

The systematic error on the normalizations of the combinatorial and jet backgrounds are calculated in a similar manner to the common ancestor's normalization error, propagating the statistical errors of the yields in the normalization regions. The combinatorial and jet normalization systematic errors are presented together since the normalizations are determined in the same iterative procedure. From Chapter 5, the combinatorial and jet normalizations are calculated in an iterative process with integrals taken over two normalization regions, one for the combinatorial normalization and one for the jet normalization, using the like-sign data and generated backgrounds. Equation 7.2 presents the general formulas for the two normalizations in the ith iteration

$$N_i^{CB} = \int_R \frac{BG^{CB}}{FG - N^{DD}BG^{DD} - N_{i-1}^{Jet}BG^{Jet}}$$
$$N_i^{Jet} = \int \frac{BG^{Jet}}{FG_{LS} - N^{DD}BG^{DD} - N_i^{CB}BG^{CB}} \tag{7.2}$$

where $\int_R$ is the integral over the entire p_T space and above 0.6 GeV/c^2 in mass, the other integrals are over the entire mass and p_T phase space, N_i^{CB} is the ith combinatorial normalization, BG^{CB} is the like-sign combinatorial background spectrum, FG is the measured like-sign pair distribution, N^{DD} is the common ancestor correlated background normalization, BG^{DD} is the common ancestor correlated background, N_i^{Jet} is the ith jet correlated background normalization and BG^{Jet} is the jet correlated background.

By propagating the statistical errors for the integrals of the data and generated backgrounds we determine the systematic errors on the jet and background normalizations. Equations 7.3 and 7.4 calculates the systematic errors for the combinatorial and jet normalization systematic errors respectively.

$$\Delta N^{CB} = \sqrt{\left(\frac{\sqrt{\int_R FG} \oplus N^{DD}\sqrt{\int_R BG^{DD}} \oplus N^{Jet}\sqrt{\int_R BG^{Jet}}}{\int_R FG - N^{DD}\int_R BG^{DD} - N^{Jet}\int_R BG^{Jet}}\right)^2 + \left(\frac{\sqrt{\int_R BG^{CB}}}{\int_R BG^{CB}}\right)^2} \tag{7.3}$$

$$\Delta N^{Jet} = \sqrt{\left(\frac{\sqrt{\int FG} \oplus N^{DD}\sqrt{\int BG^{DD}} \oplus N^{CB}\sqrt{\int BG^{CB}}}{\int FG - N^{DD}\int BG^{DD} - N^{CB}\int BG^{CB}}\right)^2 + \left(\frac{\sqrt{\int BG^{Jet}}}{\int BG^{Jet}}\right)^2} \quad (7.4)$$

where ΔN^{CB} and ΔN^{Jet} are the relative systematic errors on the combinatorial and jet normalizations, the remaining symbols have the same designation as in Equation 7.2, $\oplus$ denotes a sum in quadrature, gaussian errors are assumed for the errors of the integrals and the converging iteration values for the jet and combinatorial normalizations are applied. Both of these equations are the quadrature sum of the relative error of the background to be normalized and the relative error of the partially subtracted like-sign spectra isolating that background. Table 7.6 presents the relative errors for the combinatorial background normalization and Table 7.7 presents the jet background normalization values.

Table 7.6: Systematic errors for the combinatorial normalization

Centrality	Isolated data rel. error	$\Delta \int_R BG^{CB}$	ΔN^{CB}
0-10%	0.24229%	0.01748%	0.24292%
10-20%	0.39661%	0.04073%	0.39870%
20-40%	0.54570%	0.04058%	0.54720%
40-94%	1.46309%	0.11052%	1.46726%

Table 7.7: Systematic errors for the jet background normalization

Centrality	Isolated data rel. error	$\Delta \int BG^{Jet}$	ΔN^{Jet}
0-10%	11.25614%	2.18360%	11.46598%
10-20%	22.23269%	2.19061%	22.34035%
20-40%	31.63766%	2.02732%	31.71407%
40-94%	24.53453%	2.27446%	24.63973%

For both the jet and combinatorial backgrounds the normalization systematic error is dominated by the error in the partially subtracted data. The systematic error on the combinatorial normalization is below two percent of the normalization in each centrality. If the combinatorial background normalization errors were much larger the subtracted signal would be of limited value. The jet normalization has a much larger systematic error, between ten and thirty percent, but the jet background is a much smaller component and as a result has a reduced effect on the subtracted spectra.

7.2.3 Jet background shape error

The jet backgrounds are generated with Pythia, a p+p jet and event generator, where the pion Dalitz decay's branching ratio was enhanced to produce more correlated dielectron pairs in the simulated jets. As with the common ancestor background, the simulated jet background is weighted by the electron efficiency and filtered through the detector dead areas. The simulated jet background is isolated from the underlying simulated event correlations by normalizing and subtracting randomly generated event correlations with the same p_T distribution. The near- and away-side jet components are separated using a $\Delta\phi$ cut at 90° and the away-side components are reduced by the measured I_{AA} in Cu+Cu collisions to model jet suppression in heavy ion collisions [86].

Pythia simulates p+p jets and jet-shapes well. In the p+p dielectron measurement a systematic error on the jet background shape of 3% and 11% was assumed for the near- and away-side jet components respectively [20]. The same systematics are assumed here. Jet shape variations due to the uncertainty in the I_{AA} adjustment of the away-side jet background are also considered. Two extreme alternative jet background shapes are considered, one where the away-side jet is not suppressed, i.e. $I_{AA} = 1$, and one where the away-side jet is fully suppressed, i.e. $I_{AA} = 0$. These extremes over-estimate the jet yield variation, especially compared to the determined uncertainties in the I_{AA} measurement. This is done because the jet background takes into account the reduced away-side yields but fails to consider the possible variations in the angular ϕ correlation of the electrons due to medium effects. The extreme jet background shapes of full or no away-side jet component should bracket any angular variations due to jet modification in heavy ion collisions. The away-side jet shape variation errors are summed in quadrature with the generated shape errors assumed in the p+p measurement and applied to the subtracted spectra differentially in mass and p_T.

7.2.4 Combinatorial background shape error

The combinatorial backgrounds are generated using the event mixing technique where pairs are generated across events to ensure that only combinatorial pairs are made. This technique requires that pairs are generated between events with similar production rates, p_T distributions and acceptances. As a result we portion the events between fifty groups, with ten centrality and five z-vertex classifications. Within each group event mixing is performed and a different combinatorial background shape is produced. The combinatorial background shape error is studied by varying the event mixing centrality and z-vertex segmentation.

Figures 7.1 and 7.2 show the variation of the unlike-sign combinatorial shape with different amounts of pool segmentation for centrality and z-vertex bins respectively. Figure 7.1 contains the ratio of combinatorial shapes for various numbers of centrality pool classes over a mixed event with twenty centrality and five z-vertex pools. The combinatorial background shape with ten centrality pools is in good agreement with the shape from twenty centrality pools. Figure 7.2 shows the ratio of the combinatorial shapes for various z-vertex poolings
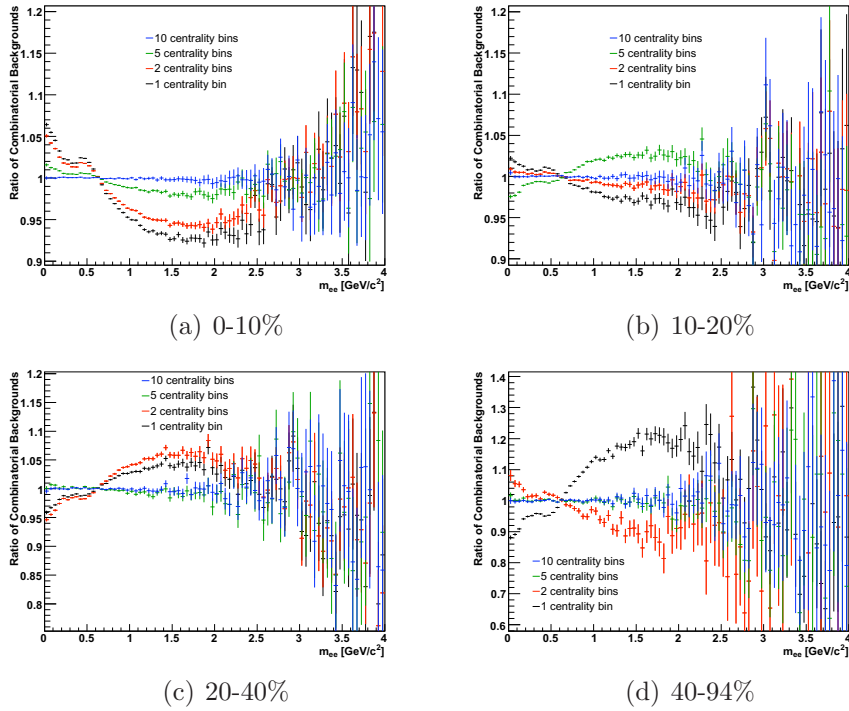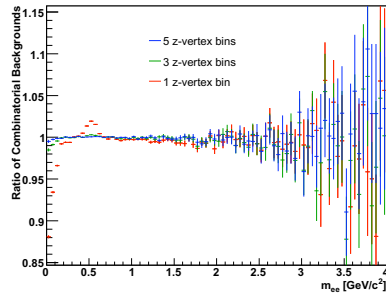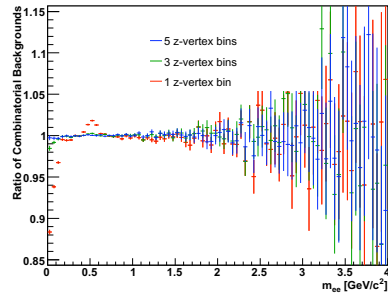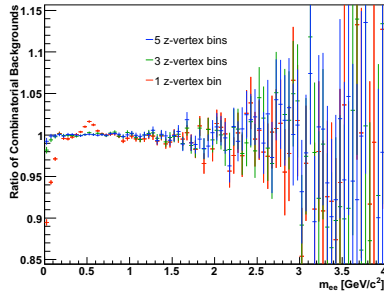
(a) 0-10%

(b) 10-20%

(c) 20-40%

(d) 40-94%

Figure 7.1: The combinatorial shape variation in unlike-sign pairs generated with different centrality pool segmentation. This is determined by taking the ratio of the combined centralities and z-vertex bins generated with respective pool segmentation over the generated background with twenty centrality bins and five z-vertex bins.
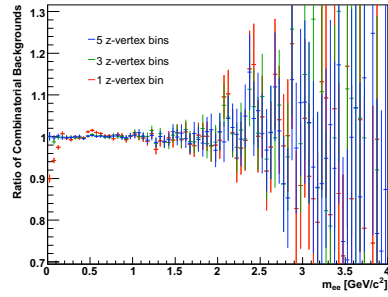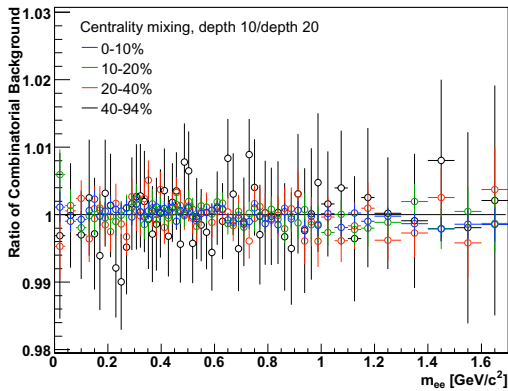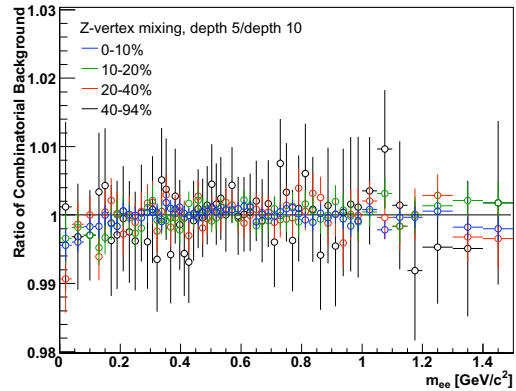
(a) 0-10%

(b) 10-20%

(c) 20-40%

(d) 40-94%

Figure 7.2: The combinatorial shape variation in unlike-sign pairs generated with different z-vertex poolings. This is determined by taking the ratio of the combined centralities and z-vertex bins generated with respective poolings over the generated background with ten centrality bins and ten z-vertex bins.

(a) Centrality depth 10/depth 20   (b) z-vertex depth 10/depth 20

Figure 7.3: The combinatorial shape variation in unlike-sign pairs generated with the best centrality and z-vertex pooling focusing on the lowest mass regions. The shape variation for each centrality group is shown. The plot on the left is determined by taking the ratio of the combinatorial background with ten centrality bins and five z-vertex bins over twenty centrality bins and five z-vertex bins. The plot on the right is calculated by taking the ratio of the combintorial background generated in ten centrality bins and five z-vertex bins over ten centrality bins and ten z-vertex bins.

over a mixed event with ten centrality and ten z-vertex bins. The combinatorial background shape with five z-vertex bins is in good agreement with the shape from ten z-vertex pools. Figure 7.3 shows the same ratios for the ten centrality pools and five z-vertex pools focusing on the lowest mass region. The systematic errors for the shape of the combinatorial backgrounds are determined according to the ratios for the ten centrality pools and five z-vertex pools respectively. These shape systematic errors are mass dependent and are characterized in mass ranges as presented in Tables 7.8 and 7.9. At high masses where the statistics are low, the histograms are rebinned before the ratios are determined providing more meaningful error values.

Table 7.8: Systematic errors for variations in the combinatorial background shape from centrality pooling for the various centrality groups

Mass Region	0-10%	10-20%	20-40%	40-94%
$m < 1.5$	0.25%	0.5%	1%	1%
$1.5 < m < 2.5$	1%	1.5%	3%	3%
$2.5 < m < 3$	5%	4%	3%	5%
$m > 3$	5%	6%	6%	15%

Table 7.9: Systematic errors for variations in the combinatorial background shape from z-vertex pooling for the various centrality groups

| Mass Region	0-10%	10-20%	20-40%	40-94%
$m < 1.5$	0.5%	0.5%	0.75%	1%
$1.5 < m < 2.5$	1%	2%	3%	4%
$2.5 < m < 3$	3%	4%	3%	5%
$m > 3$	5%	6%	3%	8%

7.3   Combined systematic errors

The efficiency correction systematic error is summed in quadrature with the systematic errors from the background subtraction and applied at each point in the one-dimensional mass projections. The subtraction errors consist of both normalization and shape errors. The shape errors are applied to each of the background components and propagated to the subtracted spectra. The normalization errors are also applied adjusting each of the background components to determine a minimal and maximal range. The normalizations are assumed to be uncorrelated.
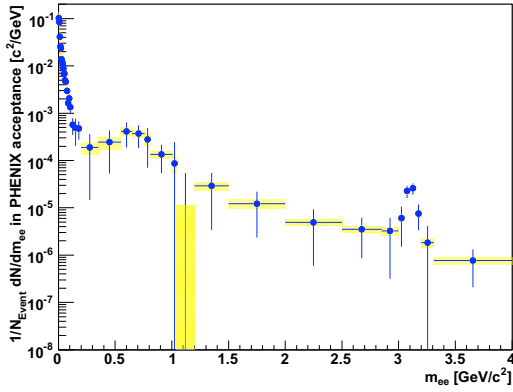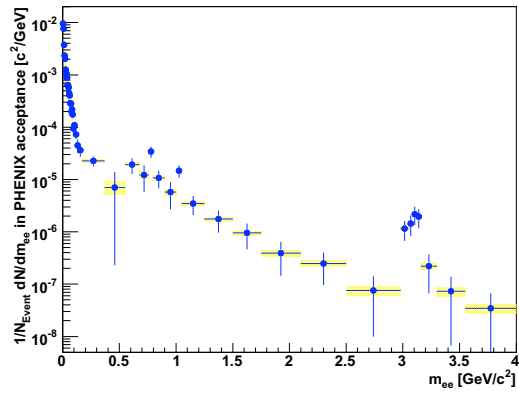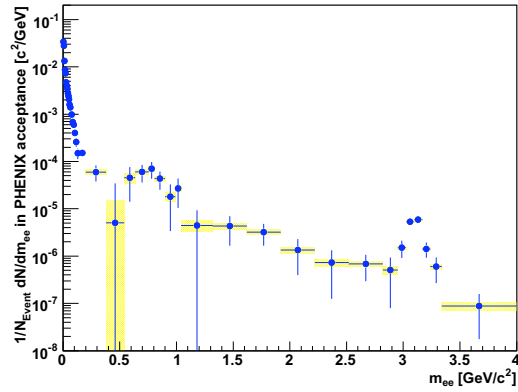
(a) 0-10%
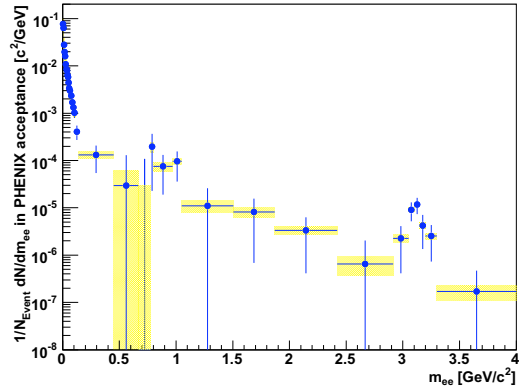
(b) 10-20%
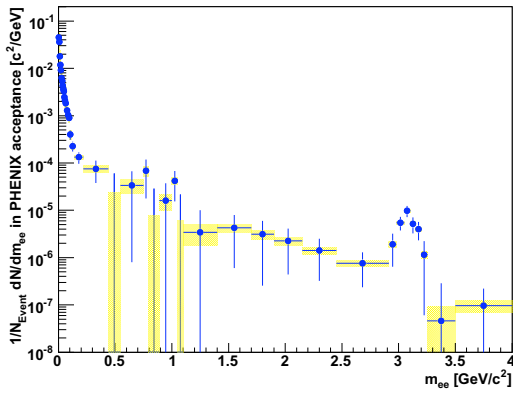
(c) 20-40%

(d) 40-94%

(e) Min. Bias

Figure 7.4: The subtracted spectra for the various centrality groupings with the systematic errors shown as a yellow band around the points.

This assumption is an over-estimate. The background normalizations are not independent. They are correlated by the requirement in the normalization process that the subtracted like-sign spectra have zero yield. This means that any increase in the jet background will result in decreases to both the combinatorial and correlated ancestor backgrounds. Similarly, a decrease in the jet background requires increases in the combinatorial and correlated ancestor background. The jet background normalization is therefore anti-correlated with the combinatorial background normalization and the common ancestor normalization and the combinatorial background normalization and common ancestor normalizations are correlated with one another. The amount of correlation and anti-correlation between the three normalizations is unknown. As a result we assume they are independent as a conservative over-estimate of the systematic errors. Figure 7.4 presents the systematic errors applied to the subtracted spectra for each centrality group. The systematic errors are presented as a yellow band around each point. The systematic errors for the minimum bias spectrum is the quadrature sum of the weighted systematic errors of the spectra in the centrality groupings.

7.4 Component variations effect on the background

Now that the background normalization and shape systematic errors have been considered, the effect of the background's systematic uncertainty on the iterative normalization procedure must be addressed. In most cases these uncertainties result in relative adjustments between the various background components with only minor adjustments to the total background. This is studied by varying individual background components according to their systematic errors, repeating the iterative normalization procedure and comparing the resulting total backgrounds. Additionally, the resulting subtracted spectra from these cross-checks are compared to the nominal subtracted spectra. First, adjustments to the common ancestor background component are presented. Then variations in the jet background component shape are studied. Finally, the mass and p_T region for the combinatorial normalization is adjusted.

7.4.1 Common ancestor background adjustment

To study the effect a roughly 20% variation in the common ancestor background subtraction has on the total background we have repeated the analysis including the iterative normalization procedure with the common ancestor background adjusted up and down by 20%. The effect of these changes on the background components, the total backgrounds and subtractions are shown in Figure 7.5. In Figure 7.5 it is important to remember that the combinatorial background component is the largest contributor to the background. So while the common ancestor and jet backgrounds have large variations, the combinatorial background component and total background are only minimally affected. The subtracted spectra is slightly affected between 0.5 and 1.5 GeV/c^2 in mass as a result of the small vari-

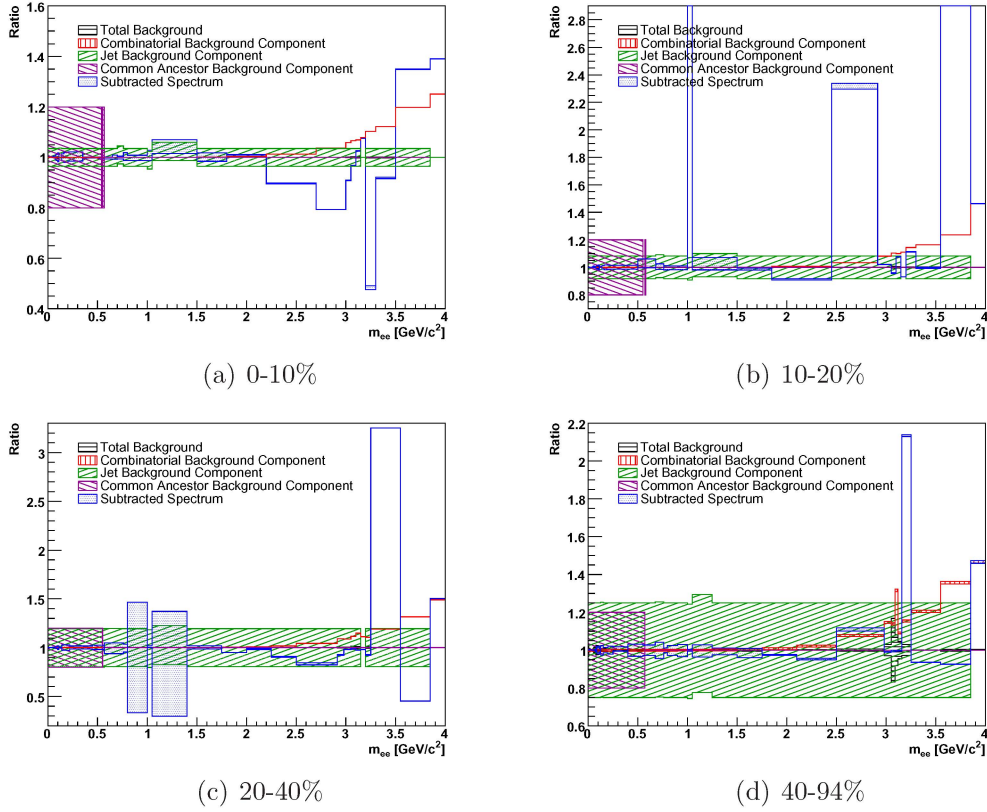(a) 0-10%

(b) 10-20%

(c) 20-40%

(d) 40-94%

Figure 7.5: The ratio of the backgrounds and subtraction with the common ancestor component changed by 20% in each direction over the backgrounds and subtraction with the expected common ancestor component. The total background is shown in black with horizontal lines, the combinatorial background is red with vertical lines, the jet and common ancestor backgrounds are green and purple respectively with diagonal lines and the subtracted spectra are the blue dotted regions.

ations in the combinatorial normalization compensating for the 20% shift in the common ancestor component.

Figure 7.6 shows a comparison between the subtracted spectra with the normalized common ancestor background and the spectra resulting in 20% adjustments to the common ancestor background normalization. There is no discernable difference.

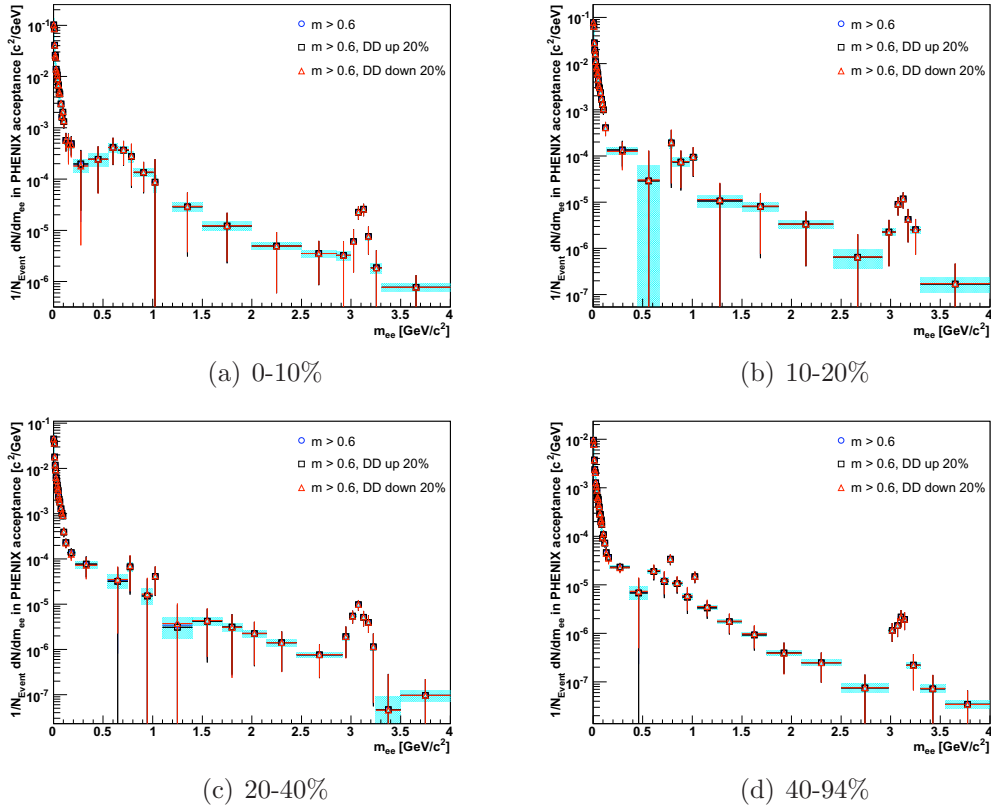(a) 0-10%

(b) 10-20%

(c) 20-40%

(d) 40-94%

Figure 7.6: The a comparison of the resulting subtracted spectra with the initial condition of the common ancestor component at its normalized position and adjusted by 20% in each direction. The iterative normalization procedure is applied resulting in separate jet and combinatorial background normalizations for the three spectra. Each of the subtracted spectra have been efficiency corrected. The light blue systematic error band is applied only to the original normalization.

7.4.2 Jet background adjustment

The range of prospective total backgrounds and subtracted spectra due to the jet background shape is studied in an similar manner as the common ancestor background. The

iterative procedure for calculating the normalizations is done using jet background components with a range of away-side jet suppression factors, I_{AA}, applied. In this way we are able to study the effects of the jet background shape on the total background and the resulting subtracted spectra.

Figure 7.7 shows the effect on the background components, total background and subtracted spectra when the jet shape is altered to include the full away-side jet or no away-side jet component. The common ancestor background component is unaffected by these changes. The jet background components show larger variations than the combinatorial background and total background. The effect on the subtracted spectra is much larger here when the jet shape is altered than when the correlated electron background was adjusted earlier in the chapter. This is because the combinatorial background normalization is more heavily anti-correlated to the jet background component than it is correlated to the common ancestor background component. In both instances, the variations in the subtracted spectra are large where the combinatorial background is largest reflecting the importance of even small alterations to the combinatorial background.

Figure 7.8 shows the variation in the resulting spectra for iteration procedures where the away-side jet background component has been adjusted from the measured I_{AA} to the one sigma minimum and maximum of the measured I_{AA} and the extreme examples of an unmodified away-side jet, $I_{AA} = 1$, and a fully suppressed away-side jet, $I_{AA} = 0$. The agreement is quite good, especially in the more peripheral centrality groups.

7.4.3 Combinatorial normalization region adjustment

Varying the normalization regions in the iterative normalization procedure provides another study of the robustness of the iterative normalization procedure and the resulting total background and subtracted spectra. The background variation as a result of these normalization regions is studied by altering the low mass limit in the combinatorial normalization region to 0.4, 0.5 and 0.7 GeV/c^2. In a separate test, the region at high and intermediate masses is restricted for mass regions between the similar lower limits, 0.4 and 0.5 GeV/c^2, and the upper limit 1 GeV/c^2. A comparison to normalization with the specific region in mass and p_T identified as containing a minimal jet background in the p+p dielectron analysis [66], between the functions $p_T - 1.5m = 0.2$ and $p_T - 0.75m = 0$, and the arcs, $\sqrt{m^2 + p_T^2} = 0.7$ and $\sqrt{m^2 + p_T^2} = 1$. Figure 7.9 shows the comparison of the subtracted spectra in each centrality group with the resulting spectra in each of the alternate normalization regions. Again the agreement between the different normalization regions is very good.

An alternate determination of the systematic error on the normalization is also done. This consists of calculating sample standard deviation among the fourteen alternate spectra shown in Figures 7.6, 7.8 and 7.9 and using this value as the systematic error on the normalization method. This is done bin-by-bin with outliers identified by a three sigma cut removed [87]. The resulting systematic errors are consistent with the results already presented in this

(a) 0-10%

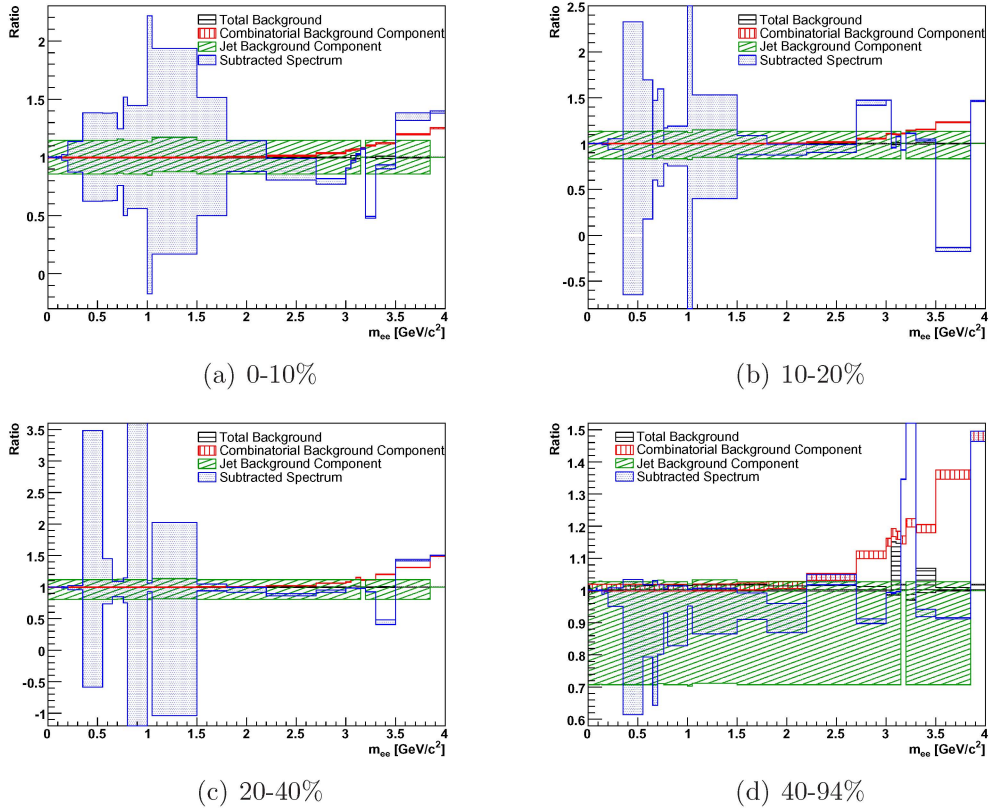(b) 10-20%

(c) 20-40%

(d) 40-94%

Figure 7.7: The ratio of the backgrounds and subtraction with the jet component shape altered to include the full away-side jet component and no away-side jet component over the backgrounds and subtraction with the expected jet component shape. The total background is shown in black with horizontal lines, the combinatorial background is red with vertical lines, the jet background is green with diagonal lines and the subtracted spectra are the blue dotted regions. The common ancestor background is unaffected by the away-side jet shape.

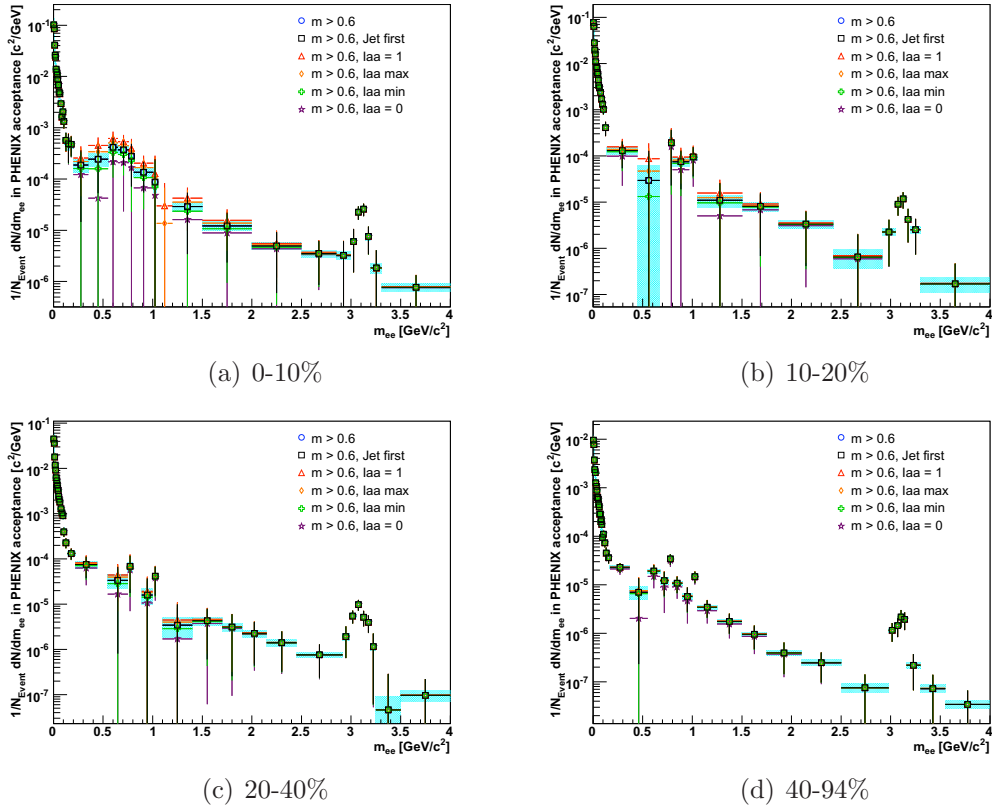(a) 0-10%

(b) 10-20%

(c) 20-40%

(d) 40-94%

Figure 7.8: The comparison of the resulting subtracted spectra with the adjustments to the away-side jet component. The iterative normalization procedure is applied resulting in separate jet and combinatorial background normalizations for the various spectra. Each of the subtracted spectra have been efficiency corrected. The light blue systematic error band is applied only to the original away-side jet component.
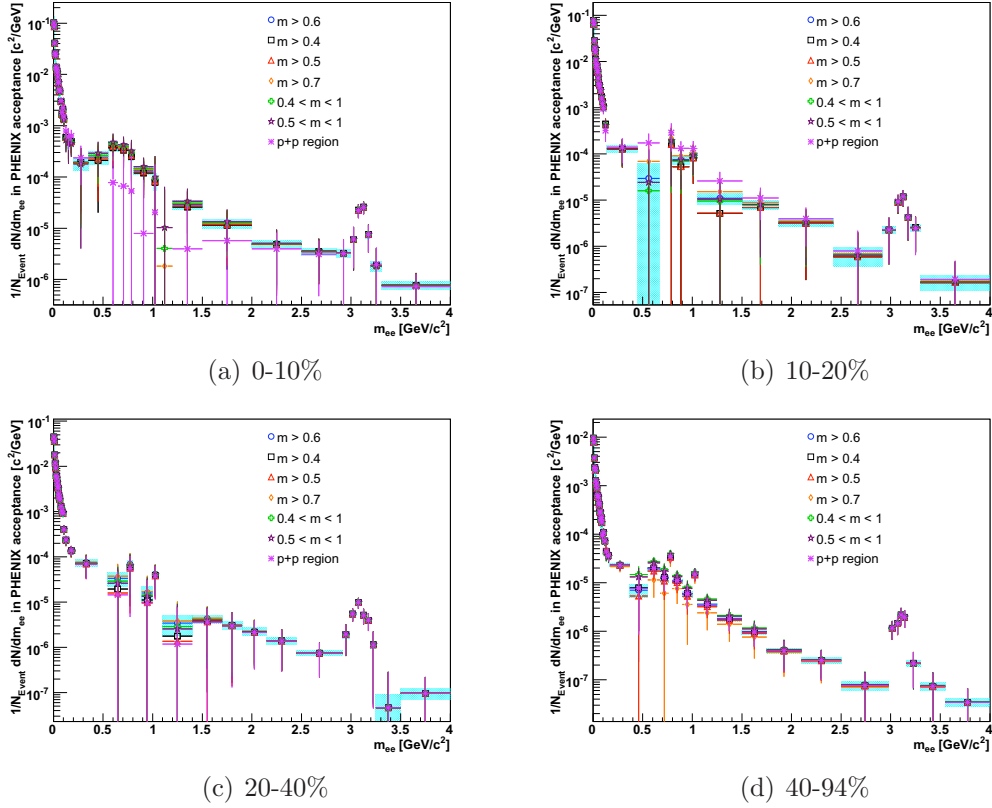
chapter.

(a) 0-10%

(b) 10-20%

(c) 20-40%

(d) 40-94%

Figure 7.9: The comparison of the resulting subtracted spectra with various combinatorial normalization regions. The iterative normalization procedure is applied resulting in separate jet and combinatorial background normalizations for the various spectra. Each of the subtracted spectra have been efficiency corrected. The light blue systematic error band is applied only to the spectra from the original normalization region.

Chapter 8

Cocktail generation

Here a brief diversion from the data analysis is taken and the calculation of the cocktail of known dielectron sources is presented. The cocktail is used to compare the data to the expected mass spectra to observe any variation in the mass spectra due to the quark gluon plasma.

The cocktail depicts the known dielectron sources from hadronic decays and heavy quark correlations. A cocktail consists of dielectron decays from light vector meson decays (ρ, ω, ϕ), Dalitz decays from light neutral mesons (π^0, η, η'), correlated heavy quark (charm and bottom) components and a Drell Yan contribution. The hadronic decays are simulated using Exodus, a locally-made phenomenological event generator described in [88]. The heavy quark and Drell Yan components are scaled Pythia calculations. The method for generating the cocktail is presented starting with the hadronic component and then the correlated heavy quark and Drell Yan components.

8.1 Hadronic cocktail generation

The hadronic cocktail component is simulated with Exodus, a phenomenological event generator [89]. Exodus generates particles within their known phase-space distributions, ie their p_T and rapidity distributions. The particles then undergo two- and three-body decays of those particles. The electron and positron decay products are filtered through the detector's ideal acceptance and resolution effects are applied. The parent hadron's relevant properties, decays and branching ratios are taken from the Particle Data Book [2] and are listed in Table 8.1. The two- and three-body decays assume a flat phase-space distributions. All of the vector mesons are assumed to be unpolarized. For Dalitz decays, decays with a lepton pair and a third particle, the third particle is not isotropic in it's rest frame. It has a $(1 + cos^2\theta)$ distribution where θ is the polar angle of the leptons in the Collins-Soper frame. Dalitz decays are simulated using the Kroll-Wada formulation [90] and the measured electromagnetic form factors from the Lepton-G collaboration.

Table 8.1: Hadronic decays and branching ratios

Decay	Branching Ratio
$\pi \to \gamma e^+ e^-$	$1.198 x 10^{-2}$
$\eta \to \gamma e^+ e^-$	$6.8 x 10^{-3}$
$\eta' \to \gamma e^+ e^-$	$9 x 10^{-4}$
$\rho \to e^+ e^-$	$4.71 x 10^{-5}$
$\omega \to e^+ e^-$	$7.16 x 10^{-5}$
$\omega \to \pi e^+ e^-$	$7.7 x 10^{-4}$
$\phi \to e^+ e^-$	$2.97 x 10^{-4}$
$\phi \to \eta e^+ e^-$	$1.15 x 10^{-4}$
$J/\psi \to e^+ e^-$	$5.94 x 10^{-2}$
$\psi' \to e^+ e^-$	$7.52 x 10^{-3}$

To calculate the combined hadronic cocktail for a given centrality, the yield, rapidity and p_T distributions for each parent meson are needed. The parent meson's rapidity distributions are assumed to be flat. The pion yield, dN_{π^0}/dy, and p_T spectrum is provided for each centrality grouping. The pion serves as a reference particle to characterize the remaining mesons. The yields and p_T distributions for the other mesons are extrapolated from the pion by assuming m_T scaling and using meson-to-pion ratios, $\frac{dN_{meson}}{dy} / \frac{dN_{\pi^0}}{dy}$. The accompanying subsections present the parametrization of the pion p_T spectra followed by a discussion of the multiplicity determinations, a description of m_T scaling and detailing additional corrections to the simulated hadronic yield for high mass hadrons. At the end of this section the hadronic component of the cocktail is presented for each centrality group.
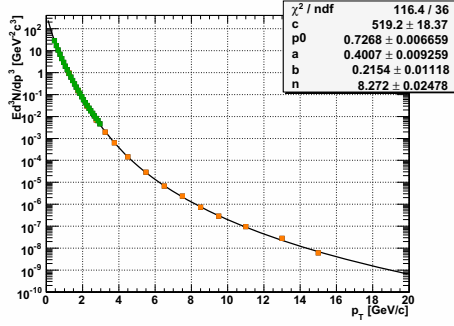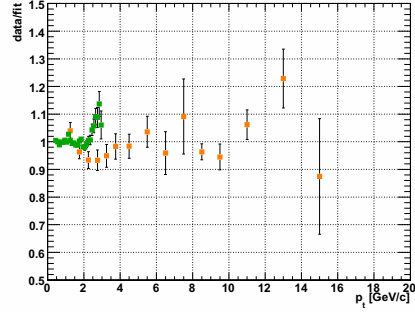
8.1.1 Fitting the pion p_T spectra

The measured pion p_T spectra in Cu+Cu collisions at PHENIX [91] [92] are used to determine the input pion p_T shape. Both charged and neutral pions are simultaneously fit assuming the charge symmetry relation, Equation 8.1.
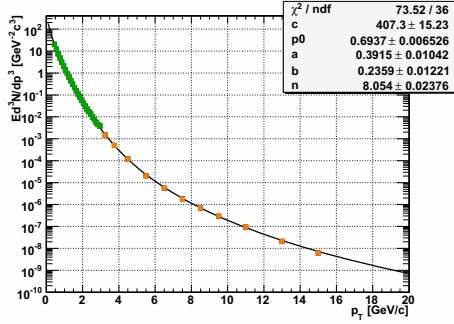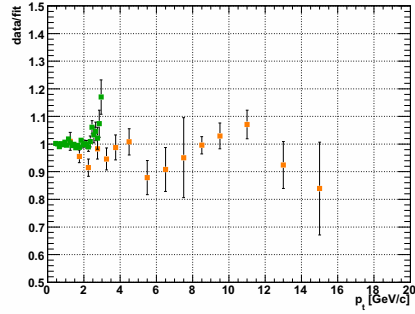
$$2 * \frac{d\sigma_{\pi^0}}{dp_T} = \frac{d\sigma_{\pi^+}}{dp_T} + \frac{d\sigma_{\pi^-}}{dp_T} \tag{8.1}$$

Neutral pions are measured in the photon channel, $\pi^o \to \gamma\gamma$, and charged pions are measured in the PHENIX Time-Of-Flight detector. The use of independently determined pion data within the same experiment ensures robust and well understood pion measurement. The inclusion of the charged pions provide more constraints on the fit at low p_T.
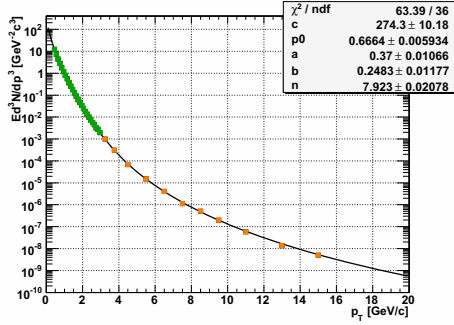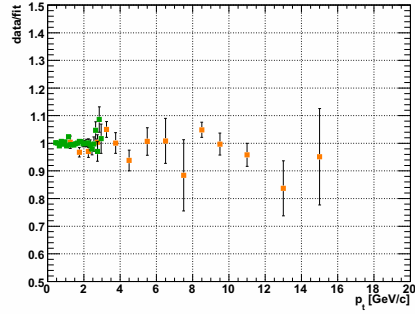
The combined charge and neutral pion p_T spectra are fit with a modified Hagedorn

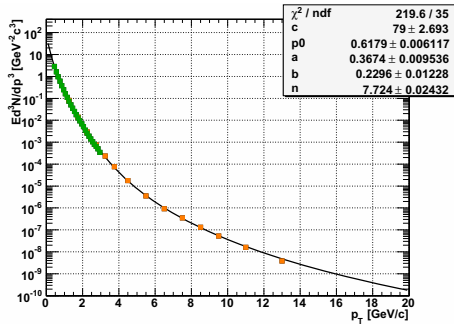| χ^2 / ndf	116.4 / 36
c	519.2 ± 18.37
p0	0.7268 ± 0.006659
a	0.4007 ± 0.009259
b	0.2154 ± 0.01118
n	8.272 ± 0.02478

(a) 0-10% p_T spectrum

(b) 0-10% Ratio

χ^2 / ndf	73.52 / 36
c	407.3 ± 15.23
p0	0.6937 ± 0.006526
a	0.3915 ± 0.01042
b	0.2359 ± 0.01221
n	8.054 ± 0.02376

(c) 10-20% p_T spectrum

(d) 10-20% Ratio

χ^2 / ndf	63.39 / 36
c	274.3 ± 10.18
p0	0.6664 ± 0.005934
a	0.37 ± 0.01066
b	0.2483 ± 0.01177
n	7.923 ± 0.02078

(e) 20-40% p_T spectrum

(f) 20-40% Ratio

χ^2 / ndf	219.6 / 35
c	79 ± 2.693
p0	0.6179 ± 0.006117
a	0.3674 ± 0.009536
b	0.2296 ± 0.01228
n	7.724 ± 0.02432

(g) 40-94% p_T spectrum
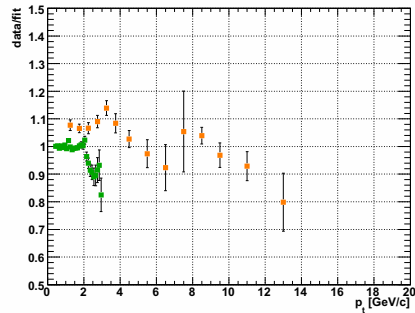
(h) 40-94% Ratio

Figure 8.1: The p_T spectra and fit information of the the charge (green) and neutral (orange) pions and the ratios of the data over the fits for each centrality group.

123

Table 8.2: Pion yield and p_T parameters

Centrality	dN/dy	A	a	b	p_0	n
$0-10\%$	83.914	574.8	0.6794	0.3976	0.2679	7.986
$10-20\%$	59.944	407.3	0.6937	0.3915	0.2359	8.054
$20-40\%$	36.612	274.3	0.6664	0.3700	0.2483	7.923
$40-94\%$	8.912	79.0	0.6179	0.3674	0.2296	7.724

exponential, Equation 8.2.

$$E\frac{d^3\sigma}{dp^3} = A\left(e^{-1\left(ap_T + bp_T^2\right)} + p_T/p_0\right)^{-n} \tag{8.2}$$

where (A, a, b, p_0, n) are the fit parameters. This fit is recalculated in each centrality grouping. Figure 8.1 shows the fit and data for the centrality groupings and the ratios of the data divided by the fit results showing the good quality of the fits. Once the pion p_T spectra have been parameterized in each centrality, the pion yields, dN_{π^0}/dy, are obtained by integrating the respective fit functions. The resulting values for the pion yields and p_T fit parameterizations are shown in Table 8.2.

8.1.2 Transverse mass, m_T, scaling

Transverse mass scaling assumes that the pion's m_T distribution is identical to the m_T distribution of the other mesons where m_T is the transverse mass as defined by Equation 8.3.

$$m_T^2 = m^2 + p_T^2 \tag{8.3}$$

This assumption is applied by replacing the pion's p_T in Equation 8.2 with $\sqrt{m_T^2 - m_{\pi^0}^2}$, for the various mesons, Equation 8.4

$$E\frac{d^3\sigma}{dp^3} = A\left(e^{-1\left(a\sqrt{m_T^2 - m_{\pi^0}^2} + b\left(m_T^2 - m_T^2\right)\right)} + \sqrt{m_T^2 - m_{\pi^0}^2}/p_0\right)^{-n} \tag{8.4}$$

where m_T is defined in Equation 8.3, m_{π^0} is the mass of the pion and the A, a, b, p_0, n values are listed in Table 8.2. The normalizations for each meson's p_T distributions, and therefore the meson yields, still need to be determined. The m_T scaling assumption is valid at high p_T [93]. At intermediate p_T the validity of this assumption is less clear. The 20% systematic errors on the cocktail cover any deviation from this assumption and contain errors from the input pion meson spectra.

As a result of m_T scaling, the meson-to-pion ratios are constant at high p_T and are listed in Table 8.3. The high p_T η/π, ω/π and ϕ/π values are known from PHENIX measurements

Table 8.3: High p_T meson-to-pion ratios

Meson	meson/π
η	0.48
ρ	1.0
ω	0.9
η'	0.25
ϕ	0.4
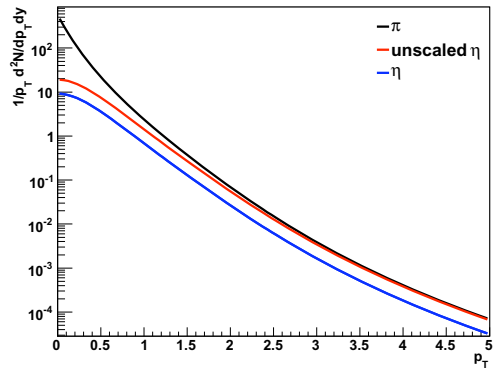
Figure 8.2: The 0-10% π^0, unscaled η created assuming m_T scaling, and scaled η p_T spectra using the high p_T η-to-π ratio in Table 8.3 to normalize the η.

Table 8.4: Inclusive meson-to-pion ratios

Centrality	η/π	η'/π	ρ/π	ω/π	ϕ/π	$J/\psi/\pi$	ψ'/π
$0-10\%$	0.1213	0.0187	0.1287	0.1120	0.0387	1.921e-5	5.111e-6
$10-20\%$	0.1205	0.0186	0.1276	0.1110	0.0385	2.146e-5	5.709e-6
$20-40\%$	0.1140	0.0174	0.1198	0.1042	0.0361	2.378e-5	6.326e-6
$40-94\%$	0.0996	0.0145	0.1011	0.0879	0.0298	1.835e-5	4.881e-6

[94] [95] [96]. The ρ/π and η'/π values are predicted by Pythia [89]. The meson p_T spectral shape from Equation 8.4 scaled by the high p_T meson-to-pion ratio, listed in Table 8.3, results in the meson's p_T spectra as shown in Figure 8.2. Integrating this function provides the inclusive meson yield. A ratio of this yield to the pion's yield gives the meson-to-pion ratio, $\frac{dN_{meson}/dy}{dN_{\pi^0}/dy}$, listed in Table 8.4. A comparison of the determined meson-to-pion ratios to the ratios of meson cross-sections known from jet fragmentation studies [2] is performed. The ratio of the cross-sections for ρ over ω, $\frac{\sigma_\rho}{\sigma_\omega}$, is 1.15 ± 0.15 and the cross-sections for η' over η, $\frac{\sigma_{\eta'}}{\sigma_\eta}$, is 0.15 ± 0.15. The values in Table 8.4 are in agreement with these ratios. Similarly the η'/π and ρ/π columns agree with the inclusive ratio LEP results, 0.018 and 0.14 respectively [89].

The J/ψ and ψ' to pion ratios are calculated in a different manner. The J/ψ values are obtained by extracting the $dN_{J/\psi}/dy$ from the J/ψ's measured B $dN_{J/\psi}/dy$ [97], which is then divided by the appropriate dN_{π^0}/dy. Since the measured J/ψ values are used the J/ψ component of the cocktail includes the reduced yield due to J/ψ suppression [86]. The ψ' values in Table 8.4 are scaled from the J/ψ as there are no measured ψ' yields in Cu+Cu collisions. At this point we have all the necessary parameters to calculate the hadronic contributions out to $4\,\mathrm{GeV}/c^2$ in mass. These parameters are almost completely extrapolated from the data with only the m_T scaling and flat rapidity distribution assumptions. The next two sections discuss adjustments to the hadronic cocktail at high mass to account for corrections to m_T scaling and radiative tails.

8.1.3 High mass corrections to m_T scaling

Transverse mass scaling may not hold with the higher mass mesons. The ϕ and J/ψ p_T spectra [96] [97] are used to confirm or correct the m_T scaling at high masses. This is done by comparing the measured p_T spectra and the Exodus generated p_T spectra that assumes m_T scaling. For both the ϕ and J/ψ, independent PHENIX measurements in the dielectron channel are used. In the case of the ϕ, the measured data [96] and the Exodus result are consistent. We conclude that m_T scaling holds for the ϕ in Cu+Cu collisions.

The measured J/ψ p_T spectra is not in agreement with the Exodus generated J/ψ p_T spectra; m_T scaling does not hold for the J/ψ. The measured J/ψ p_T distribution is param-

Table 8.5: Parameters for the J/ψ p_T adjustment

Centrality	A	N	p_0	n
$0-10\%$	0.0336	$5.2956 * 10^{-8}$	3.6636	4.9530
$10-20\%$	0.1575	$5.2955 * 10^{-8}$	3.6636	4.9530
$20-40\%$	0.1615	$7.4978 * 10^{-8}$	4.3337	4.3337
$40-94\%$	0.6476	$8.1636 * 10^{-8}$	13.3182	13.3182

eterized so that the proper p_T distribution is used in the hadronic cocktail. Equation 8.5 is fit to the J/ψ p_T distribution with the parameters N, p_0 and n.

$$1/\left(2\pi p_T\right) dN_{J/\psi}/dp_T = N/(1 + p_T^2/p_0^2)^n \tag{8.5}$$

Table 8.5 shows the fit parameter values for each centrality. Since the J/ψ [97] was measured in groups of 0-20%, 20-40%, 40-60% and 60-94%, the 40-60% and 60-94% groups are combined creating a 40-94% group. The 0-20% J/ψ measurement is applied to both the 0-10% and 10-20% centrality groups. Once the J/ψ p_T spectra is properly characterized, the J/ψ component of the cocktail is generated using the measured J/ψ p_T distribution. An overall scale factor, A, is also applied to maintain the known J/ψ-to-pion ratio from Table 8.4. This is particularly important for the 0-10% and 10-20% centrality groups where the individual J/ψ-to-pion ratios are known but only the combined 0-20% J/ψ p_T distribution is available. Figures 8.3 show the comparison of the cocktail p_T distributions for the ϕ and the corrected J/ψ overlaid with the independently measured data points for the ϕ and J/ψ for each centrality group.

8.1.4 Radiative tails in the J/ψ and ψ'

The J/ψ and ψ' components of the cocktail must also be corrected for their radiative decays creating extended tails below the J/ψ and ψ' in the spectra. The radiative tail shapes are identical to those used in the p+p and Au+Au dielectron analyses [20]. The PHENIX aperture and resolution effects are applied. The radiative shapes are normalized to the J/ψ and ψ' yields determined earlier in this chapter. An example of this correction is shown in Figure 8.4 for the 0-10% centrality grouping.

Once all of the corrections are applied we combine each of the components from Exodus to create a cocktail containing only hadronic sources. Figure 8.5 shows the hadronic component of the cocktail for each centrality grouping with each of the hadronic components displayed. The minimum bias spectrum in Figure 8.5(e) is calculated with a weighted average of the spectra in the centrality groups. It can also be simulated in Exodus using the minimum bias meson to pion ratios and pion p_T spectra for the input parameters. Both methods produce the same minimum bias hadronic cocktail spectrum.
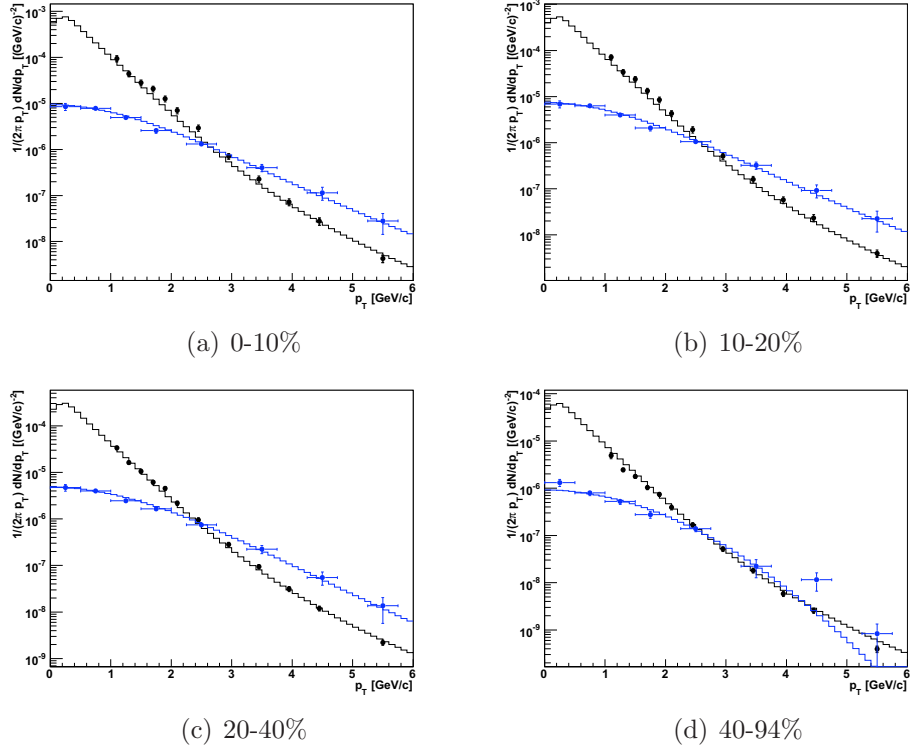
(a) 0-10%   (b) 10-20%

(c) 20-40%   (d) 40-94%

Figure 8.3: The p_T spectra of the ϕ (black) and J/ψ (blue) from the corrected cocktail and measured spectra [98] [99].
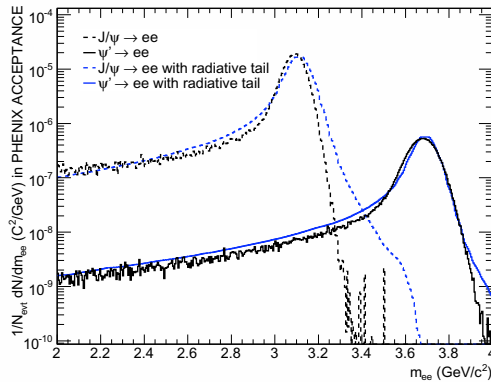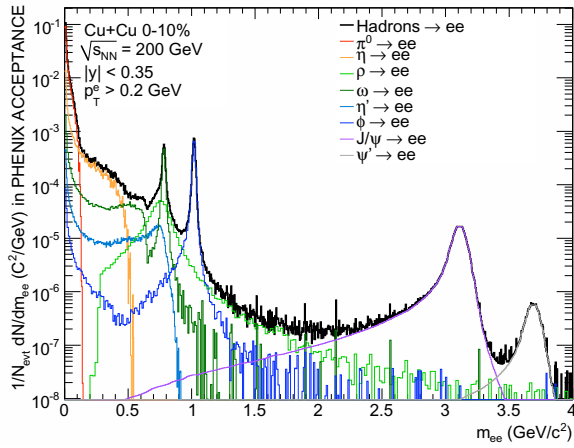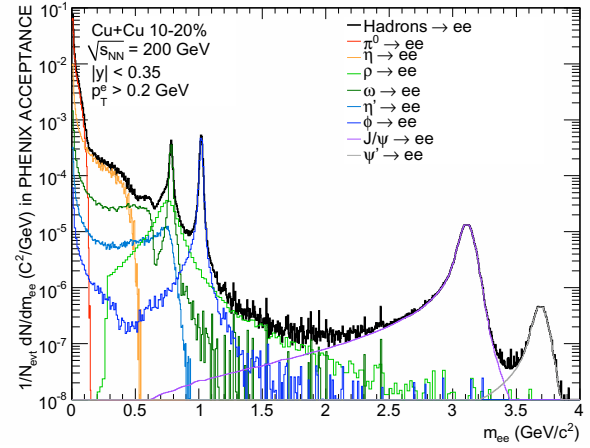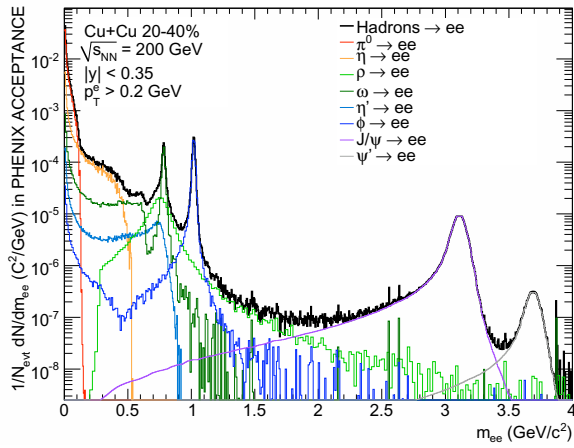

Figure 8.4: The 0-10% cocktail J/ψ and ψ' mass spectra with and without the radiative tail correction applied.
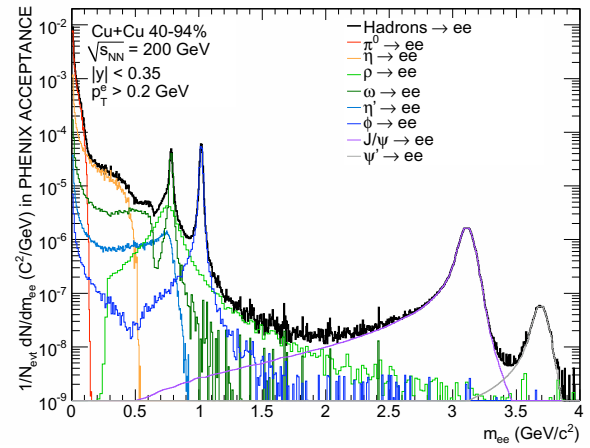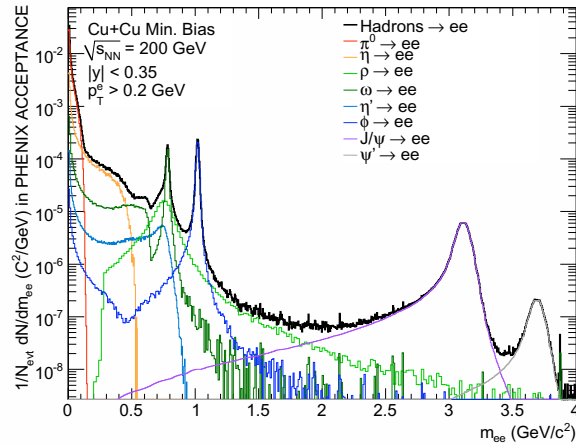
Figure 8.5: The dielectron hadronic cocktail with only the EXODUS generated components included for all of the centrality groupings.
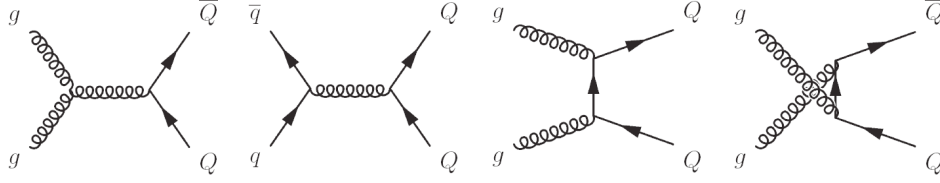
Figure 8.6: First order Feynman diagrams of heavy quark (Q) production from gluons (g) and light quarks (q).
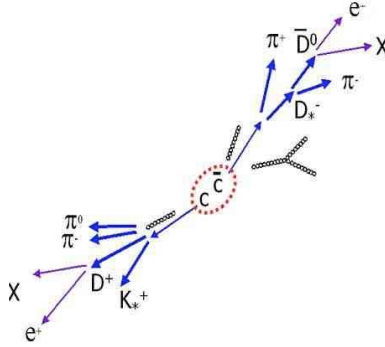
Figure 8.7: Diagram of the $c - \bar{c}$ dielectron correlation through open charm mesons.

8.2 Correlated heavy quark and Drell Yan

Once the known hadronic processes are well simulated we must address the dielectron correlations from heavy quark and Drell Yan production. These are simulated using Pythia, an event generator for p+p collisions. The parameterization of Pythia is discussed in detail in [100]. First we will present the heavy quark components and then the Drell Yan.

The correlated heavy quark component of the expected yield from the semi-leptonic decays of D and B mesons. Heavy quarks are pair-produced in the collision; diagrams of first order processes for heavy quark production are presented in Figure 8.6. The heavy quarks combine with light quarks during hadronization becoming D and $\bar{D}$ or B and $\bar{B}$ mesons. These open charm and open bottom meson pairs maintain a correlation from the heavy quark production process. When both of the mesons semi-leptonically decay the final state electrons and positrons maintain this correlation. This is depicted for $c - \bar{c}$ pairs in Figure 8.7. A similar decay chain exists for $b - \bar{b}$ pairs with B mesons. This indirect correlation is similar to the correlated jet background discussed in Chapter 4. Decay products contain correlations passed down through the kinematic decay process.

The Drell Yan component, shown in Figure 8.8, is due to quark-antiquark annihilation in hadron-hadron interactions, creating a Z boson or virtual photon which decays into a
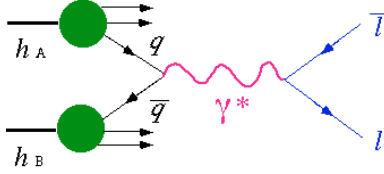
Figure 8.8: Diagram of the Drell Yan interaction with a mediating virtual photon.

Table 8.6: Number of parton collisions in Cu+Cu collisions

Centrality	N_{Coll}
$0 - 10\%$	182.7
$10 - 20\%$	59.9
$20 - 40\%$	36.6
$40 - 94\%$	8.9
Minimum Bias	51.8

lepton pair. This process was first measured at Brookhaven National Laboratory at the Alternating Gradient Synchrotron with muons in the final state [101]. The mass of the produced dielectron pair is known to follow Equation 8.6

$$m_{ee} = x_1 x_2 s_{NN} \tag{8.6}$$

where $x_i\sqrt{s_{NN}}$ is the momentum of one of the interacting quarks. At $\sqrt{s_{NN}} = 200$ GeV energies the Drell Yan process contributes primarily at high masses, above 3 GeV/c^2. The Drell Yan dielectron production is calculated to next leading order using parton distributions functions obtained from deep inelastic scattering measurements where a lepton collides with a nucleon.

The heavy quark and Drell Yan components of the cocktail are generated by Pythia with a CTEQ5L parton distribution function with modifications detailed in [20]. Earlier work compared the Pythia Drell Yan shape to Werner Vogelsang's next to leading order calculations and found agreement within 20% for masses below 4 GeV/c^2. In the Pythia simulation, the angular correlation for mid-rapidity dielectron pairs is a result of the k_T of the simulated partons. Our simulations used a k_T of 1.5 GeV/c, but the effects of various k_T values were also studied. The heavy quark and Drell Yan components from Pythia are filtered by the ideal PHENIX aperture. The p+p cross-sections for the $c - \bar{c}$, $b - \bar{b}$ and Drell-Yan components are used and scaled upward by the number of parton collisions in the nucleus-nucleus collision, N_{Coll}. Table 8.6 shows the N_{Coll} values for each of the Cu+Cu centrality groupings. [20]
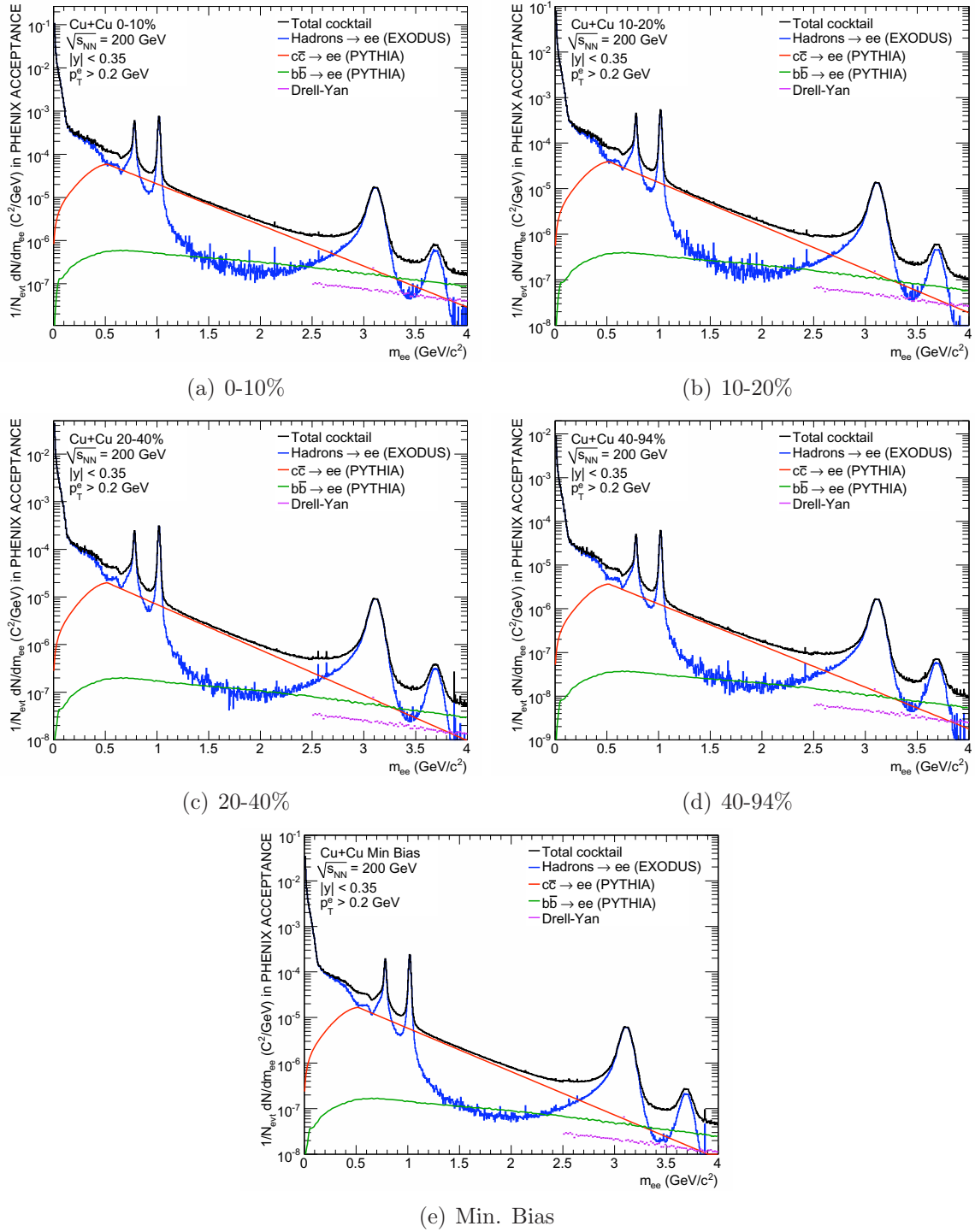
Figure 8.9: The combined cocktail mass spectra in the various centralities in black. The hadronic component is shown in blue, the charm, bottom and Drell Yan components are shown in red, green and purple respectively.
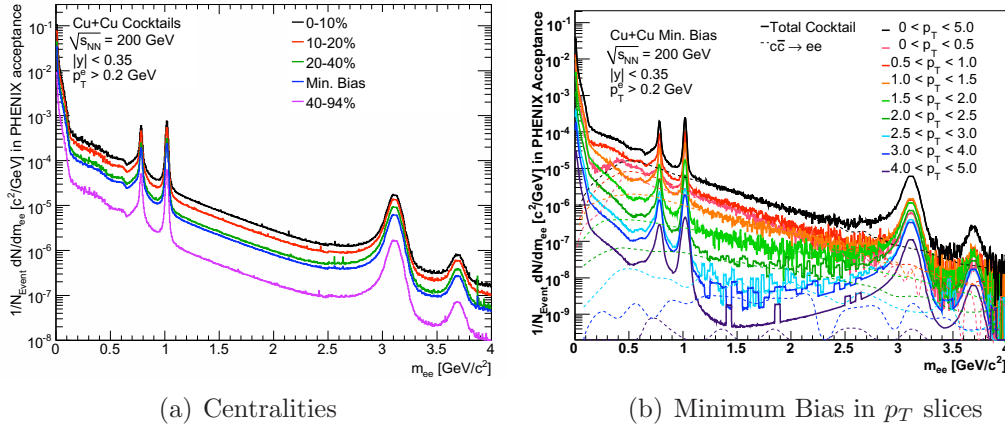
(a) Centralities   (b) Minimum Bias in p_T slices

Figure 8.10: The dielectron cocktail for each of the centrality groups including the minimum bias is shown on the left. On the right the Min. Bias cocktail is shown in p_T slices.

N_{Coll} scaling is required because Pythia models hadron+hadron interactions, not heavy ion interactions. As a result Pythia can not describe the known suppression and elliptic flow in high p_T single electrons [39]. The ramifications of these heavy ion effects on the heavy quark component in the dielectron spectrum are not known. A study assuming random angular orientation and the measured non-photonic single electron p_T distribution is presented in Section 8.2.1.

Figure 8.9 shows the complete dielectron cocktail in each of the four Cu+Cu centrality groups and the minimium bias. The charm component peaks at masses of 0.6 GeV/c^2 where it rivals the hadronic sources in yield particularly in the 0-10% centrality group. In the intermediate mass region between the ϕ and J/ψ the charm component is the dominant source of signal. The bottom component has a much lower yield than the charm in the measured dielectron mass range. It is a relevant source only for masses beyond the J/ψ. The Drell Yan component is the smallest component and does not provide a substantial contribution at any region of this measurement but is included for completeness. In Figure 8.10(a) the various cocktails for the different centralities and the minimum bias are shown. The decreasing cocktail yield with centrality is evident.

The dielectron mass cocktail can also be separated in pair p_T slices. This presents a nice picture of the topology of the expected contributions in the mass-p_T phase space as seen in Figure 8.10(b). The yield decreases as the slices move from low to high pair p_T slices. The exception to this is the lowest p_T slice, $p_T < 0.5 GeV/c$, where the PHENIX aperture hole at very low mass and p_T leads to a drop at around 0.2 GeV/c^2 in mass for both the hadronic and charm cocktail components. The charm component of the cocktail is largest at low pair p_T. The cocktail slices with pair p_T's above 2.5 GeV/c have minimal contributions from the charm component. The bottom and Drell Yan components are not included in this plot

133

although they are expected to have increased significance at high p_T.

8.2.1 Random heavy quark component

To account for the potential variation in the heavy quark components due to flow and the heavy ion p_T spectrum, Alberica Toia generated a random heavy quark component. This was done by taking the Au+Au non-photonic single electron p_T distribution and assuming a flat angular distribution. Since the non-photonic single electron spectrum is used, correlations from both the charm and bottom quarks are included in the resulting random heavy quark component.

(a) $c - \bar{c}$ Correlations   (b) With p+p Cocktail
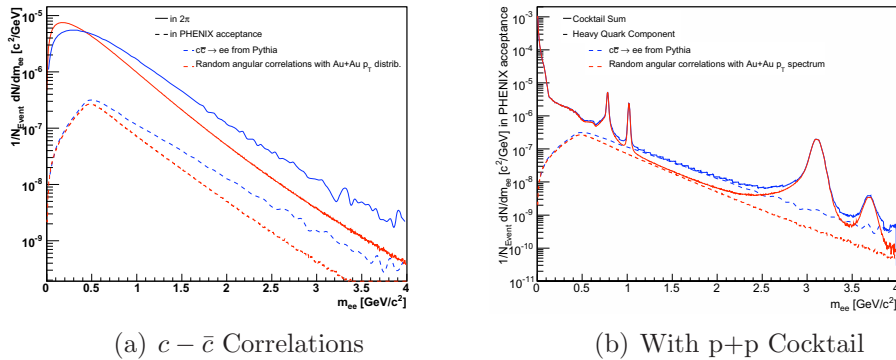
Figure 8.11: On the left the $c - \bar{c}$ correlation from Pythia (black) and the random heavy quark correlation (red) with and without the PHENIX acceptance applied is shown. On the right the heavy quark correlations are shown with a p+p cocktail for comparison.

The comparison between the $c - \bar{c}$ correlation from Pythia and from the random heavy quark correlation is also considered in p_T slices. It is interesting to note that while the randomly oriented component is smaller that the Pythia charm component at low transverse momenta. It is larger at high transverse momenta. This is most likely because the a $b - \bar{b}$ contribution is in the random spectrum from the input Au+Au non-photonic single electron p_T spectrum while the Pythia charm component contains only the charm contribution.

8.3 Comparison to data

With a well determined dielectron cocktail, the data are compared to the expected signals and any anomolous yields are determined. Figure 8.13 shows the data overlaid with the generated cocktail. In each centrality bin the pion Dalitz yield is well matched and the peaks from the ω, ϕ and J/ψ resonances are seen. Beneath each plot, the ratio of the data over the cocktail confirms this agreement. The most central spectrum, 0-10%, shows a
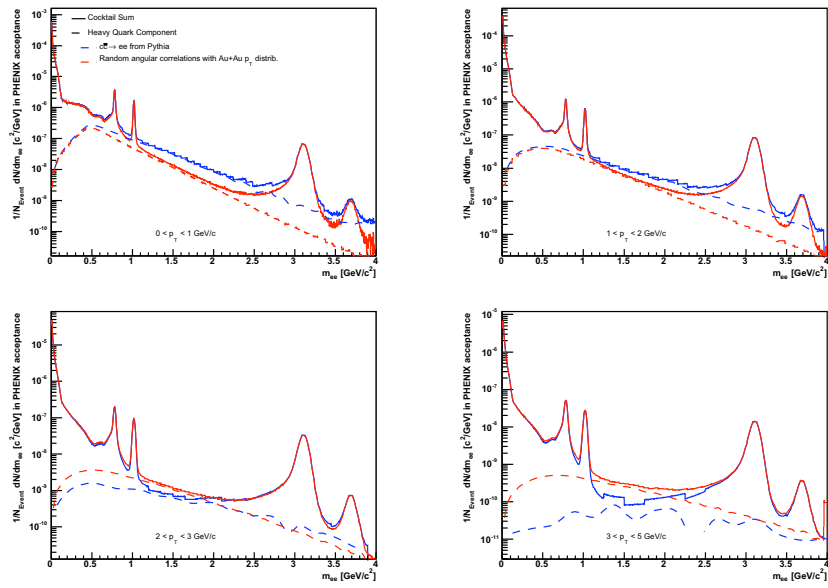
Figure 8.12: The $c - \bar{c}$ correlation from Pythia (black) and the random heavy quark correlation (red) in p_T slices shown with the p+p hadronic cocktail. The p_T slices 0-1, 1-2, 2-3, and 3-5 GeV/c are shown.

(a) 0-10%

(b) 10-20%
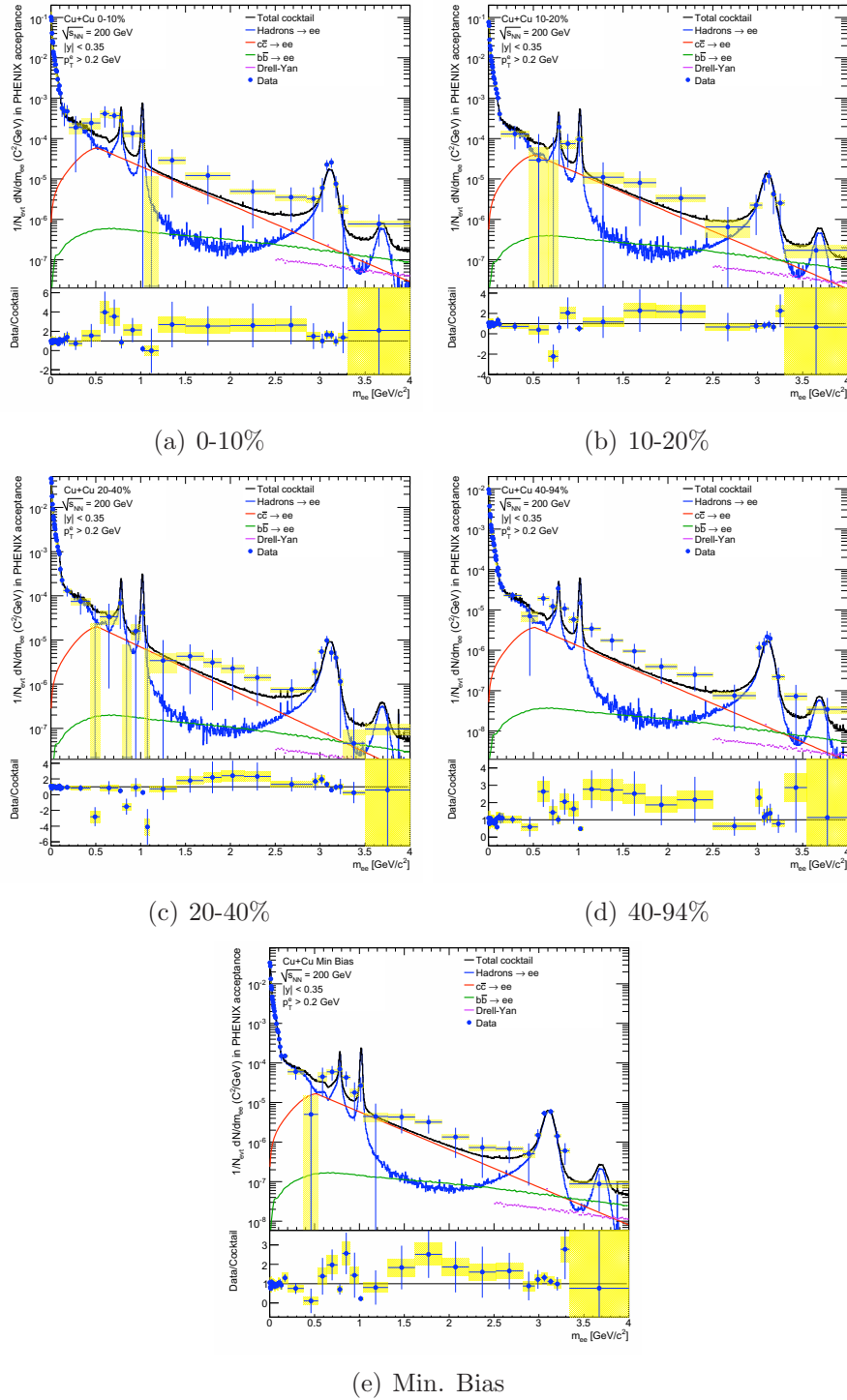
(c) 20-40%

(d) 40-94%

(e) Min. Bias

Figure 8.13: The Cu+Cu dielectron spectra in blue compared to the combined cocktail mass spectra in the various centralities in black. The hadronic component is shown in blue, the charm, bottom and Drell Yan components are shown in red, green and purple respectively.

136

slight excess over the cocktail in the low mass region below the ω meson. As the collisions become more peripheral the excess in the low mass region disappears. The 10-20% and 20-40% spectra agree with the cocktail albeit with large uncertainties. The most peripheral spectrum, 40-94%, shows an elongated enhancement over the cocktail in the intermediate mass region, between the ϕ and J/ψ, that extends to lower masses.

The π, η and η' produce a large hadronic yield that we are not directly interested in, it is useful to remove these components from the data and compare the results to a partial cocktail where these signals are also removed. This is done in Figure 8.14. Both the statistical and systematic errors in the data have increased due to the propagation of the errors from the removed π, η and η' components. The cocktail shapes with the π, η and η' removed are considerably different, making it easier to decipher the low and intermediate mass regions. Unfortunately the error bars are quite large making it difficult to conclude much from these plots, especially at low masses. The pion subtraction removes any ability to determine signal at masses below 0.1 GeV/c^2.

Further subtraction of the remaining hadronic sources, the ρ, ω, ϕ, J/ψ and ψ, results in Figure 8.15. The imprecise 10-20% and 20-40% spectra have been combined to form a mid-central spectrum of 10-40%. The subtraction of the ω, ϕ and J/ψ resonances leads to large statistical and systematic errors in the subtracted spectra near the peaks. The correlated charm, bottom and Drell Yan contributions are shown with the random heavy quark component. In both the peripheral and central spectra the remaining continuum spectra are larger than the expected heavy quark and Drell Yan contributions at intermediate masses. The mid-central spectrum is consistent with the expected heavy quark contributions but the points are consistently above the expected heavy quark contribution. It is not clear whether the additional yield in the intermediate mass region is the result of a heavy quark correlations, Drell Yan or a direct photon source. As mentioned in Chapter 1, the NA60 experiment at CERN determined that the excesses in their intermediate mass region was from thermal photons not heavy quarks [65].

In Figures 8.13, 8.14 and 8.15 show a slight excess in the 0-10% at masses between 0.54-0.75 GeV/c^2 and excesses in the 0-10% and 40-94% spectrum at masses between 1.2-2.87 GeV/c^2. To ensure that these excesses are not the result of under subtracting the backgrounds, we calculate the necessary increase in the total background needed to remove these excesses and consider the effects of this increased background on the unlike- and like-sign spectra. For the 0-10% spectrum a 0.7037% increase in the total background is required to remove the excess above the cocktail in the mass region 0.54-0.75 GeV/c^2. For the 40-94% spectrum a 11.2913% increase in the total background is required to remove the excess above the cocktail in the mass region 1.2-2.87 GeV/c^2. Since neither the 10-20% or 20-40% centrality spectra show significant excesses this exercise is not performed on these spectra.

Figure 8.16 shows the unlike- and like-sign spectra with and without the additional subtraction, the blue points are the data as previously subtracted and the purple points are the data with the additional factor of the total background removed. Comparing the unlike-
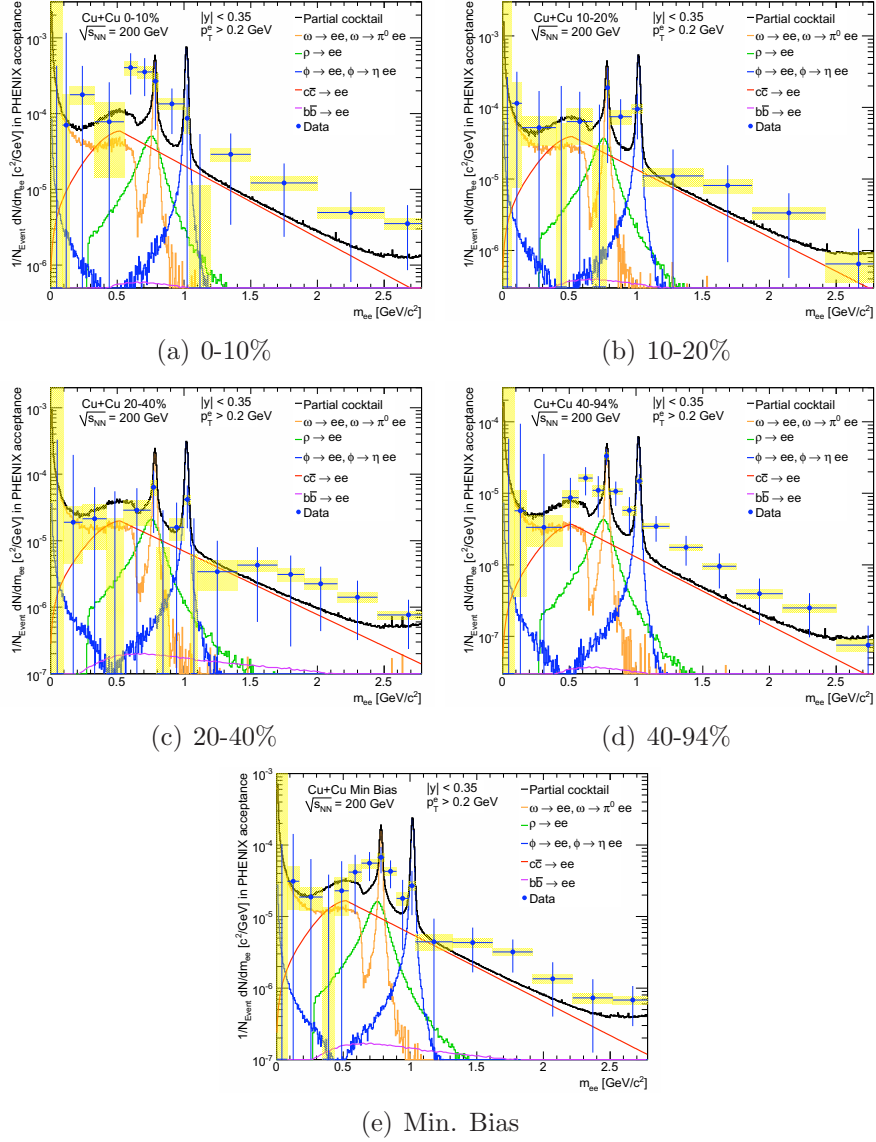
(a) 0-10%

(b) 10-20%

(c) 20-40%

(d) 40-94%

(e) Min. Bias

Figure 8.14: The Cu+Cu dielectron spectra with the π, η and η' cocktail signals subtracted compared to a partial cocktail where the π, η and η' are also removed. The correlated charm and bottom components are shown and included in the partial cocktail. The Drell-Yan component is included in the partial cocktail but it is not shown because it has a negligible yield in this mass region.
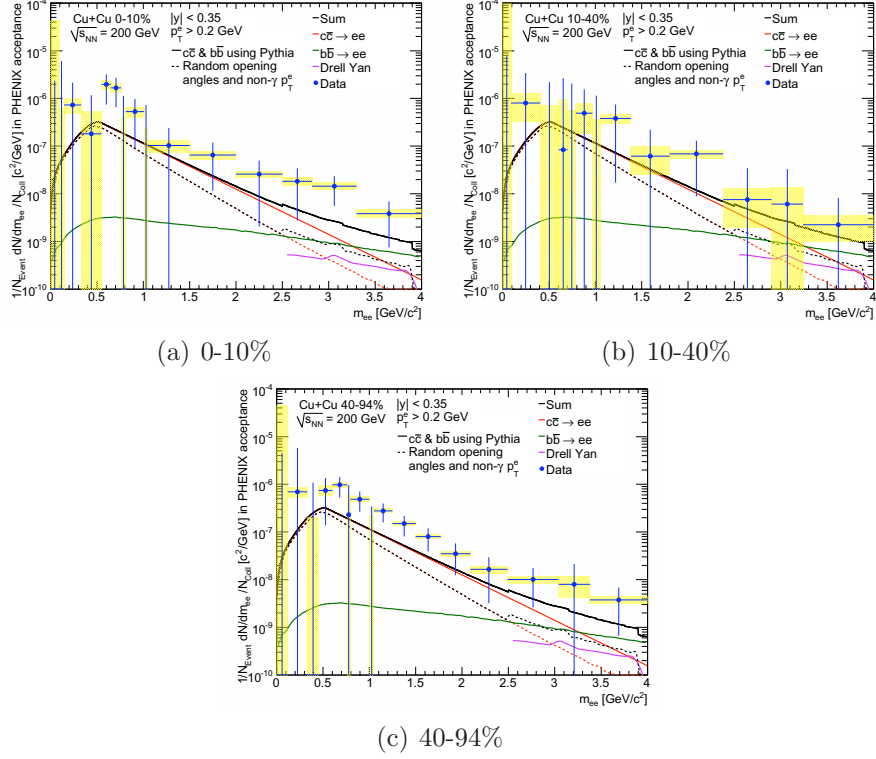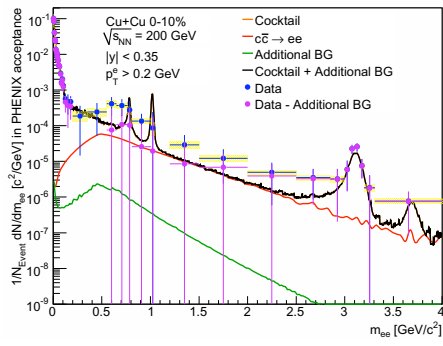
(a) 0-10%

(b) 10-40%

(c) 40-94%

Figure 8.15: The 0-10%, 10-40% and 40-94% spectrum scaled by N_{Coll} with the hadronic components removed using the cocktail. The charm, bottom and Drell Yan correlations simulated with Pythia are also shown with the heavy quark component simulated using the measured non-photonic single electron p_T spectrum and random angular correlations.
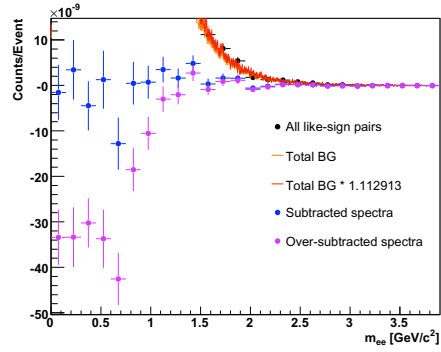
(a) 0-10%, Unlike-sign spectrum
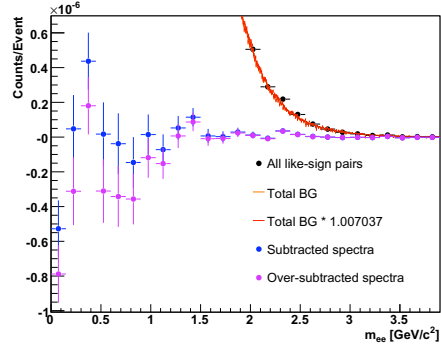
(b) 0-10%, Like-sign spectrum
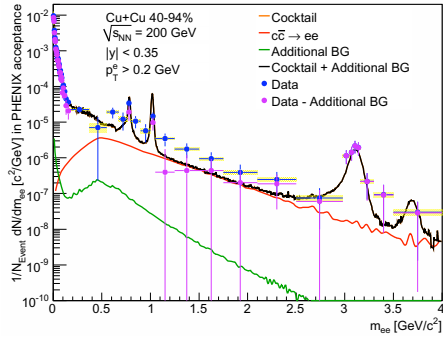
(c) 40-94%, Unlike-sign spectrum

(d) 40-94%, Like-sign spectrum

Figure 8.16: The subtracted spectrum (blue) is shown with the same spectrum where an additional 0.7% or 11% of the total background is removed (purple) for the 0-10% and 40-94% centralities respectively. On the left, the efficiency corrected unlike-sign spectrum is compared to the cocktail (black). The additional efficiency corrected background (green) is also shown. On the right the like-sign spectra is shown with the total background increased by the same factor as in the unlike-sign. The like-sign spectrum and backgrounds are not efficiency corrected.

140

Table 8.7: Like-sign yields with and without the additional subtraction

| Centrality	Yield	Yield with additional subtraction
$0-10\%$	$-2.48 * 10^{-6} \pm 2.75 * 10^{-3}$	$-1.23 * 10^{-2} \pm 2.75 * 10^{-3}$
$40-94\%$	$-3.84 * 10^{-7} \pm 9.23 * 10^{-5}$	$-1.23 * 10^{-3} \pm 9.24 * 10^{-5}$

sign spectra with the additional background subtraction to the cocktail in the regions of the earlier determined excess, 0.54-0.75 GeV/c^2 for 0-10% and 1.2-2.87 GeV/c^2 for 40-94%, confirms that this additional subtraction method does remove these excesses. In Figures 8.16(a) and 8.16(c) the unlike-sign spectra result is over-subtracted and has negative yields in the mass region between 0.2-0.5 GeV/c^2 for the 0-10% and 0.2-1.2 GeV/c^2 for the 40-94%.

The effect of the additional subtraction on the like-sign spectra is shown in Figures 8.16(b) and 8.16(d). A further reduction of the like-sign spectra brings it significantly below zero for masses below 1 GeV/c^2. Since the signal to background ratio for the excess in the most central spectrum is a smaller than the excess in the peripheral spectrum this additional subtraction has a larger effect on the peripheral spectrum. Table 8.7 shows the variation in the like-sign yields with the standard subtraction and with the additional subtraction. The like-sign yields are taken over the entire mass region. The expected like-sign yield is zero. An order of magnitude over-subtraction of the like-sign yield results from the additional subtraction needed to remove the excess above the cocktail in the unlike-sign spectra. For both centrality groups the over-subtraction is larger than the error of the integrated yield. This confirms that the excesses above the cocktail are not the result of insufficient subtraction of the known background components but are the result of additional physics signals in the spectra.

8.3.1 Comparison to data in p_T slices

To study these enhancements at low and intermediate masses, we consider the spectra as a function of p_T. This is done by slicing the mass spectra in various p_T ranges for both the data and the cocktail. The p_T ranges 0-1, 1-2, 2-3, and 3-5 GeV/c are used. Figure 8.17 presents this for each of the centrality groups with the various p_T slices scaled for visual clarity.

In the 0-10% centrality group the majority of the low mass enhancement is evident at low p_T. However we also see an excess in both the low and intermediate mass regions in the high p_T slices. These high p_T excesses have a larger excess relative to the cocktail but they are produced at a lower rates than the low p_T excess. The 10-20% and 20-40% spectra do not have an excess in the low mass region at low p_T, but they also see smaller excesses at high p_T's in the low and intermediate masses. In the 40-94% spectrum the majority of the intermediate mass enhancement is in the low p_T slice. The trend of smaller excesses at high p_T for the low and intermediate masses continues in the peripheral spectrum. For the
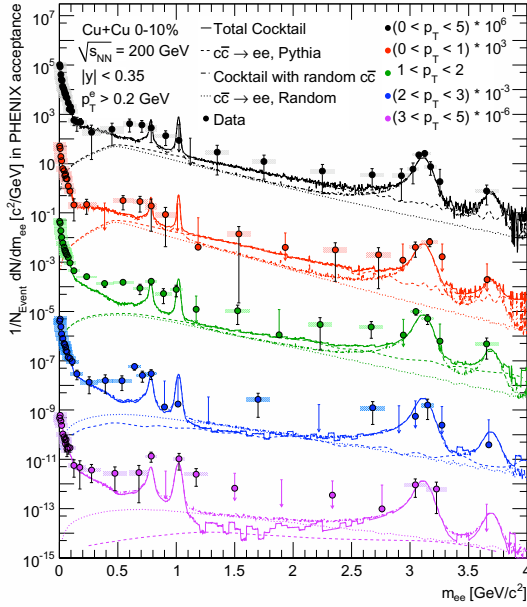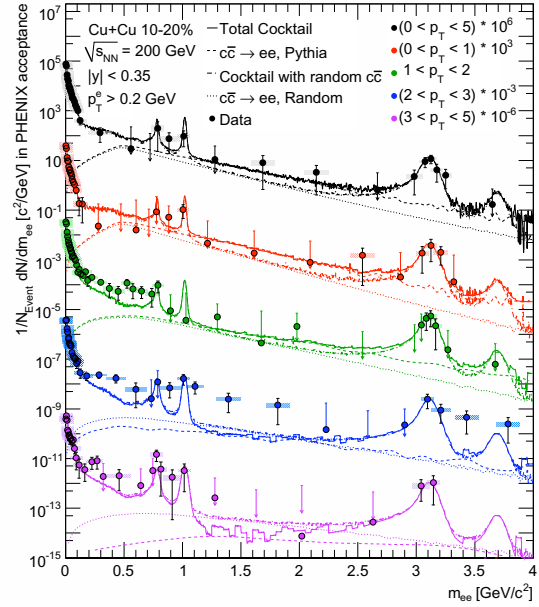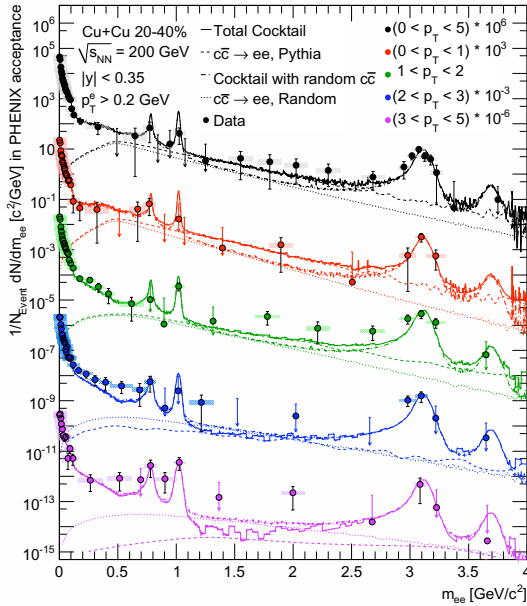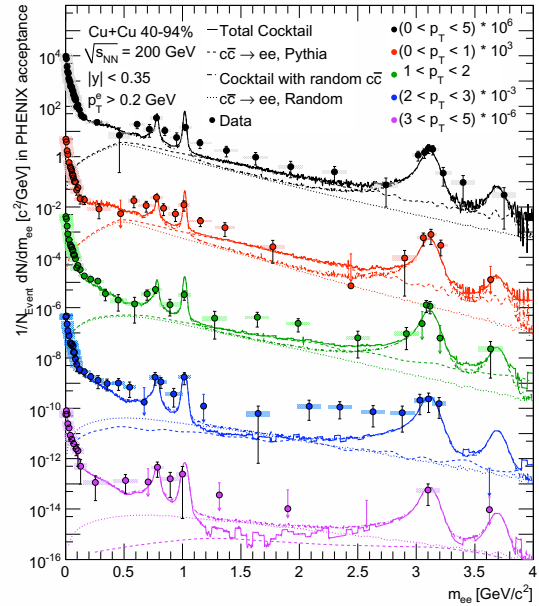
Figure 8.17: Data and cocktail comparison for all p_T slices shown by centrality. The cocktail contains the hadronic and charm components but not the correlation due to bottom or Drell-Yan. A second cocktail contains the random heavy quark contributions. The cocktails are shown with the data in the same color. The systematic error band for each point is presented in the same tone.

20-40% and 40-94% these high p_T excesses are seen at p_T's above 2 GeV/c. The 0-10% and 10-20% spectra show similar excesses down to p_T's of 1 GeV/c.

Chapter 9

Comparisons and Conclusions

The Cu+Cu mass spectra are compared to the measured dilepton spectra in different collision systems and theoretical calculations. These comparisons provide an additional mechanism to study the enhancements in the dilepton mass spectra. Comparisons to the other PHENIX dielectron spectra will be presented with reference to results from other experiments when relevant. The theoretical comparisons use scaled Au+Au calculations applied to the central Cu+Cu dielectron measurement. Finally conclusions and ideas for future measurements are presented.

9.1 Comparison to other systems

The PHENIX $\sqrt{s_{NN}} = 200$ GeV p+p and minimum bias d+Au and Au+Au dielectron spectra are presented in Figure 9.1 with their respective hadronic cocktails. The p+p spectrum uses 2005 triggered data from $\sqrt{s_{NN}}=200$ GeV p+p collisions [40]. This measurement was completed by Torsten Dahms. The p+p measurement shows the dielectron spectrum without the any quark gluon plasma effects. It agrees very well with the hadronic cocktail, so much so that an independent charm cross section was determined from this measurement [66]. The good agreement in p+p provides confidence in the hadronic cocktail simulation.

The minimum bias d+Au spectrum uses 2008 triggered data from $\sqrt{s_{NN}} = 200$ GeV d+Au collisions at PHENIX [102]. This analysis is the preliminary work of Jason Kamin. The d+Au spectrum also agrees very well with the cocktail. Cold nuclear matter effects have no effect on the dilepton mass spectrum. This is in agreement with the proton+nucleus dilepton measurements at CERES [59] and NA60 [65].

The Au+Au dielectron result uses 2004 minimum bias data from $\sqrt{s_{NN}} = 200$ GeV collisions at PHENIX [40]. This measurement was a first of its kind analysis completed by Alberica Toia. The Au+Au spectra shows a large excess above the cocktail in the low mass region extending from 0.15 to 0.75 GeV/c^2. As with the p+p and d+Au spectra, the data reproduces the π, ω, ϕ and J/ψ resonances. All three spectra agree in the intermediate mass

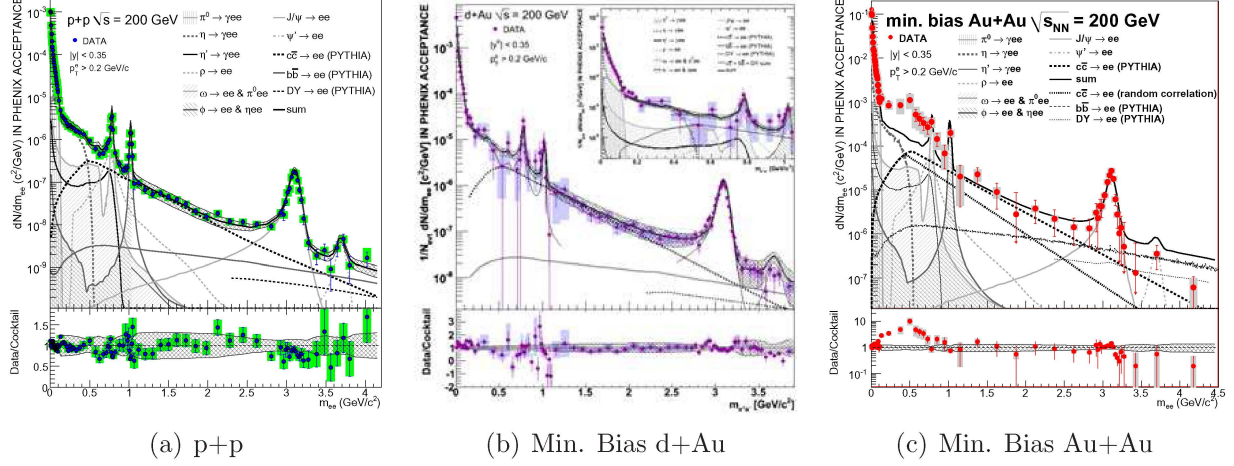|		
(a) p+p	(b) Min. Bias d+Au	(c) Min. Bias Au+Au

Figure 9.1: The PHENIX dielectron mass spectrum in p+p, d+Au and Au+Au at $\sqrt{s_{NN}} = 200$ GeV. The p+p and Au+Au spectra are published [40], the d+Au spectrum is a preliminary result [102].

region with the correlated charm contribution calculated by Pythia.

The variation of the mass spectra with centrality is shown in Figure 9.2; all of the PHENIX dielectron mass spectra are scaled and shown in N_{Coll} order. In this comparison it is apparent that the very substantial low mass excess seen in central Au+Au collisions decreases as the collisions become more peripheral. The comparison of the 0-10% Au+Au, 10-20% Au+Au and 0-10% Cu+Cu spectra scaled by $1/N_{Part}$, in Figure 9.3(a), nicely shows the excess increasing in yields and extending to lower masses as collisions become more central. Figure 9.3(b) shows the shape comparison of the 40-60% and 60-92% Au+Au spectra with the 40-94% Cu+Cu. The peripheral Cu+Cu intermediate mass excess, not seen in the p+p or d+Au spectra, is also evident in the 40-60% and 60-92% Au+Au spectra.

For a more quantitative understanding of the low mass enhancement the scaled yields as a function of centrality are presented in Figure 9.4 for various collision systems. Figure 9.4(a) shows the PHENIX dielectron yields in the very low and low mass regions. Figure 9.4(b) shows the CERES 158 AGeV Pb+Au enhancement factor, the ratio of the yield over the cocktail, as a function of multiplicity, $dN/d\eta$, for masses below 0.2 GeV/c^2 and between 0.2 and 0.6 GeV/c^2. Both of the plots show good agreement with the cocktail at very low masses, in the region where the pion Dalitz decay dominates. This agreement provides confidence that the efficiency correction is applied properly. At low masses, between 0.15 and 0.75 or 0.2 and 0.6 GeV/c^2, there is a remarkable excess that increases faster than linear with centrality for both the PHENIX and CERES data.

The yields in the intermediate mass range as a function of N_{Part} are presented in Figure 9.5 for various collision systems. Figure 9.5(a) shows the PHENIX yields in the intermediate
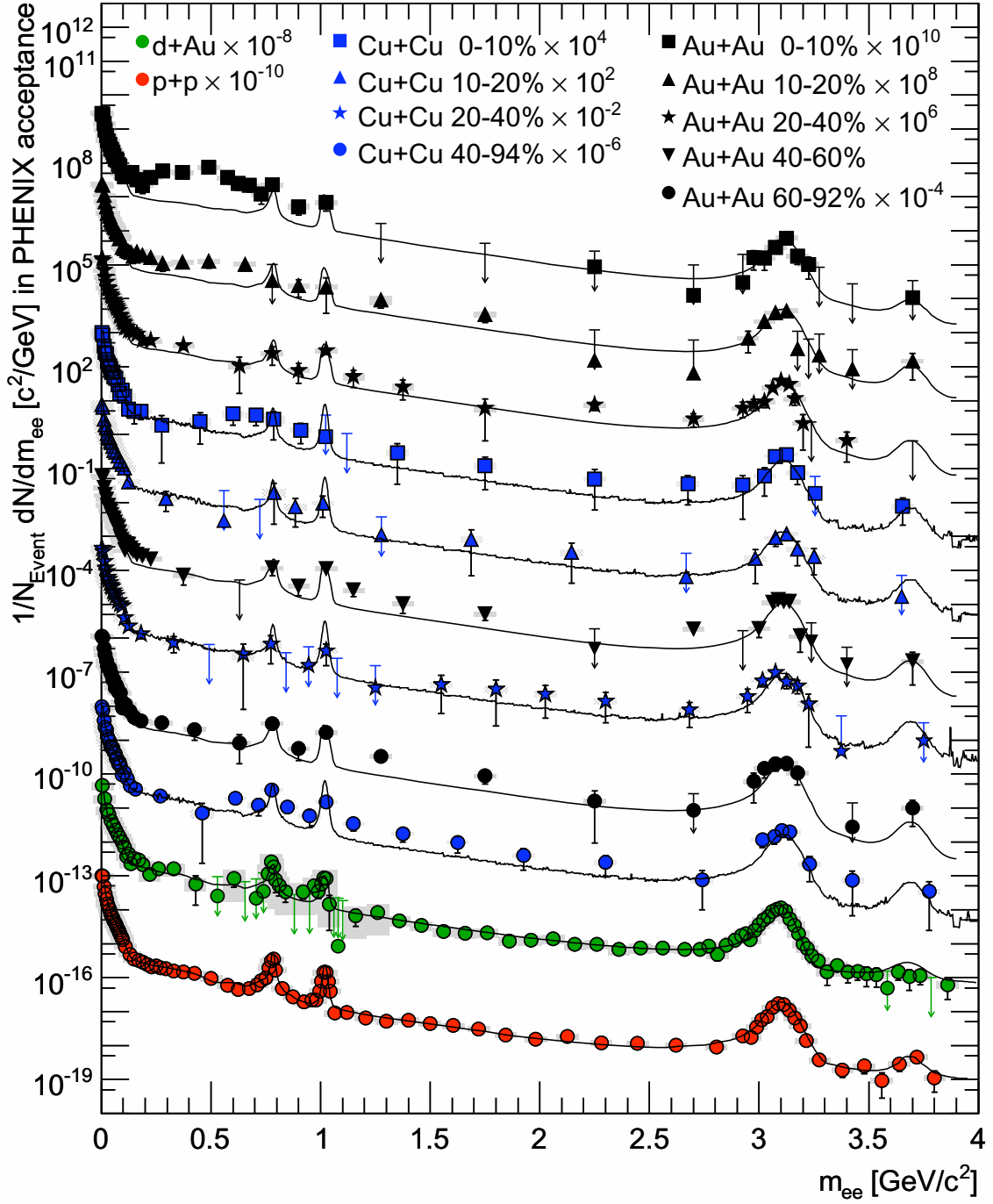
Figure 9.2: All of the PHENIX dielectron measurements in each system in N_{Coll} order. The Au+Au spectra are shown in black, the Cu+Cu spectra are in blue, the d+Au spectrum is green and the p+p spectrum is red. Each spectra is compared to it's cocktail using the Pythia heavy quark correlated components. The spectra are scaled as listed in the legend.
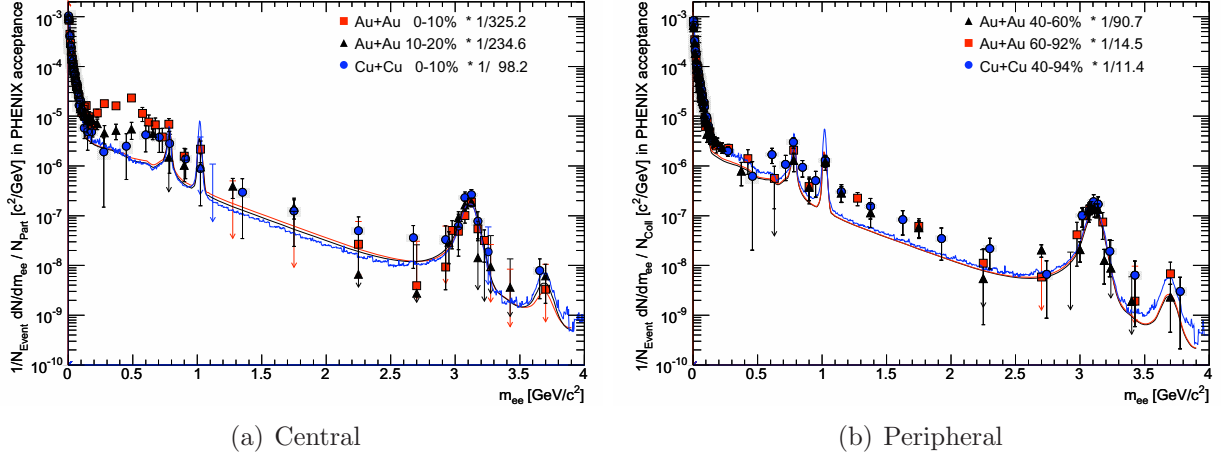
(a) Central   (b) Peripheral

Figure 9.3: On the left, PHENIX 0-10% and 10-20% Au+Au and the 0-10% Cu+Cu dielectron spectrum are shown scaled by $1/N_{Part}$. On the right, the PHENIX 40-60% and 60-94% Au+Au and the 40-94% Cu+Cu dielectron spectra are shown scaled by $1/N_{Coll}$. The respective cocktails for the various spectra are also shown.

mass region, from 1.2 to 2.87 GeV/c^2, scaled by N_{Coll} with the expected correlated heavy quark yields, the charm correlations from Pythia and the random heavy quark component. The p+p and d+Au agree well with the expected correlated charm yields from Pythia. The most central Cu+Cu and peripheral Cu+Cu and Au+Au yields are somewhat larger than expected; this reflects the behavior seen in Figure 9.3(b) and in Chapter 8. Figure 9.5(b) presents NA60's 158 AGeV In+In excess factors in the mass region, 1.16 to 2.56 GeV/c^2. The NA60 data show a clear increase in the enhancement with at a rate of N^2_{Part}. The NA60 enhancement is from a thermal photon source. It differs from the Drell Yan mass shape and is not due to off-vertex decays as heavy quark correlated pairs are. The higher energies obtained at RHIC result in increased heavy quark production rates. The PHENIX yields at intermediate masses may also contain thermal photons or heavy quark modifications. Unfortunately, the error bars in PHENIX yields in the intermediate range are sufficiently large that no trend in centrality can be seen beyond N_{Coll} scaling.

The p+p and Au+Au mass spectra have been further studied differentially in p_T. This is published in the 0 to 1.2 GeV/c^2 mass range [40] but recently extended out to masses of 4 GeV/c^2. The d+Au spectrum is not yet available in p_T slices. The substantial Au+Au low mass excess is primarily in the lowest p_T range below 1 GeV/c. Smaller excesses are seen in the high p_T slices at low and the intermediate masses for both the p+p and minimum bias Au+Au spectra. The majority of the low mass excess is in the low p_T spectrum. The 158 AGeV Pb+Au CERES dilepton spectrum shows a similar trend for p_T's above and below 0.5 GeV/c, Figure 9.7. The high p_T CERES spectrum has a similar falling trend extending
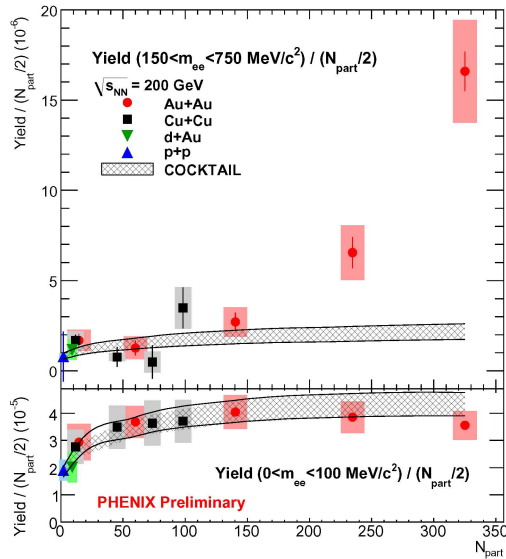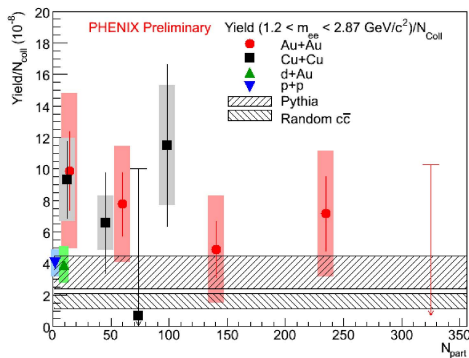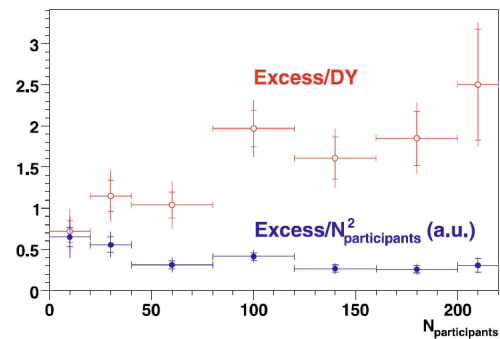
(a) PHENIX
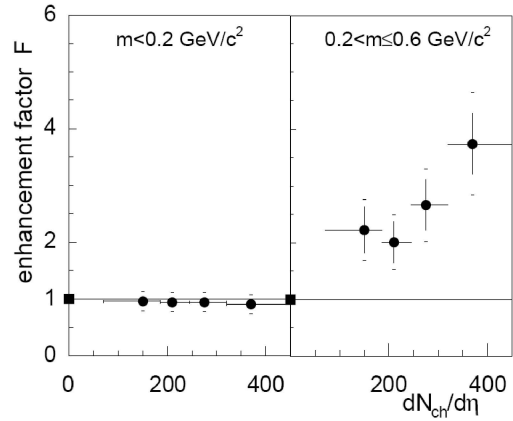
(b) CERES

Figure 9.4: The low mass dilepton excess as a function of centrality. On the left, the yields per N_{Part} from the PHENIX data in each collision system are presented as a function of N_{Part} with the expected cocktail yields. On the right, the 158 AGeV Pb+Au CERES low mass excess is presented as an enhancement factor (yield/cocktail) as a function of multiplicity, $dN/d\eta$.

(a) PHENIX

(b) NA60

Figure 9.5: The intermediate mass dilepton yield as a function of N_{Part}. On the left, the yields per N_{Coll} from the PHENIX data in each collision system are presented with the expected correlated charm yields. On the right, the NA60 158 AGeV In+In dilepton excess factors in the mass range 1.16 and 2.56 Gev/c^2 are presented. [65]
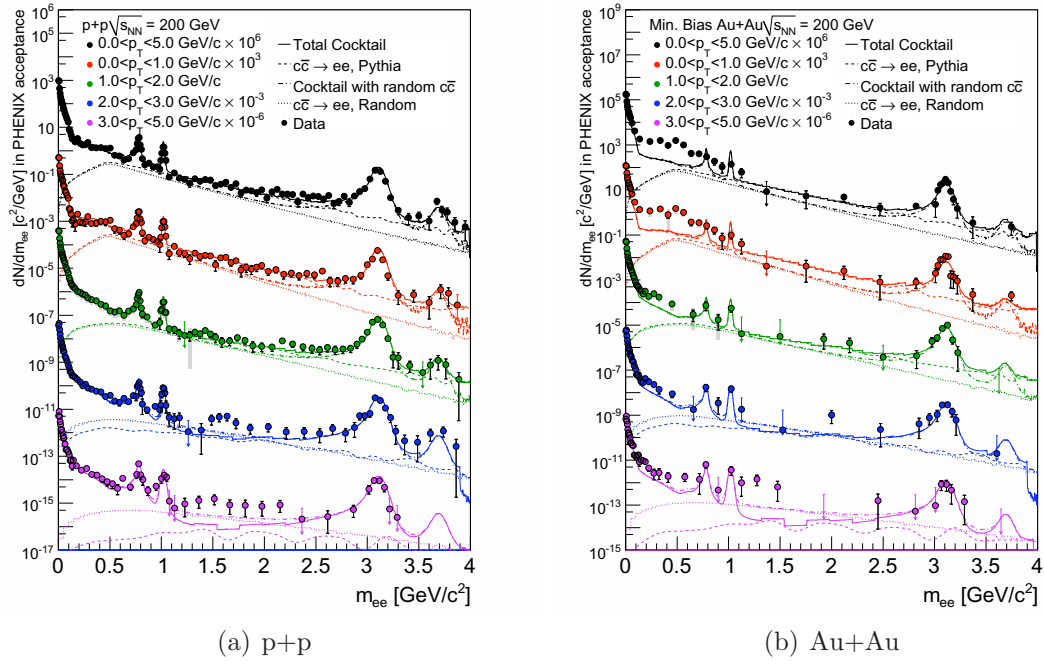
148

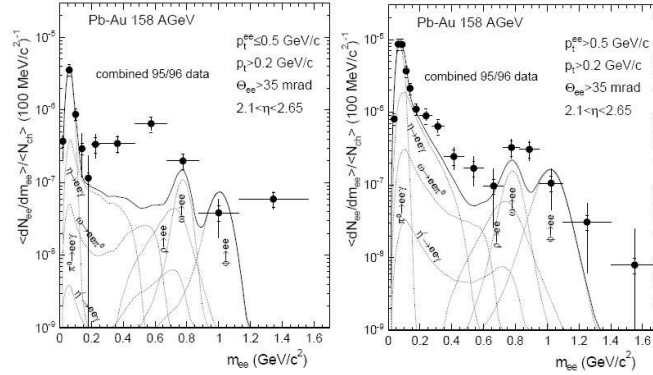Figure 9.6: The PHENIX p+p and minimum bias Au+Au at dielectron mass spectra in p_T slices. [40]

Figure 9.7: The CERES 158 AGeV Pb+Au spectra divided by p_T above and below 0.5 GeV/c. [59]

to masses above the ϕ as is seen in the high p_T heavy ion PHENIX spectra.

In Figure 9.8, the shapes of the p+p, Cu+Cu and Au+Au p_T sliced mass spectra are compared. The lowest p_T slice, $0 < p_T < 1$ GeV/c, contains the majority of the low mass excess in the minimum bias Au+Au and central Cu+Cu spectra and the intermediate mass excess in the peripheral Cu+Cu spectrum. Between p_T's of 1 and 2 GeV/c, the minimum bias Au+Au and 0-10% and 10-20% Cu+Cu show a large excess in the low mass region. The peripheral Cu+Cu and p+p show a much smaller excess in this region with some of the yield extending to higher masses. The $2 < p_T < 3$ and $3 < p_T < 5$ GeV/c slices show significant yields in the low and intermediate masses for all of the spectra. The more central collisions appear to have increased yields at the low masses. The intermediate mass excesses appear to be an extension of the low mass excess suggesting that they are also photonic in origin. However, the high p_T cocktail comparisons must be cautioned because the cocktail in these p_T slices contains the only correlated charm component. The bottom and Drell Yan components are not included. At higher p_Ts, we expect that the bottom contribution will become more significant at lower masses. The additional cocktail line with random heavy quark correlations contains both the charm and bottom contribution. It is still below the high p_T spectra, but above the cocktail with the Pythia charm correlations.

Figure 9.9 contains the scaled yields in the low and intermediate mass regions as a function of p_T. The data are compared with the expected cocktail yields. The lower plot in Figure 9.9(a) shows that the N_{Part} scaled yields for masses below 0.1 GeV/c^2. These agree well with the cocktail yields as a function of p_T. The upper plot shows N_{Part} scaled yields in the mass region 0.15 to 0.75 GeV/c^2. The minimum bias Au+Au and 0-10%, 10-20% Cu+Cu yields are above the cocktail for p_T above 1 GeV/c. Below 1 GeV/c, the minimum bias Au+Au has a large excess but the Cu+Cu measurements are less significant. The scaled yield for the 0-10% Cu+Cu is in agreement with the cocktail in this range; this is most likely because
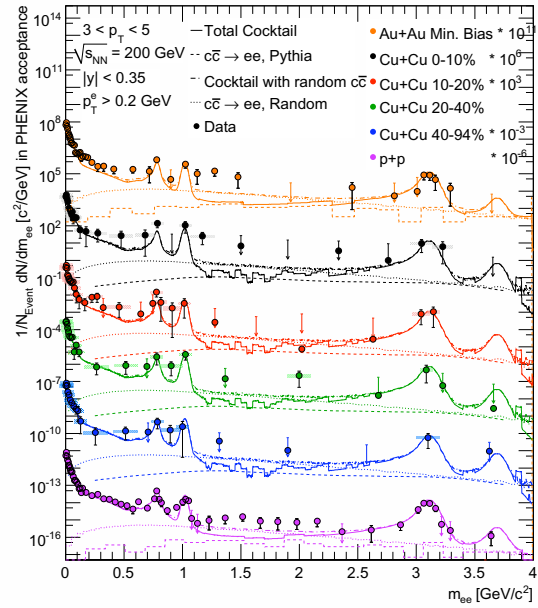
150
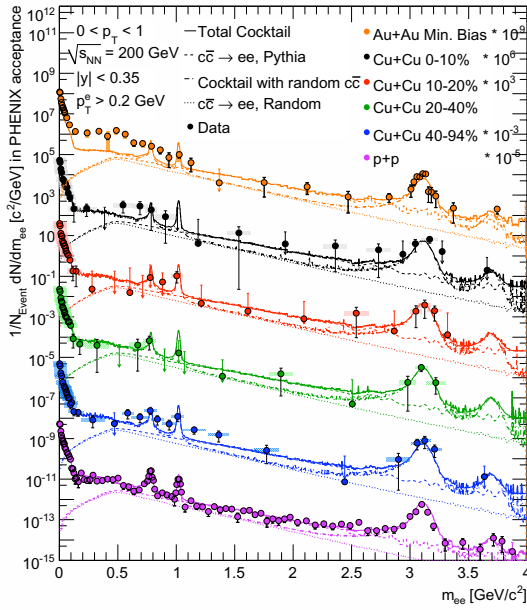
(a) $0 < p_T < 1$ GeV/c
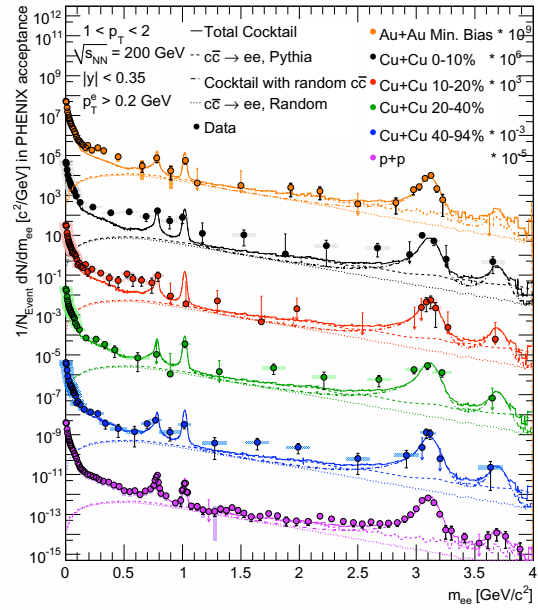
(b) $1 < p_T < 2$ GeV/c
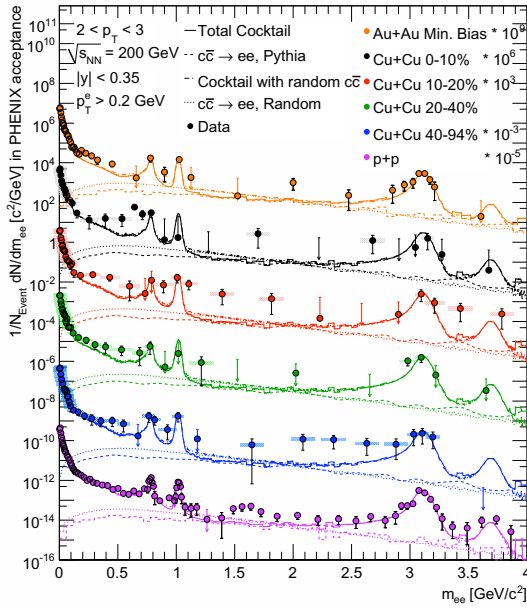
(c) $2 < p_T < 3$ GeV/c

(d) $3 < p_T < 5$ GeV/c

Figure 9.8: The p+p, Cu+Cu and Au+Au PHENIX dielectron mass spectra in the p_T ranges 0-1, 1-2, 2-3 and 3-5 GeV/c.
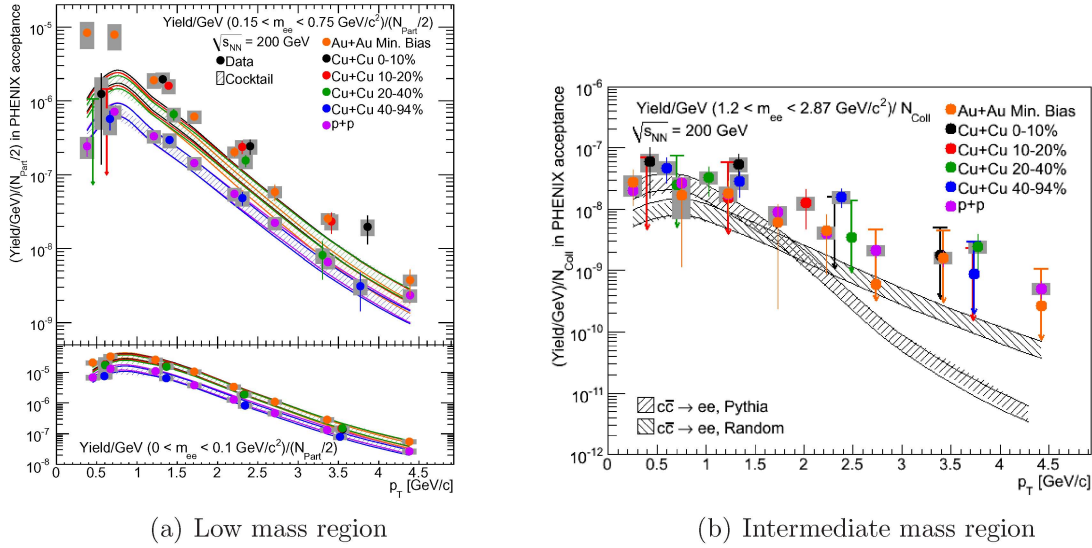
151

(a) Low mass region

(b) Intermediate mass region

Figure 9.9: The PHENIX dielectron yields as a function of p_T in each system.

the mass window extends down to 0.15 GeV/c^2 and the Cu+Cu low mass excess does not go below 0.5 GeV/c^2 in mass.

Figure 9.9(b) shows the N_{Coll} scaled yields in the intermediate mass region as a function of p_T. All of the yields are above the expected yields for p_T above 1 GeV/c. The most striking feature of this plot is that the p_T dependance of the yield seen in the data does not match the correlated charm trend from Pythia. This is not unexpected. Pythia does not reproduce the measured p+p non-photonic single electron p_T spectrum [88]. The addition of a correlated bottom component may ease the discrepancy at high p_T.

At very low masses, between 0.12 and 0.3 GeV/c^2, and p_T's above 1 GeV/c the excesses in the PHENIX p+p and Au+Au spectra are identified as virtual direct photons. The p+p and Au+Au spectra in this region illuminate the low momentum photon spectrum resulting in a determination of the initial temperatures of the Au+Au system between 300 and 600 MeV. The direct virtual photon measurement was pioneered in the p+p and Au+Au dielectron continuum measurement. [42] [40]

The direct photon shape is modeled using Kroll-Wada formulaism filtered into the PHENIX acceptance. Once the direct virtual photon line shape is determined, the dielectron spectrum is fit in high p_T ranges with the cocktail and the simulated direct photon component, Equation 9.1.

$$f_{data} = (1 - r_{\gamma^*}) \, f_{cocktail} + r_{\gamma^*} f_{direct} \tag{9.1}$$

where $f_{cocktail}$ is the cocktail line shape, f_{direct} is the direct photon component and the r_{γ^*} parameter is the ratio of the direct virtual photon over the inclusive virtual photon. A fit

with a r_{γ^*} value of zero means that the cocktail fully describes the data and there is no virtual photon component. A fit with a r_{γ^*} parameter of one means that all dielectron pairs are from direct virtual photons and there are no pairs from hadronic decays.

(a) Min. Bias Cu+Cu spectrum

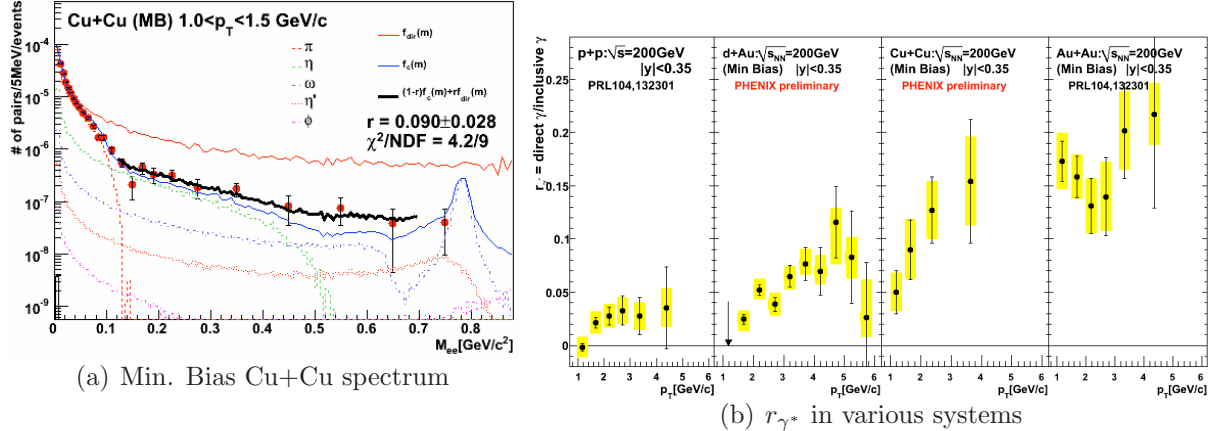(b) r_{γ^*} in various systems

Figure 9.10: On the right, f_{direct} and $f_{cocktail}$ are shown with an independantly analyzed high p_T Min. Bias Cu+Cu spectrum. Both the data and the simulations are filtered into the PHENIX aperture for the p_T range between 1 and 1.5 GeV/c. The data is fit with Equation 9.1 in the mass region 0.15 to 0.3 GeV/c^2 to find the amplitude of the direct virtual photon component, r_{γ^*}. The resulting fit is shown in the range 0.15 to 0.7 GeV/c^2. On the left, the various r_{γ^*} values are shown as a function of the dielectron pair's p_T for Cu+Cu, Au+Au, p+p and d+Au collisions. These are compared with theoretical pQCD calculations of the direct virtual photon fraction [103]. [104]

An independent dielectron analysis has extrapolated the direct photon component for the minimum bias Cu+Cu spectrum. This is a preliminary result by Daisuke Watanabe [104]. Figure 9.10(a) shows this fit for the Min. Bias Cu+Cu spectrum sliced in the p_T range 1 to 1.5 GeV/c and fit over mass range 0.15 to 0.3 GeV/c^2, the fit function is shown from 0.15 to 0.7 GeV/c^2. These fits are calculated in various p_T slices and the r_{γ^*} value is determined for each. Figure 9.10(b) shows the r_{γ^*} parameter as a function of the dielectron pair p_T ranges. It is clear from Figure 9.10(a) that the direct photon line shape is consistent with the high p_T dielectron spectrum out to masses of 0.7 GeV/c^2. It may hold at even higher masses in the Au+Au spectrum accounting for some of the excesses in the intermediate mass region.

9.2 Theoretical comparisons

Little theoretical work has been done in the Cu+Cu system. The one exception is a study of the hadronic contribution using a statistical hadronization model that includes an increases

in the relative strangeness production [105]. In Cu+Cu the hadronic contribution from the statistical hadronization model agrees with the hadronic cocktail describe in Chapter 8. The low mass excess is not explained.

The PHENIX $\sqrt{s_{NN}} = 200$ GeV minimum bias Au+Au spectrum was compared to theories from three groups, one for each panel in Figure 9.11(a). On the left, curves by Rapp and van Hees are presented. Rapp and van Hees calculate a broadened ρ as a result of hadronic many-body interactions in the hadron gas as described in Chapter 1. They also produce a dropping mass curve to represent Brown-Rho scaling. The center plot contains HSD curves made by Cassing, Bratkovskaya and Linnyk, these curves follow the PHSD method described in Chapter 1. Both a broadened ρ and a broadened and dropping ρ curves are presented. The rightmost plot shows theory curves from Dusling and Zahed [106]. These are calculated using a chiral reduction formulism to calculate the effects on the ρ in the hadron gas. A partonic component from quark annihilation is also included. None of the theories adequately describe the Au+Au low mass excess particularly in the region below 0.6 GeV/c^2.

We extend the theoretical calculations for the Au+Au system to the central Cu+Cu measurement. This is done by scaling the theoretical hadronic yields by N_{Part} and the partonic yields by N_{Coll}. These scaled theoretical contributions are added to the Cu+Cu cocktail with the ρ meson excluded. The ρ is not included in the cocktail because the theoretical hadronic components contain the ρ component. Figure 9.11(b) presents a comparison between the 0-10% Cu+Cu data and the scaled theoretical contributions. The 0-10% Cu+Cu data is well described by the Rapp and van Hees and the HSD lines at low masses. Unfortunately the data are unable to distinguish between the dropping and broadening curves in the Rapp and van Hees comparison and the broadened and dropping ρ from HSD.

The theoretical comparison can be further tested by comparing them to the spectra differentially in p_T. Figure 9.12 shows the minimum bias Au+Au and central Cu+Cu spectra in the p_T ranges, $0 < p_T < 1$ GeV/c and $1 < p_T < 2$ GeV/c. In the lowest p_T range the Cu+Cu spectrum is well described by both the Rapp and van Hees and HSD curves. This suggests that the low mass excess in Cu+Cu collisions is a result of modified ρ mesons produced in pion annihilation in the hadronic gas phase. In the 1-2 GeV/c p_T range, the similarities between Rapp and van Hees and Dusling and Zahed for both the hadronic and partonic components are evident. The excess yield is not described by the theories. The HSD curves come the closest to describing the low mass excess in the 1-2 GeV/c p_T range. However, another dielectron source is evident. The direct virtual photon component mentioned earlier in this chapter is the high p_T low mass dielectron source.

9.3 Conclusions

In conclusion, the central Cu+Cu spectrum shows a low mass excess above the hadronic cocktail. The low mass excess in Cu+Cu is smaller than the large excess seen in Au+Au
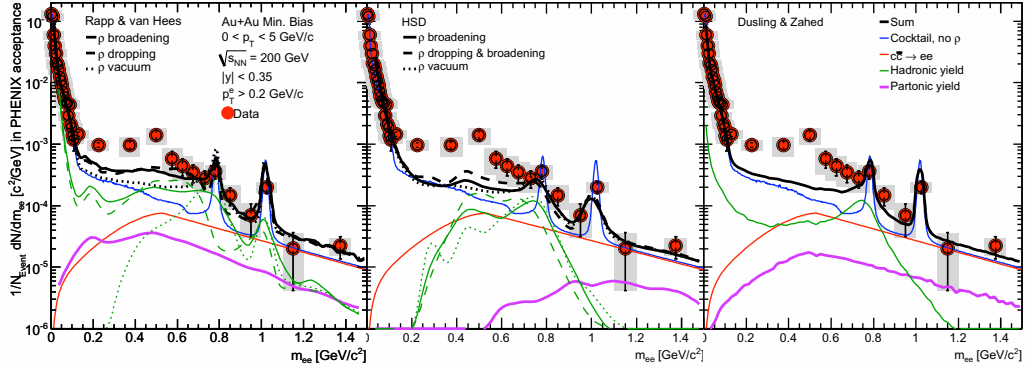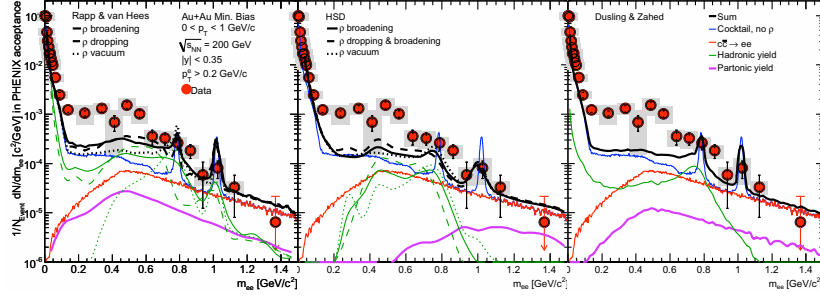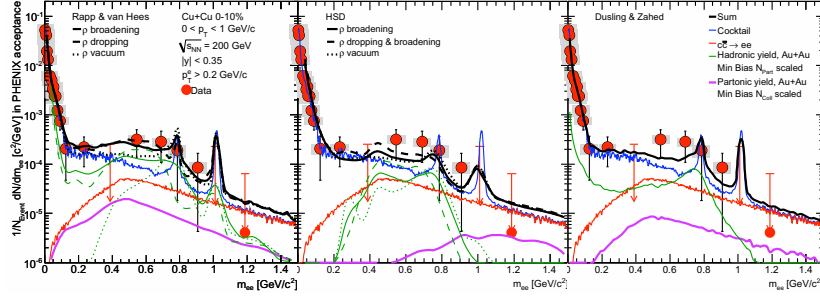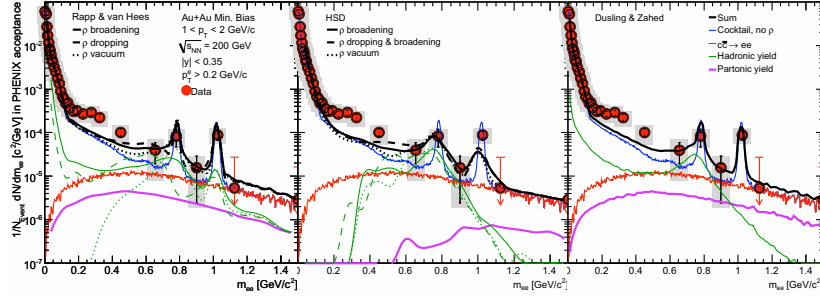
(a) Au+Au Min. Bias
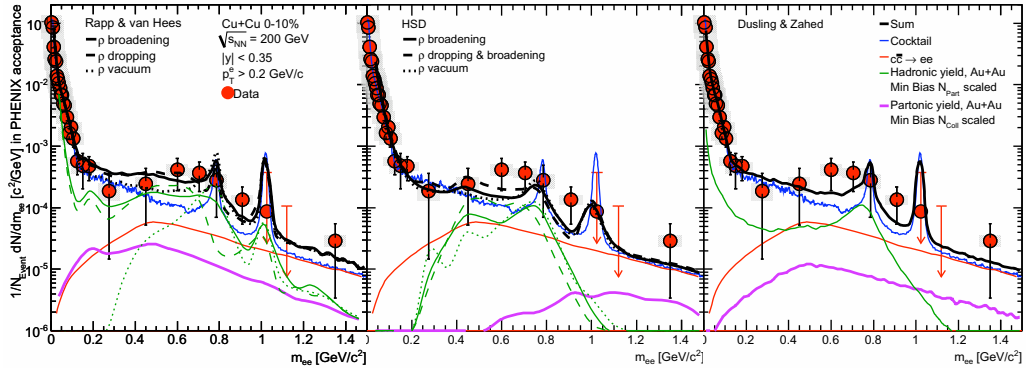
(b) 0-10% Cu+Cu

Figure 9.11: The low mass PHENIX dielectron spectra in Min Bias Au+Au and 0-10% Cu+Cu compared to theoretical curves from Rapp and van Hees, Cassing an Bratkovskaya, and Dusling and Zahed. The Cu+Cu hadronic and partonic curves are N_{Part} and N_{coll} scaled versions of the Au+Au. [40]

(a) Au+Au Min. Bias, $0 < p_T < 1$ GeV/c

(b) 0-10% Cu+Cu, $0 < p_T < 1$ GeV/c

(c) Au+Au Min. Bias, $1 < p_T < 2$ GeV/c

(d) 0-10% Cu+Cu, $1 < p_T < 2$ GeV/c

Figure 9.12: The low mass p_T sliced PHENIX dielectron spectra in Min Bias Au+Au and 0-10% Cu+Cu compared to theoretical curves from Rapp and van Hees, Cassing an Bratkovskaya, and Dusling and Zahed. The Cu+Cu hadronic and partonic curves are N_{Part} and N_{coll} scaled versions of the Au+Au. [40]
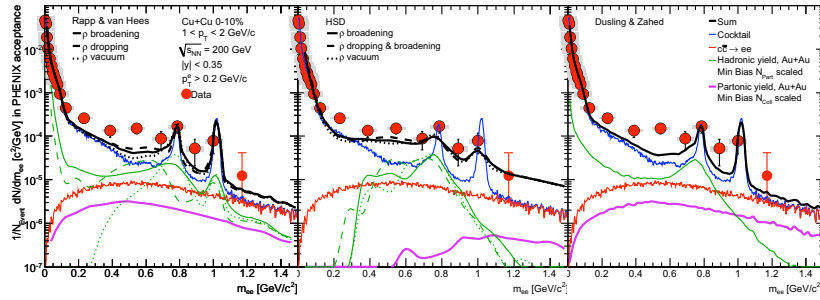
and only extends down to masses of 0.54 GeV/c^2. Shape comparisons with the 0-10% and 10-20% Au+Au spectra suggests that as collisions become more central the low mass excess grows faster than linear with N_{Part} and extends to lower masses. When the low mass excess is considered differentially in p_T, the majority of the yield is located at low p_T. The low p_T, low mass excess in 0-10% Cu+Cu is well described by theory curves from many-body hadronic interactions and hadron string dynamics.

There exists additional excess yields at high p_T in both the low and intermediate mass regions. The high p_T, low mass excess is described by direct virtual photons. In intermediate masses the excess is most likely due to a combination of bottom correlations and direct photon contributions.

Future of the dielectron measurements at PHENIX will benefit new detector systems and increased statistics. The Silicon Vertex Detector [107] will allow us to determine secondary vertices. It will allow future measurements to discern between intermediate mass dielectron pairs from correlated heavy quarks and those from direct photons. The Hadron Blind Detector detector (HBD) [108] reduces backgrounds by identifying electrons from pion Dalitz decay and conversions and removing them from our electron sample before making pairs. Not only are the pion Dalitz and conversion background pairs removed but the combinatorial backgrounds will be drastically reduced. This detector successfully took p+p data in 2009 and Au+Au data in 2010; analyses of this data are in progress.

Bibliography

[1] O. Linnyk, Journal of Physics G: Nuclear and Particle Physics **38**, 025105 (2011).

[2] K. Nakamura et al. (Particle Data Group), Journal of Physics G **37**, 075021 (2010), URL http://pdg.lbl.gov/index.html.

[3] D. Griffiths, *Introduction to Elementary Particles* (John Wiley and Sons, Inc., New York, NY, 1987).

[4] This assumes running coupling where $\alpha_S = 0.39$.

[5] F. Halzen and A. D. Martin, *Quarks and Leptons: An Introductory Course in Modern Particle Physics* (John Wiley and Sons, Inc., New York, NY, 1984).

[6] S. Bethke, Progress in Particle and Nuclear Physics **58**, 351 (2007).

[7] J. Bartke, *Introduction to Relativistic Heavy In Physics* (World Scientific, Hackensack, NJ, 2009).

[8] M. Nguyen, Ph.D. thesis, Stony Brook University, Stony Brook, NY (2009).

[9] C.-Y. Wong, *Introduction to High-Energy Heavy-Ion Collisions* (World Scientific, New York, NY ??, 1994).

[10] K. Adcox et al., Nuclear Physics A **757**, 184 (2005).

[11] J. C. Collins and M. J. Perry, Physics Review Letters **34**, 1353 (1975).

[12] N. Cabibbo and G. Parisi, Physics Letters B **59**, 67 (1975).

[13] E. Shuryak, Physics Letters B **78**, 150 (1978).

[14] R. Rapp and J. Wambach, Advances in Nuclear Physics **25**, 1 (2000).

[15] R. Vogt, *Ultrarelativistic Heavy-Ion Collisions* (Elsevier, New York, NY, 2007).

[16] V. Koch, International Journal of Modern Physics E **6**, 203 (1997).

[17] S. Weinberg, Physical Review Letters **18**, 507 (1967).

[18] J. Goldstone, Il Nuovo Ciment **19**, 155 (1961).

[19] G. Sterman, *An Introduction to Quantum Field Theory* (Cambridge Universtiy Press, New York, NY, 1993).

[20] T. Dahms, Ph.D. thesis, Stony Brook University, Stony Brook, NY (2008).

[21] D. A. Bromley, in *Treatise on Heavy-Ion Science*, edited by D. A. Bromley (Plenum Press, New York, NY, 1984), vol. 1, chap. 1, pp. 3–132.

[22] P. Freier, E. J. Lofgren, E. P. Ney, F. Oppeneimer, H. L. Bradt, and B. Petters, Physics Review **74**, 213 (1948).

[23] E. M. Friedlander and H. H. Heckman, in *Treatise on Heavy-Ion Science*, edited by D. A. Bromley (Plenum Press, New York, NY, 1984), vol. 4, chap. 4, pp. 403–562.

[24] T. Matsui and H. Satz, Physics Letters B **178**, 416 (1986).

[25] S. S. Adler et al., Physical Review C **71**, 049901 (2004).

[26] A. Sickles, Ph.D. thesis, Stony Brook University, Stony Brook, NY (2005).

[27] J. D. Bjorken, Physical Review D **27**, 140 (1983).

[28] J. Jalilian-Marian and V. Koch, Physical Review C **58**, 3763 (1998).

[29] P. Braun-Munzinger, K. Redlich, and J. Stachel, in *Quark Gluon Plasma 3*, edited by R. C. Hwa and X.-N. Wang (World Scientific Publishing, 2003), p. 491.

[30] J. Adams et al., Nuclear Physics A **757**, 102 (2005).

[31] B. B. Back et al., Nuclear Physics A **757**, 28 (2005).

[32] I. Arsene et al., Nuclear Physics A **757**, 1 (2005).

[33] S. S. Adler et al., Physical Review Letters **91**, 182301 (2003).

[34] S. S. Adler et al., Physical Review Letters **94**, 232301 (2005).

[35] S. Afanasiev et al., Physical Review Letters **99**, 052301 (2007).

[36] S. S. Adler et al., Physical Review Letters **96**, 032301 (2006).

[37] A. Adare et al., Physical Review Letters **98**, 172301 (2007).

[38] A. Adare et al., Physical Review Letters **98**, 162301 (2007).

[39] A. Adare et al., Physical Review Letters **98**, 172301 (2007).

[40] A. Adare et al., Physics Review C **81**, 034911 (2010).

[41] A. Adare et al., Physics Review Letters **101**, 162301 (2008).

[42] A. Adare et al., Physics Review Letters **104**, 132301 (2010).

[43] M. Martinez and M. Strickland, Physics Review C **78**, 034917 (2008).

[44] T. Englemore, Nuclear Physics A **830**, 853c (2009).

[45] A. Adare et al., Physics Review C **83**, 044912 (2011).

[46] G. E. Brown and M. Rho, Physical Review Letters **21**, 2720 (1991).

[47] G. E. Brown and M. Rho, arXiv?? nucl-th/0509002v1 (2005).

[48] T. Hatsuda and S. H. Lee, Physical Review C **46**, 34 (1992).

[49] J. W. Holt, G. E. Brown, T. T. S. Kuo, J. D. Holt, and R. Machleidt, Physical Review Letters **100**, 062501 (2008).

[50] D. Trnka et al., Physical Review Letters **94**, 192303 (2005).

[51] G. Q. Li, C. M. Ko, and G. E. Brown, Physical Review Letters **75**, 4007 (1995).

[52] G. E. Brown and M. Rho, Physics Report **363**, 85 (2002).

[53] E. L. Bratkovskaya, W. Cassing, and O. Linnyk, Physics Letters B **670**, 428 (2009).

[54] H. S. Matis et al., Nuclear Physics A **583**, 617c (1994).

[55] G. Agakishiev et al., Physics Letters B **690**, 118 (2010).

[56] M. H. Wood et al., Physics Review C **78**, 015201 (2008).

[57] R. Baur et al., Nuclear Instrumentation Methods A **343**, 87 (1994).

[58] G. Agakichiev et al., Nuclear Instrumentation Methods A **371**, 16 (1996).

[59] G. Agakichiev et al., European Physics Journal C **41**, 475 (2005).

[60] D. Adamova et al., Physical Review Letters **91**, 042301 (2003).

[61] M. C. Abrea et al., Physics Letters B **410**, 327 (1997).

160

[62] K. Banicz et al., Nuclear Instrumental Mentods A **546**, 51 (2005).

[63] R. Arnaldi et al., Physics Review Letters **96**, 162302 (2006).

[64] M. C. Abreu et al., European Physics Journal C **14**, 443 (2000).

[65] R. Arnaldi et al., Physic Review Letters **100**, 022302 (2008).

[66] A. Adare et al., Physics Letters B **670**, 313 (2009).

[67] R. Rapp, in *AIP Conference Proceedings on the International Workshop on Chrial Symmetry in Hadrons and Nuclei*, edited by J. M. Nieves, E. Oset, and M. J. V. Vacas (American Institute of Physics, 2010), vol. 1322, p. 55.

[68] Jie Zhao presented at Quark Matter 2011 for the STAR collaboration.

[69] J. Adams et al., Physical Review Letters **92**, 092301 (2004).

[70] E. V. Shuryak and G. E. Brown, Nuclear Physics A **717**, 322 (2003).

[71] R. Rapp, Nuclear Physics A **725**, 254 (2003).

[72] Http://www.bnl.gov/rhic/complex.asp.

[73] Https://www.phenix.bnl.gov/WWW/run/drawing/index.html.

[74] K. Adcox et al., Nuclear Instruments and Methods in Physics Research A **499**, 469 (2003).

[75] M. Allen et al., Nuclear Instruments and Methods in Physics Research A **499**, 549 (2003).

[76] C. Adler, A. Denisov, E. Garcia, M. Murray, H. Strobele, and S. White, Nuclear Instruments and Methods in Physics Research A **499**, 433 (2002).

[77] C. Adler, A. Denisov, E. Garcia, M. Murray, H. Stroebele, and S. White, Nuclear Instruments and Methods in Physics Research A **470**, 488 (2001).

[78] M. Aizawa et al., Nuclear Instruments and Methods in Physics Research A **499**, 508 (2003).

[79] K. Adcox et al., Nuclear Instruments and Methods in Physics Research A **499**, 489 (2003).

[80] Y. Akiba et al., Nuclear Instruments and Methods in Physics Research A **453**, 279 (2000).

[81] Y. Akiba et al., Nuclear Instruments and Methods in Physics Research A **433**, 143 (1999).

[82] L. Aphecetche et al., Nuclear Instruments and Methods in Physics Research A **499**, 521 (2003).

[83] S. Butsyk, Ph.D. thesis, Stony Brook University, Stony Brook, NY (2005).

[84] Https://www.phenix.bnl.gov/WWW/run/05/dataprod/dp.html.

[85] Https://www.phenix.bnl.gov/WWW/run/04/dataprod/QA/index.php.

[86] J. Jia, Journal of Modern Physics E **16**, 2000 (2007).

[87] Outliers are identified using Chauvenet's criterion, requires a statistical weight of more that 0.5. This is consistent with a 3σ cut since our sample size is 14.

[88] A. Adare et al., Physical Review Letters **97**, 252002 (2006).

[89] Internal PHENIX Analysis Note 089 by Ralf Averbeck, Yasuyuki Akiba and Takashi Hachiya.

[90] N. M. Kroll and W. Wada, Physical Review **98**, 1355 (1955).

[91] A. Adare et al., Physics Review Letters **101**, 162301 (2008).

[92] Internal PHENIX Analysis Note 559 by Masahiro Konno.

[93] A. Adare et al., Physical Review D **83**, 052004 (2001).

[94] S. Adler et al., Physical Review C **75**, 024909 (2007).

[95] A. Adare et al., Physical Review C (2010).

[96] A. Adare et al., Physics Letters C **83**, 024909 (2011).

[97] A. Adare et al., Physical Review Letters **101**, 122301 (2008).

[98] Internal PHENIX Analysis Note 770 by Dimitri Kotov, Alexander Milov, Maxim Naglis, Victor Riabov and Yuri Riabov.

[99] Internal PHENIX Analysis Note 638 by Kushal Das, Anthony D. Frawley, Alexander Lebedev, Xie Wei and Susuma Oda.

[100] K. Adcox et al., Physical Review Letters **88**, 192303 (2002).

[101] L. M. Lederman and B. G. Pope, Physical Review Letters **27**, 765 (1971).

[102] Jason Kamin presented at Quark Matter 2011 for the PHENIX collaboration.

[103] L. E. Gordon and W. Vogelsang, Physics Review D **48**, 3136 (1993).

[104] Daisuke Watanabe presented at the Winter Workshop on Nuclear Dynamics 2011 for the PHENIX collaboration.

[105] J. Manninen, E. L. Brakovskaya, W. Cassing, and O. Linnyk, European Physics Journal C **71** (2011).

[106] K. Dusling and I. Zahed, Nuclear Physics A **825**, 212 (2009).

[107] J. Heuser et al., Nuclear Instruments and Methods in Physics Research A **511** (2003).

[108] ArXiv 1103.4277v1 by W. Anderson et. al. submitted to Nuclear Instruments and Methods.